On Star-Planet Interaction: Magnetospheric Dynamics and Atmospheric Evolution

Matthew Alan Tilley

A dissertation submitted in partial fulfillment of the
requirements for the degree of

Doctor of Philosophy

University of Washington

2018

Reading Committee:

Erika M. Harnett, Chair

Robert M. Winglee

Victoria Meadows

Program Authorized to Offer Degree:
Earth and Space Sciences

University of Washington

Abstract

On Star-Planet Interaction: Magnetospheric Dynamics and Atmospheric Evolution

Matthew Alan Tilley

Chair of the Supervisory Committee:
Professor Erika M. Harnett
Department of Earth and Space Sciences

With the explosion of exoplanetary discoveries, the question of planetary habitability is at the forefront, and generates many interesting and complex questions. One of those questions: Are planetary global magnetic fields necessary for the development of complex surface organics and the development of life? Does a global field protect planetary atmospheres? What detection signatures can be gleaned from a planet or moon with a global field as opposed to one without? We have a wealth of in situ magnetospheric data from Earth, as well as solar system planets and their moons from several vital satellite missions, such as the Voyager missions, the Pioneer missions, Galileo, Cassini, Messenger, MAVEN, and New Horizons. Due to the distances involved, it is not tenable to send satellites to obtain data at exoplanetary bodies, so we rely on simulations and using solar system data as analog environments to help set ground truth validation for the numerical work.

In this dissertation, I use a multifluid plasma model for gas giant magnetospheres to predict the potential dynamical consequences and detection signatures for giant exoplanets in a warm orbit ($\sim$0.2 AU). I discuss the dynamics of plasma loss from an exomoon injected torus, and how the total mass flux out of the system is altered by increased stellar wind forcing as a function of orbital semi-major axis. Detection signatures for such a planet, including transit depth modifications due to plasma densities and radio emissions, show promise for further detecting and characterizing future systems. I also improve the multifluid model by implementing a full treatment of pressure anisotropy at Saturn, with a focus on

the dynamics and structure of the magnetosphere. The improvements to the physics of the model generate more accurate system when compared to Cassini data; the anisotropic simulations show stronger current confinement of the Enceladus torus, consistent and well-structure flux interchange events, and global corotational convection that match more closely with the Cassini data than the isotropic model.

Turning from giant planets to terrestrial, I use a coupled one-dimensional photochemical and radiative-convective climate model to investigate the effects of M dwarf stellar flare activity on an Earth-like atmosphere for an unmagnetized planet in the nominal habitable zone. I find that EM-only activity - even to the level of some of the most active stars yet observed - is insufficient at the age of the universe to reduce the ozone column to the point that UV-C radiation can reach the surface. However, repeated proton events from frequent daily flare activity, which has been observed on several M dwarfs, can erode the ozone column by several orders of magnitude, allowing the surface of the planet to be bathed in UV-C, which is sterilizing and detrimental to the development of complex organic structures. The ability of a strong planetary magnetic field to deflect incoming stellar wind and flare-energized protons seems to be of import to maintain surface habitability.

I also use scaling laws to predict a potential atomic oxygen auroral signal from Proxima Centauri b, the detection of which would constrain the presence of an atmosphere and point to the presence of a magnetic field. The increased forcing from Proxima Centauri's stellar wind is expected to drive powerful emissions, orders of magnitude stronger than at Earth, and within easy reach of the next generation of observational telescopic instruments.

Magnetic fields do seem to be important for both detection and potential shielding of the atmosphere of exoplanets, but much work remains to be performed. Future observations combined with simulations validated against solar system star-planet interactions will likely provide answers to these questions, and perhaps lead to a focus on specific planetary targets for extensive investigation of astrobiological interest.

TABLE OF CONTENTS

LIST OF FIGURES

ACKNOWLEDGMENTS

The work during my last 5.5 years would not have been achieved without support from some amazing people.

My advisor, Erika Harnett, has provided guidance and encouragement that has been invaluable to my development as a scientist. My committee members, Robert Winglee, Victoria Meadows, and Michael McCarthy have likewise contributed their time and patience to help guide me towards a broader scientific outlook. Numerous students from both the Department of Earth and Space Sciences, as well as the Astrobiology Program are owed a thanks for their supportive conversations - both professional and personal.

I would like to also acknowledge my parents, Glenda Cowan and Donald Tilley, and my sister, Paige Jones, for fostering my lifelong love of science, mathematics and experimentation. Finally, I would like to thank my wife, Elizabeth Walker-Tilley, for her unrelenting support, encouragement, and patience. She has helped me to realize that perseverance and determination can drive one to conquer the mightiest of obstacles.

The UW Astrobiology Program and NAI Virtual Planetary Laboratory have provided generous financial support for research and travel during my time in the dual-title Ph.D. program, and provided many beneficial opportunities for professional development. I also would like to acknowledge the International Space Science Institute (ISSI), following useful discussions at ISSI Team Meeting "Coordinated Numerical Modeling of the Global Jovian and Saturnian Systems."

Chapter 1

INTRODUCTION

The first exoplanet was confirmed only 26 years ago (Wolszczan and Frail, 1992), and at present, there are 3,605 confirmed extrasolar planets and 4,496 planetary candidates awaiting confirmation (NASA, 2018). Instruments such as the Hubble Space Telescope (HST) and Kepler have opened our eyes to the truth that every star we see (and, statistically, those we can't) likely have planetary companions. Morton and Swift (2014) have suggested that observational statistics imply there are $\sim$2 planets for every nearby M dwarf, and up to 0.8 Earth-like planets in those stars' habitable zones. Characterizing these planets, even our closest neighbor - Proxima Centauri b (Anglada-Escudé et al., 2016), is a difficult and complex task that requires an ever-growing toolset. Current methods allow measurement of host star characteristics, orbital parameters, planetary mass, and for a few worlds - insight into the atmosphere of the planet. Spitzer and HST, for instance, have detected water vapor, alkali metals, and potential clouds on H_2-dominated hot Jupiter to sub-Neptune planets (e.g., Redfield et al., 2008; Wakeford et al., 2013; Kreidberg et al., 2014). The James Webb Space Telescope (JWST), scheduled for launch in early 2019 and upcoming Extremely Large Telescopes (ELTs) on the ground will allow us to probe the atmospheres of ever smaller planets from the visible through mid-infrared spectrum in the next 5-10 years. Beyond these capabilities, future mission concept such as the Large UV Optical Infrared Surveyor (LUVOIR) may characterize the atmospheres and surfaces of dozens of habitable zone terrestrial planets from UV to NIR wavelengths.

Only a few decades older than exoplanetary discovery, is the science of space weather, or star-planet interaction via magnetic fields and charged particles. Of particular scientific benefit from the 20th century's Cold War was the initiation of the space race, which confirmed predictions for the solar-terrestrial connection of geomagnetic storms (e.g. Chapman and Ferraro, 1930) and Parker's detailed solar wind outflow theory (Parker, 1958) via ob-

servations taken by the Soviet *Luna 1* satellite in 1959 (e.g., Harvey, 2007, for a historical review). Similarly, and simultaneously, rocket-based experiments and satellites discovered Earth's magnetosphere (and its interaction with the solar wind), the Van Allen belts, and particle precipitation that affects Earth's upper atmosphere (e.g., Gillmor and Sprieter, 1997, for a historical review).

More recently, satellite instrumentation on missions such as Ulysses, IMP-8, SOHO, and Stereo-A/B have driven solar wind discoveries. Voyager 1 and 2, the Mariner and Pioneer missions, Galileo, Cassini, and New Horizons have given us plasma and/or magnetic data from every planet in the solar system - and a fair number of the natural satellites orbiting those planets - in addition to extended solar wind data throughout the heliosphere (e.g. Schubert and Soderlund, 2011; Borovikov and Pogorelov, 2014; Bagenal et al., 2016, and references therein). While measurements of exoplanet stellar-magnetospheric interaction will remain challenging over the next few decades, new systems and technologies may allow us to search for direct confirmation and characterization of exo-magnetospheres. However, even without direct measurements of planetary magnetospheric interactions, detailed simulations and the application of solar system measurements as analogs can illuminate these crucial star-planet interactions that affect a planet's potential to support an atmosphere and ocean. This is especially true for planets orbiting M dwarfs, the Galaxy's most common type of star, which display strong activity levels (Hawley et al., 2014) that can impact atmospheric loss processes (Dong et al., 2017; Garcia-Sage et al., 2017) and photochemistry (Segura et al., 2005). Radio astronomy is a powerful observational tool, unique to magnetospheric interactions, and this science will accelerate as large baseline interferometric systems such as Low Frequency Array (LOFAR) and Square Kilometer Array (SKA) (Zarka, 2007; Zarka, Lazio and Hallinan, 2015, e.g.) come online and to their full potential in the near future.

1.1 Star-Planet Interactions

Ignoring gravity, there are two primary ways in which a star can interact with a planetary body (and/or its satellites) - electromagnetic fields, and particle radiation. Both of these processes can have a dramatic effect on how an atmosphere develops and evolves over

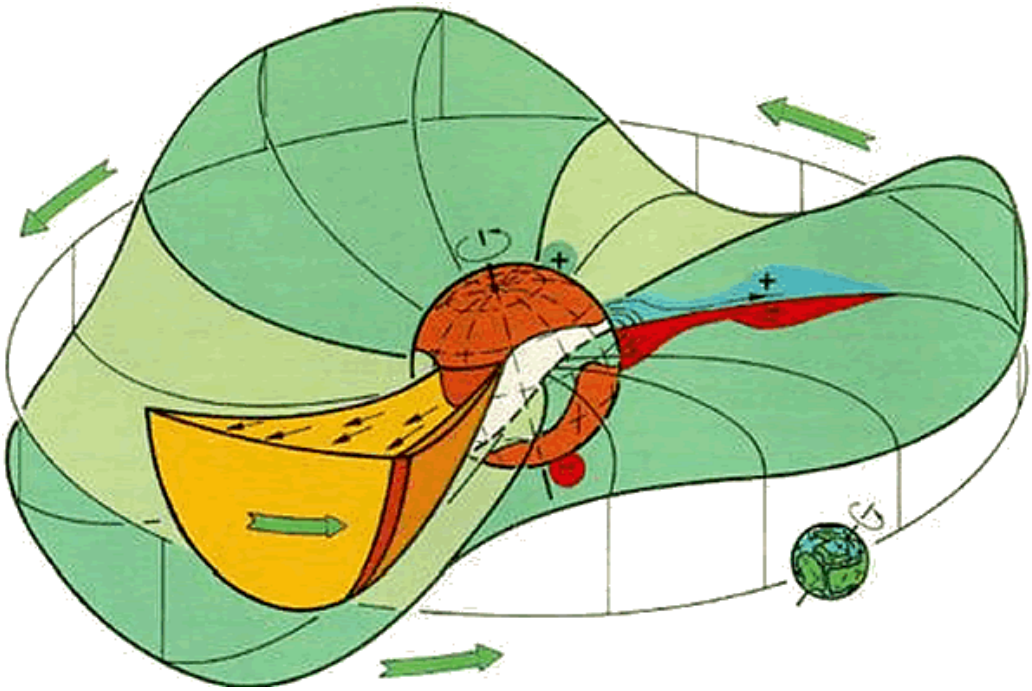

Figure 1.1 The so-called 'ballerina skirt' representing the electrical current sheet in the outflowing Parker spiral of the solar wind Alfvén (1977).

astronomical timescales, and sometimes on much shorter ones. There are two primary components to any magnetospheric interaction: 1) a stellar wind and radiation, and 2) the planetary magnetic environment.

The Sun's energetic outflow of ionized gas was proposed by Arthur Eddington in the early 20^{th} century, but it wasn't given its name until until Eugene Parker presented analysis detailing the hydrodynamic flow and subsequent heating of the corona, with gravity's inverse radial dependence allowing a transition to a constant, supersonic flow of plasma (Parker, 1958) (see, e.g., Fig. 1.1. Validation of the wind came soon thereafter when it was first measured in 1959 by the Soviet satellite, *Luna 1* (Harvey, 2007). Since then, the field of stellar atmospheres has become quite an active field of research, with observations, analysis, and models suggesting that there are stellar winds driven purely by radiation pressure in the hottest stars, as well as winds generated by active stellar hosts with strong rotation and convective processes producing intense magnetic fields (such as the Sun, and early M dwarfs). Since we have no method to measure, in situ, these winds from other stars, we

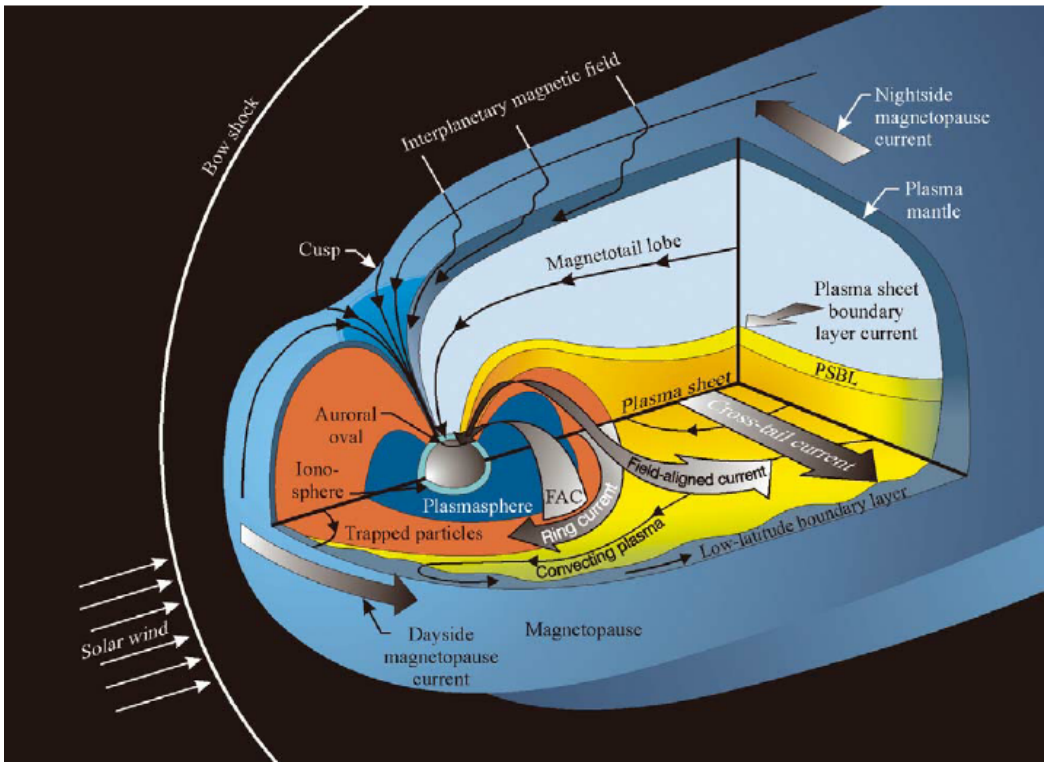

Figure 1.2 The complex interaction between Earth's magnetosphere and the solar wind (Parks, 1991).

must rely on indirect methods of measurement such as identifying the pressure balance between an astrosphere and the surrounding interstellar material (e.g. Wood et al., 2004; Wood, 2004; Wood et al., 2005), and magnetohydrodynamic (MHD) modeling based on what limited observational information we can glean from these stars (e.g. Cohen, Kashyap, Drake, Sokolov, Garraffo and Gombosi, 2011; Cohen et al., 2014; Garraffo, Drake and Cohen, 2016; Garraffo et al., 2017).

The stellar winds in this work are all considered to be magnetized winds, i.e., the outflowing plasma carries with it the extended, stretched field of the star generating the wind. When such a wind encounters a magnetized planet, it deposits some of its energy into the system which drives dynamic processes in the magnetosphere and atmosphere of the planet. One can think of this interaction as a flowing, electrified fluid deflected by and passing around an obstacle, except the fluid and obstacle are magnetized which can result in ener-

gization of the fluid through electromagnetic interactions. Fig. 1.2 shows the typical cartoon of the solar wind interacting with the Earth's magnetosphere, and the resulting complexity.

There is some pressure balance between the flowing, magnetized stellar wind - carrying with it a radially decreasing density of plasma and an intrinsic magnetic pressure which is balanced by the plasma and magnetic pressure in the planetary field. Where this interaction is balanced is the boundary of the magnetopause, and this signifies a separation between the two regimes. If the wind is supersonic (flowing faster than the local speed of sound, $v_s = \sqrt{\frac{k_B T}{m}}$) and/or super-Alfvénic (flowing faster than the local Alfvén speed, $v_A = \frac{B}{\sqrt{\mu_0 \rho}}$), there will be a shocked, magnetized plasma present on the wind-side of the boundary which results in heating of the plasma. Note that this general sort of interaction can also be expected for a moon orbiting in a rotating planetary magnetic field, e.g., Ganymede at Jupiter or Titan at Saturn. There is some level of energy deposition on the magnetosphere by the constant flow of the stellar wind. The kinetic and magnetic energies deposited drive particle energization, which can in turn enhance magnetic reconnection events, produce colorful displays of auroral activity, or result in instabilities that drive powerful radio emissions. The energy transferred can also result in both the enhanced outflow of plasma, or the precipitation of energetic charged particles into the upper atmosphere of the planet or moon, or into the surface of an airless body.

Of the solar system bodies, every planet except for Venus, Mars and Pluto have been observed to produce a dynamo-generated, intrinsic magnetic field. One planetary satellite, Ganymede at Jupiter, has also been observed to have a strong, intrinsic field. Other bodies in the system all exhibit some level of magnetic interaction with the solar wind, despite having no intrinsic magnetic moment, through their ionospheres - spherical, conducting shells of charged particles in the upper atmospheres of these bodies that serve to deflect the magnetic wind flowing from the Sun - though at a much lower altitude than those bodies with intrinsic fields.

From what we know of planetary science, it is likely that the solar system is not special, and we can safely assume a large percentage of extrasolar planets discovered also generate an intrinsic magnetic field and interact directly with their stellar hosts. No in situ observations are currently possible, and while information from remote observations can provide

some constraints on, e.g., planetary orbital characteristics, planetary mass, stellar type and activity, this information is limited, so we must rely on generalizing observationally validated solar system simulations. Even with instrumentation currently available, at least one extreme case of star-planet interaction for HD 179949 has been observed to suggest magnetospheric interaction driving periodic chromospheric heating (Shkolnik, Walker and Bohlender, 2003).

Planetary magnetic fields have a complicated relationship with the concept of habitability. Given the deflection of stellar wind by planetary magnetospheres, it might be assumed that these global fields provide an effective shield against atmospheric erosion by space weather, and are therefore promote the preservation of habitable environments over astronomical timescales. However, noting effects such as the polar wind outflow, atmospheric expansion by Joule heating, and ion pickup loss, it becomes apparent the situation is more complex and cannot be boiled down to such a simple relationship. Also there is the 92 bar atmosphere of Venus, an unmagnetized planet.

There has been an effort using analysis and scaling arguments to model extrasolar magnetospheric interaction, beginning shortly after the first exoplanet was confirmed. The initial impetus was the study of potential radio emission via cyclotron emission as a method for detection and characterization (e.g., Farrell, Desch and Zarka, 1999; Zarka et al., 2001; Grießmeier, Zarka and Spreeuw, 2007). More complicated models came soon thereafter, including ideal MHD simulations for hot Jovians (e.g., Preusse et al., 2005, 2007; Vidotto, Jardine and Helling, 2010; Cohen, Kashyap, Drake, Sokolov, Garraffo and Gombosi, 2011; Cohen, Kashyap, Drake, Sokolov and Gombosi, 2011). As observations from Kepler began to suggest the abundance of terrestrial planets, modeling efforts started investigating at potential effects of the presence or lack of a magnetosphere on detection and habitability due to stellar activity of M dwarf hosts (e.g., Cohen et al., 2014; Cohen et al., 2015; Garraffo, Drake and Cohen, 2016; Garraffo et al., 2017).

1.2 Dissertation overview

This dissertation presents results from modeling star-planet interactions with a focus on both magnetospheric dynamics and atmospheric evolution. The models used include a 3D

multifluid plasma model, and a 1D coupled, photochemical-climate model, the results of which are synthesized to provide insight about the ability for global planetary magnetic fields to protect potentially habitable environments. The results presented here are intended to contribute to the investigation of magnetospheric dynamics in the solar system, as well as magnetospheric impact on planetary detectability and contribution to planetary habitability, for both giant and terrestrial planets, and their satellites.

The first section of this work uses an isotropic, 3D multifluid plasma model to show that plasma dynamics for rapidly rotating, giant exoplanets differ from those observed in our own solar system. Specifically, the process of inner magnetospheric mass transport down the magnetotail transitions from being dominated by the interchange instability to following a simple Vasyliunas cycle. Despite this, there remains potentially sufficient density in exomoon tori that could contribute to detection and characterization of exomoons via transit signal alteration. I also show that planetary radio emission is likely to be significant for planets with low-inclination rotation in face-on warm or hot orbits with axisymmetric magnetic fields.

The second section focuses on comparison between simulations with a 3D multifluid model with a full treatment of anisotropic plasma pressure for Saturn, focused on determining the effects of plasma pressure anisotropy on magnetospheric dynamics. This section highlights the importance of including pressure anisotropy in producing more physically accurate modeling for solar system (and extrasolar planets), which suggests that it is important if we are to use such simulations as baselines for accurate simulations of extrasolar planets. The effects of pressure anisotropy at Saturn include confinement of plasma to the equatorial plane, alterations in magnetospheric convective patterns, force balance in a rapidly rotating system, pressure structures and the resulting plasma flow and loss from the system. These alterations could affect the orbital environment of, e.g., Enceladus and Titan, and the predicted density alterations could have effect on observations for Saturn-like exoplanets.

Part three of this work changes focus to smaller bodies, and presents study on the effects of repeated M dwarf flaring on a planet with an Earth-like atmosphere orbiting in the habitable zone. For active M dwarfs, stellar magnetic activity is commonly more

frequent and more energetic than that produced by our Sun. This increased activity, and close orbits of potentially habitable planets, significantly alters the planetary atmospheric chemistry through energetic charged particle precipitation; this alteration points to potential difficulties for surface habitability on world orbiting active M dwarfs.

The fourth section uses scaling arguments in combination with empirical models to predict the specific case of optical auroral emission at Proxima Centauri b. The planet is unique in its namesake proximity, and makes potential direct observation of magnetospheric processes possible. Detection of auroral emission could be used to constrain the presence of global magnetic field for the planet in addition to characterizing the atmosphere. Potentially detectable radio emission is discussed, as well, which would verify the presence of a global planetary magnetic field.

Lastly, there is short discussion of preliminary work done regarding, e.g.: 1) the modification of exoplanetary transit signals directly from exomoon plasma tori - providing direct observational evidence of an exomoon and its constituent makeup, 2) the simulation of the magnetosphere of Proxima Centauri b - with both the isotropic and anisotropic models, and 3) effects of pressure anisotropy on the magnetospheric structure at Saturn, which is related to the second section.

1.3 Relevance to Astrobiology

This thesis contributes to efforts mentioned in Section 5 of the 2015 Astrobiology Strategy Document (Hays et al., 2015), namely the effort in "identifying, exploring and characterizing environments for habitability and biosignatures." The simulation and analytical study of magnetic and particle interactions between stars and their orbiting planets is key to determining the habitability of planetary systems by accurately predicting surface and atmospheric interactions that can drive chemical evolution in the environments, e.g., atmospheric hazes like those at Titan, ozone loss from stellar activity, and icy-moon surface chemistry.

Chapters 3 and 4 of this dissertation are primarily focused on giant planets that - while not directly habitable - provide the corotating 'planetary wind' magnetic environment through which potentially habitable exomoons orbit; interactions between the exo-

moons and planetary plasma environment can provide detection signatures for potentially habitable exomoons (see, e.g., § 7.2.1 for overview and preliminary result), and accurately characterizing the magnetospheres of these planets is key to understanding the atmospheric or surface conditions experienced by these orbiting potentially habitable exomoons (e.g. Chyba, 2000). Chapter 3 shows that the presence of such exomoons orbiting giant planets as far as 0.2 AU from their stellar host could contribute to transit modifications, and the follow-up preliminary work in § 7.2.1 shows that exomoon atmospheric constituents could be constrained by transit modification from plasma tori. Chapter 4 is focused on improving the multifluid plasma model with updated physics to ensure more accurate prediction for both solar system and extrasolar system giant planetary bodies, with improvements validated against observations at Saturn.

Chapter 5 and 6 focus on the habitability and detection of terrestrial, potentially habitable exoplanets - including Proxima Centauri b. The effects of M dwarf activity on atmospheric evolution and the resulting surface habitability of Earth-like exoplanets orbiting in the nominal habitable zone is crucial for understanding habitability throughout the universe, as M dwarfs host the highest number of habitable planets in the galaxy The study of Proxima Centauri b's potential auroral activity could be key to characterizing the atmosphere and/or constraining the presence of the magnetic field of the planet with future observations. Preliminary work performed on the magnetosphere of Proxima Centauri b is also important as we don't yet understand how well such an environment could deflect energized particles from the very active Proxima Centauri.

While solar-terrestrial interactions have been studied for over a century, and extrasolar detection studies have been ongoing for a few decades, the study of general star-planet magnetic interactions as they pertain to habitability and detection is a relatively new area, and one that is complicated. The efforts here are steps forward towards expanding that area of study, and providing stepping stones for future efforts.

Chapter 2

NUMERICAL METHODS

While instrumentation can be sent to most places of interest in the solar system, these craft can only measure physical conditions along a single trajectory embedded in complex, large scale interactions. In concert with data-based validations, magnetospheric simulations provide deeper insight into dynamics and evolution in a complex, three dimensional space. In the case of extrasolar systems, data validated simulations are an imperative tool for characterizing these distant star-planet systems.

2.1 Multifluid Plasma Model

The 3D multifluid model separately tracks multiple, individual ion species, denoted below by subscript α in Eqs. (1) - (3), the conservative forms for mass, momentum and pressure (thermal energy density). The fluid ion species have arbitrary mass-to-charge ratio set in the code (e.g., 1 for H^+, 16 for O^+, etc.), but since the multifluid code cannot differentiate the physics of multiply-ionized species from singly-ionized species with identical m/q ratios, all simulated ion results could represent either (e.g., m/q of 16 could be O^+ or S^{++}). The assumption is that the total population is dominated by singly ionized species, which is energetically reasonable for the regimes chosen, event for ions present at orbits near the sun (e.g. Zurbuchen et al., 2008).

$$\frac{\partial \rho_\alpha}{\partial t} + \nabla \cdot (\rho_\alpha \mathbf{v}_\alpha) = 0 \tag{2.1}$$

$$\rho_\alpha \frac{d\mathbf{v}_\alpha}{dt} = q_\alpha n_\alpha (\mathbf{E} + \mathbf{v}_\alpha \times \mathbf{B}) - \nabla P_\alpha - \left(\frac{GM_P}{R^2}\right) \rho_\alpha \hat{\mathbf{r}} \tag{2.2}$$

$$\frac{\partial P_\alpha}{\partial t} = -\gamma \nabla \cdot (P_\alpha \mathbf{v}_\alpha) + (\gamma - 1)\mathbf{v}_\alpha \cdot \nabla P_\alpha \tag{2.3}$$

where ρ_α is the mass density, $\mathbf{v}_\alpha$ is the bulk velocity, n_α the number density and q_α the charge. G is the gravitational constant, M_P and R are the planetary mass and radial

distance from the planet (Saturn, for the present work), $\mathbf{E}$ is the electric field, and $\mathbf{B}$ is the magnetic field. P_α is the pressure associated with each ion species, α, and γ is the adiabatic index (5/3).

Electrons in the model are treated as a charge-neutralizing, mass-conserved fluid, and assumed to be in steady-state or drift motion (i.e. $dv_e/dt = 0$), which simplifies Eq. 2.2 for electrons to

$$\mathbf{E} + \mathbf{v}_e \times \mathbf{B} + \frac{\nabla P_e}{e n_e} = 0. \tag{2.4}$$

Given quasi-neutrality, and the definitions for current density, $\mathbf{J}$, and Ampére's Law, the pressure completes the description of electron dynamics:

$$n_e = \sum_i n_i, \qquad \mathbf{v}_e = \sum_i \frac{n_i}{n_e}\mathbf{v}_i - \frac{\mathbf{J}}{e n_e}, \qquad \mathbf{J} = \frac{1}{\mu_0}\nabla \times \mathbf{B} \tag{2.5}$$

$$\frac{\partial P_e}{\partial t} = -\gamma \nabla \cdot (P_e \mathbf{v}_{de}) + (\gamma - 1)\mathbf{v}_e \cdot \nabla P_e \tag{2.6}$$

where e is the magnitude of electron charge, n_e is the electron number density, and P_e is the pressure of the electron fluid. One can then substitute the Eqs. 2.5 into Eq. 2.4 to obtain the modified Ohm's law,

$$\mathbf{E} = -\sum_i \frac{n_i}{n_e}\mathbf{v}_i \times \mathbf{B} + \frac{\mathbf{J} \times \mathbf{B}}{e n_e} - \frac{1}{e n_e}\nabla P_e + \eta \mathbf{J}, \tag{2.7}$$

where η is the resistivity, which is added only in the ionosphere to allow finite conductivity. Everywhere else, η is zero so there is no anomalous resistivity in the model. The strength gained by modeling the electron and ion-species separately is that the model retains Hall and pressure gradient terms in the modified Ohm's Law, Eq. 2.7, which are sufficient to drive reconnection. One can substitute Eq. 2.7 into Eq. 2.2 to obtain the ion momentum,

$$\begin{aligned} \rho_\alpha \frac{d\mathbf{v}_\alpha}{dt} = q_\alpha n_\alpha \left(\mathbf{v}_\alpha - \sum_i \frac{n_i}{n_e}\mathbf{v}_i \right) \times \mathbf{B} + \frac{q_\alpha n_\alpha}{e n_e} (\mathbf{J} \times \mathbf{B} - \nabla P_e) \\ -\nabla P_\alpha + q_\alpha n_\alpha \eta \mathbf{J} - \left(\frac{G M_P}{R^2} \right) \rho_\alpha \hat{\mathbf{r}}. \end{aligned} \tag{2.8}$$

If one assumes a single ion species (single-fluid MHD) or a single velocity for all species (single-fluid, multi-species MHD), then Eq. 2.7 reduces to a form inherent to ideal MHD, and the first term of Eq. 2.8 disappears. It is this contribution from tracking multiple species with independent velocities that allows the multifluid model the capture ion cyclotron effects. The equations for the multifluid model were solved using a second order Runge-Kutta method on a nested grid.

2.2 Treatment of Pressure Anisotropy

For the work in Chapter 4 of the present work, the multifluid model was modified from an isotropic treatment of the ion fluids' pressures to include a full treatment of ion pressure anisotropy. Eq. 2.3, above, is the isotropic form of the ion pressure in the multifluid model (used in Chapter 3, and for comparison in Chapter 4), which by definition assumes the ion fluid pressures are equivalent in all directions.

Previous 3D magnetospheric simulations that have incorporated pressure anisotropy into their terrestrial MHD models (Meng et al., 2012, 2013) use the well-known Chew-Goldberger-Lowe (CGL) formulation (Chew, Goldberger and Low, 1956). The CGL treatment is given as:

$$P_{ij} = P_{\parallel}\hat{b}_i\hat{b}_j + P_{\perp}(\delta_{ij} - \hat{b}_i\hat{b}_j) \tag{2.9}$$

The CGL formulation only assumes gyrotropic contributions to anisotropy, and maintains a single, uniform isotropization factor throughout the magnetosphere which requires an artificially controlled relaxation to avoid runaway anisotropies. While the CGL formulation is popular, and can capture some effects of plasma fluid anisotropy, due to the above constraints, the CGL approach is a gross simplification of the dynamics in all but the least dynamic magnetohydrodynamic systems, given that most systems have orders of magnitude variations in, e.g., magnetic field strength, plasma density and plasma temperature.

To obtain the full treatment of ion pressure anisotropy, we start from the Vlasov equation, and calculate the second moment - pressure tensor - including symmetric off-diagonal components (e.g., Chapman and Cowling, 1970; Siscoe, 1983). The full tensor treatment

we employ was derived in Kidder (2011) (and in this work in Appendix A), and can be expressed as:

$$\frac{\partial \overline{\overline{\mathbf{P}}}_\alpha}{\partial t} + \nabla \cdot \left(\mathbf{v}_\alpha \overline{\overline{\mathbf{P}}}_\alpha \right) + \nabla \mathbf{v}_\alpha \cdot \overline{\overline{\mathbf{P}}}_\alpha + \left(\nabla \mathbf{v}_\alpha \cdot \overline{\overline{\mathbf{P}}}_\alpha \right)^T + \frac{q}{m_\alpha} \left[\left(\overline{\overline{\mathbf{P}}}_\alpha \times \mathbf{B} \right) + \left(\overline{\overline{\mathbf{P}}}_\alpha \times \mathbf{B} \right)^T \right] + \nabla \cdot \overline{\overline{\mathbf{Q}}} = 0 \tag{2.10}$$

This treatment alters the conservation of ion fluid momentum, Eq. 2.8 above, to contain a tensor pressure, so the gradient pressure term, ∇P_α, becomes a divergent term, $\nabla \cdot \overline{\overline{\mathbf{P}}}_\alpha$. The electron fluid remains isotropic.

All elements of the symmetric pressure tensor are retained which means that the total number of equations is twice that of the isotropic simulation codes. In our full treatment, as in the CGL treatment, the heat flux term is neglected ($\nabla \cdot \overline{\overline{\mathbf{Q}}} = 0$), which is a reasonable assumption if the system is strongly controlled by convection as in global magnetospheric systems.

Further discussion on the physics of pressure anisotropy can be found in Chapter 4.

2.3 1D Coupled Photochemical-Climate Model

The model used in Chapter 5 is based on the work of Segura et al. (2010), and consists of two time-dependent, coupled, one dimensional atmospheric models: a radiative-convective climate model and a photochemical model run for an Earth-like atmosphere.

The radiative-convective climate model itself is a hybrid of two models: 1) a δ two-stream scattering algorithm that is used to calculate fluxes and uses correlated-k coefficients (4 terms) to parameterize absorption by important atmospheric species, e.g., O_3, CO_2, H_2O, and CH_4 over 38 spectral partitions (Kasting and Ackerman, 1986; Toon et al., 1989; Pavlov et al., 2000); 2) for the thermal-IR wavelengths, the rapid radiative transfer model (RRTM) implemented by Segura et al. (2003) was used. The RRTM uses 16-term sums in each spectral band where k-coefficients are calculated to give high spectral resolution where Doppler broadening is important. The combination of these two models are used to generate the atmospheric temperature structure from 1 bar to 10^{-5} bar, divided into

51 pressure layers. Timesteps were adaptive, and determined by the temperature profile differences between prior and present times.

The photochemical model solves 217 reactions that link 55 chemical species, from 0 to 64 km altitude in 0.5 km steps. Photolysis was calculated using a δ two-stream routine that allowed scattering between molecular gases and the included aerosol species (Segura et al., 2003). Timesteps were solved using an implicit reverse Euler method, with initial timestep set to 10^{-4} s, with increasing magnitude as the system reaches equilibrium.

The coupling layer allowed the climate and photochemical model to cross-communicate and synchronize the atmospheric temperature structure, H_2O profiles and chemical alterations made for each timestep. The pressure layers calculated in the radiative-convective model were interpolated to the fixed altitude structure in the photochemical model, and then back, during the coupling procedure.

More details on the modifications made to the model that enhanced the capabilities from Segura et al. (2010) are reported in Chapter 5.

Chapter 3

EXTRASOLAR GIANT MAGNETOSPHERIC RESPONSE TO STEADY-STATE STELLAR WIND PRESSURE AT 10, 5, 1, AND 0.2 AU

3.1 Overview

This chapter reports on the effort of modeling giant, rapidly-rotation magnetosphere in increasingly warm orbits. A three-dimensional, multifluid simulation of a giant planet's magnetospheric interaction with steady-state stellar wind from a Sun-like star was performed for four different orbital semi-major axes - 10, 5, 1 and 0.2 AU. We simulate the effect of the increasing, steady-state stellar wind pressure related to the planetary orbital semi-major axis on the global magnetospheric dynamics for a Saturn-like planet, including an Enceladus-like plasma torus. Mass loss processes are shown to vary with orbital distance, with the centrifugal interchange instability displayed only in the 10 AU and 5 AU cases which reach a state of mass loss equilibrium more slowly than the 1 AU or 0.2 AU cases. The compression of the magnetosphere in the 1 AU and 0.2 AU cases contributes to the quenching of the interchange process by increasing the ratio of total plasma thermal energy to corotational energy. The strength of field-aligned currents (FAC), associated with auroral radio emissions, are shown to increase in magnitude and latitudinal coverage with a corresponding shift equatorward from increased dynamic ram pressure experienced in the hotter orbits. Similar to observed hot Jovian planets, the warm exo-Saturn simulated in the current work shows enhanced ion density in the magnetosheath and magnetopause regions, as well as the plasma torus which could contribute to altered transit signals, suggesting that for planets in warmer (>0.1 AU) orbits, planetary magnetic field strengths and possibly exomoons - via the plasma torus - could be observable with future missions.

This work has been published as Tilley, Harnett and Winglee (2016).

3.2 Introduction

Planetary science has undergone a recent renaissance, from both in-situ observations of solar system missions, and the inundation of exoplanetary discoveries by recent observational efforts. Our understanding of planetary formation, evolution and general physical characteristics has until recently been based solely upon those bodies found in our local system; exoplanetary observations have informed us that our system is one in a field of near-infinite variation. Given this fact, we must work to abstractly quantify a framework for the systems to progress in planetary science. Approximately two-thirds of confirmed exoplanets are giant planets ($\geq$ 0.01 M_{Jup}) that orbit their host stars at relatively small distances (a $\leq$ 0.5 AU) (Han et al., 2014). This fact serves to both challenge our notions of planetary formation and evolution, and to provide opportunities to develop new approaches to study planetary configurations to interpret and support the observational data.

A key question addressed in recent works about planetary evolution is the rate at which mass is lost from the atmosphere. The study of aeronomy for giant exoplanets has indicated that thermal and non-thermal processes both contribute strongly to mass loss for these giant bodies (e.g. Yelle, Lammer and Ip, 2008). The overall system of exoplanetary mass transport involves escaping atmospheric species from the upper planetary atmosphere and active satellites outward throughout the surrounding magnetic environment. A large amount of material escaping from the atmosphere of a planet is likely to become ionized and contribute to dynamics in the planetary magnetosphere. The inclusion of this magnetic environment is a step towards a comprehensive view of planetary systems; the magnetic environment not only contributes to mass transport, but to the potential generation of detectable radio signals that can be used for detection and characterization (e.g. Zarka, 2007), as well as potential alterations of transit light curves which would allow some insight into planetary characteristics (e.g. Vidotto, Jardine and Helling, 2010; Llama et al., 2013; Ben-Jaffel and Ballester, 2014; Nichols et al., 2015; Alexander et al., 2015).

Recently, the question of exomoon habitability has become quite important, as the detection of these bodies in the habitable zone of the stellar hosts is now possible (Heller and Barnes, 2013). The environment through which potentially habitable exomoons orbit

can be a highly dynamic magnetized plasma system that picks up ionized species, as well as injecting energized species into the upper atmosphere of the satellites, affecting the atmospheric chemistry and mass loss rates from these smaller bodies (e.g. Brown, Lebreton and Waite, 2009). Alternatively, the impact of energized charged particles on the surface of an icy moon can drive the formation of organic molecules, creating the building blocks necessary for the formation of life (e.g. Chyba, 2000; Hand, Carlson and Chyba, 2007). The balance between such processes will inform a habitable satellite versus an uninhabitable one, and therefore the inclusion of the magnetic star-planet-moon interaction is key to developing an accurate model for predicting the atmospheric state of an observed exomoon.

A magnetized stellar wind can couple directly with planetary magnetospheres through reconnection at the magnetopause and down the magnetotail (Dungey, 1961) and provides external forcing through viscous interaction (Axford and Hines, 1961). The Dungey reconnection framework is known to be a significant driver of magnetospheric interaction with the solar wind, as reconnection dominates production of plasma flows. Corotation and viscous flows are thought to be as important for rapidly rotating magnetospheres with significant internal plasma sources, like Jupiter and Saturn, though it is still not clear to what extent relative to the Dungey-type magnetospheric picture (e.g. Brice and Ioannidis, 1970; Delamere and Bagenal, 2010). Determining the response of planetary magnetospheres to various stellar wind conditions is a primary task in comparative planetary science. Key to this task is understanding the relative contribution to the global dynamics of magnetospheric systems of both external processes, e.g. stellar wind characteristics, and internal processes, e.g. rapid corotation of heavy-ion plasma transmitted by the corotating planetary magnetic field. The imperative of understanding this balance is especially true for those planets which are subject to both significant external and strong internal processes, such as Saturn. The balance between these internal and external drivers contribute to the processes of mass loss, as well as the energization of particles throughout the magnetosphere, setting up vastly different potential orbital environments for satellites.

At $\sim$10 AU, the magnetosphere of Saturn experiences $\sim$0.01$\times$ the stellar wind dynamic ram pressure as the terrestrial magnetosphere due to decreased steady-state solar wind density, but the magnetospheric cross-section of Saturn is $\sim$400$\times$ larger. This leads to

a scaling for the incident power by the solar wind on the magnetosphere of Saturn that is $\sim$4$\times$ that of Earth under similar conditions (e.g. Zarka, 1998). At Earth, however, the magnetosphere is almost entirely externally driven by the solar wind due to a slower rotation combined with the lack of significant internal ion sources.

Given only the amount of forcing by the solar wind on Saturn and the scaling mentioned above, one could simply assume that Saturn's magnetospheric dynamics in response to the solar wind are much like Earth's. While the mass of Saturn is two orders of magnitude greater than Earth, the effects of gravity in Saturn's magnetosphere are similar to that of Earth's for similar scales; at one bar of atmospheric pressure at Saturn, the gravitational acceleration is just 6.5% greater than that at Earth's surface. Saturn's magnetosphere, however, has two primary characteristics that differentiate it from Earth's: a rapid corotation with the planet itself, a factor of $\sim$2.2 greater than Earth, and a constant source of water group heavy-ions, e.g. OH^+ and O_2^+, formed from H_2O that is continuously injected at $\sim$4R_S by Enceladus; these neutrals subsequently undergo ionization and pick-up to corotate with Saturn's magnetosphere (Tokar et al., 2008). At just a few percent concentration, these heavy ions can strongly affect the dynamics of the inner magnetosphere by carrying the bulk of the kinetic energy of corotation, and dominating the pressure over H^+ (e.g. Thomsen et al., 2010). The injection of these heavy-ions provides a constant source of mass input to the magnetosphere of Saturn, the loss of which is drained through global, magnetospheric processes that are not currently well-understood. An open question that is relevant to the Saturn-like system discussed in this chapter concerns how injected heavy ion plasma transports out of the magnetosphere with varied stellar wind external forcing.

Though internal heavy-ion effects at Saturn are key to understanding global magnetospheric behavior, the solar wind dynamic ram pressure also controls large scale dynamics, and directly influences the radio power radiated by giant planetary magnetospheres, like Saturn's Kilometric Radiation (SKR). Radio emissions can be controlled by the variations in the solar wind (Desch, 1982; Desch and Rucker, 1983), which drives related large scale dynamics throughout both the dayside and nightside magnetosphere, and Dungey-like reconnection events in magnetotail or cusp regions (e.g. Bunce et al., 2005; Cowley et al., 2005; Mitchell et al., 2005). This radio emission behavior has been observed throughout the

solar system for all planets with a global magnetic field (Desch and Kaiser, 1984). However, there are at least two sources of power for radio emissions observed in the solar system - solar wind and rotation - the aforementioned simple scaling estimates extrapolated from observations throughout the solar system indicate that certain exoplanets may emit detectable radio emissions driven by stellar wind-magnetosphere interaction.

Several authors have used global simulations to investigate the direct magnetic star-planet interaction (SPI) for closely orbiting hot Jovian planets which, until the Kepler mission, was the most commonly observed configuration due to selection bias of the detection methods involved (e.g. radial velocity method). For example, Preusse et al. (2007) used ideal MHD simulations to investigate the star-planet interactions of giant planets for varying orbital distances of 0.01-0.2 AU around a Sun-like star. The majority of the cases studied took place within the Alfvén and sonic critical radii of the star which allows direct feedback of planetary plasma onto the star. However, the simulated case in the super-Alfvénic region at 0.2 AU showed a planetary magnetosphere very much like the compressed dayside dipole and stretched magnetotail structure exhibited by the solar system planets with significant global magnetic fields. Ideal MHD was also used to investigate SPI for an observed, transiting exoplanet, HD 189733b (Cohen, Kashyap, Drake, Sokolov, Garraffo and Gombosi, 2011); the models predicted reconnection events that induce a significant planetary magnetospheric mass loss on the order of 10^{-12} $M_{Jupiter}$ yr^{-1}, and that the energy dissipated by SPI could explain modulations in the Ca II lines previously observed for the host star (e.g. Shkolnik et al., 2008). The same model was then used to investigate the effects of a coronal mass ejection (CME) on a hypothetical hot gas giant, $\sim 1.5 R_{Jup}$, which yielded magnetospheric predictions involving significant changes to planetary magnetospheric response. Field-aligned current systems were altered from the two lobe model, common to Earth and the giant planets under nominal conditions in our solar system, to resemble Alfvén-wave driven wings around the planet, similar to those formed at Io and Europa, which has implications on the processes of energy distribution from the CME into the magnetosphere (Cohen, Kashyap, Drake, Sokolov and Gombosi, 2011). Llama et al. (2013) used a 3D MHD stellar wind model and an analytical planetary bow shock model to investigate the potential for a dense planetary bow shock region to contribute to transit observations for HD 189733

b, and found that indeed for a star with similar composition to the Sun, such absorption of the emitted stellar Mg 2 is possible given the authors' assumption of low temperature magnetosheath plasma. Ben-Jaffel and Ballester (2014) used a particle-in-cell (PIC) code to investigate the effects of a potential satellite produced plasma torus on transit curves for WASP-12 b and HD 189733 to explain the early ingress identified in observations (Fossati et al., 2010; Haswell et al., 2012; Nichols et al., 2015; Alexander et al., 2015). These findings open an exciting new vista on planetary science. The findings suggest that it is possible to extract exoplanetary characteristics from transit light curves, with appropriate modeling and data analysis. In combination with radio emissions, we could eventually piece together a more complete understanding of the exoplanets that have been confirmed as instrumentation and modeling intersect and improve.

With the exception of Ben-Jaffel and Ballester (2014), the efforts mentioned above were carried out using single fluid, 3D ideal MHD models, and developed an initial global analysis of stellar wind influence on the planetary magnetosphere of hot gas giants. These simulations differ from the ones used in the present work in their use of ideal MHD simulations and focus on Jovian planets in very hot orbits ($\sim$0.02 AU). Ideal MHD simulations, however, fail to capture some important physics driven by the mass differences between heavy and light ions but are captured by the multifluid model (e.g. Winglee, Harnett and Kidder, 2009). This paper presents the results for 3D multifluid simulations of Saturn-like planets, which are relatively smaller and magnetically weaker than the hot Jovians mentioned above, and therefore closer in mass to the majority planets being discovered. The investigation includes the Saturn-like planet at various semi-major axes, the closest of which is $\sim$0.2 AU, which is approximately one order of magnitude farther from the host star than the previously mentioned simulations. A Saturn-like planet was chosen as baseline instead of a Jupiter-like for three main reasons. First, the recent wealth of Cassini data provides a more comprehensive baseline for the validation case at 10 AU so that the starting point is data-driven. Second, the weaker planetary magnetic field allows for a less computationally intensive load for the 3D simulation - the Alfvén speed calculated at the inner boundary often sets the timestep of the simulation. Lastly, a smaller injection rates produce a more stable satellite plasma torus with less mass lost to the inner boundary due to pressure

gradients.

The work herein is a next step for the study of stellar-extrasolar gas giant magnetospheric interactions, investigating potential plasma populations including ionospheric outflows of heavy-ions or injection by natural satellites. The heavy ions can dominate the corotational kinetic energy of the magnetosphere at a rate of only a few percent of the total plasma population. High heavy-ion injection rates also have an influence on magnetospheric pressure balance with the stellar wind by increasing the internal plasma pressure of the magnetosphere (e.g. Pilkington et al., 2015). Building on the previous works, the efforts in this chapter will contribute to a ground truth for warm gas giant magnetospheric response to stellar wind. We use our simulations with this regard.

The 3D global multi-fluid, multi-scale model, is outlined in § 2.1, with boundary and initial conditions discussed below in § 3.3 & 3.4. § 3.7, 3.8, 3.9, and 3.10 contain the discussion and results of our simulations.

3.3 Simulation Grid

For each simulation in the present work, the following grid parameters were kept static across all planetary simulations. The simulation's Cartesian coordinate system is such that x is in the direction of a planet-star line in the equatorial plane of the planet, positive pointing away from the star. The z axis is aligned with the planetary rotation axis positive towards the northern magnetic pole as the magnetic configuration of the planet is axisymmetric. The y direction completes a right-handed coordinate system, and points in the direction of the tangent to planetary orbital motion.

Five cubic, nested grids were used for each case in the study, with the innermost grid centered on the planet with an inner boundary at 2.0 R_P. This inner grid is $\pm 12 R_P$ in the x- and $y-$directions, and $\pm 6 R_P$ in the z-direction, with a resolution of $0.2 R_P$ in all dimensions. Each higher-order grid increases the resolution by a factor of 2, and so the outermost grid is a factor of 16 larger, but not necessarily centered on the planet. The outermost grid extends from -$128 R_P$ sunward to $256 R_P$ down the magnetotail in the x-direction, $\pm 192 R_P$ in the y-direction, and $\pm 96 R_P$ in the z-direction. This scaling allows the multifluid model to capture dynamics across multiple scales, from a fraction of a planetary radius, up to

Table 1. Stellar wind conditions and magnetopause parameters

	10 AU	5 AU	1 AU	0.2 AU/D/S
n_H^+ (cm^{-3})	0.065	0.26	6.5	162.5
T_H^+ (eV)	1.2	2.5	4.7	39.0
P_{dyn} (nPa)	0.022	0.088	2.2	55.0
IMF $\|B\|$ (nT)	0.51	1.0	5.1	27.2
IMF $\|B_z\|$ (nT)	-0.13	-0.26	-1.3	-6.4
IMF ϕ (deg)	84.3	80.5	45.0	14.0
R_{MP} (R_P)	20.9	16.0	10.1	5.9/6.6/3.1

Note. — Stellar wind conditions and the resulting magnetopause standoff distance for each of the 4 cases discussed. The stellar wind parameters for the two additional cases at 0.2 AU (D - dense, S - slow) are the same as the 0.2 AU base case; only planetary parameters were altered, which led to differing values for the substellar magnetopause distance.

massive structure formation down the magnetotail.

3.4 Initial Conditions

The 3D multifluid code tracks three distinct, separate ion species and a separate electron fluid. H^+ is present in the solar wind, and is also present in the Saturn-like planet's ionosphere and plasma torus. Two heavier species are tracked: a 18 amu ion fluid, representing potential medium mass species such as O^+, or H_2O^+, and a heavier fluid at 32 amu, representing more massive ions such as O_2^+. The planetary body for each baseline simulation case

is assumed to be identical to that of Saturn, in terms of radius, mass, obliquity, rotation, magnetic field, and ionosphere so that comparisons are solely reliant upon the changing dynamic ram pressure (except for two cases at 0.2 AU discussed below). Saturn was chosen to set a strong, ground truth baseline from the wealth of Cassini observations available (e.g. Dougherty, Esposito and Krimigis, 2009).

A Sun-like, G-type star, is assumed to generate the stellar wind for each case in this study. The stellar wind, consisting of a quasi-neutral plasma comprised of H^+ and electrons, is blown into the grid system from the negative x-direction, at a speed of 450 km/s in the direction of the positive x-axis, with the IMF direction calculated according to a Parker spiral. The planetary rotational axis is aligned to simulate an equinox seasonal configuration. Each case represents the simulation at a different orbital semi-major axis around the star: 10 AU, 5 AU, 1 AU, and 0.2 AU; the latter distance at 0.2 AU includes a base case, with only the effects of stellar wind pressure from the hotter orbit taken into account, and two additional studies. The additional studies include the baseline dynamic ram pressure from the stellar wind at 0.2 AU, with the addition of one case with a decreased planetary rotation rate, to investigate potential gravitational tidal effects, and one case with higher ionospheric and satellite torus plasma density to account for increased photoionization (see Section 3.6). The radial temperature dependence of the incident stellar wind is provided by the synthesis of Voyager 2 data and temperature-velocity relations, after Richardson and Smith (2003). Density of the stellar wind was assumed to follow a R^{-2} isotropic expansion scaling relation, following Voyager 2 observations (e.g. Belcher et al., 1993). The interplanetary magnetic field (IMF) carried by the stellar wind plasma follows the assumption of a Parker spiral, i.e. $B_r \propto R^{-2}$ and $B_\phi \propto R^{-1}$ - see Table 1 for details. To isolate the effect of dynamic forcing from the steady state stellar wind's pressure on the planetary magnetosphere, the orientation of the z-component of the IMF is held consistently in a negative orientation, or parallel to the equatorial dipole field of the Saturn-like planet. Future work is planned to address the effects of an open-type magnetospheric interaction - including Dungey-type reconnection. For each case mentioned above, Table 1 contains the relevant steady-state conditions.

3.5 Plasma Torus

An Enceladus-like plasma torus was included in the model, and maintained for each semi-major axis at which the simulations were run. The plasma torus was injected equally across azimuth with Gaussian cross-section, with a mean at 4 R_P, σ=0.5 R_P, which gives a volume of $\sim 2\pi^2 4R_P^3$. Ionization rates for the plasma torus were calculated for Saturn, given the expected rates for charge exchange, electron impact ionization, ionization-dissociation reactions, electron recombinations reactions, dissociative electronic recombination reactions and photolytic reactions as given by Fleshman, Delamere and Bagenal (2010); these calculations are in line with Cassini observations for the H_2O-group species ratios reported in Wilson et al. (2015). Three species were injected into the torus : H_2O-group ions (H_2O^+, O^+, OH^+, and H_3O^+), H^+, and O_2^+. The 18 amu H_2O-group ions are injected at a rate of $\sim 1.2\times10^{28}$ ions/s, which correlates to the upper limits of Cassini and Hubble observations for the Enceladus plasma torus and neutral cloud source. The H^+ and O_2^+ ions are injected at a rate relative to the H_2O^+ rates of $\sim$7.3% and $\sim$0.19%, respectively for a total of $\sim$360 kg/s plasma injected. While these are the prominent ion species in the magnetosphere of Saturn, we assume that for the exo-Saturns, the discussion centers around elements/molecules with mass to charge ratios near 1, 18 and 32 amu C^{-1}. The model's simulated dynamical variation between heavy ion fluids that differ by a few percent (e.g., 16 vs. 18 amu C^{-1}) is small, and so these simulations can be taken to represent the behavior of general ionized species with mass to charge ratios of $\pm$ $\sim$15%.

Heavier(lighter) ion species mass would contribute to higher(lower) pickup ion energies, and larger(smaller-)-radius bulk cyclotron motion for the injected ions in the model, and contribute more strongly(weakly) to the corotational energy of the system. When comparing the injected torus between the 3 masses in the present simulation, the 1 amu injected plasma is more tightly bound to the radial region at 4 R_P when compared to the 18 and 32 amu ions. Corotationally-driven transport is largely influenced by the ion fluid with the greatest corotational energy - at a Saturn-like planet, the 18 amu ion group. It would be interesting to explore the inner magnetospheric configuration and mass transport reliance on both the mass of injected species and relative concentrations of those ions. Such an investigation

is best performed in a future effort, as the present work is focused on the response of a Saturn-like configuration to steady-state stellar wind changes

3.6 Considerations at 0.2 AU

Three additional factors were taken into account when considering the planetary configuration at 0.2 AU: 1) tidal dissipation leading to planetary rotational changes affecting the generation of the planetary magnetic field, 2) increased radiation due to stellar proximity, and 3) orbital stability of the internal source of heavy-ions, or exo-Enceladus.

Tidal dissipation in the planet for the 0.2 AU case was considered by using a solution to determine the locking timescale, τ, using the constant phase-lag method described in Appendix E of Barnes et al. (2013). τ was calculated over a range tidal dissipation factors, $Q = 1 \times 10^5$-1×10^6 where k_2, the Love number was set to 0.3, and initial eccentricity set to 0.3. For the lower value of $Q = 1 \times 10^5$, the planet reached a 3:2 spin-orbit resonance, like Mercury in the solar system, after ∼2.08 Gyr, but never synchronously locked; for the upper bound of $Q = 1 \times 10^6$, the planet had only doubled its spin period (from ∼10.7 h to ∼20.4 h) after 10 Gyr. In light of these results, a case at 0.2 AU was run for the scenario with a rotational period of ∼522.78 h, which corresponds to a 3:2 spin-orbit resonance mentioned above. Following the scaling for a planetary magnetic field from Sánchez-Lavega (2004), $B \propto \sqrt{\omega}$, this weakens the planetary magnetic field by a factor of ∼7 to ∼$3{\times}10^{-6}$T at the equator; this case is referred to as the 0.2AU slow case.

The effect of increased stellar electromagnetic flux was considered, but for the base case at 0.2 AU, both ionospheric density at the inner boundary of 2 R_P as well as the rate of ionization in the plasma torus at 4 R_P were kept constant to isolate the effect of increased stellar wind dynamic ram pressure on magnetospheric dynamics. However, a separate case at 0.2 AU included an inner boundary and satellite torus density increased by a factor of ∼530, which is an increase proportional to the ratio of photoionization and photolysis to overall ionization for the relevant ionic species, assuming a simple isotropic R^{-2} dependence on the stellar flux; this case is referred to as the 0.2AU dense case. Similarly, the conductance of the ionosphere has been increased for the latter case by the same amount, so that the ratio of conductance to mass input is maintained.

Lastly, there was some concern about the dynamical stability of an exomoon heavy-ion source over long timescales for a giant planet at 0.2 AU. Following Barnes and Obrien (2002), one can calculate the maximum possible extant satellite mass as

$$M_m \leq \frac{2}{13}\left[\frac{(fa_p^3)}{3M_*}\right]^{13/6} \frac{M_p^{8/3} Q_p}{3k_{2p} T R_p^5 \sqrt{G}}, \tag{3.1}$$

where f is a constant fraction of the satellite's Hill radius, a_p is the planetary semi-major axis, M_* is stellar mass, M_p is the planetary mass, Q_p and k_{2p} is the tidal dissipation parameter discussed above, T is the age of the system, R_p is the planetary radius, and G is the gravitational constant. Using Saturn's planetary parameters at 0.2 AU around a solar analog, the tidal quantities discussed above, and calculating at the age of the current solar system, the upper bound satellite mass calculated is $M_m \leq 2.01\times10^{23}$ kg, or 1.86×10^3 Enceladus' mass and $\sim$2.25 Io's mass. Given this result, the present study is performed under the assumption that the presence of a heavy-ion source produced by an Enceladus-like satellite in the inner magnetosphere is present and stable for a giant planet in this warm orbit.

The model explores the effects of viscous (IMF B_z consistently parallel to the equatorial planetary magnetic field), steady-state stellar wind forcing on the magnetosphere of a gas giant; the planetary magnetosphere exhibits several modified characteristics of the structure and plasma transport, including enhanced magnetotail reconnection in the compressed cases identified by the formation of thin current sheets in regions of reconnection. One obvious effect is the compression of the magnetosphere by the increase in overall ram pressure on the planetary field. Table 1 shows the dynamic ram pressure, and the simulated magnetopause standoff distance. This compression of the magnetosphere has a strong effect on the dynamics related to mass loss from the magnetic environment such as alteration of the radial structure of the inner magnetosphere, which in turn leads to a different mass flow profile. Similarly, the compression of this magnetic boundary ensures that at some point, the boundary layer is dominated by the high densities of injected plasma from the moon at 4 R_P; this changes the potential optical depth of the bow shock. The details are in the subsections that follow.

3.7 Interchange Instability and Mass Transport

The picture for mass transport from a giant, rapidly rotating magnetosphere down the magnetotail and out into the stellar wind is not completely understood, but it is known that processes such as the centrifugal interchange instability strongly contribute to such transport for rapidly-rotating, magnetized planets (e.g. Kivelson and Southwood, 2005; Thomsen, 2013). The centrifugal interchange instability can be likened to the Raleigh-Taylor instability, but with the centrifugal force from planet's rapid rotation in lieu of gravity. Cold, dense heavy-ion plasma from the near-planet magnetosphere (herein, the Enceladus analog's orbit at $\sim$4 R_P) exchanges with the hot, diffuse plasma radially adjacent, and carries with it magnetic flux; these dense plumes possibly undergo small magnetic reconnection events and are lost from the inner magnetosphere. However, for the magnetosphere to be unstable to flux interchange, two facts must hold: the gradient of equatorial plasma flux tube content must be negative with increasing radial distance, and the thermal energy of the magnetospheric plasma must be less than that of the corotational energy (Hill, 1976).

The marginal interchange stability criterion with respect to the flux tube content (FTC) is given by Hill (1976) as:

$$\frac{\partial}{\partial r_{eq}}\left(\frac{\rho_{eq} r_{eq} g}{B_{eq}}\right) = 0 \tag{3.2}$$

where ρ_{eq}, r_{eq}, and B_{eq} are the equatorial mass density, radial distance and magnetic field magnitude, respectively. For a rotationally-aligned, planetary magnetic dipole, as for the present system, the field geometric factor, g, can be approximated as $g(L) \approx 4L^{1/2} - 3$, where L is the equatorial radial distance in terms of planetary radii. For a configuration where the quantity in Eq. 3.2 is negative, the system will be unstable to interchange, i.e. if total flux tube content is decreasing with increasing radial distance from the planet.

Total flux tube content in the multifluid model was calculated by tracing closed magnetic field lines as a function of L-shell, over a colatitude range corresponding to the north and south magnetic foot points for each L-shell value, from the plasma torus at 4 R_P to the identified magnetopause for each case. The contributing number of the dominant species,

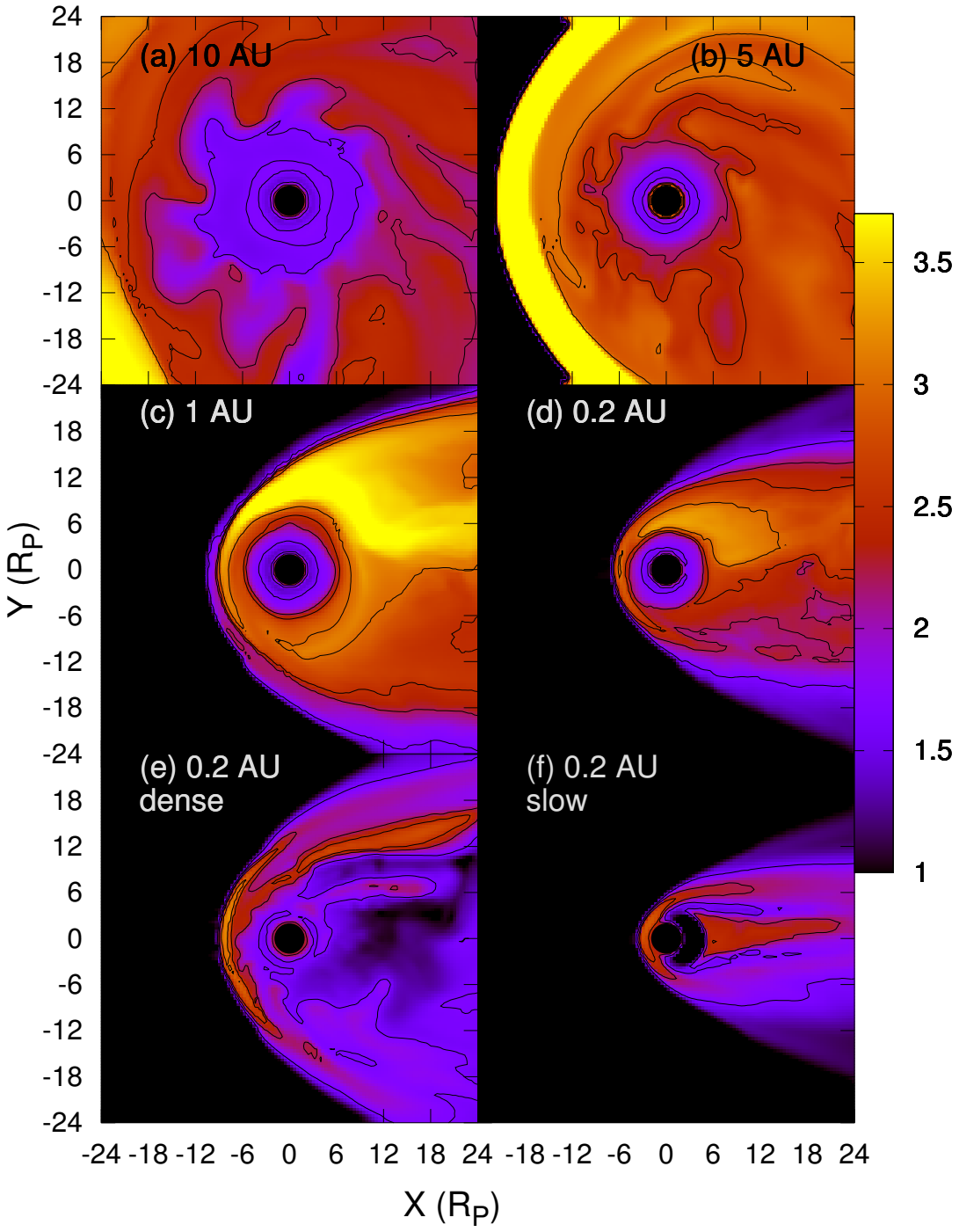

Figure 3.1 A view from above the planetary northern pole, showing the 18 amu ion temperature (eV) in the equatorial plane. The static temperature for the stellar wind for each case, given in Table 1, has been removed for improved visualization.

18 q/m ions, for each point was added to obtain $\mathrm{N}_{ion}\mathrm{L}^2$, which is given by (e.g. Sittler et al., 2008):

$$N_{ion}L^2 = 4\pi R_P^3 L^4 \int_{\theta_N}^{\theta_S} n_{ion}(L,\theta) sin^7\theta \, d\theta \tag{3.3}$$

where θ_N and θ_S are the magnetic foot points in the north and south hemispheres per L-shell, respectively.

The thermal energy density of the magnetospheric plasma is given by the plasma pressure, $P = \sum_s n_s k_B T_s$, where n_s is the number density, k_B is Boltzmann's constant, and T_s is the temperature summed over electrons and all ion species, s. The corotational energy density is given by the kinetic energy density for all ion species (electrons are neglected), $E_{cor} = \frac{1}{2}\sum_s \rho_s v_s^2$ where v_s is the corotational velocity of ion species, s.

The panels in Fig. 3.1 show the temperature of the most abundant ion species, the 18 amu ions, to illuminate the outflowing cool, dense fingers and inflowing tenuous, hot injections for the 10 and 5 AU cases. The 18 amu species is injected by the satellite at $4\mathrm{R}_P$ at more than an order of magnitude higher input than any other species, and therefore will drive the inner magnetospheric dynamics - including the interchange processes. The temperature is shown from above the northern pole of the planet, for the plasma located in the equatorial plane as the centrifugal force is highest at low latitudes. It is readily apparent that the top two panels (left, 10 AU, and right, 5 AU) display the formation of the interchange fingers as have been measured in rapidly rotating magnetospheres, such as Saturn's (e.g. Burch et al., 2005; Mauk et al., 2005; André et al., 2005; Persoon et al., 2005). The middle two panels (1 AU on left, and 0.2 AU on right) show a distinct lack of the interchange process, but like all cases of convection-dominated magnetospheres, they exhibit the well-known Vasyliunas cycle of magnetospheric plasma flow (Vasyliunas, 1983). Interestingly, the 0.2 AU dense case (bottom panel of Fig. 3.1) shows potential interchange-like fingers forming, as opposed to the base case in the middle right panel. To understand these behaviors, we must investigate the conditions for stability, outlined above. Overall for the 0.2 AU cases, plasma generated in the satellite torus is likely to rapidly flow out to the magnetopause, and then be forced to flow down the tail, contributing directly to an increased density near the boundary of the

magnetopause (see § 3.10). That mass is carried around the magnetosphere and out into the stellar wind, lost from any contribution to the inner magnetospheric processes. Likewise, for the 0.2 AU slow case, the orbit of the satellite at 4 R_P takes the ion producing exomoon across the magnetopause, directly into the magnetosheath and shocked stellar wind.

The quantities from Eq. 3.3 and the ratio of total thermal to corotational energy densities are calculated for the simulation results in Fig. 3.2. Note that these quantities are time-averaged for 6 planetary rotations (∼64 hours). The abscissa for this figure is given as R_{fMP}, which represents the fraction of the distance from the plasma torus to the magnetopause identified in Table 1, chosen to give comparable similar scaling for each case. The top panel in Fig. 3.2 shows the total FTC for the 18 amu C^{-1} ions in each baseline planetary configuration, and the 0.2 AU dense case. When comparing the 10 AU case in Fig. 3.2 to the Cassini data baseline in Sittler et al. (2008), it is noted that the present simulation overestimates the total FTC in the center of the torus and at ∼10 R_P by approximately a factor of 2, but the peak FTC radial location (∼6.5 R_P) and peak FTC value (1.55×10^{34} ions) agree well with the CAPS data. Two issues explain the differences: 1) the present simulation is injecting what is thought to be the upper end of the estimation for Enceladus' plasma input (∼360 kg s^{-1}) from the satellite at 4 R_P, and 2) the simulation is run with isotropic pressure/temperature, while at Saturn there is a strong perpendicular anisotropy leading to confinement of heavy ions to the equatorial plane. Therefore there is an overestimate of ion content located on field lines at middle and high latitudes, inflating the total FTC.

The instability criterion, Eq. 3.3, is met in all cases, though for the 10 and 5 AU cases, the condition is met in the middle magnetosphere, as opposed to the near plasma torus location for the 1 AU and 0.2 AU cases. This is consistent with Cassini observations at Saturn of a broad peak in flux tube content in the 6-8 R_P range (e.g. Sittler et al., 2008; Chen et al., 2010). In the 10 and 5 AU cases, we do see interchange occurring at approximately the magnetospheric radii measured by the Cassini mission (top panels of Fig. 3.1). For the cases at 1 AU and 0.2 AU, it is apparent that the interchange-unstable condition for a negative gradient in the flux tube content is met throughout nearly the entire magnetosphere from torus to magnetopause. However, the bottom panel of Fig. 3.2 shows

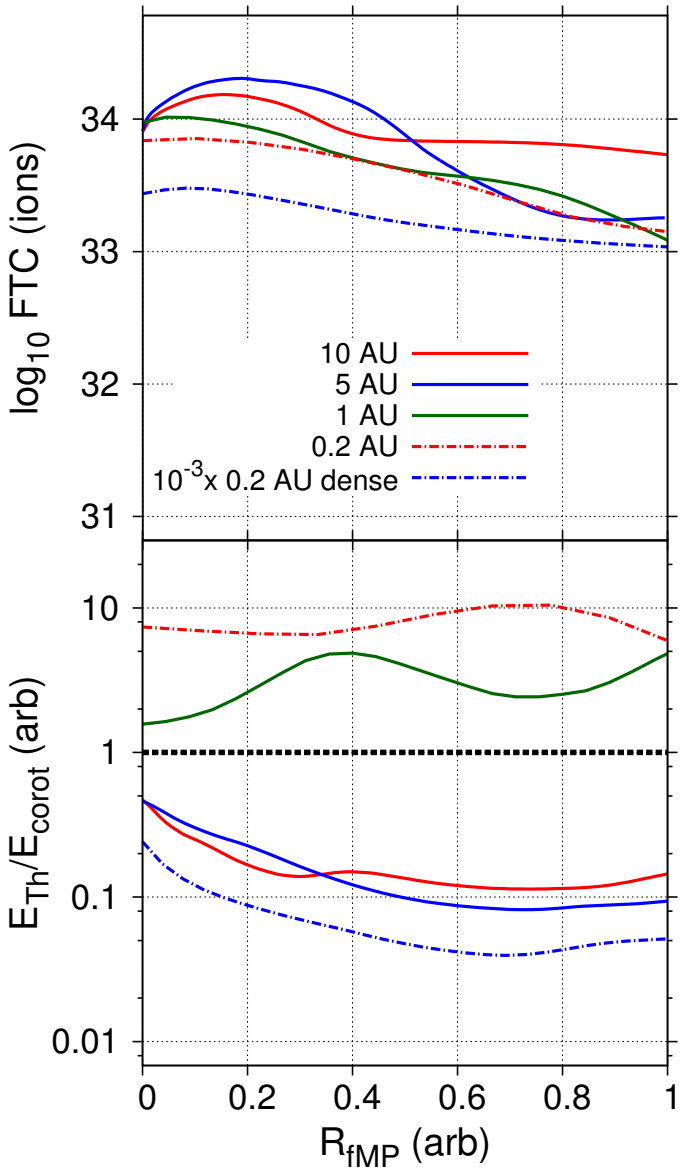

Figure 3.2 **Top:** Flux-tube content (FTC) of W^+ ions for each case, in total ions for a givenL-shell (note the 0.2 AU dense case is scaled down by 3 orders of magnitude for comparison). **Bottom:** The ratio of thermal energy density to corotational energy density. The abscissa for each plot is R_{fMP}, which is simply the fraction of the distance between the injected plasma torus at 4 R_P, and the identified magnetopause as measured in Table 1. Both top and bottom plots are averaged over 6 Saturnian rotations, and the lower plot only is an azimuthally-averaged radial profile.

the ratio of thermal energy to kinetic corotational energy. For a magnetospheric region to be unstable to interchange, this quantity must be less than unity. For the 10 AU, 5 AU and 0.2 AU dense cases, this second condition leaves a broad range of radial regions unstable to interchange. The cases at 1 AU and 0.2 AU baseline both show dominance by the total thermal energy, ruling out the development of the interchange fingers, as seen in Fig. 3.1. These results imply that mass loss and flux transport in the 1 and 0.2 AU cases have been forced into a configuration akin to the terrestrial magnetosphere, i.e., driven more by the stellar wind than by corotation.

It is likely that a Saturn-like planet with a semi-major axis between 5 and 1 AU will be unstable to interchange, but at some orbital distance that mechanism might become completely damped out. If not, before reaching 1 AU, one would expect for the magnetosphere to become stable to interchange due to the compression of the magnetopause which both increases the thermal energy of the plasma, while simultaneously decreasing the corotational energy by restricting the spatial regions of corotation. This is what happens in the present simulations at 1 and all 0.2 AU cases - the magnetosphere becomes much more controlled by the characteristics of the stellar wind as opposed to the corotational driving exhibited at larger orbital radii.

If the interchange instability is damped out, this suggests that magnetospheric mass loss rates would be more uniform and less bursty in nature. The lack of interchange could also drive expectations for potential exoplanetary auroral observation across the electromagnetic spectrum, due to the coupling of the magnetosphere to the ionosphere of the planet (e.g. Sittler, Blanc and Richardson, 2006; Nichols, 2011, 2012). More discussion follows in Sec. 3.9 below.

However, the cases studied here are artificial, as the goal was to isolate the effects of the external forcing by the stellar wind pressure - the increased rates for photoionization and photolysis were not considered except for the 0.2 AU dense case. The corresponding stability criteria shown in the lower panel of Fig. 3.2 suggest that the 0.2 AU dense case is dominated by the huge influx of photo-produced cold ions picked up in the satellite plasma torus. Despite the fact that the ratio of thermal to corotational energies are both linear with respect to the increased density, the corotational velocities are static with respect to

radius for the 0.2 AU simulations while the azimuthally averaged temperatures are much lower for the 0.2 AU dense case due to the domination of the thermal landscape by the very dense, cold injected plasma.

The following question is raised: is there a location between 1 and 5 AU where the increase in photon flux leading to increased ionospheric and plasma torus densities override the effects of the compression of the magnetosphere and produce a system unstable to interchange? At 0.2 AU, the increase in photolysis and photoionization grant an overall plasma density increase by a factor of ∼530 when compared to Saturn at 10 AU; it is not a strict $1/R^2$ relationship due to the fact that photoionization and photolysis are only one aspect of the ionization process, as discussed in § 3.5 and 3.6. Given that, one expects at 1 AU to find an increase in total ionization of a factor of ∼21 over that at 10 AU. Whether such an increase is sufficient to dominate the magnetosphere of the planet at 1 AU to the extent that is seen in the 0.2 AU dense case, and at what point would such a model suggest a complete dampening of the interchange are open questions

3.8 Magnetospheric Mass Loss

The process of how a body loses atmospheric atomic and molecular species, and their inherent contribution to the chemical evolution of an atmosphere, remains a question in planetary science. The question of depletion is one that is central the habitability of a planet or moon, and is governed by several thermal and non-thermal processes (e.g. Yelle, Lammer and Ip, 2008). Escaping species are ionized and controlled by the magnetic environment around the planet, and therefore the rates at which magnetospheric plasma is lost is related to the overall atmospheric mass loss rate for a planet. The multifluid model employed in the present work sets the density at the ionospheric boundary to be constant, replenishing any loss due to convection or pressure gradients, as such the outflow of atmospheric material is included, but not in a rigorous fashion. The primary source in the present model is that produced in the satellite torus. At equilibrium, the torus at 4 R_P is injecting ∼360 kg/s total of 1, 18 and 32 amu C^{-1} ions - ∼350 kg/s of which is the 18 amu C^{-1} species.

Fig. 3.3 is the outflow rate in ions s^{-1} for the 18 amu ion species at the outermost

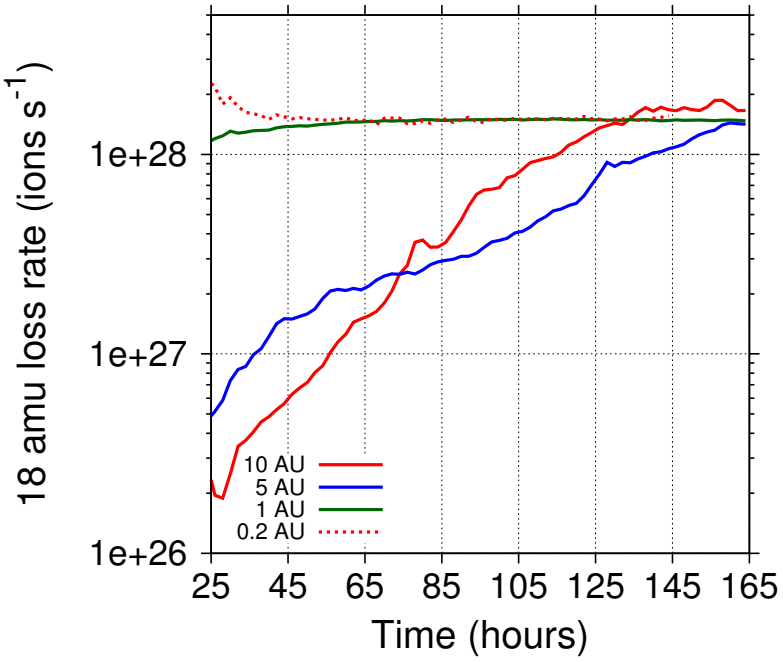

Figure 3.3 Plasma ion flux outflow at the outermost tailward boundary for 18 amu ions as a function of time.

boundaries of the simulation, outlined in § 3.3 for 10, 5, 1, and 0.2 AU cases. The special cases of 0.2 AU dense and 0.2 AU slow are not included in the figure as they both reach equilibrium outflow equal to their torus and ionospheric input very early in the process, similar to the 0.2 AU baseline case. It is worth noting that all baseline cases reach the same equilibrium outflow mass loss rate of $\sim 1.2 \times 10^{28}$ ions s^{-1}. The presence or absence of the centrifugal interchange instability does not affect the absolute mass loss rate over sufficiently long timescales, but instead extends the relative time scale for the magnetosphere to reach equilibrium outflow during recovery after transient events. Over long timescales, all plasma injected is lost to either the inner boundary of the planet, or down the magnetotail into the flowing stellar wind.

It is possible that the chosen inner boundary conditions contribute to the overall outflow rates shown in Fig. 3.3. There is no forced outflow at the inner boundary, with ion pressures and densities held constant in each timestep, replenishing any that flow out, or absorbing any ions that flow in. Some loss at the inner boundary is expected, as the inward pressure gradient on the planet side of the Enceladus-like torus, and longer simulations may show equilibrium values below that of total input from the torus and ionospheric sources.

In the simulated magnetospheres which are unstable to interchange (10 AU and 5 AU), there is a significant relative lag time before the outflow rate of 18 amu ions matches that of the injected rate of $\sim 1.2 \times 10^{28}$ ions s^{-1}. After the initial simulation equilibrated from the passage of the stellar wind at approximately 25 hours, the 5 AU case shows a lower rate of change for the ion outflow compared to the 10 AU case; the former takes approximately 140 hours to reach the equilibrated outflow rate, whereas the latter does so in approximately 100 hours, despite a factor of ~ 2.5 lower starting outflow rate. Therefore, not only does the presence of interchange affect time scale to reach outflow equilibrium, but the results suggest that the strength of interchange may affect the features of the mass loss rate as the magnetosphere 'refills' and approaches equilibrium.

This agrees with the conditions shown in Fig. 3.2, which indicates that while both the 5 AU and 10 AU cases are unstable to interchange, the window of instability for the 5 AU case is narrower than that of 10 AU, as seen by the distance between the peak and identified magnetopause for the 18 amu species flux-tube content (FTC) in the upper panel.

However, the gradient for the 5 AU case is larger, overall. The 10 AU case shows a window at distances greater than ∼0.18 R_{fMP}. Both cases are considered unstable to interchange throughout the magnetosphere, by the thermal to corotational energy ratios. This narrower window for the 5 AU case suggests a magnetosphere less unstable to interchange despite the steeper gradient, and therefore a less significant rate of increase in the rate of ion outflow occurs as seen in Fig. 3.3; the simulation suggests the 5 AU magnetosphere requires a longer time to reach the equilibrium outflow rate than the 10 AU magnetosphere. The cases for 1 AU and 0.2 AU are both stable against the interchange process, and reach the equilibrium outflow rate rapidly after initial passage of the stellar wind.

The outflow rates in Fig. 3.3 suggest that stronger external forcing will drive a higher outflow rate after initial passage of the stellar wind. That could be likened to the passage of a coronal mass ejection (CME) or corotating interaction region (CIR) in an otherwise quiescent period; this suggests that planets with magnetospheric configuration that have sufficient radial extent to be unstable to interchange will respond initially with lower outflow. The rate of increase for the outflowing mass flux is related to the strength of the interchange instability for that magnetospheric configuration. For planetary orbital distances with increasing stellar wind dynamic ram pressure, the rate of mass loss acceleration will vary according to the overall size of the magnetosphere, i.e. the pressure balance between the stellar wind and the corotating, plasma-laden planetary magnetic field.

For decreasing semi-major axes, the increase in stellar wind dynamic ram pressure eventually compresses the magnetosphere to the point where it is no longer unstable to interchange, bringing the system from one with mass loss dominated by internal processes to one driven by external processes. This compression forces plasma species out of the system in a more rapid fashion as the corotating region of the magnetosphere is more tightly bounded by the flow of the stellar wind and corotating plasma is lost due to the viscous interaction. The magnetospheres that are dominated by internal processes are more robust against rapidly changing stellar wind conditions, which would contribute to a more stable rate of overall mass loss from the system.

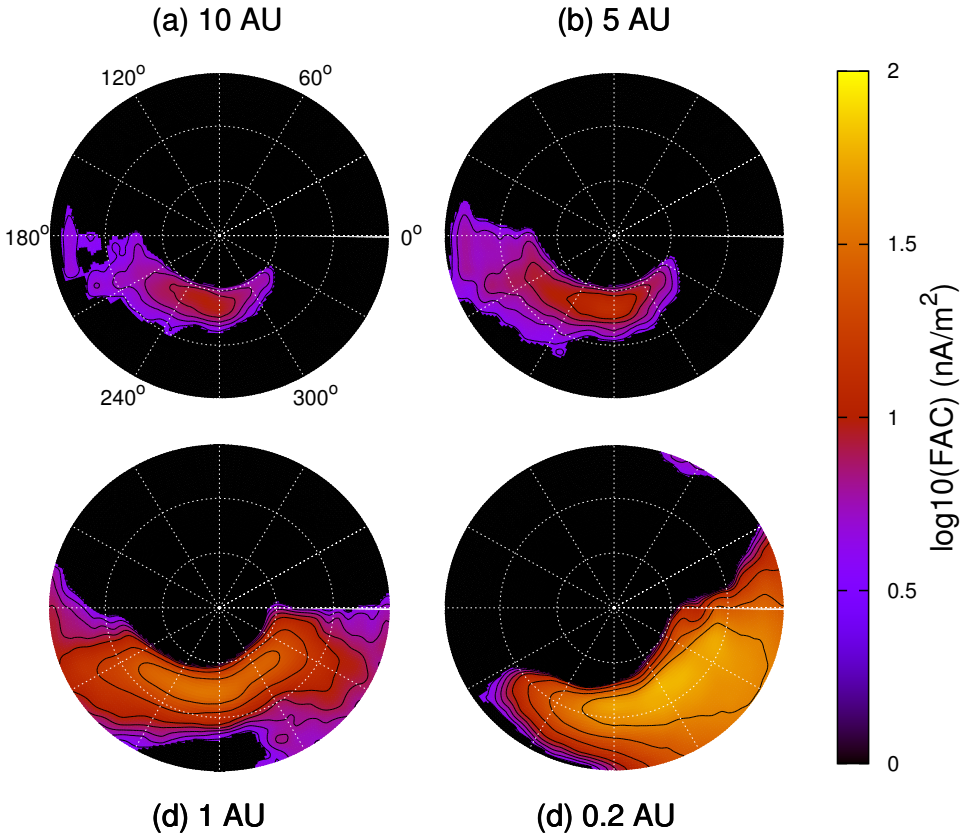

Figure 3.4 Time-averaged projections of upward-flowing field-aligned currents (FAC) at an altitude of 2.2 R_P in the northern hemisphere of the Saturn-like planet. The radial distances correspond to 75(15), 60(30), and 45(45) degrees (co-)latitude. $0^o(180^o)$ points to local noon(midnight). The contours correspond to $\log_{10}$ FAC values of 0.6, 0.7, 0.8, 0.9, 1.0, 1.2, 1.4, and 1.6 nA m^{-2}.

3.9 Field-Aligned Currents and Auroral Radio Emissions

The multifluid model does not simulate kinetic processes (e.g., electron cyclotron instabilities) inherent in generating auroral radio emissions (ARE), but it does capture large-scale current systems and has validated heritage accurately simulating planetary auroral activity (e.g. Harnett, Winglee and Lerud, 2010). In general, the power of planetary radio emission for planets with global magnetic fields has been suggested to respond directly to increased forcing from the stellar wind for rapidly rotating, giant planets like Saturn (e.g. Desch, 1982; Desch and Rucker, 1983). Kimura et al. (2013) found that the peak flux density of

Saturn's ARE exhibited a positive correlation with the dynamic pressure of the solar wind on the timescale of the solar cycle. The behavior of increasing power output of planetary radio emissions seems to directly correlate to the incident kinetic and magnetic pressures on the magnetosphere for all magnetized planets in the solar system with observed non-thermal, magnetospheric radio emissions (e.g. Desch and Kaiser, 1984). It is reasonable to expect other magnetized bodies in all planetary systems with significant stellar wind to follow a similar behavior (Zarka, 2007).

While transient solar wind events (e.g. reconnection at the magnetopause and resulting magnetotail dynamics) can drive increased behavior in radio emission, we focus on forcing of the magnetosphere by increasing the steady-state dynamic pressure of the stellar wind. The multifluid model predicts a clear increase in FAC magnitude with increased stellar wind dynamic ram pressure, which is in accordance with the increased radio flux density observed during the solar cycle at Saturn (Kimura et al., 2013). However, this is counter to what one expects through a scaling study of corotation enforcement for giant magnetospheres (e.g. Nichols, 2011, 2012). In general, one expects less torque required to maintain the angular momentum of corotation for a smaller (more highly compressed) magnetosphere, and therefore a lower magnitude current system is expected.

In the present study, we explicitly hold the IMF B_Z component to be negative (parallel to the equatorial planetary dipole field), and therefore Dungey-type, equatorial magnetotail reconnection is not observed in the simulations. However, plasma is lost from the inner magnetosphere down the tail for all simulated cases, with strong interchange outflow expressed for the 10 and 5 AU cases, and a continuous loss of plasma 'bubbles' for all cases (Kivelson and Southwood, 2005), that leaves depleted flux tubes flowing planetward as they return on the dayside from down-tail. It can be seen in Fig. 3.1 for the 1 AU and 0.2 AU cases that plasma on the dayside is heated significantly through the return flow process, and becomes supercorotational.

We propose that the cases simulated in the present work at 1 AU and 0.2 AU have been compressed across a threshold from being a corotationally driven magnetosphere - like that at Jupiter and Saturn - to one dominated by the increased forcing from the stellar wind. This increased forcing has led to higher tension in the magnetotail, and therefore a stronger

response in return flow from down the magnetotail, which flows back towards the planet in a constant state of supercorotation. This supercorotating return flow (which is consistent with the Vasyliunas cycle return flow) was predicted and observed at Saturn, and has been proposed to strongly influence planetary auroral emission (e.g. Talboys et al., 2009; Masters et al., 2011).

Fig. 3.4 shows a polar projection of the simulated upward-flowing, time-averaged field aligned currents above the northern hemisphere of the planet at an altitude of $\sim$2.2 R_P for each of the four base cases. Note that the location and magnitude of the baseline case at 10 AU is in good agreement with measurements made by Cassini when projected along planetary dipole magnetic field lines to the visible auroral region of Saturn @ $\sim$1.02R_P (e.g. Talboys et al., 2011). The peak field-aligned current (FAC) at 10 AU is $\sim$7.2 nA m^{-2}, with a total magnitude of $\sim$0.82 MA rad^{-1} at a colatitude of $\sim$19.1^o at 2.2 R_P. Predicted peak currents for the warmer orbits are 1.54, 3.82, and 9.90 MA rad^{-1} for the 5, 1, and 0.2 AU cases, respectively. The 0.2 AU dense case was similar to the 0.2 AU baseline in terms of latitude, though exhibited lower magnitude. The 0.2 AU slow case did not exhibit any discernible field-aligned currents in the model - as the weakened magnetic field was compressed completely to the inner boundary of the simulation, and injected plasma from the satellite was lost directly to the stellar wind for more than half of the torus volume.

Following Zarka (2007), we can calculate the anticipated median radio power output based solely on the incident kinetic power on the Saturn-like planet at 0.2 AU - $\sim 7.2\times10^{10}$W - a value that is nearly twice that of Jupiter's decametric median radio power. That being said, the incident IMF Parker spiral geometry at 0.2 AU for a Sun-like star as in the present work is expected to produce a lower incident Poynting flux onto an already compressed magnetosphere. Zarka (2007) gives the dissipated power as:

$$P_d = \epsilon K \left(V B_\perp^2/\mu_0\right) \pi R_{MP}^2, \tag{3.4}$$

where ϵ is a reconnection efficiency of 0.1-0.2, K is a function that is related to the reconnection in response to the magnetospheric state - open or closed, V is the incident stellar wind speed, $B_\perp$ is the measure of the IMF perpendicular to the direction of stellar wind

flow, μ_0 is the vacuum permeability, and R_{MP} is the magnetopause standoff distance. For a Saturn-like dipole configuration, K is given by $\cos^4(\theta/2)$, where θ is the angle between the IMF embedded field and the planetary dipole. If we calculate the value of Eq. 3.4 for our Saturn-like planet at 0.2 AU (with the IMF values from Table 1), and compare with the value for Jupiter's decametric median radio power reported in Zarka (2007), we obtain a ratio of $\sim 5.5\times10^{-3}$ which gives us a predicted power of $\sim 1.1\sim10^{8}$W. This value is more in line with Saturn's kilometric radiation (SKR) output. It is still not clear which of the two incident powers - kinetic or magnetic - is the primary driver of emitted radio power for magnetized planets, though relative efficiencies have been suggested. The Kronian system is roughly equally driven by both rotation and magnetic IMF conditions, as opposed to the terrestrial system (primarily magnetic IMF driven) or Jovian system (primarily rotationally driven).

Another feature in Fig. 3.4 is the latitudinal position of the field-aligned currents for each case. Field-aligned currents are part of a complete circuit, with currents running in a loop from the ionosphere of the planet, along a field line down to the equatorial plasma sheet, radially to or from the planet along the plasma sheet, and then back along a field line to close in the ionosphere. It is these radial, equatorial currents which enforce corotation of the magnetosphere, due to the J×B force, as seen in Eq.2.8. The location of these field aligned currents falls within areas of subcorotation in the magnetospheres, but this is unlikely to be the cause for the magnitude increase observed in the simulation output. An extensive scaling study was performed in Nichols (2011, 2012) regarding this current system for Jovian planets, and its results suggest that for a purely corotational magnetosphere, compression leads to lowered corotation-enforcing field aligned current systems. In Fig. 3.4, the opposite is seen - with higher compression leading to an increased FAC magnitude. This suggests that the current system seen in the present simulations is not solely produced as a part of the corotational system.

With increasing stellar wind ram pressure, the magnetopause is compressed which disallows the corotation of inner magnetospheric plasma at distances beyond this boundary, but leads to a high shear flow at this boundary between open and closed field lines. For the 10 AU case, the peak of the FAC occurs at $\sim 70.9^{o}$ latitude at 2.2 R_P, which corresponds to

an equatorial distance of ∼20.5 R_P which is in the middle to outer dayside magnetosphere, indicating a likely corotational source. In Fig. 3.4, the FAC peak for the latitude for the 1 and 0.2 AU cases is located at ∼65.8° and ∼55.9°, respectively, which correspond to the corotational regions at ∼13.1 and ∼7.0 R_P- approximately coincident with the dayside flank magnetopause location in each case. There is increased upward current at lower latitudes approaching midnight, and the high-latitude inner boundary of the upward FAC plotted for the two cases at 1 and 0.2 AU agrees well with the separatrix between the open and closed field lines. Taking this last point into account, along with the star-ward supercorotation seen in the Vasyliunas cycle return flow, and the increased stellar wind ram pressure at these orbital distances, the increase in the upward flowing FAC is likely generated by the shear flow near the magnetopause boundary.

It should also be noted that latitudinal extent of the current distributions plotted in Fig. 3.4 correspond to a limitation of the simulation - namely that the simulation was run with lower resolution (∼0.2 R_P) in the inner magnetosphere and at the magnetopause boundaries. This limitation washes out the finer structure that one expects for these systems.

The predicted latitudes of the field aligned current systems in Fig. 3.4 allow for an abstract spatial understanding of how such planetary configurations would project their radio signals into space. Fig. 3.5 shows a heat map for the emitted planetary radio signal onto a celestial sphere around the planet for the 10 AU and 0.2 AU cases (see Appendix B). The axes defining latitude and longitude for the planets are aligned with the magnetic moment, and for the Saturn-like planet, the rotational axis as the field is axisymmetric. The emissions were generated between 04:00 and 16:00 planetary local time (PLT), corresponding to Cassini observations of Saturnian Kilometric Radiation (SKR) emission at Saturn (Cecconi et al., 2009), and were latitudinally symmetric in the northern and southern hemispheres. The top row corresponds to the planetary configuration at 10 AU, and the bottom at 0.2 AU. The left column corresponds to a relatively wider beaming angle for the emitted radio power for each of the northern and southern hemispheres (see Appendix B), and the right column corresponds to a relatively narrow beaming angle. The two selected beaming angles correspond to 400 kHz and 200 kHz (left and right columns, respectively in Fig. 3.5) and

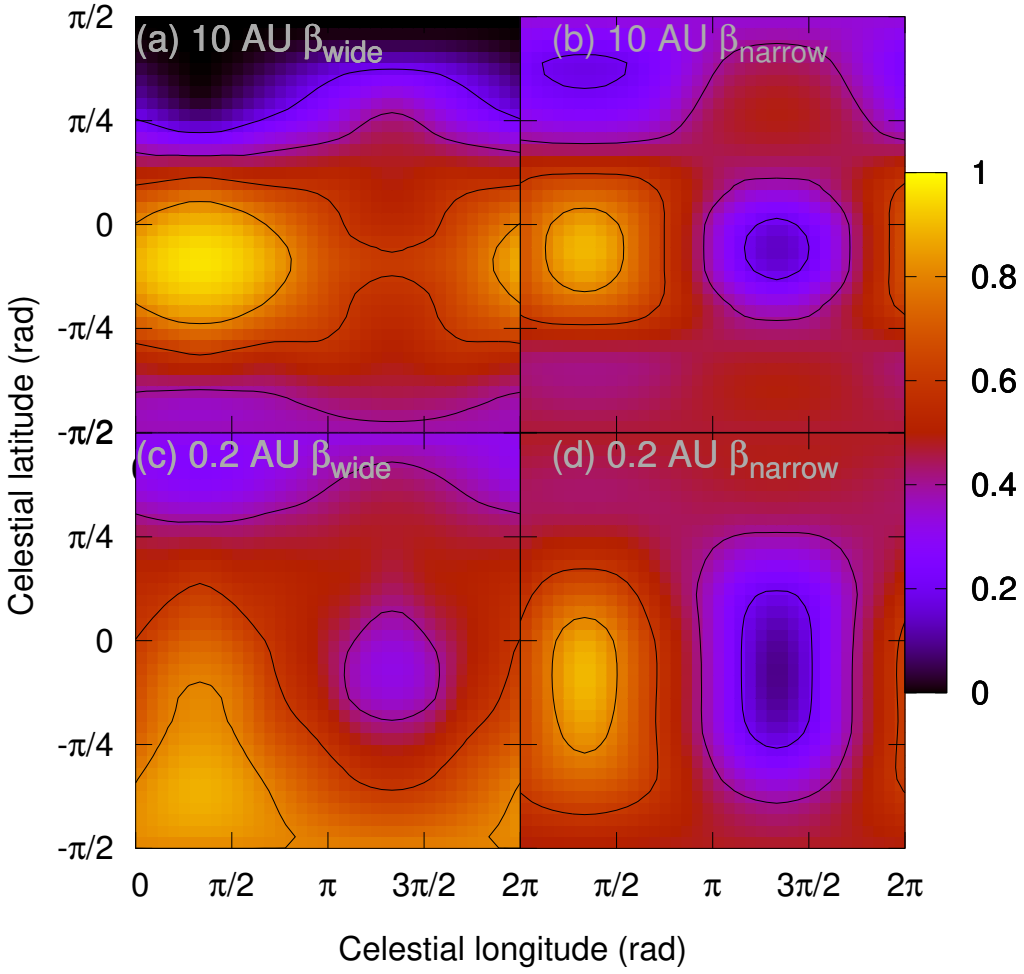

Figure 3.5 Heat map generated by radio emission projected onto a celestial sphere centered on the planet. **Left column:** emissions with a wide beaming angle ($90^o/60^o$ for the northern/southern hemispheres) for the planetary configurations at (a) 10 AU, and (c) 0.2 AU. **Right column:** narrower beaming angle emissions ($65^o/45^o$ for the northern/southern hemispheres) for the planetary configurations at (b) 10 AU, and (d)0.2 AU.

as measured by Cecconi et al. (2009) as an illustrative example of the projected geometric differences. Note that the hemispherical asymmetry in Fig. 3.5 is due to the different beaming angles measured in Cecconi et al. (2009), rather than emission location. Symmetric emission altitudes and latitudes were assumed.

For the wide angle emissions in the left column, it is noteworthy that the projected radio emission is quite dissimilar for the 10 AU and 0.2 AU cases, the difference being due to the latitudinal variation between the FACs generating the radio emissions. If the combination of rotational (in this case of an axisymmetric magnetic dipole) and orbital inclination of the planet was aligned so that line of sight to our point of observation (e.g. Earth) lay in the region of high emitted power overlap - 'edge on' for the 10 AU case and 'face on' or poleward for the 0.2 AU case - radio signals with power on par with Jupiter decametric radiation (or higher) could be detected. The signals for the 10 AU cases - both wide and narrow beaming angles - are similar to a lighthouse beam, and would be expected with periodicity matching that of the orbital period for the planet. However, for the 0.2 AU wide beaming angle case (lower left panel of Fig. 3.5), the situation is more interesting. Note that for a Saturn-like planet with an oppositely oriented magnetic dipole, the locations of upward- and downward-flowing current systems would be reversed, ultimately changing the projection onto the celestial sphere.

One can run a simple calculation to estimate the power reaching Earth for such a distant source. We assume isotropic emission, a 400 kHz frequency, and use the idealized power calculations from above for a Saturn-like planet in a 0.2 AU orbit, at a distance of 10 parsecs from Earth. The signals reaching us would be $\sim$0.19 mJy and 0.29 μJy for the best-case, kinetically-controlled 7.2×10^{10}W emission and worse-case, magnetically driven 1.1×10^{8}W emission, respectively. The former is at the threshold of current radio instrumentation, and the latter is beyond the technological horizon. This calculation explicitly ignores sources of noise and dispersive effects due to interstellar material.

For such a close semi-major axis, it is unlikely that direct observation (optical, IR, UV) could occur for said planet. Transit and radial velocity methods are strong at that distance, given a very narrow window of orbital inclinations - if there exists even a moderate amount of orbital inclination relative to our line of sight, then these methods will not be

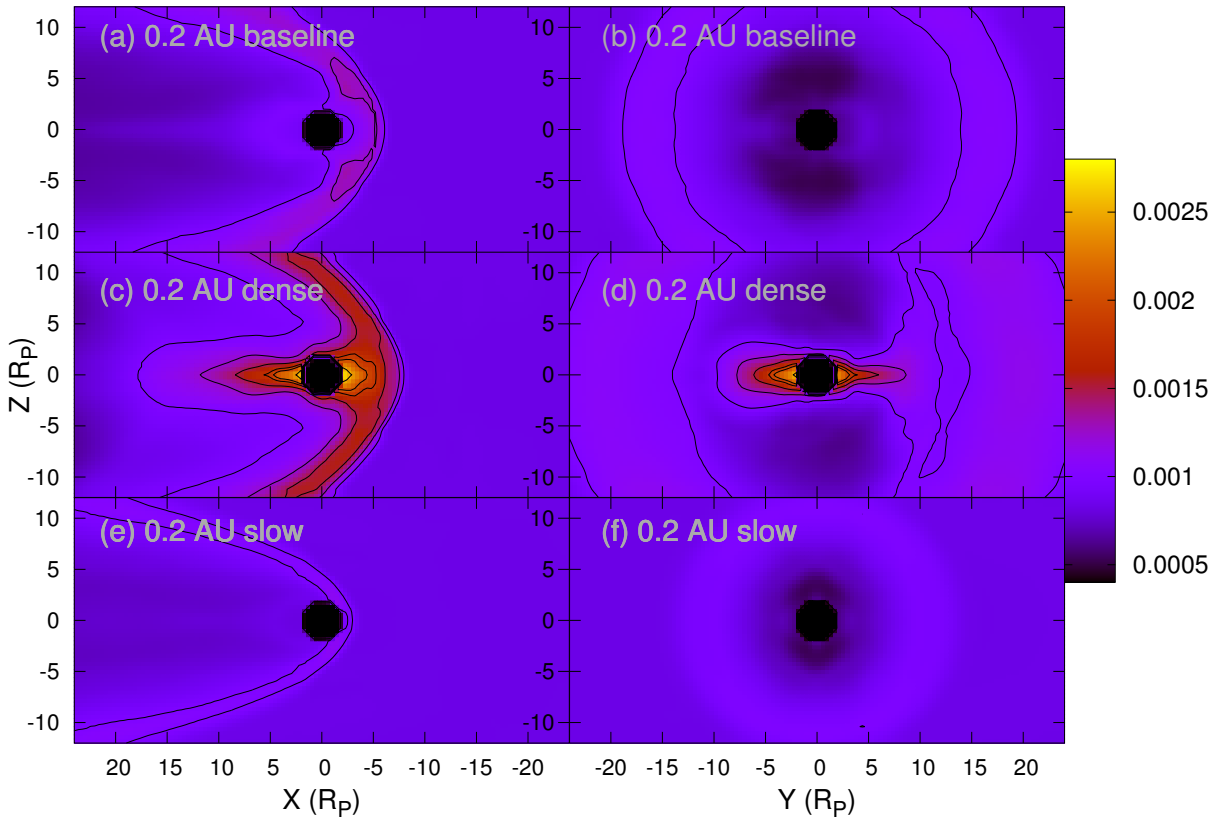

Figure 3.6 Optical depth, τ, for stellar emitted Mg-II predicted for (a) and (b) the 0.2 AU baseline, (c) and (d) the 0.2 AU dense case, and (e) and (f) the 0.2 AU slow case. The left column corresponds to the ahead-shock case (likely for hotter orbits), and the right column corresponds to the sub-solar shock case (likely for warm orbits). Contours correspond to the hash marks on the colorbar - τ = 0.0005, 0.001, 0.0015, 0.002, and 0.0025.

reliable. However, if the combination of orbital and rotational inclinations is such that our line of sight was anywhere in the southern hemisphere of the planet, it is likely that some of the planetary emitted radio power could be detectable with near constant visibility and emission (modulated by stellar activity and magnetospheric response). Based solely upon availability of emitted radio geometry in the example of Fig. 3.5, the potential number of planets observable relative to those constrained by orbital configurations amenable to transit or radial velocity measurement could dramatically increase with the use of radio observation. Granted, radio observation has its own set of difficulties to overcome (e.g. need for a large interferometric baseline, Earth's ionosphere).

The simulated data in Fig. 3.5 is highly simplified, as we don't simulate the kinetic processes involved in the radio emissions. Our model does not have the ability to predict absolute spectral flux density or more exact radio auroral locations and geometry. The figure merely suggests that the stellar wind dynamic ram pressure and magnetospheric dynamics can directly control not only the field aligned current systems related to power output by ARE, but likewise the celestial coverage of such emissions will be altered for stronger forcing. In the continuum of planetary configurations, some similarity is maintained, while differences arise from the increased dynamic ram pressure; this simple analysis offers an initial view at predicting and characterizing the future observations of radio emissions by giant exoplanets once basic facts about the magnetic properties are observed

3.10 Implications for Transit Signal Modifications

There is potential for the increased plasma densities in both the satellite-generated plasma tori and the bow shock of a warm or hot planets to affect transit light curve observations. Ben-Jaffel and Ballester (2014) showed that the inclusion of satellite-generated plasma tori could contribute to the signatures of early ingress for transit observations for both HD 189733 b and WASP-12b. Observations have also been made with the Hubble Space Telescope (HST) that suggest increased bow shock density for these planets has potentially modified transit signals, but other effects - such as absorption by a dense Roche lobe or systematic uncertainties - have not been ruled out (e.g. Llama et al., 2011, 2013; Nichols et al., 2015; Alexander et al., 2015).

Unlike the work above on WASP-12b and HD 189733 b, we have assumed our warm-Saturn is orbiting a Sun-like star, though at a cooler orbit of 0.2 AU. This situation is similar to the exoplanet HD 33283 b (as well as numerous unconfirmed Kepler objects of interest (KOI)), orbiting its G3V host with a semi-major axis of 0.168 AU (Johnson et al., 2006), though transit is not the method of discovery for this planet. Given a similar stellar type, we assume the composition of the host of our star is like that of the Sun; in particular, the ratio of Mg to H,

$$\frac{n_{Mg}}{n_H} \simeq 6.76 \times 10^{-5}, \tag{3.5}$$

is taken to be the same as the reported ratio in solar abundance (Grevesse, Asplund and Sauval, 2007).

Using the above assumptions, we have calculated the optical depth for the Mg 2 doublet at 279.55 and 280.27 nm in the magnetosphere of our hypothetical warm Saturn, given by

$$\tau = 4 \int n_{Mg\,\mathrm{II}}\, \sigma_{Mg\,\mathrm{II}}\, dS, \tag{3.6}$$

where $n_{Mg\,\mathrm{II}}$ is the number density of Mg 2 ion relative to the number density of protons in the simulation given by Eq. 3.5, $\sigma_{Mg\,\mathrm{II}}$ is the extinction cross-section of Mg II, taken $\sigma_{Mg\,\mathrm{II}} = 6.5 \times 10^{-14}$ cm^2, as given in Llama et al. (2011), with detailed background in Lai, Helling and Van den Heuvel (2010). It should be noted that the opacities calculated using this method for the magnetosheath region are reliant upon the plasma temperature remaining at $\sim 10^4$ K ($\sim$0.86 eV) which is highly unlikely in such systems. Temperatures in the present work, for instance, reach up to $\sim$5 keV ($\sim 5.8 \times 10^7$ K)in the magnetosheath at 0.2 AU. However, the plasma torus temperatures are a few orders of magnitude lower, at $\sim$30 eV.

The optical depth absorption profiles for an ahead-shock are shown in the left column of Fig. 3.6. The top panel shows the base case for our warm exo-Saturn at 0.2 AU, in which the highest values of optical depth reach $\sim$0.0013, and is located in the interior of the magnetosphere and just outside in the magnetosheath, generated by the pileup of the

shocked stellar wind. The plasma torus contributes weakly. The middle panel shows the 0.2 AU dense case, in which the increased ionization from the stellar host is taken into account as the base case holds all quantities as they are expected at 10 AU. In this case, we see that the increased ionization rates in the upper ionosphere of the planet, as well as the satellite plasma torus contribute more strongly to the optical depth enhancement than the simple pileup of density at the bow shock of the magnetosphere - and the overall optical depth reaches a value of $\sim$0.0027. The heavy ions lost from the ionosphere (in this case assumed to be Mg 2) are contained in the inner magnetosphere, unable to radially propagate as seen in § 3.7; the enhanced density from the satellite torus plasma in areas both interior to the magnetopause, and in the magnetosheath and bow shock regions contributes directly to an increase in optical depth in those regions. The orbit of the satellite at 4 R_P ensures the ion producing exomoon is contained by the magnetopause (except in the 0.2 AU slow case), but plasma collects in the boundary region and piles up internally against the magnetopause, creating a strong ion density that flows to high latitudes within the magnetosphere.

One could assume a plasma torus with a much higher concentration of Mg 2, given volcanic activity, for instance. Singly ionized Mg - at a mass to charge ratio of 24 amu C^{-1} - would behave similarly to the 18 amu C^{-1} injected in the present study. If we assume volcanic input of Mg instead of the water-group ions in our plasma torus, the optical depths calculated in Fig. 3.6 with a pure Mg 2 plasma torus would be quite optically thick ($\tau >$ 1) - particularly for systems like the 0.2 AU dense case, where the torus densities reach a few times $\sim 10^3$. However, the photon count at the desired wavelengths for Mg 2 absorption from a Sun-like star is low, and the presence of other species would be beneficial.

The potential effect on transit light curve observations from both the plasma torus and the enhanced magnetosheath region is shown in such a configuration. Near the inner boundary of our simulation, at 2 R_P, the optical depth reaches values of more than double the highest in the base case, at a level $\sim$0.0027. The shocked region shows an enhancement of $\sim$40%, with optical depths up to $\sim$0.0018. While these depths are not near the 1% or so anomalies observed by HST for the hot Jovians (Nichols et al., 2015), future missions will likely reach lower sensitivity; taking into account a dense plasma torus as discussed above for the 0.2 AU dense case, and that a torus-producing moon will have less restricted

conditions on its stability at 0.2 AU than 0.02 AU, the potential for transit modifications from giant magnetospheres in a warm orbit should be considered.

This spreading of the satellite generated heavy ion plasma from the torus region to cover such a large area interior to the magnetopause could indicate a strong signature in the transit light curves, depending upon through which portion of the magnetosphere the stellar flux is observed. The strength of the transit signal modification predicted here is detectable by current technology, and future instrumentation. In this analysis, it is noted that we calculated the optical depth for a doublet line emission for only a single species, and assume an actual observation would encompass many wavelengths across stellar ion species to increase the photon count across the stellar spectrum.

An expanded discussion of exomoon detectability and characterization can be found in § 7.2.

3.11 Concluding Remarks

We have simulated the effects of stellar wind dynamic ram pressure on a Saturn-like exoplanet with an Enceladus-like plasma torus using a 3D multifluid plasma model. The simulation at 10 AU sets a baseline, with inputs from Cassini data. All planetary parameters are kept constant, varying only the stellar wind dynamic ram pressure in each case, aside from the two special cases of 0.2 AU dense and 0.2 AU slow. The simulation output suggests the following:

1. The planetary magnetosphere for a Saturn-like planet with an Enceladus-like satellite plasma torus becomes stable to centrifugal interchange at some point moving starward from a semi-major axis of 5 AU to 1 AU, given constant ionospheric and satellite torus density. The stability criteria shown in Fig. 3.2 support this conclusion. For a Saturn-like system, the ratio of thermal energy to corotational energy crosses the threshold of stability at unity between 5 and 1 AU.

2. The present work suggests there is an direct relationship between magnetospheric compression and time scale to reach equilibrium mass loss. Highly compressed magnetospheres (e.g. 0.2 AU and 1 AU in the present work) reach equilibrium mass loss

rate rapidly, and are stable to interchange. While the equilibrium value for mass loss is equivalent for each semi-major axis studied, less compressed magnetospheres (e.g. 5 AU and 10 AU) start with a lower outflow rate after quiescent stellar wind passage, but fall within the window of instability for centrifugal interchange. The multifluid simulations suggest that while interchange does not affect the overall mass loss rate of a planetary system, stronger instability (like that at 10 AU, when compared to 5 AU) can reduce the time scale to reach mass outflow equilibrium.

3. For warmer orbits, the magnitude of auroral-related field aligned-currents (FAC) are increased, with a corresponding broadening of latitudinal spread and equatorward locations. This has implications for planetary auroral radio signatures.

4. From the perspective of characterizing potential radio observations of exoplanets, the coverage of radio emissions varies broadly with increasing stellar wind dynamic ram pressure and beaming angle (emission frequency). Emissions with wide beaming angles are more impacted from the increase in steady state stellar wind pressure, leading to a large portion of the celestial sphere around the planet having higher radio coverage.

5. UV transit observations could be impacted by the bow shock and/or satellite generated plasma torus for a planet at a warmer orbit of $\sim$0.2 AU. This leads to potential planetary characterization for a larger population of giant planets than just hot Jovians.

In the present work, we simulated hypothetical magnetospheres for giant, rapidly-rotating planets in increasingly warmer orbits. All orbits were outside the critical Alfvén radius for the Sun-like star, and so no direct star-planet interaction (SPI) was simulated. Future work will include more simulations in the transition region between 5 AU and 1 AU for the Saturn-like planet, a case at 0.2 AU which includes the effects of the dense and slow cases, simultaneously. It would also be interesting to simulate a terrestrial planet analog to compare with the Saturn-like planet, effects of CME events, a more varied IMF configuration, and seasonal effects due to the rotational inclination of the planet. The inclusion

of a high-resolution grid around a potentially habitable exomoon orbiting at distances of various planetary radii is also a future goal.

Chapter 4

THE EFFECTS OF PLASMA PRESSURE ANISOTROPY AT SATURN

4.1 Overview

The Kronian magnetosphere is a rapidly-rotating, axisymmetric system and driven by the mass loading of primarily H_2O^+ group ions picked up at the orbit of Enceladus. Previous 3D models of the Kronian system have not taken into account the high amount of plasma pressure anisotropy that has been observed by Cassini and reported in the literature. This plasma pressure anisotropy is a source of free energy that can have significant effects on the magnetic structure and plasma dynamics throughout the magnetosphere. This work directly compares the simulations of two 3D multifluid models of the Kronian magnetospheric system with identical inputs - one model run with isotropic plasma pressure, and one with a full treatment of plasma pressure anisotropy, including non-gyrotropic components. The anisotropic model shows a higher degree of agreement with Cassini observations with respect to, e.g., the magnetodisc structure of the system, plasma temperature distribution, plasma convection, and current systems.

4.2 Introduction

Pressure anisotropy is an important source of free energy that can drive instabilities as well as influence mass transport in a plasma; the anisotropy can be thought of as a measure of pressure relative to local magnetic field direction (e.g., $P_\perp$ vs. $P_\parallel$).

Cassini observed significant plasma pressure anisotropy in both H_2O-group ions and protons in the inner to middle magnetosphere of the Kronian system. The large anisotropies at Saturn were first reported and analyzed by Sittler et al. (2008) and Wilson et al. (2008), with values as large as $P_\perp/P_\parallel$ = 5-8 for water group ions, W^+, in the inner magnetosphere. Thomsen et al. (2010), in a survey of ion parameters at Saturn, noted that anisotropies were

the likely cause of differences in flow speeds and low latitude plasma characteristics seen between the overall data survey in Thomsen et al. (2010), and earlier, limited Cassini analyses. An analysis of Cassini Plasma Spectrometer (CAPS) data throughout the Kronian magnetosphere was reported in Wilson et al. (2013), and found accounting for ion temperature anisotropy in their analysis more correctly reproduced an offset in the observed noon-midnight electric field and resulting plasma convection from the $\mathbf{E}\times\mathbf{B}$ drift. Kane et al. (2014) analyzed anisotropic ion data from Cassini's Ion Neutral Camera (INCA) to study plasma convection, and found that the nightside convection is predominantly azimuthal to $\sim$50 R_S with significant radial component due to slippage of the ionosphere-magnetosphere coupling through field-aligned currents (FAC); compared to Jupiter, there was no local time asymmetry. From fundamental analysis, and the above in situ observations, we know there is a correlation between anisotropy and plasma convection, confinement of plasma to the equatorial plane, as well as mass transport to the outer magnetosphere.

Recently, efforts to couple pressure anisotropy and magnetohydrodynamic (MHD) modeling have been reported, with general investigations of anisotropic effects in 1D and 2D plasmas, as well as global simulations. Hirabayashi and Hoshino (2013) studied global reconnection in anisotropic plasmas, and found that the presence of strong anisotropy increases the reconnection rate by 10%-30% in slow shocks. Kelvin-Helmholtz instabilities have been studied in anisotropic MHD by Prajapati and Chhajlani (2010) and found that the growth rate of such instabilities is destabilized by increasing pressure anisotropy. Global MHD simulations for Earth's magnetosphere have shown anisotropic effects directly result in the formation of eastward ring current, enhanced night-side plasma pressure, altered thickness of the magnetosheath, a shorter tail, and a much smaller Earthward plasma jet from the tail reconnection site (Meng et al., 2012, 2013). However, all the above efforts included a formulation for anisotropy, known as the Chew-Goldberger-Low (CGL) approximation (Chew, Goldberger and Low, 1956), which maintains a single, uniform isotropization factor throughout the magnetosphere. Due to this factor, the CGL approach is a gross simplification of the dynamics in the Kronian system, given that the system has orders of magnitude variations in magnetic field strength, plasma density and plasma temperature.

Efforts to include a full treatment of pressure anisotropy have been reported for the

terrestrial and Jovian magnetospheres. Ion anisotropies are shown to drive substorm enhancements, including effects on onset timing and outflow rates (Winglee and Harnett, 2016*a*). Similarly, the anisotropic Jovian magnetosphere was studied, and a correlation between polar outflow rates and the torques that drive the wobble in the corotating, axially tilted magnetosphere (Winglee and Harnett, 2016*b*).

The work in this section investigates the effect of plasma pressure anisotropy on mass transport in Saturn's magnetosphere, compared to identical simulations performed by a version with only isotropic pressure included.

4.2.1 Physics of Plasma Pressure Anisotropy

The origin of plasma pressure anisotropy associated with the second moment is correlated with the flow and convection of plasma - as in the solar wind (e.g., Marsch, 2012), as well as gyrotropic processes (Chew, Goldberger and Low, 1956). Analyzing the form of the fully anisotropic treatment of pressure anisotropy in Eq. 2.10, the terms can be described as:

$$\nabla \cdot \left(\mathbf{v}_\alpha \overline{\overline{\mathbf{P}}}_\alpha \right) \quad \text{(Advection and compression)} \tag{4.1}$$

$$\nabla \mathbf{v}_\alpha \cdot \overline{\overline{\mathbf{P}}}_\alpha + \left(\nabla \mathbf{v}_\alpha \cdot \overline{\overline{\mathbf{P}}}_\alpha \right)^T \quad \text{(Strain and shear)} \tag{4.2}$$

$$\frac{q}{m_\alpha} \left[\left(\overline{\overline{\mathbf{P}}}_\alpha \times \mathbf{B} \right) + \left(\overline{\overline{\mathbf{P}}}_\alpha \times \mathbf{B} \right)^T \right] \quad \text{(Gyration due to the magnetic field)} \tag{4.3}$$

with the off-diagonal terms in Eq. 4.2 producing a source of non-gyrotropic anisotropy from the fluid strain (velocity shear) (e.g. Del Sarto, Pegoraro and Califano, 2016), along with the gyroscopic sources in Eq. 4.3. Including these terms in the model makes the simulation a 10-moment ion multifluid model, compared to the 5-moment isotropic model - effectively doubling the computation time in solving the differential equations.

To relate the results of the full treatment of pressure anisotropy to the well-known CGL approach, we define the bases of $\mathrm{P}_\parallel$ which is the pressure along the local magnetic field direction, and $\mathrm{P}_\perp = \left(P_{\vec{v}\times\vec{B}} + P_{\vec{B}\times\left(\vec{v}\times\vec{B}\right)} \right)/2$, pressure perpendicular to the local magnetic field. Note the two perpendicular terms are orthogonal - the former term associated with plasma convection, and the latter related to the $\vec{E} \times \vec{B}$ direction which will contribute in

regions where the scale length comparable to the ion gyroradii.

The free energy of plasma pressure anisotropy can alter magnetospheric dynamics, through the generation of instabilities. One can measure the effects of anisotropy through the dimensionless ratio:

$$\alpha \equiv \mu_0 \frac{P_{\parallel} - P_{\perp}}{B^2} \tag{4.4}$$

with values of α >1 driving a firehose instability, and α <-1 producing a mirror instability (e.g., Siscoe, 1983). These effects of anisotropy are related to the plasma β, and can be neglected in regions where β is not of order unity. The present model does not explicitly limit or dissipate any instabilities, and allows the system to evolve physically without restraint.

4.3 Simulation Setup

For both the simulations compared here, isotropic and anisotropic, we used the following grid parameters. A Cartesian coordinate system such that x is in the direction of a planet-star line in the equatorial plane of the planet, positive pointing away from the star. The z axis is aligned with the planetary rotation axis, positive towards the northern magnetic pole as the magnetic configuration of the planet is approximately axisymmetric. The y direction completes a right-handed coordinate system, and points in the direction of the tangent to planetary orbital motion.

Five cubic, nested grids were used for each case in the study, with the innermost grid centered on the planet with an inner boundary at 2.0 R_P. This inner grid is $\pm 12 R_P$ in the x- and $y-$directions, and $\pm 6 R_P$ in the z-direction, with a resolution of $0.2 R_P$ in all dimensions. Each higher-order grid increases by a factor of 2, and so the outermost grid is a factor of 16 larger, but not necessarily centered on the planet. The outermost grid extends from -$128 R_P$ sunward to $256 R_P$ down the magnetotail in the x-direction, $\pm 192 R_P$ in the y-direction, and $\pm 96 R_P$ in the z-direction. This scaling allows the multifluid model to capture dynamics across multiple scales, from a fraction of a planetary radius, up to massive structure formation down the magnetotail.

The solar wind conditions were set to density of 0.0625 cm^{-3}, temperature ~1.2 eV, velocity of 450 km s^{-1} in the X-direction, and for the parallel IMF case (para), an IMF with B_y (B_z) = -0.495 (-0.128) nT. Two other cases were also simulated: 1) an anti-parallel case (anti) with a value for B_z of 0.128 nT and all other parameters the same as the above, and 2) a low solar wind pressure case (lowp), with parallel IMF and v_{SW} = 400 km/s, with a density of n = 0.0125 cm^{-3}. The simulations tracked three ion species: 1) water group ions, W^+, injected by Enceladus, 2) protons in the solar wind as well as from Enceladus, H^+, and 3) O_2^+ ions from the Enceladus torus.

For the anisotropic run, all plasma was initialized with isotropic pressure and allowed to evolve throughout the simulation with no further alteration to the level of anisotropy. The exception to this is the injected plasma from the Enceladus plasma torus. The injected ion fluids were assumed prior to ionization with initial neutral thermal speed less than the speed of plasma corotation at the point of injection, so the injected ions were picked up with $P_\perp > P_\parallel$. The Enceladus torus was injected with a total of ~360 kg s^{-1} of plasma, ~342 kg s^{-1} of which were water group (W^+) ions, and the remaining ~18 kg s^{-1} were H^+ and O_2^+. This is the same process reported in § 3.5.

All simulations were performed with an equinox seasonal orientation for planetary rotational inclination, and three cases were run in both the anisotropic and isotropic models: 1) anti-parallel (closed magnetosphere) IMF, 2) parallel (open magnetosphere), and 3) low pressure solar wind (closed IMF).

Note that all radial plots in this work are averaged over equatorial azimuth and time (~100 hours) for all simulations, unless otherwise mentioned.

4.4 Anisotropy effects on magnetospheric structure and dynamics at Saturn

Including plasma pressure anisotropy improves the physics-based modeling of the multifluid model, and therefore its predictive capability, and suggests that the ion anisotropies contribute to several structural and dynamical signatures. Below, we show that including ion pressure anisotropy allows the multifluid model to capture more physically realistic processes, which leads to closer agreement between simulation data and observations; such agreement is particularly affected in the inner magnetosphere, including radial averages of

ion densities and temperatures, as well as overall global parameters such as corotation, interchange formation and azimuthal currents.

4.4.1 Measure of anisotropy, azimuthal current, and equatorial force balance

The multifluid model including anisotropy was run with no anomalously set anisotropy, and no relaxation timescales; the physics of the anisotropic ion dynamics is controlled solely by the derived pressure equation, Eq. 2.10. Only the initial anisotropy of the injected ion material in the Enceladus torus at 4 R_S was explicitly set, and was scaled according to the amount of net corotational pickup energy at ∼4 R_S for each of the species - W^+ (water group ions, H_2O^+, H_3O^+, OH^+, O^+) (18 amu, average), H^+ (1 amu) and O_2^+ (32 amu). At this radial distance, the flow speed (∼39.5 km/s) exceeds the thermal speed of the neutral cloud (∼12.5 km/s), so the pickup ions exhibit anisotropic temperatures/pressures ($P_\perp > P_\parallel$). In no other location is the anisotropy set explicitly.

Fig. 4.1 shows ion anisotropy for H_2O^+ and H^+, both as azimuthally and time averaged radial profile (left column), and a snapshot of a cut through the magnetic equatorial plane for the parallel and IMF case (right column). The dynamics of Saturn's magnetosphere are driven by the relatively high-mass water group ions (∼18 amu), as they comprise the large majority (∼92%) of all ions injected into the corotating system by Enceladus. In the center of the Enceladus injection region at ∼4R_S, the anisotropy for water group ions is significant ($P_\perp/P_\parallel > 3$). With increasing radial distance, however, one notes that the anisotropy actually flips to the opposite anisotropy condition ($P_\parallel/P_\perp \approx 1.25$) for a few planetary radii in the middle magnetosphere in all cases. The average for the water group ions (protons) drops to ∼0.8 (0.75) at ∼7 R_S. This region is associated with the interchange instability (discussed in Chapter 3) and was extensively studied in previous work with the isotropic version of the multifluid model by Kidder, Winglee and Harnett (2009) and Snowden, Winglee and Kidder (2011). The large-scale interchange is still strongly seen in the present work, in both the isotropic and anisotropic simulations.

It is interesting to note the dashed, colored lines in the left column of Fig. 4.1, as they represent the different solar wind forcing on the Kronian system. The dashed red line

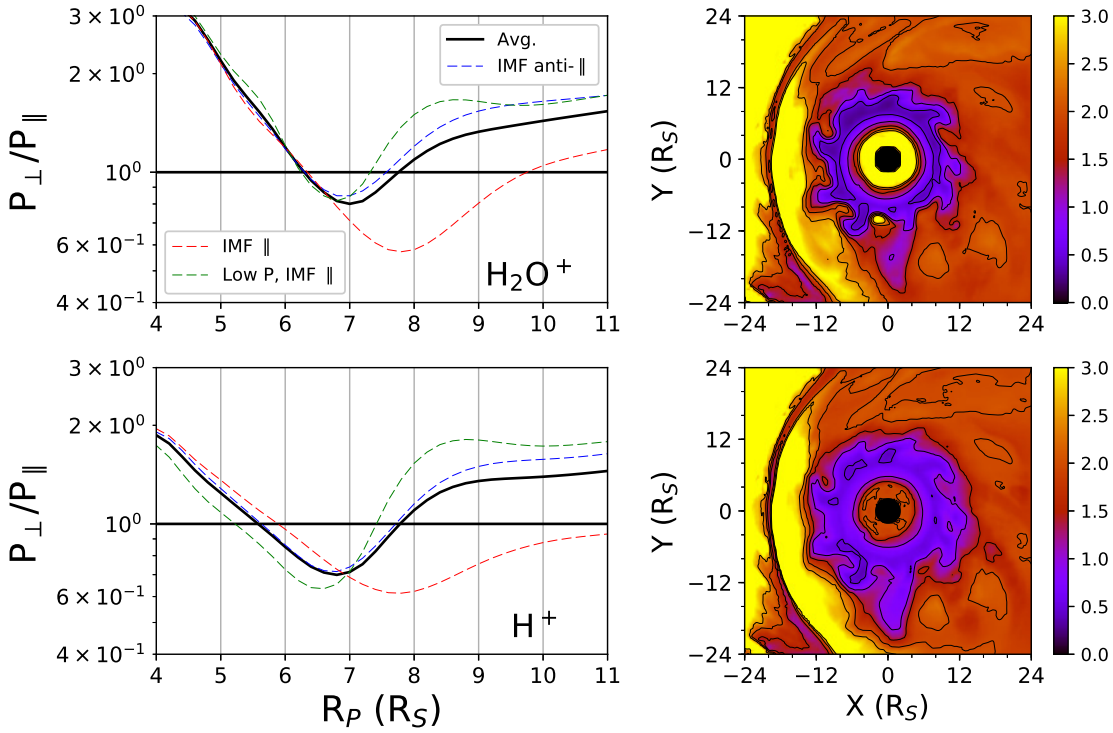

Figure 4.1 **Top left:** Azimuthal, time-averaged, radial measure of anisotropy for W^+ ions. **Bottom left:** Azimuthal, time-averaged, radial measure of anisotropy for H+ ions. In both cases, the solid black line is the average, and the dashed lines represent the parallel-IMF (red), anti-parallel IMF (blue), and low pressure simulations (green). **Top right:** Equatorial slice of W^+ anisotropy. **Bottom right:** Equatorial slice of H^+ anisotropy. Both slices represent the parallel-IMF simulation.

represents a system driven by parallel IMF, or a 'closed', Axford & Hines viscous driven or Vasyliunas-cycle driven magnetosphere; the dashed blue line represents the anti-parallel IMF, or an 'open', Dungey-style magnetosphere; the green dashed line represents the parallel or 'closed' system, but with a factor ∼6.3 less dynamic ram pressure. The viscous, 'closed' magnetosphere system shows the highest degree of inversion for both ion species, with parallel-dominated anisotropy 33% (14%) stronger than the average for the W^+ (H^+) ions. As the magnetosphere is closed, and the primary way for mass loss from the system is down the magnetotail (in addition to some at high latitude, cusp reconnection events), the more consistently mass loaded, corotating system would exhibit a higher propensity for stretched magnetic flux, in conjunction with the parallel heating of those ions.

To compare the degree of anisotropy directly with Cassini observation, we select ion temperatures from only the dayside (9-15 LT), equatorial (within ±5° latitude) magnetosphere according to the data analysis method used in Wilson et al. (2008). The top row of Fig. 4.2 shows the multifluid radial profiles from 5-11 R_S from 900 - 1500 local time for both H_2O^+ and H^+ ions, for both the parallel (dashed red line) and anti-parallel (dashed blue line) IMF cases. The bottom row represents comparison of the average from the multifluid simulations (solid black line) to the Cassini CAPS results (multicolored crosses) reported in Wilson et al. (2008). Note that the IMF orientation at the time of the CAPS instrument measurements is unknown.

For both ion species, the multifluid simulation shows a strong dayside pressure anisotropy, in agreement with Cassini observations. The trend is similar to that of the CAPS measurements, though the magnitude of anisotropy is lower than reported by Wilson et al. (2008), as seen in the bottom rows of Fig. 4.2. Particularly, in the inner magnetosphere ($R_S \lesssim 8$) there is a large difference between the CAPS data and the simulated results.

One reason is that the multifluid simulation does not include the physical presence of the Enceladus moon itself, instead injecting plasma in a symmetric azimuthal torus at a cadence of ∼1 minute. The presence of the physical moon will perturb the magnetic field of the system, forming alfven wings and associated currents due to the presence of an internal, spherically symmetric conducting layer. Further, the ion pressure on the ram and lee sides of the moon will be quite different, driving temperature perturbations. Both of

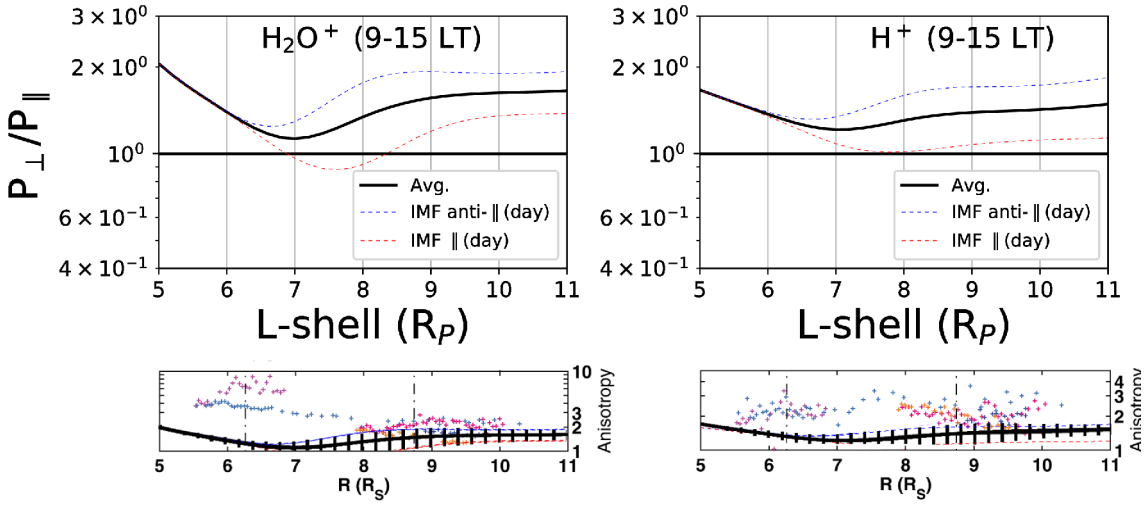

Figure 4.2 **Top row:** W^+ and H^+ anisotropy on the dayside (0900-1500) within 5° of the equator. **Bottom row:** The same quantities compared to Cassini/CAPS anisotropy measurements from Wilson et al. (2008) (adapted from Wilson et al. (2008). The error bars represent the 1-σ uncertainty in the multifluid model.)

these alterations from the physical moon can energize ions and enhance populations with much higher temperatures and degree of anisotropy.

A second contributing reason for this difference could be related to the seasonal tilt of the Kronian dipole during the time of Cassini data collection reported in Wilson et al. (2008) (2005-2006, northern pole pointed away from the Sun, or Kronian northern winter); the multifluid simulations here were all run with the dipole in an equinox position as we are not focused on seasonal effects. During summer or winter, the stresses on the Kronian magnetosphere are asymmetric, and bend the plasma sheet north or south into a bowl shaped plasma sheet in the nightside. This produces dynamic differences between the inner/middle and outer magnetosphere, and puts Cassini orbits at the nominal equatorial latitudes (±5°) which samples ion populations in the lobe regions of the magnetosphere. The simulated data here are from an idealized slice near the equatorial region, again in equinox. Unfortunately, CAPS data for measurements during equinox are sparse due to hardware difficulties.

The water group ions injected by Enceladus, along with the rapid corotation of the

planetary magnetosphere, produce centrifugal, pressure gradient and anisotropy forces that generate outflowing plasma that stretches the planetary magnetic field lines shown as the purple regions in the right column of Fig. 4.1.

In Fig. 4.1, one can see an anisotropy inversion occurs between 6-8 R_S where $P_\perp/P_\parallel$ <1. In the right column, this corresponds to the darker, purple colors in the middle magnetosphere. The anisotropy inversion seen in the equatorial region is related to the parallel thermal energization of the plasma as the equatorial magnetic field is stretched by the increasing centrifugal forces of the corotating plasma. As discussed in Northrop and Birmingham (e.g., 1982); Kivelson (e.g., 2015), ions convecting radially outward will be energized parallel to the magnetic field, therefore decreasing the measure of perpendicular anisotropy. It is in this region that we see the stretched field forming the Kronian magnetodisc, and we can further verify this by looking at the force balance in the modeled system.

The overall force balance between the azimuthal current, plasma pressure gradient, centrifugal force, and the anisotropic contribution can be estimated as below (e.g., Sergis et al., 2010):

$$\rho\frac{v_\phi^2}{r} - \frac{\partial P}{\partial r} - \frac{P_\perp}{R_C}\left(\frac{A-1}{A}\right) \approx J_\phi B_z \tag{4.5}$$

where ρ is the total ion mass density, v_ϕ is the azimuthal plasma velocity, r is the equatorial radial distance, $P(P_\perp)$ is the total (perpendicular) plasma pressure, A is the measure of plasma anisotropy $P_\perp/P_\parallel$, J_ϕ is the azimuthal (ring) current, and B_z is the equatorial z-component of the planetary magnetic field. The third term on the LHS of Eq. 4.5 shows that in a corotating plasma dominated by parallel pressure (A < 1), the force is enhanced in the radially outward direction, driving radial flow. Similarly, this outward force produced by strong parallel anisotropy is responsible for the formation of the magnetodisc at Saturn and Jupiter (e.g., Kivelson, 2015).

The top left panel of Fig. 4.3 shows the modeled azimuthal current for both the anisotropic (solid red) and isotropic (dashed blue) versions of the model. One immediately obvious difference is the comparatively high current in the near Enceladus torus equatorial magnetosphere from ∼4.5-8 R_S in the anisotropic simulation. This is explained by comparing

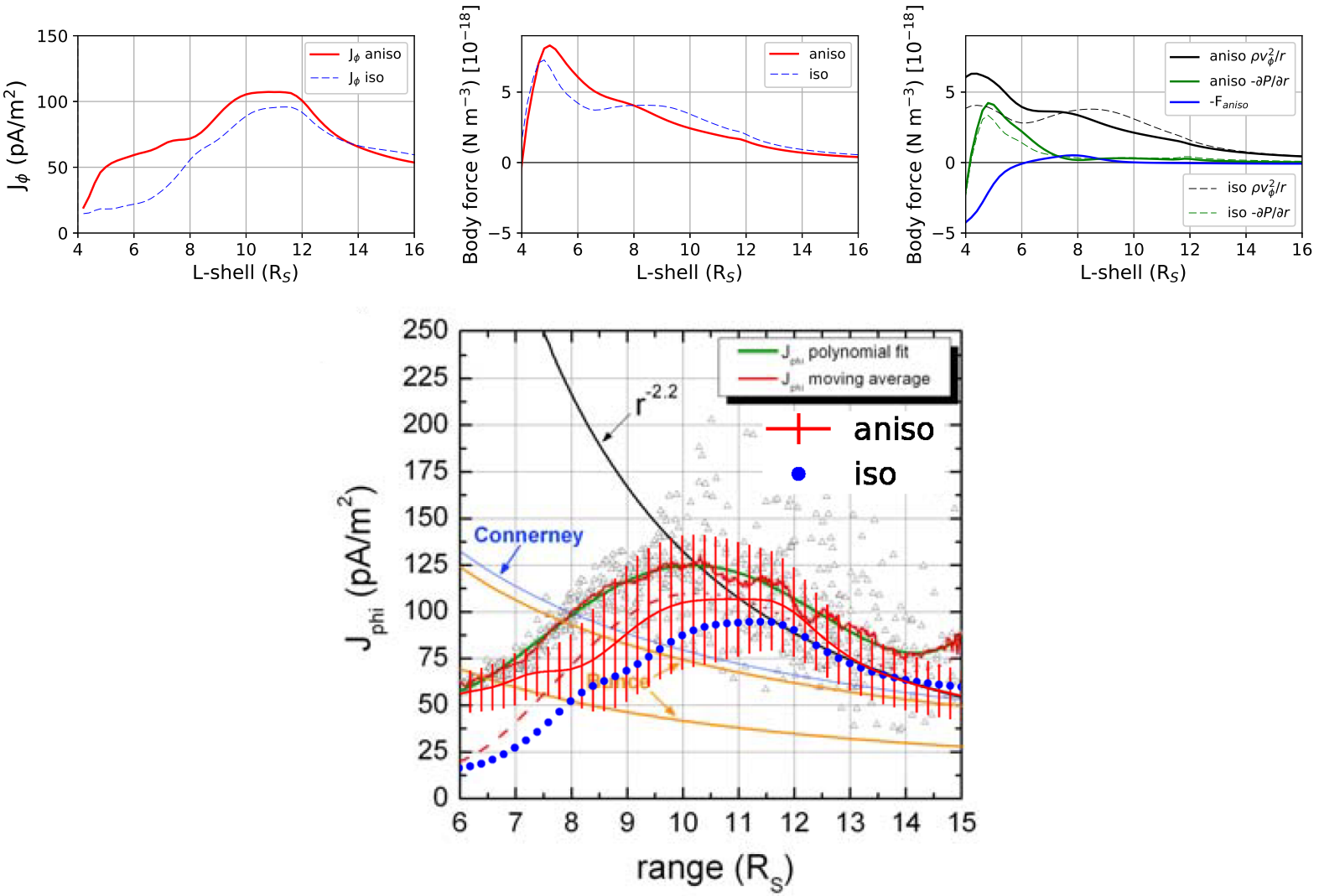

Figure 4.3 **Top left:** Azimuthal current density for the anisotropic (solid red) and isotropic (dashed blue) simulations. **Top middle:** Body force in the magnetosphere for the anisotropic (solid red) and isotropic (dashed blue) simulations. **Top right:** Force components for the anisotropic (solid) and isotropic models (dashed); components are centrifugal (black), pressure gradient (green), and the anisotropic force (blue). **Bottom:** Comparison of the anisotropic (red with 1σ uncertainty error) and isotropic (blue dotted) simulations to Cassini data from Sergis et al. (2010) (adapted from Sergis et al. (2010)).

the two models, with regard to the overall force balance, as seen in the top center panel of Fig. 4.3, which represents the LHS of Eq. 4.5. There, we can see that the anisotropic model (solid red), when compared to the isotropic model (dashed blue), simulates a system that requires a higher azimuthal current to balance the overall body force produced by the centrifugal, pressure gradient and anisotropic/curvature terms.

The top right panel of Fig. 4.3 sheds some light on the driving physics. One can see that in both the anisotropic (solid lines) and isotropic (dashed lines) cases, the centrifugal force (black) dominates the overall balance. In particular, the anisotropic centrifugal contribution is larger than the isotropic centrifugal contribution by up to $\sim$55%, which is approximately the respective difference between the two models' equatorial densities at those radial distances (see discussion in § 4.4.2 below). This difference is expected, as the strong perpendicular pressure anisotropy in the (near-)torus region represents an equatorial confinement of the Enceladus-injected W^+ ions which would not be present in the isotropic model. The pressure gradient (green) is similarly larger in this region for the anisotropic model, due to the steeper density profile near the torus. However, the anisotropic force (solid blue) provides some correction to the overall force balance in the anisotropic model, making the overall force magnitudes comparable. Comparison to Cassini shows better agreement with the anisotropic model (cf. Sergis et al., 2017), with respect to the overall body force and individual terms from Eq. 4.5.

A comparison to Cassini ring current data from Sergis et al. (2010) can be seen in the bottom panel of Fig. 4.3. The primary Cassini/MIMI/CAPS comparison we are primarily interested in are the polynomial fit (solid green line) and moving average (thin red line) which are derived from the Cassini/MIMI/CAPS data points (grey triangles); the red solid line with 1-σ uncertainty and blue dotted line are the results from this work - the anisotropic and isotropic model, respectively. The Cassini/MIMI/CAPS data represent data from Cassini from September 2005 to May 2006, during Kronian winter. The results from the multifluid model are azimuthally averaged over $\sim$100 hours of simulation in an equinox configuration. Despite these differences, the the uncertainty in the multifluid model overlaps consistently with data, and more accurately than the isotropic model. A future study involving the seasonally based differences could be interesting to determine the

specifics of seasonal magnetospheric response.

4.4.2 Anisotropic contributions to temperature and density

The inclusion of pressure anisotropy in the multifluid model has significant effect on the dynamics and structure of the magnetosphere at Saturn. Fig. 4.4 shows the temperature and density in the Kronian magnetosphere, as simulation data that is time-average, azimuthally-averaged, and case-averaged over both the parallel and anti-parallel cases for the water group ion (W^+) and H^+ ions (left column), and equatorial snapshots of W^+ $\log_{10}$ temperature and number density for the anisotropic (middle column) and isotropic (right column) parallel IMF cases.

In the upper left panel of Fig. 4.4, the radial average temperature structure for both the water group ions (red) and protons (blue) in the magnetosphere show similar trends with the inclusion of pressure anisotropy. Both ion species in the anisotropic simulation (solid lines) exhibit a lower overall temperature compared to the isotropic simulation (dashed lines) in the Enceladus torus (W^+ (H^+) - ∼30 (6.5) eV for anisotropic, vs. ∼47 (8.1) eV for isotropic), with the trend extending radially outward to ∼7 R_S, where the temperature in the anisotropic case becomes equivalent or higher, in the case of the H^+ ions. Extending outward towards the magnetopause, all simulated cases underpredict the temperature compared to Cassini measurements from Thomsen et al. (2010), seen below in Fig. 4.5. The multifluid model does not include kinetic effects, so some energizing processes present in the Kronian magnetosphere are not captured in the simulations. Fig. 6 of Bagenal and Delamere (2011) shows that the magnetosphere becomes dominated by these energetic ions at ∼12 R_S, so beyond that radial distance we would expect divergence.

The anisotropic and isotropic cases are similar with regard to the radially averaged temperature of the W^+ ions, underpredicting by a factor of 10-20% compared to the lower bound of Cassini measurements (e.g., Thomsen et al., 2010). The H^+ ion temperatures in the anisotropic simulation differ from observation by a factor of ∼2-3, but the isotropic case is lower by an order of magnitude in the outer magnetosphere (15-20 R_S).

The $\log_{10}$ density radial, equatorial profile is shown in the left column, bottom panel

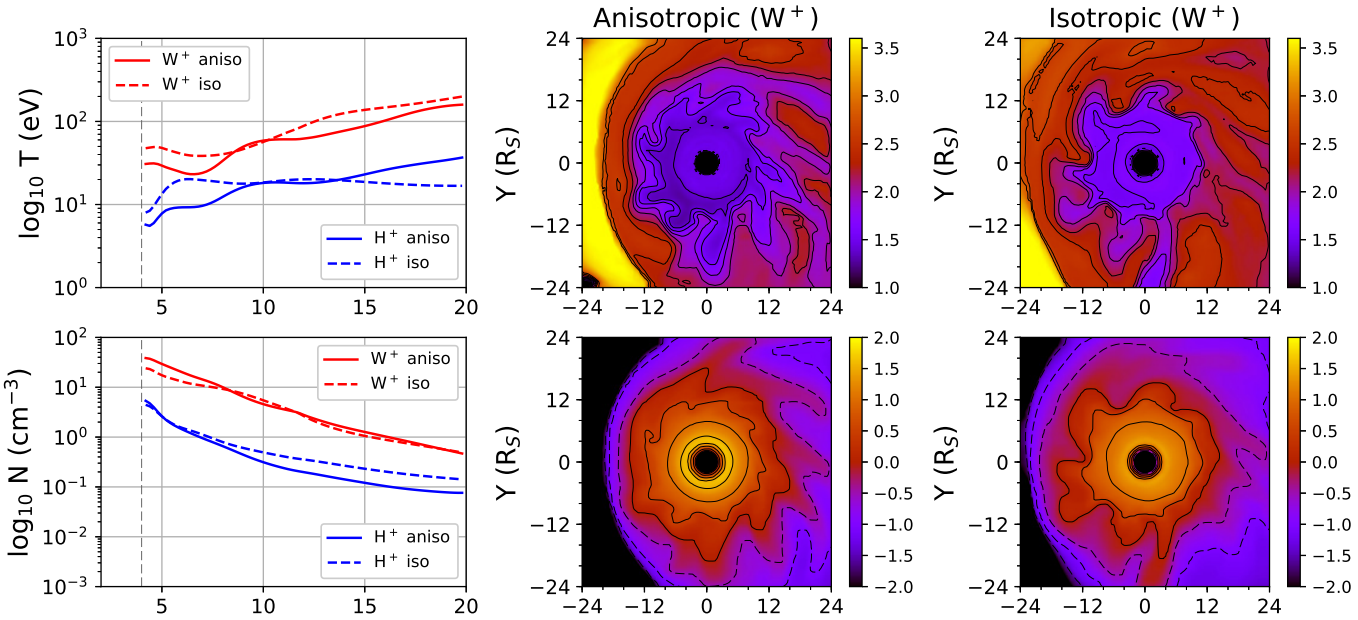

Figure 4.4 **Left column:** Azimuthal, time-averaged radial measures for W^+ (H^+) ions in red (blue) are plotted for the anisotropic (solid) and isotropic (dashed) models. **Middle and right columns:** Equatorial slices for the W^+ ions from the anisotropic (middle) and and isotropic (right) models for the parallel-IMF simulations. **Top row:** Log_{10} ion temperature. **Bottom row:** Log_{10} ion density.

of Fig. 4.4. Results for the anisotropic model (solid lines) and isotropic model (dashed lines) are shown for both W^+ (red) and H^+ (blue). The anisotropic model predicts an Enceladus torus density increased by a factor of ∼60% over the isotropic model (∼38 cm^{-3} vs. ∼24 cm^{-3}) for the W^+ ions, which more closely matches Cassini observations (e.g., Persoon et al., 2009; Thomsen et al., 2010; Bagenal and Delamere, 2011, for reviews, see also Fig. 4.5). The average H^+ densities at 4 R_S in both the anisotropic and isotropic cases agree well with Cassini measurements, with the anisotropic model predicting an H^+ density ∼24% higher than the isotropic model (∼5.6 cm^{-3} vs. ∼4.5 cm^{-3}). The simulated outer equatorial magnetosphere densities are higher than the average, but still within range of the low-latitude Cassini measurements, with the anisotropic case for H^+ ions falling closer to the middle of the trend, as shown below in Fig. 4.5.

Comparing with the diffusive equilibrium model of Persoon et al. (2009), we find that the predicted ion density gradients for both W^+ and H^+ were in closer agreement for the anisotropic model. From the Cassini observations, Persoon et al. (2009) found radial dependence of $L^{-4.3}$ ($L^{-3.2}$) for the W^+ (H^+) ion density gradients between ∼5-10 R_S. The anisotropic (isotropic) multifluid model predicted W^+ density gradients of $L^{-3.2}$ ($L^{-1.5}$) and H^+ density gradients of $L^{-3.0}$ ($L^{-2.4}$). One significant difference, again, is that Cassini orbits for observational measurements were taken from above, across, and below the equatorial plane - up to ±3.5 R_S above or below; the multifluid measurements presented here are from a slice through the exact simulated equator.

In Fig. 4.4, the Enceladus torus stands out as the bright yellow band at 4 R_S in the bottom row, middle column equatorial anisotropic slice when compared to the bottom row, right column isotropic example. One contributing factor to the more tightly constrained Enceladus torus in the anisotropic model is from the azimuthal current structure we see in the left panel of Fig. 4.3 above. As shown in Fig. 4.3, the anisotropic model (solid red line) predicts a factor of ∼3 stronger azimuthal current at 5 R_S when compared to the isotropic model (dashed blue line) (∼47 pA m^{-2} vs. ∼16 pA m^{-2}). This implies that current confinement driven by the azimuthal current contributes strongly to the stability and maintenance of the Enceladus-injected plasma torus. In this region $\mathbf{J}\times\mathbf{B}$ is in the inward radial direction ($\mathbf{J}$ in direction of corotation, or counter-clockwise, and B in the equatorial

plane is in the -$\hat{\mathbf{z}}$-direction). Spiraling, dense bands are also present the anisotropic density slice, which are not seen with strong signature in the isotropic slice. Below, we discuss this as it pertains to centrifugal interchange and mass flow in the system, which can be seen anisotropic (middle) column of both the top (temperature) and bottom (density) rows of Fig. 4.4.

Fig. 4.5 shows the radial extent of equatorial azimuthal averages for the anisotropic and isotropic simulations as they compare to the analysis of Cassini data by Thomsen et al. (2010), as well as the same comparison for previous results reported in Snowden, Winglee and Kidder (2011). The error bars in all figures represent the 1-σ uncertainty, in particular for the anisotropic model in the top two panels, and for the isotropic model from Snowden, Winglee and Kidder (2011) in the bottom two panels. The azimuthal averages from Snowden, Winglee and Kidder (2011) were calculated differently than in the present work, with data averaged over points taken at 15 minute cadence for 12 total hours at only four points in local time (midnight, dawn, noon, and dusk) during Kronian winter. The averages from the present work's multifluid simulations were interpolated at 1° azimuthal intervals at 30 minute cadence over ∼120 hours during Kronian equinox. Solar wind conditions were kept constant in the multifluid simulations, where they were fluctuating in Snowden, Winglee and Kidder (2011). The latter simulations also included a physical representation of Titan, and a high-resolution subgrid around the moon itself; as discussed above, the physical presence of the moon could also contribute to differences seen in the system.

The top two panels show that in the inner magnetosphere, the temperatures and densities for the anisotropic and isotropic models agree with data, but this agreement diverges once the middle and outer magnetospheric distances are compared. There is no or little significant difference between the two implementations, as evidenced by the uncertainty on the anisotropic model. Temperatures are under predicted in the outer magnetosphere, and densities are over predicted in the outer radii, opposite that of the temperature predictions. Once again, the differences in Kronian season could be contributing in the middle and outer magnetosphere, where Cassini measurements are taken from the winter lobe region (tenuous, relatively hotter plasma), and the multifluid results show idealized equatorial measurements in equinox (dense, cooler plasma). When calculating the ion pressures, these

over- and underpredictions are washed out in the combination of the two variables and the results are in agreement with Cassini data for total plasma pressure against the multifluid model's simulated pressures as we'll discuss below.

4.4.3 Anisotropic contribution to Kronian plasma flow

In Kidder, Winglee and Harnett (2009), the strength of centrifugal interchange was shown to be related to the IMF direction, i.e., a stronger interchange instability was present in the simulated data for the anti-parallel IMF driven Kronian magnetosphere. The solar wind in that simulation was initialized and run in accordance to the winter seasonal tilt of the Kronian system, which caused a 'bowl' type effect in the tailward plasma sheet, consistent with Cassini observations. Kidder, Winglee and Harnett (2009) suggested that magnetic reconnection in the tail, as a result of the IMF orientation, contributed to a mass loading of the bend plasma sheet, which then corotates around and contributed to stronger centrifugal interchange occurrence. In this work, the opposite is seen - most likely due to the fact that this simulation was not run in Kronian winter, but equinox, and therefore does not have the bowl shaped plasma sheet. Similarly, as seen in Fig. 4.1, the parallel IMF case has stronger parallel anisotropy in the region where the interchange occurs, leading to stronger outflow due to centrifugal forcing.

In Fig. 4.6, we see a time series of images illustrating observed flux interchange and outer magnetosphere mass loading for both the anisotropic (left column) and isotropic (right column) simulations. Both columns show a $\log_{10}$ scale temperature in electron volts (eV), with counter-clockwise rotational motion over a complete, $\sim$10-hour period (nearly one Kronian rotation, which is $\sim$10.65 hours) with each plot representing a 2 hour timestep. In the anisotropic case, we clearly see more well-defined, outflowing fingers of cool, dense plasma from the Enceladus torus when compared to the isotropic case. In stronger agreement with the Cassini data, the 'fingers' formed by the outflowing plasma injected by Enceladus at 4 R_S are more numerous, well-formed and consist of lower temperature ions in the anisotropic simulation.

The high plasma density injected in the Enceladus torus contributes to the strong for-

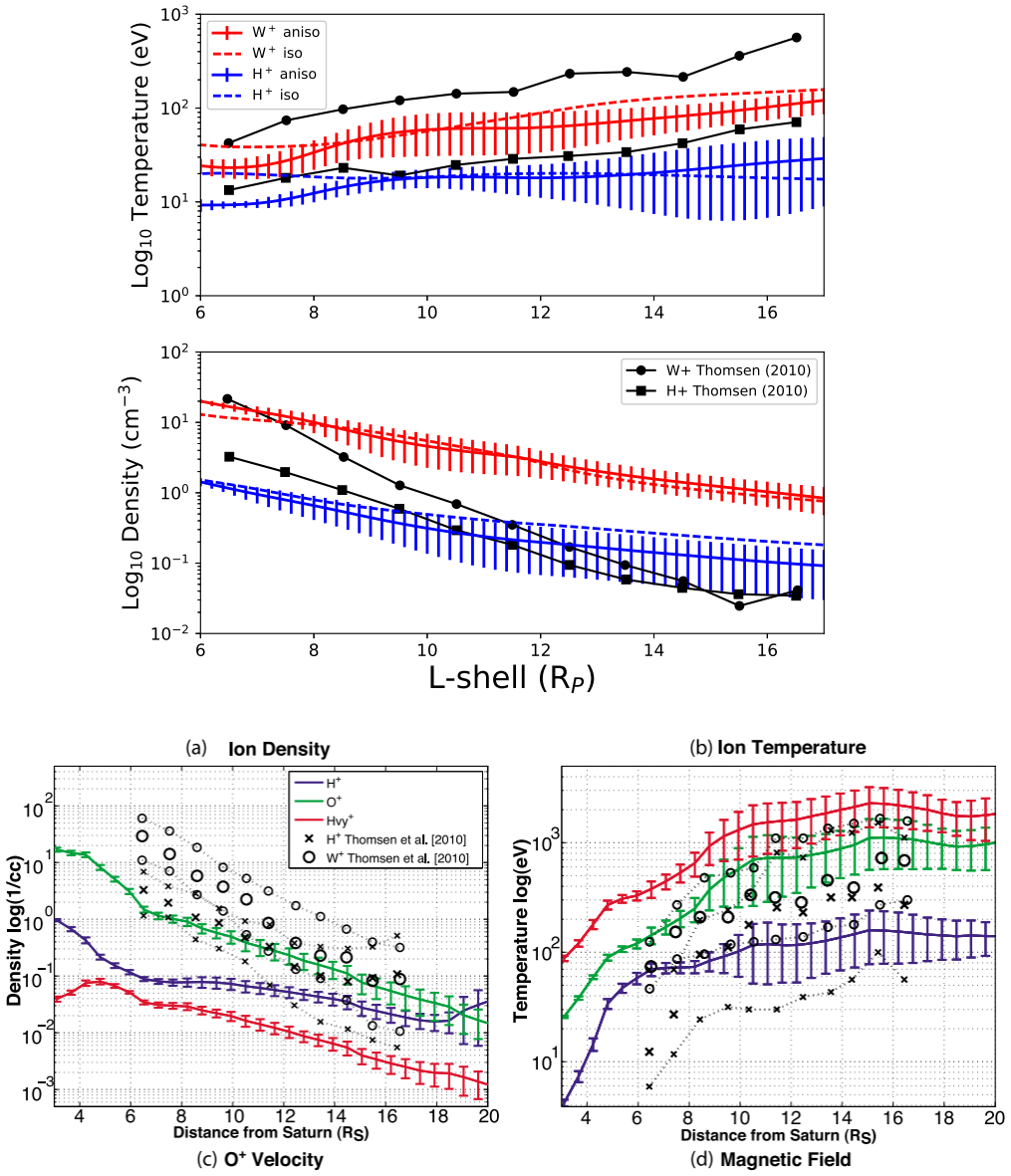

Figure 4.5 **Both:** Azimuthal, time-averaged radial measures of the anisotropic (solid) and isotropic (dashed) simulations for W^+ ions (red) and H^+ ions (blue) compared to compiled, averaged Cassini data for W^+ (black with circles) and H^+ (black with squares) from Thomsen et al. (2010). **Top panel:** Log_{10} equatorial temperatures. **Bottom panel:** Log_{10} equatorial densities. (adapted from Thomsen et al. (2010)).

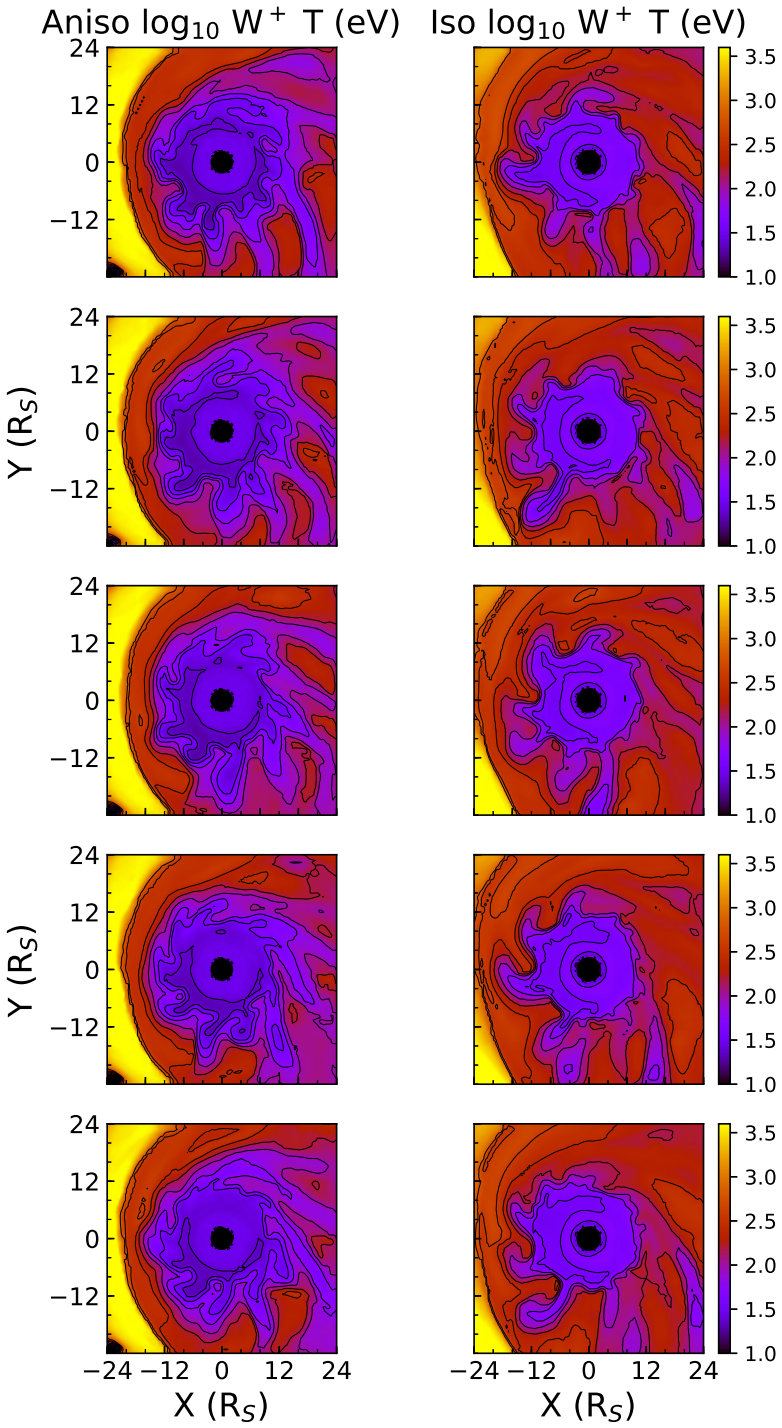

Figure 4.6 **All:** Equatorial slice of the $\log_{10}$ temperature for W^+ ions over a full rotation (top to bottom) for the anisotropic (left column) and isotropic (right column) simulations.

mation of outflowing fingers in both simulations. The mass injection in the present work was at an upper bound for plasma input by Enceladus, at ∼360 kg s^{-1} (∼342 kg s^{-1} of which are 18 amu C^{-1} water-group ions); this introduces a very strong outward centrifugal and pressure gradient forces as seen in Fig. 4.3. Due to the high perpendicular pressure anisotropy of the injected Enceladus torus plasma, as well as that of the middle and outer magnetosphere, the ions are more strongly confined to the equatorial region in the inner and outer magnetosphere, which amplifies the outward centrifugal component when compared to the isotropic simulation (see § 4.4.4 below, in particular Fig. 4.10). The magnetic flux associated with these regions then undergoes interchange, with outward radially adjacent flux, carrying with it the cool plasma. The interchange instability is reliant upon equatorial corotational forces, which is stronger in the anisotropic simulation due to the confinement of plasma to the equatorial regions. For these reasons, the anisotropic simulations show more consistent formation of well-formed 'fingers' of cool plasma interchanging outward into the magnetosphere.

The structure is more regular in the anisotropic case, but one aspect stands out - the fact that these 'fingers' do not survive corotation through the nightside of of the magnetosphere in the isotropic case. This is a nice example of plasma flow down the duskside magnetotail via the Vasyliunas cycle (e.g. Vasyliunas, 1983). The 'fingers' in the anisotropic simulation shown in the left column of Fig. 4.6 flow radially outward from the torus region, and as the Alfvén speed of the plasma falls below the local flow speed, the magnetic field and bands of cool plasma become swept back by the motion of rotation. After a few planetary rotations, the bands of cool plasma expand rapidly into long structures that lag further behind corotation with increasing radius, forming spiral-like structures.

As the fingers approach the magnetopause, the velocity shear against that solar wind interaction also contributes to the bending, while simultaneously compressing the cool plasma. The bands are allowed to expand farther, radially, after rotation carries them through the dayside into dusk, local time, and there - they extend. Here, as predicted in the Vasyliunas cycle, there is a loss of the plasma down the duskside as the structures break when rotating through dusk at ≥20 R_S. As opposed to ejection via a plasmoid generated by magnetic flux merging, this process creates 'drizzle' of plasma down the dusk flank (e.g. Bagenal, 2007).

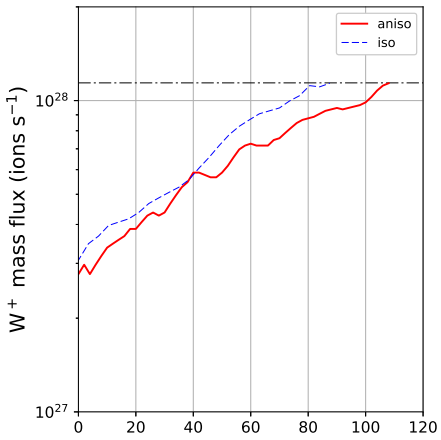

Figure 4.7 W^+ ion flux mass flux out of the system for the anisotropic (solid red) and isotropic (dashed blue) simulations.

The plasma that does not break free or 'drizzle' eventually rotates through the nightside into dawn, where they meet with the sparse, heated plasma contained in the returning magnetic flux and the bands undergo the cycle again.

This process of spiral formation is not as strong in the the isotropic simulations, as seen in the right column of Fig. 4.6. There is a similar formation of plasma 'fingers' or bands, but these cool plasma fingers disappear more consistently as they rotate from dusk to night, local time, by 'drizzling' as opposed to large plasmoid ejections. The W^+ ions in the isotropic simulation have a higher pressure/temperature parallel to the magnetic field in the outer, dusk and nightside magnetosphere ($\geq$20 R_S) by a factor of $\sim$2. As discussed above, this increased parallel pressure leads to ballooning and stretching of the field line, which leads to small flux merging events and resulting plasma loss. Therefore, in the isotropic simulation we rarely see any surviving, corotating pattern of alternating dense, cool bands of plasma interspersed with the hotter, tenuous injection rotating through the nightside to the early local morning, as seen in both the anisotropic simulation and Cassini observations (e.g. Mauk et al., 2009, for a review).

One can also see this effect while tracking the overall mass flux of the system, which is calculated as mass output (loss to inner or outer boundaries) less the mass input (stellar wind, torus, ionosphere) in the outer box of the simulation for all species. Fig. 4.7 shows

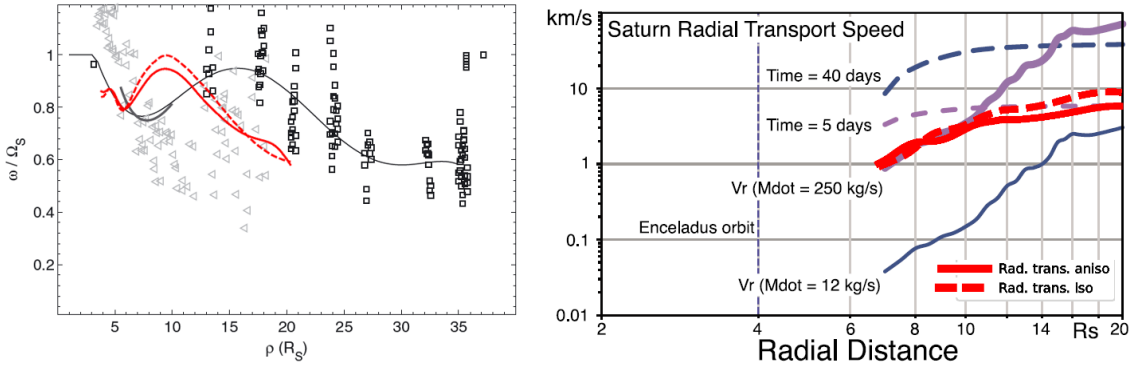

Figure 4.8 **Both:** Comparison to Cassini data for the anisotropic (solid red) and isotropic (dashed red) models. **Left panel:** Equinox corotation data from Voyager data (grey triangles) and winter Cassini data (black squares) with fit from Achilleos, Guio and Arridge (2010) (adapted from Achilleos, Guio and Arridge (2010)).**Right panel:** Radial transport speeds and time to loss from Bagenal and Delamere (2011) (adapted from Bagenal and Delamere (2011)).

the net W^+ ion mass leaving the system, for both the isotropic and anisotropic simulations, normalized to a start point after initialization of the simulation. The isotropic simulation reaches the torus input equilibrium value of 1.14×10^{28} approximately 30% faster than the anisotropic simulation. Since the ionospheric, solar wind, and plasma torus inputs are equal, the more rapid mass loss down the dusk flank noted above contributes to this process strongly, as the anisotropic model has a higher ion population confined to the equatorial plane.

As discussed in § 4.4.1, magnetospheric corotational speeds are related to the centrifugal term of force balance, and this motion contributes plasma convection and the 'drizzling' mass loss discussed above. Fig. 4.8 shows comparisons between Cassini data and the multifluid prediction for corotational speeds reported in Achilleos, Guio and Arridge (2010) in the left panel. The anisotropic (red solid line) and isotropic (red dashed line) are in line with the grey triangles (Voyager data, (Richardson, 1998)) and solid squares (Cassini data, (Kane et al., 2008)), with the solid black line representing the fit by Achilleos, Guio and Arridge (2010) based on the Cassini data only. One could argue that the multifluid results fit best with the Voyager data, which was gathered in 1980-1981 - a period of northern vernal equinox at Saturn; the multifluid model was also run in an equinox configuration. A simple

chi-squared fitness test for the anisotropic (isotropic) multifluid data compared to satellite datasets returns $\chi^2 = 6.03$ (7.05) for the Voyager data, and $\chi^2 = 11.18$ (12.82) for the Cassini data. It is worth noting that the overall shape is similar to the fit of both sets of satellite data, individually, though the pattern is more compressed; this is likely because of the higher compression of the magnetosphere ($R_{mp} \approx 21$) from higher than average solar wind dynamic pressure in the multifluid simulations. Both the anisotropic and isotropic models are similar but one can see the difference in mass loading in the anisotropic model by the lower corotational speed throughout the magnetosphere because of the higher equatorial mass retention that was discussed above. A higher retained mass in the magnetosphere is likely to slow corotation, given the same ionospheric conductance ($\sim$0.6 S in the multifluid simulations). One notable difference here is that the multifluid data represents total, average corotational speeds for all species, where the data from Thomsen et al. (2010) is split into species. Regardless, the trend fits fairly well, and is within 1-σ for some radii.

The right panel of Fig. 4.8 shows a comparison of radial transport speeds between averaged models by Bagenal and Delamere (2011) based on all published, in situ measured plasma properties in the Kronian magnetosphere to that point. For reference, the solid violet line represents a Enceladus-torus and ionospheric plasma production of $\sim$250 kg s^{-1}, which is closest to our upper-limit value of $\sim$342 kg s^{-1}. The anisotropic model (solid red line) and isotropic model (dashed red line) both show decent agreement with the high-mass case from Bagenal and Delamere (2011), in the middle magnetospheric region. However, as with other properties, the radial transport speeds diverge from observation and end up with values of $\sim$7-10 km s^{-1} between the low mass (12 kg s^{-1}) and high mass cases from Bagenal and Delamere (2011). The isotropic model shows overall higher radial transport rate, which we see in Fig. 4.9 drives a higher rate of mass loss down-tail.

Insight into the results in Figs. 4.7 and 4.8 can perhaps be gleaned in the top row of Fig. 4.9. The schematic in the left panel is from Vasyliunas (1983), and represents the Vasyliunas cycle, which represents the pattern of plasma flow in rapidly rotating magnetospheres. Comparing this flow pattern in the drawing to the velocity fields for the heavy ion mass in the simulated system shows that we can identify roughly these patterns, e.g., where the magnetic-X and magnetic -O lines exist in the simulated system. The color scale

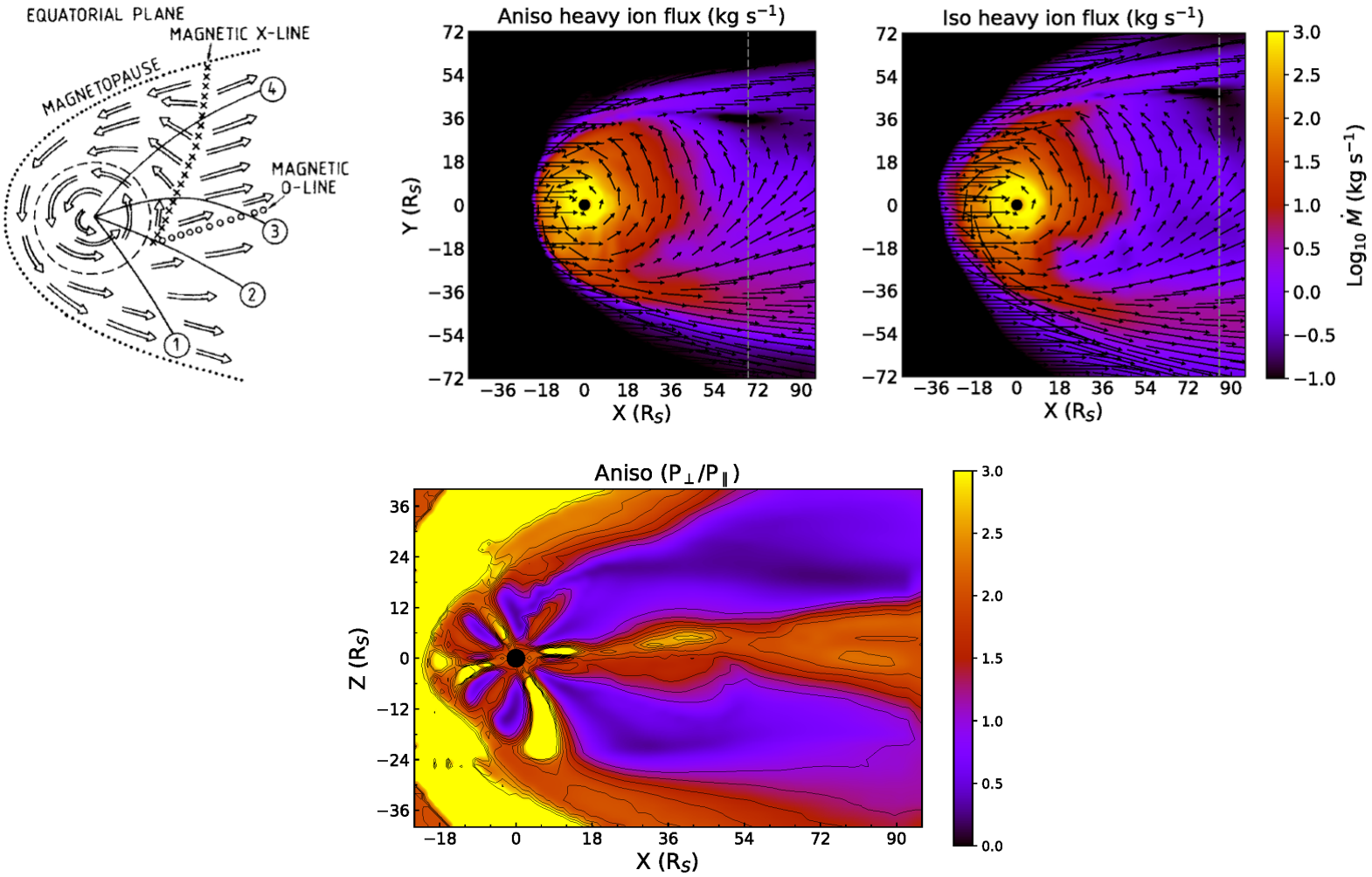

Figure 4.9 Comparison of equatorial mass flux for the heavy ion species (W^+ and O_2^+) to the Vasyliunas cycle (top left) for the anisotropic (top middle) and isotropic (top right) simulations. (adapted from Vasyliunas (1983)). The vertical grey lines represent where return flow (corotation) breaks down. The bottom panel shows the measure of pressure anisotropy for a meridional cut from noon to midnight.

on the equatorial snapshots of the anisotropic (middle) and isotropic (right) simulations represent the heavy ion (W^+ and O^+) mass flux (kg s^{-1}) in the system $\dot{M} = \rho V A$, where ρ is the heavy ion mass density, V is the bulk velocity of the heavy ion fluid, and A is the cross-sectional area through which the mass travels.

It is possible that the chosen inner boundary conditions contribute to the overall outflow rates shown in Fig. 4.7. There is no forced outflow at the inner boundary, with ion pressures and densities held constant in each timestep, replenishing any that flow out, or absorbing any ions that flow in. Some loss at the inner boundary is expected, as the inward pressure gradient on the planet side of the Enceladus torus at 4 R_S, and longer simulations may show equilibrium values below that of total input from the torus and ionospheric sources.

One immediate factor can be identified - the overall mass flux out of the system for the isotropic (right panel) case is higher than in the anisotropic case (middle panel), as is evidenced by the overall larger area of active mass flow down-tail, and into the solar wind. This is obvious from the wider magnetospheric cavity shown in the pattern of mass loss, as well as the mid-tail flank regions that flare out more drastically. As mentioned above, the region of mass loss down the dusk flank of the magnetopause is significantly higher due to the larger area shown above, which contributes to the steeper slope, and more rapid equilibration, in Fig. 4.7. Similar to the results of data analysis in Kane et al. (2014), we did not see any evidence of steady-state reconnection in the system (though intermittent plasmoids/flux tubes were observed at $\geq$45 R_S downtail); this is likely due to the supression down-tail by the strong perpendicular anisotropy. Compared to the results of Kidder, Winglee and Harnett (2009), we see less steady-state reconnection as the 'bowl' shaped current sheet present in the previous work (due to seasonal tilt) was not present in the present work (equinox, no seasonal tilt), and therefore did not drive more frequent or steady-state reconnection.

Mcandrews et al. (2009) and Kane et al. (2014) observed that the corotation or enforced return flow is not present beyond ~55-60 R_S, and we see here that plasma pressure anisotropy contributes. The top middle panel of Fig. 4.9 shows the anisotropic simulation, and corotation extends out to ~65 R_S (vertical grey dashed line); the right panel shows the isotropic simulation, with corotation occurring out to ~85 R_S (vertical grey dashed line).

The bottom panel in Fig. 4.9 represents the measure of pressure anisotropy ($P_\perp/P_\parallel$) for all ion species, for a meridional cut from noon to midnight. Note that there is a strong parallel anisotropy in the lobe regions down the magnetotail. This high parallel measure of anisotropy contributes to lower the Alfvén speed, which in turn implies less efficient communication between the planetary ionosphere and magnetotail along the tailward magnetic field lines (e.g. Kivelson, 2015). This lack of efficient communication is seen in the weaker enforcement of corotation.

An additional factor contributing to this this is the overall higher plasma temperature for the isotropic simulations. This overall higher ion temperature, given similar densities, will produce higher magnetospheric pressures to push back against the inflowing solar wind, and lead to a less compressed magnetosphere. All other parameters being equal, higher ion temperatures contribute to higher plasma β, which can lead to instability and increased diffusion. In § 4.4.4 and § 4.4.5 we discuss the differences between the anisotropic and isotropic simulations with respect to the magnetospheric pressure and magnetic structure.

4.4.4 Contribution to total plasma pressure

In the present work, the anisotropic model shows improvement over the isotropic model with respect to the inner magnetospheric temperatures and densities. Global magnetospheric simulations have not performed well with respect to the heating necessary to produce the pressure observed in giant magnetospheres, and here, too, ion temperatures are lower by up to a factor of 8 or so at large L values for both isotropic and anisotropic simulations. As mentioned above, we inject $\sim 1.14\times10^{28}$ W^+ ions per second in the Enceladus torus, which is at the upper limit of expected plasma production for the system. One result is that the densities in the outer magnetosphere are higher than observed, by an order of magnitude or so. Given that thermal pressure is defined as $P = nk_BT$, where n is the number density, k_B is Boltzmann's constant, and T is the ion temperature, the limitation of the multifluid model in producing realistic temperatures in the outer magnetosphere is offset by the increased density to produce reasonable pressures - and therefore dynamics - for the system. This is not to say pressure driven dynamics by sparse, hot plasma will result in the same as those

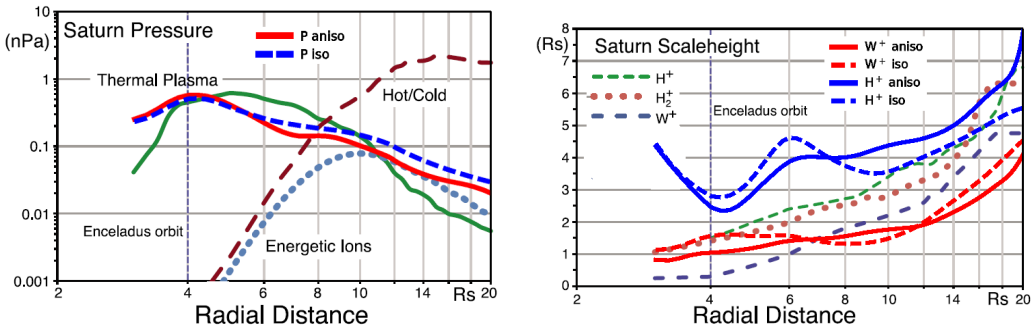

Figure 4.10 **Left:** Thermal plasma pressure for the anisotropic (solid red) and isotropic (dashed blue) for all species compared to compiled, average Cassini data (solid green, left panel, and dashed green and dashed blue, right panel). **Right:** Plasma scale height comparison with Cassini data for W^+ (red) and H^+ (blue) ions for the anisotropic (solid) and isotropic (dashed) simulations (adapted from Bagenal and Delamere (2011)).

driven by dense, cool plasma - but with equal pressures - it merely suggests that overall pressure driven dynamics should be similar.

Fig. 4.10 shows a comparison between the compiled in situ data from Bagenal and Delamere (2011) and the multifluid models. In the left panel, the green solid line represents the radial extent of the average pressure in the Kronian magnetosphere - to which we are directly comparing the anisotropic (solid red) and isotropic (dashed blue) models. The inner most region plotted here, at 3 R_S, is overpredicted by the multifluid simulations, likely due to the upper limit density that we are injecting at Enceladus - this has the effect of increased density between the torus and the inner boundary at 2 R_S. Throughout the magnetosphere, both the anisotropic and isotropic models do fairly well at predicting the pressures, even overpredicting in the outer magnetosphere (due to upper limit density injections, and sampling near the very center of the dense current sheet) - where global models typically underpredict the pressure. It is interesting to note that around Enceladus, the pressure fit is quite good, but as soon as the energetic ions not represented in the multifluid model become significant around 5 R_S, the multifluid simulations show a marked decrease in the magnitude of thermal pressure since it does not include much of these energizing processes.

The right panel of Fig. 4.10 shows a comparison between the multifluid models and

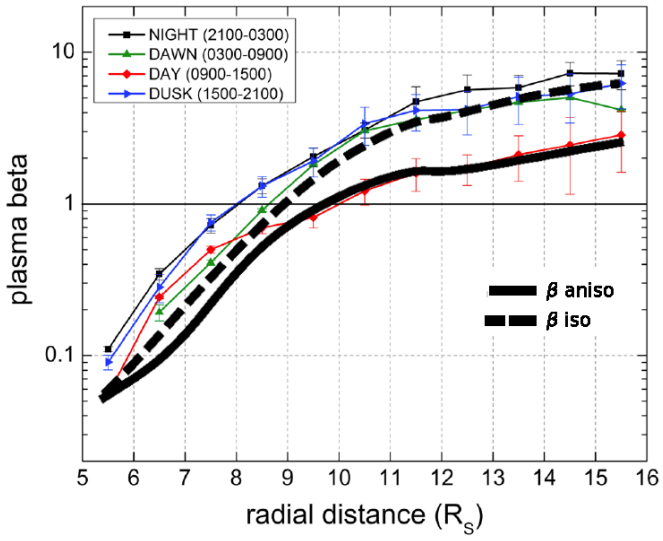

Figure 4.11 Plasma β comparison for the anisotropic (solid black) and isotropic (dashed black) simulations against local time averaged Cassini data (adapted from Sergis et al. (2017)).

averaged, in situ data for the density scale height of the equatorial plasma sheet, defined as (Persoon et al., 2009):

$$H = \left[\frac{2}{3}\frac{k_B T_{i,\|}}{m_i \Omega^2 R_S^2}\right]^{\frac{1}{2}}, \tag{4.6}$$

which is given in units of Saturn radii, where k_B is Boltzmann's constant, $T_{i,\|}$ is the temperature parallel to the magnetic field, m_i is the ion mass, Ω is the rotation rate of the plasma, and R_S is the radius of Saturn. The data analysis of Persoon et al. (2009) reported the radial dependence of the scale height as $L^{1.5}$ ($L^{1.4}$) for the W^+ (H^+) ions. The fit for the radially, azimuthally averaged anisotropic (isotropic) simulated data for the W^+ ions are $L^{1.35}$ ($L^{0.8535}$), and for the H^+ ions are L1.1 ($L^{0.621}$). The ability of the anisotropic model to evolve the parallel ion temperature through our full treatment of the anisotropic model leads to a stronger agreement with the Cassini observations.

Compared to the compiled, averaged data in Bagenal and Delamere (2011), the trend agreement is good for both ion species in the multifluid models, with both W^+ and H^+

ions a factor of ∼2-3 higher in the inner magnetosphere ($R_S \leq 8$). In the middle and outer magnetosphere, the W^+ ions start under predicting, due to lower $T_{\parallel}$, where the H^+ species in both anisotropic and isotropic simulations tend to slightly overpredict the scale height, by around 30%, and then agree well with the averages from Bagenal and Delamere (2011) from 15-20 R_S. This is primarily due to a combination of the lower corotational rates in the outer magnetosphere compared to Cassini data, as seen in Fig. 4.8, and the relatively higher parallel temperature anisotropy in the outer magnetsphere for H^+. Again, with respect to the W^+ ions, we see a missing piece of the global multifluid model as it pertains to outer magnetospheric ion energization. The scale height results in Fig. 4.10 also point to the increased consistency in the formation of the interchange instability discussed above. Namely, we highlight the lower scale height (which depends on $T_{\parallel}$) which is attributable to the perpendicular dominated temperature in the W^+ ions (which constitute a large majority of the mass in the system) from ∼3-8 R_S and again from ∼12-20 R_S. This particular feature signifies the confinement of plasma to the equatorial plane, driving a stronger centrifugal force. The region from ∼8-12 R_S is one in which the ions are dominated by parallel temperature, as seen in Fig. 4.1 and therefore shows an increased scale height in this region for the anisotropic model, when compared to the isotropic model.

Fig. 4.11 shows a comparison between derived values of the plasma beta, from Cassini measurements by Sergis et al. (2017) that is split into local time quadrants, and the local time averaged multifluid models. The anisotropic (solid, thick black line) and isotropic models (dashed, thick black line) fit well in the range of Cassini measurements. Notably, the anisotropic average is quite similar to the dayside (0900-1500 LT) quadrant, and the isotropic model follows the dusk (1500-2100) and night (2100-0300) data quite closely. Given the over all lower temperatures in the anisotropic model, as seen in Fig. 4.4, it stands that the plasma beta should be similarly lower - given identical magnetic field structure. The underprediction of both models is also evident in the inner magnetosphere, up to ∼9 R_S.

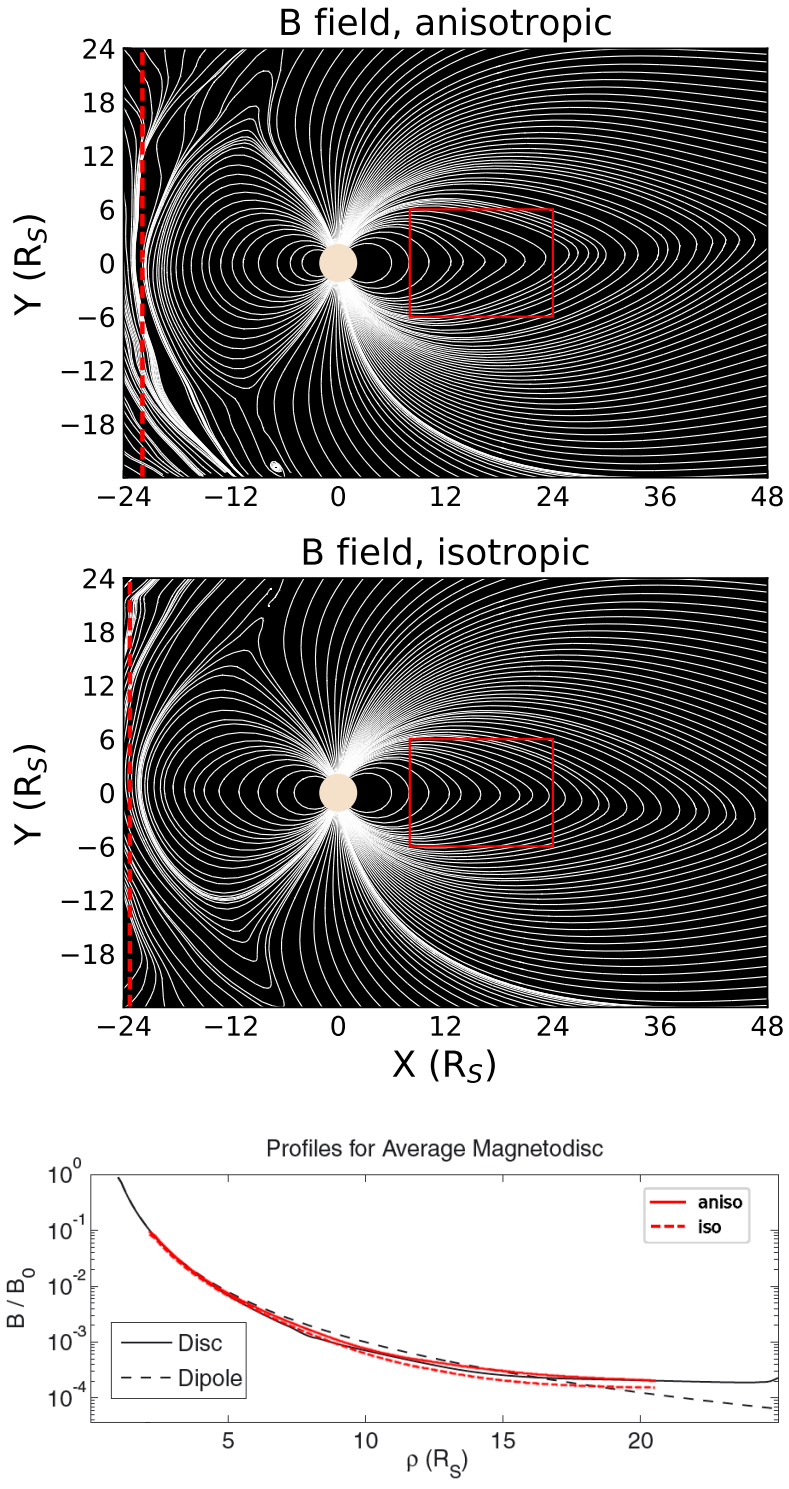

Figure 4.12 test

4.4.5 Preliminary look at magnetospheric structure

Since the anisotropic model predicts a lower overall temperature for the magnetospheric plasma, we see what one should expect when compared to the isotropic model (with higher average temperatures) - more compression of the magnetopause given the same solar wind dynamic pressure (e.g. Pilkington et al., 2015; Sorba et al., 2017). An example of this can be seen in the top two panels of Fig. 4.12, where the solar wind is blowing from left to right. The vertical dotted red line on the left side of each figure notes the location of the magnetopause (identified by the separation between open/closed field lines, in agreement with the location of the magnetopause current), which is at $\sim$21.9 ($\sim$23.3) R_S for the anisotropic (isotropic) simulation.

The field structure in the tail region also shows differences, due to the increased body forces present in the anisotropic model. The red rectangles in the tail regions for Fig. 4.12 highlights a region where the inclusion of anisotropy produces a difference in the model; that is, while both simulations form a stretched field (magnetodisc), we see the radius of curvature in the field is smaller in the anisotropic simulation. Similarly, in the bottom panel of Fig. 4.12, we see the increase in magnetic field magnitude from the anisotropic system due to the significant perpendicular anisotropy in the middle-outer magnetosphere - which brings the system closer to agreement with purely analytical models. It is interesting that the top and middle panels (anisotropic and isotropic models, respectively) show a different phase of the tailward plasma sheet oscillation, indicating a difference in periodicity despite being taken at the same point in time in the respective simulations.

Due to the overall differences in force balance, it would be interesting to determine how the inclusion of pressure anisotropy drives difference in response to varying solar wind conditions. Similarly, how do field aligned currents and the overall current system change in this comparison?

4.5 Concluding Remarks

We included a full treatment of pressure anisotropy in a global multifluid model of the Kronian magnetosphere. The model includes non-gyrotropic effects and required no forced

relaxation term or instability timescales. The model shows improvement in the predictive capabilities - particularly for the inner magnetosphere - that can be captured by the multifluid approach.

1. Pickup ions with strong perpendicular anisotropy injected in the Enceladus tori rapidly propagate out, experience an inversion to the anisotropic ratio (to parallel dominated) stretching field lines and generating cool, dense fingers of plasma that stretch out into the middle magnetosphere. Cassini/CAPS anisotropy data from (Wilson et al., 2008) are limited to the dayside, low latitude measurements. The model underpredicts the level of perpendicular anisotropy in the Kronian magnetosphere compared to the data, though it follows a similar trend; the cuts through the anisotropic model were taken from a slice perfectly along the magnetic equator, where Cassini data was taken during orbits within 5° of the equator - sampling near-lobe plasma and fields. It should also be pointed out that seasonal tilt effects likely contribute significantly to many differences seen between the Cassini/CAPS data and the multifluid model, due to the changes regarding magnetospheric forcing.

2. The significant perpendicular anisotropy in the multifluid model confines plasma to the equatorial plane and generates an increase in the body force experienced by the corotating equatorial magnetosphere. In turn, the system requires a larger ring current to close the current system and attempt to sustain force balance and corotation. Additionally, the anisotropic model produces a much stronger current confinement of the Enceladus plasma torus, with more significantly steeper density gradient in the inner magnetosphere, which agrees more closely with Cassini observations - an improvement of up to a factor of an entire R_S scaling.

3. The anisotropy has observable effects on the convection and flow of plasma. The nightside alternating bands of cool, outflowing and hot, inflowing plasma from the interchange instability was more well-defined in the anisotropic simulation (as opposed to the more uniform temperature structure in the isotropic simulation), agreeing with the observations by Cassini. The more distinct and longer lived cool, dense bands

of plasma survive rotation through the nightside of the magnetosphere, and average corotation speeds are slower in the anisotropic model due to the increased equatorial mass load, also indicating better agreement with Cassini data, in these respects. Both systems show agreement with the Vasyliunas cycle of plasma flow, with the anisotropic system exhibiting a more compact structure, with tighter magnetic O-lines and X-lines, which denote the pattern of mass loss. Correspondingly, the mass flux from the isotropic system occurs more rapidly, due to a higher rate of bulk 'drizzling' down the dusk flank of the magnetosphere.

4. The multifluid model's predicted equatorial ion scale height agreed well with Cassini observations, both from specific Cassini/RWPS measurements and with compiled, averaged data over approximately the first half of Cassini's lifetime. The ability of the anisotropic model to track the parallel ion temperature separately from the perpendicular ion temperature led to a better agreement with Cassini data.

5. Overall pressure structure agrees well with Cassini observations throughout the magnetosphere - from Enceladus torus to magnetopause. Radial, azimuthal averages of plasma beta for both models agreed with compiled Cassini data analysis results from Sergis et al. (2017). This is most likely from the high density injected at the Enceladus torus ($\sim$360 kg s^{-1} for all ions, an upper bound) as the higher densities in the outer magnetosphere balance the global model's lower than observed temperatures.

Overall, anisotropy has a significant effect on accurately simulating the the plasma characteristics and dynamics in the Kronian magnetosphere. A follow-up study to the present one will investigate into the differences in magnetic structure and reconnection between the anisotropic and isotropic models. The simulated results of the radial temperature structure highlights an opportunity for future improvement in a global multifluid model - such as including populations of separately tracked particles that are self-consistently coupled to the ion fluids of the multifluid model. This could allow the model to capture some kinetic processes, address the lack of outer magnetospheric heating mechanisms present in global fluid models, and lead to a lower density injection requirement.

Chapter 5

MODELING REPEATED M-DWARF FLARING AT AN UNMAGNETIZED EARTH-LIKE PLANET IN THE HABITABLE ZONE

5.1 Overview

This chapter presents work in effort to understand the impact of active M-dwarf stars on the atmospheric equilibrium and surface conditions of a habitable zone, unmagnetized Earth-like planet; these processes are likely key to assessing M dwarf planet habitability. Previous modeling of the impact of electromagnetic (EM) radiation and protons from a single large flare on an Earth-like atmosphere indicated that significant and long-term reductions in ozone were possible, but the atmosphere recovered. However, these stars more realistically exhibit frequent flaring with a distribution of different total energies and cadences. Here we use a coupled 1D photochemical and radiative-convective model to investigate the effects of repeated flaring on the photochemistry and surface UV of an Earth-like planet unprotected by an intrinsic magnetic field. As input, we use time-resolved flare spectra obtained for the dM3 star AD Leo, combined with flare frequencies and total energies (typically $10^{30.5}$ to 10^{34} erg) from the 4-year Kepler light curve for the dM4 flare star GJ1243, with varied proton event impact frequency. Our model results show that repeated EM-only flares have little effect on the ozone column depth, but that multiple proton events can rapidly destroy the ozone column. Combining the realistic flare and proton event frequencies with nominal CME/SEP geometries, we find the ozone column for an Earth-like planet can be depleted by 94% in 10 years, with a downward trend that makes recovery unlikely and suggests further destruction. For more extreme stellar inputs O_3 depletion allows a constant $\sim$0.1-1 W m^{-2} of UV-C at the planets surface, which is likely detrimental to organic complexity. Our results suggest that active M dwarf hosts may comprehensively destroy ozone shields and subject the surface of magnetically-unprotected Earth-like planets to long-term radiation that can damage complex organic structures. However, this does not preclude habitability,

as a safe haven for life could still exist below an ocean surface.

This chapter is submitted and in revision at *Astrobiology.*

5.2 Introduction

Whether M dwarf planets are good targets in the search for life is still an open problem of high complexity. There exist several factors that make such planets promising targets. Rocky planets are easier to detect around these low mass stars (0.5 to 0.08 $M_{\odot}$) with current techniques and instruments. Red dwarfs are abundant in the solar neighborhood, they spend $\sim 10^{10}$ years in the main sequence, and biosignatures like N_2O and CH_4 may be more abundant and potentially easier to detect (see reviews by Tarter et al., 2007; Scalo et al., 2007; Shields, Ballard and Johnson, 2016). Three dimensional planetary atmospheric models have dispelled concerns of atmospheric collapse by extreme temperature differences between the illuminated and dark hemispheres (e.g., Dole, 1964) for tidally-locked planets orbiting M dwarf hosts in the habitable zone; the models applied to this problem showed that atmospheric circulation can distribute the stellar energy, lowering the temperature difference (e.g. Joshi, Haberle and Reynolds, 1997; Joshi, 2003). Active M dwarf host stars, however, exhibit magnetic activity originated by the interaction of their atmospheres with their magnetic fields driven by their mostly or totally convective interiors. One consequence of magnetic activity are flares, unpredictable releases of energy that range from "microflares" ($\sim 10^{29}$ ergs as measured in the U band, ~3320-3980 Å) to high energy flares with total energies as large as 10^{34} ergs (e.g., Hawley and Pettersen, 1991; Hawley et al., 2014). Since the habitable zone around these stellar hosts is located at a fraction of an astronomical unit (AU), the energy flux from these events that impact potentially habitable worlds is increased by at least an order of magnitude compared to Earth.

Active M dwarfs exhibit flare activity with widely varying flare energies and frequencies, but generally following a power-law probability distribution (e.g., Hilton, 2011; Hawley et al., 2014). The most active of these dM3-dM5 stars have been observed to produce dozens of flares per day with total energies $\geq 10^{30}$ erg, and potentially catastrophic events like the Great Flare of ADLeo at 10^{34} erg (Hawley and Pettersen, 1991) at a frequency of once per month. Compare this to average solar activity with the highest frequency of a single event

per day of energy $\sim 10^{27}$ erg, up to approximately one 10^{31} erg event per year (e.g., Crosby, Aschwanden and Dennis, 1993). One of the largest observed solar flare events, known as the Carrington Event of 1859, had an estimated total energy of $\sim 10^{32}$ erg (e.g., Cliver and Dietrich, 2013), a full two orders of magnitude lower than the most energetic events observed on active M dwarfs.

There are two aspects of flare events that could negatively impact the habitability of a planet by altering the atmospheric composition: increase in electromagnetic flux, and an eruption of energized charged particles. The energy injected by a flare into the stellar atmosphere results in a rise and peak of photometric brightness, known as impulsive phase. A gradual flare decay phase follows where the energy input decreases until the star slowly returns to quiescent state. During flare events the luminosity of the star in the X-ray, UV and visible increases up to 3 orders of magnitude (Scalo et al., 2007), which can photochemically alter the upper atmosphere of a planet. For a planet that does not have atmospheric constituents (e.g., O_3, CO_2) to absorb this short wavelength radiation, the surface could be regularly irradiated.

The second impactful aspect of flare events involves stellar energetic particles (SEP) that can be accelerated during the impulsive phase of flares. Our knowledge of these events comes only from solar correlations, as we have no method by which they can be remotely observed. Their effect on the atmosphere of a habitable planet likely depends on several factors: the particle energies, presence and orientation of a planetary magnetic field, and the chemical composition of the atmosphere. The probability of a proton event being associated with a stellar flare is dependent on the flare energy, with solar microflares ($\leq 10^{27}$ erg) only rarely producing weak particle events, but the chance for a large flux of energetic particles reaches a near certainty for flares $\sim 10^{28.3}$ erg (GOES class X2) and above (e.g., Yashiro et al., 2006; Hudson, 2011; Dierckxsens et al., 2015). While not every proton event will hit a potentially habitable planet due to the combined geometry of the active regions of the star and the planetary orbit (e.g., Khodachenko et al., 2007), M dwarf planets we consider are under significant threat. These planets orbit at fraction of an AU, and the stellar hosts exhibit high frequency, high energy flare events indicating the effects of multiple impacting proton events could be significant.

Studies on the effects of space weather on habitability have become crucial with the discovery of planets such as Proxima Centauri b and the TRAPPIST-1 systems' multiple habitable zone planets. Planetary atmospheric escape can be caused by XUV radiation that heats the planets exosphere driving a hydrodynamic wind that carries away the planetary atmosphere (e.g. Luger and Barnes, 2015); non-thermal processes such as the increased polar wind and ion pickup escape can potentially remove vast quantities of heavy ions such as N^+ and O^+ from the atmosphere (e.g., Ribas et al., 2016; Airapetian et al., 2017; Garcia-Sage et al., 2017); increased forcing of the magnetosphere by either steady state or transient stellar wind events can also be impactful for atmospheric loss, and the subsequent atmospheric outflow (e.g., Dong et al., 2017; Garraffo, Drake and Cohen, 2016; Garraffo et al., 2017). However, there is so far less effort into studying the effects of space weather events on the chemical evolution of planets that retain their atmosphere, and how habitability might be affected in such instances.

Segura et al. (2010) performed the first study for understanding the effect of a single, high energy flare (and associated SEP) on the atmospheric chemistry of a habitable planet; their study investigated the impact of an event equivalent to the 1985 April 12 flare from the M dwarf AD Leonis (AD Leo) (Hawley and Pettersen, 1991) on an Earth-like planet located within its habitable zone. The planetary atmosphere had a similar composition to that of present Earth (0.21 O_2, 1 bar surface pressure) and was located to receive the same integrated stellar flux as our planet. They simulated the effects from both UV radiation and protons on the atmospheric chemistry of a hypothetical habitable planet with a 1-D photochemical model coupled to a 1-D radiative/convective model. Observations available for this flare included UV spectroscopy (1150 - 3100 Å) and optical spectroscopy (3560 - 4440 Å), but no evidence of SEPs were available. To include particles, Segura et al. (2010) used a relationship found for solar X-ray flare intensity and proton fluxes (Belov et al., 2005). X-rays flare intensity were obtained from the Neupert effect, an empirical relation between the flare energy emitted in the UV and the X-ray peak luminosity (Mitra-Kraev et al., 2005). They estimated a proton flux associated with the flare of 5.9×10^8 protons cm^{-2} sr^{-1} s^{-1} for particles with energies > 10 MeV. Then they calculated the abundance of nitrogen oxides produced by the flare by scaling the production of these compounds during

a large solar proton event called the Carrington event.

Their results indicated that the UV radiation emitted during the flare does not produce a significant change in the ozone column depth of the planet. When SEPs were included, the ozone depletion reached a maximum of 94% two years after the flare for a planet with no magnetic field. At the peak of the flare, the calculated UV fluxes that reached the surface, in the wavelength ranges that are damaging for life, exceed those received on Earth during less than 100 s. Segura et al. (2010) concluded that flares may not present a direct hazard for life on the surface of an orbiting habitable planet.

Recent studies have been performed to determine the effect of flare electromagnetic energy on the habitability of planetary systems. The TRAPPIST-1 system has been investigated by Vida et al. (2017) in a recent *Kepler/K2* study showing at $\sim$0.75 cumulative flares per day of energy between 1.26×10^{30}-1.24×10^{33} erg. This could produce detrimental UV flux at the potentially habitable planetary surfaces of TRAPPIST-1 b-h. OMalley-James and Kaltenegger (2017) investigated the potential UV related surface habitability of the TRAPPIST-1 system, and found that the oxic state of the atmosphere is key to protecting the surface, with even a thin-oxygen atmosphere ($\sim$0.1 bar) sufficient to keep UV-C from reaching the surface with any intensity. Estrela and Valio (2017) has observed superflares in the Kepler-96 system up to $\sim1.8\times10^{35}$ erg, and simulated the effects on both Archean and present-day Earth-like atmosphers, and found that the presence of an O_3 layer is crucial to protection of life under such highly irradiating events.

Aside from Segura et al. (2010), these previous studies do not investigate the effects of proton events associated with stellar magnetic activity, nor the resilience and evolution of the O_3 column on a potentially habitable planet to such events. AD Leo, the star used for the Segura et al. (2010) study, is one of the most magnetically active M dwarfs known. During decades only flares from the most active M dwarfs were studied because the UV emission from mid- and low-active red dwarfs fall below the detection threshold of the available instruments. Observations performed using *Hubble Space Telescope* showed that UV emission from chromospheric activity was also present on those stars usually classified as non-active (Walkowicz, Johns-Krull and Hawley, 2008; France et al., 2012, 2013), while the *Kepler/K2* mission (e.g., Hawley et al., 2014; Davenport et al., 2014) and the *MOST*

instruments (Davenport et al., 2016) showed a more detailed view on flares frequency from low mass stars.

The present work extends the results from Segura et al. (2010) to determine the effect of multiple M dwarf flares and energetic proton events on a potentially habitable world by taking advantage of the more recent observational campaigns noted above. We have updated the models used in Segura et al. (2010) (see § 5.3.1) to study the effect of multiple events on an atmosphere with similar composition of present Earth to determine the potential effects on the O_3 column and related biologically relevant UV flux at the surface of the planet.

5.3 Methods

5.3.1 Improvements extending Segura et al. (2010)

A modified version of the 1D coupled radiative-convective and photochemical model used by Segura et al. (2010) is used in in the present work. The radiative-convective climate model itself is a hybrid of two models: 1) a δ two-stream scattering algorithm that is used to calculate fluxes and uses correlated-k coefficients to parameterize absorption by important atmospheric species, e.g., O_3, CO_2, H_2O, and CH_4; 2) for thermal-IR wavelengths, the rapid radiative transfer model (RRTM) implemented by Segura et al. (2003) was used. The RRTM uses 16-term sums in each spectral band where k-coefficients are calculated to give high spectral resolution where Doppler broadening is important.

The photochemical model solves 217 reactions that link 55 chemical species. Photolysis was calculated using a δ two-stream routine that allowed scattering between molecular gases and the included aerosol species (Segura et al., 2003). Timesteps were solved using an implicit reverse Euler method, with initial timestep set to 10^{-4} s, with increasing magnitude as the system reaches equilibrium.

The coupling layer allowed the climate and photochemical model to cross-communicate and synchronize the atmospheric temperature structure, H_2O profiles and chemical alterations made for each timestep. The pressure layers calculated in the radiative-convective model were interpolated to the fixed altitude structure in the photochemical model, and then back, during the coupling procedure. All other details and inputs to the model not

discussed below are identical to those discussed in §2-3 in Segura et al. (2010).

In the present work, we made four important modifications: § 5.3.2 describes how we unfixed the mixing ratios for three major atmospheric constituents (N_2, O_2, and CO_2) to achieve a more realistic mass balance; § 5.3.3 the treatment used for multiple flare events and flare lightcurve evolution based on recent observations; § 5.3.4 discusses the considerations made regarding the interaction between multiple stellar proton events and the upper atmosphere; § 5.3.5 discusses the extension of the stellar optical-NIR spectrum during flare events.

5.3.2 Unfixed mixing ratios for O_2, CO_2, N_2 and Henry coefficients

For the single flare work addressed in Segura et al. (2010), the volume mixing ratios, *f*, of major atmospheric constituents O_2, CO_2, and N_2 were fixed at values corresponding to values of 0.21, 3.55×10^{-4}, and 0.78, respectively. In the present work, these mixing ratios are enforced only at the surface layer of the planet, and all layers of the atmosphere above the surface were unfixed – allowing these species to photochemically respond to the stellar inputs.

Of particular note are the responses of O, O_2 and N_2 during the creation of NO_x species generated by proton events. Previous studies have found that each ionized pair created in the upper atmosphere from precipitating energetic particles results in the production of 1.25 N atoms, particularly N(4S) and N(2D) (Porter, Jackman and Green, 1976), and a NO_x production rate of 1.3 to 1.6 per pair (Rusch et al., 1981). The generation of NO_x is driven by the dissociation of N_2 into the constituent, excited N-atoms which then react with O_2 to produce NO and O:

$$N(4S) + O_2 \rightarrow NO + O \quad \text{(R1)}$$

$$N(2D) + O_2 \rightarrow NO + O \quad \text{(R2)}$$

and O_3 reacts with the produced NO to generate NO_2:

Table 1. Henry coefficients, mixing at z=0 km

Species	k_H [mol kg^{-1} bar^{-1}]	d(ln(k_H))/d(1/T) [K]	f (z=0) [arb]
O_2	1.3×10^{-3}	1500	0.21
CO_2	3.55×10^{-2}	2400	3.55×10^{-4}
N_2	6.25×10^{-4}	1300	0.78

Note. — Henry coefficients and surface mixing ratios for each unfixed species.

$$NO + O_3 \rightarrow NO_2 + O_2. \quad \text{(R3)}$$

Following the method of proton injection in Segura et al. (2010), we directly modify the atmospheric column to simultaneously include the NO and NO_2 profiles at or near the peak of the flare events; the excited N atoms are not directly injected. The amount of NO_x directly input into the upper atmosphere to emulate production by proton precipitation (and therefore pair production) sets the amounts N_2 and O_2 removed by the formulating reactions (as well as O_3, and the addition of O). For each NO molecule we inject, 0.5 N_2 and 1 O_2 molecules were immediately removed from the atmospheric column, and one O atom was added. For the case of NO_2 molecules injected at a specific altitude, the abundances are predicate on the previous formation of NO, as seen in Eq. R3; during the formation of NO_2 from NO, 1 O_3 molecule is removed, and per the reactant NO that drove the production of the NO_2, 0.5 N_2 molecules are removed from the atmospheric column, and 1 O atom is added. Note that the product O_2 from Eq. R3 is cancelled by the assumed pre-production of the NO molecule, which consumes an O_2 as in Eqs. R1 and R2. For simulations containing multiple proton events, we limit the maximum NO (NO_2) injected into the atmosphere by the amount of available reactant O_2 (O_3) in the atmospheric column.

As a consequence of unfixing the mixing ratio of CO_2, its abundance was increased

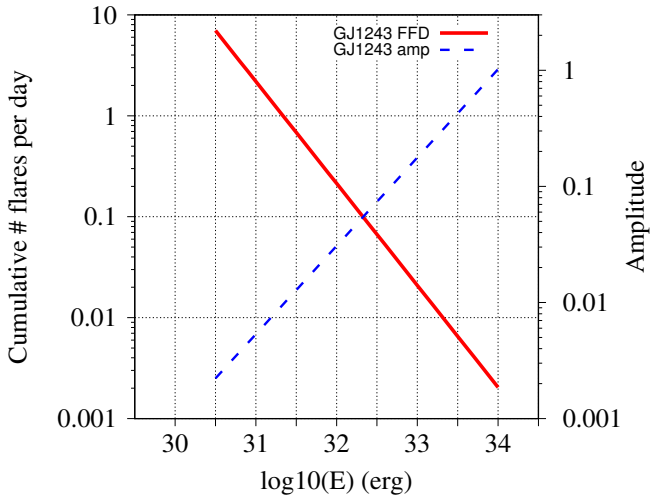

Figure 5.1 The flare frequency distribution (FFD) and amplitudes observed from GJ1243 - used to generated flare distributions in the present work.

in the stratosphere by methane oxidation (Yung and DeMore, 1999), as we will show in Sec. 5.5.3. Rainout and saturation for the new unfixed species were also modified to be temperature dependent, and the appropriate Henry coefficients are shown in Table 1 along with the initial mixing ratios at the surface level of the atmospheric column. All of the above changes to the 1D model did not significantly alter O_2 and N_2 during steady-state from their uniform altitude mixing ratio profiles of 0.21 and 0.78, respectively.

5.3.3 Multiple flare events from Kepler observations

To address the effects of multiple flares on the atmosphere, we built upon the ADLeo flare template used in the previous work of Segura et al. (2010) by using statistical results from Kepler observations of the M4 star GJ1243. We incorporated the observations of the flare energies, durations, and amplitudes from GJ1243 (Hawley et al., 2014), which included analysis of over 6100 GJ1243 flares measured over 11 months at 1-minute cadence. These observations also resulted in the empirical flare lightcurve evolution template we employ (Davenport et al., 2014). The following are scaling relations derived from Hawley et al.

(2014) that we used to determine flare amplitude (relative increase in U-band flux), flare frequency, and event durations:

$$\log_{10} \frac{\Delta F_U}{F_U} = 0.7607 \log_{10} E - 25.855 \tag{5.1}$$

$$\log_{10} \nu = -1.01 \log_{10} E + 31.65 \tag{5.2}$$

$$\log_{10} t = 0.395 \log_{10} E - 9.269 \tag{5.3}$$

where F_U is the stellar flux in the Johnson U-band, E represents the flare energy in ergs, ν is the flare frequency given in cumulative flares per day, and t is the duration of the flare events in seconds which ranges from ∼600 s to ∼14,500 s for flares of energy $10^{30.5}$ erg and 10^{34} erg, respectively. Fig. 5.1 shows a plot of the flare frequency and amplitudes as a function of the energy used to generate our flare distributions.

The present work explores several separately generated distributions of stellar flare events with duration of one month, six months, one year, 10 years, and 15 years. We simulated flares at a rate of ∼7 per day with energies in the Johnson U-band from a minimum of $10^{30.5}$ erg up to a maximum of 10^{34} erg, which occurs with frequency of 1 flare per ∼489 days according to the flare frequency distribution (FFD) for GJ1243 reported in Hawley et al. (2014), and shown in Fig. 5.1. An example extended, temporal flare distribution with ∼1277 (2555) flares over six months (one year) was generated from the GJ1243 FFD, and can be seen in Fig. 5.2. As seen in Fig. 5.1, an amplitude of ∼1.04 corresponds to a flare with energy 10^{34} erg - approximately the energy of the great flare of ADLeo reported by Hawley and Pettersen (1991) - and $\sim 2.25 \times 10^{-3}$ corresponds to a flare of size $10^{30.5}$ erg from GJ1243.

Cliver and Dietrich (2013) estimate the solar Carrington event of 1859 to be on the order of 5×10^{32} erg, events which by Eq. 5.1 have an amplitude of ∼0.075. However, any reference to 'Carrington-size' flares in the present work were calibrated by proton fluence ($\sim 1.1 \times 10^{10}$ cm^{-2}), rather than total flare energy, and correspond to a total energy of $\sim 10^{31.9}$ erg, with a flux amplitude of ∼0.0223. Flare flux was allowed to stack, allowing the simulation of complex flaring events as seen in the inset of the top panel in Fig. 5.2.

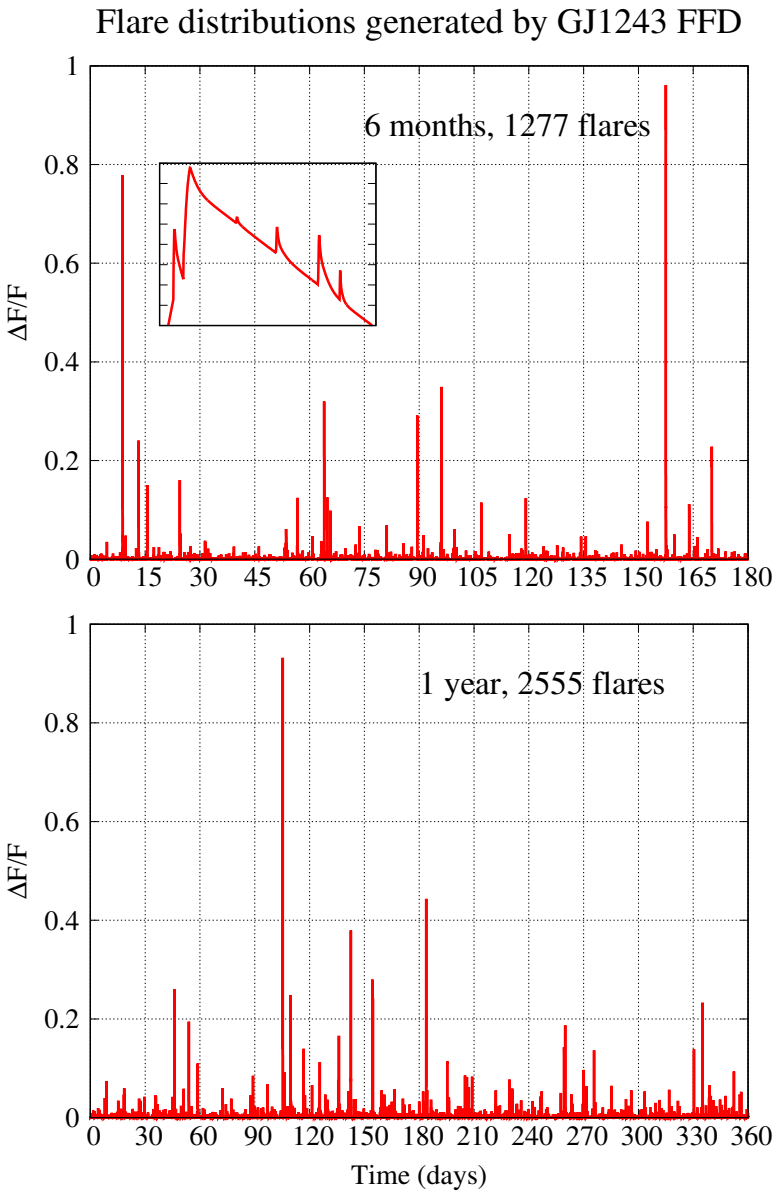

Figure 5.2 **Top:** Six months, flare distribution (1277 events) generated from the GJ1243 FFD. The inset identifies an example complex flare near ∼9 days, produced by flare flux stacking. **Bottom:** One year flare distribution (2555 events) from the GJ1243 FFD.

The flare lightcurve template was also modified in the present work. Following Davenport et al. (2014), we fit each flare event to a lightcurve template granting a rapid impulsive phase, and extended decay phase. Fig. 5.3 shows a relative comparison between the lightcurve shape used in Segura et al. (2010) and an equivalent 10^{34} erg flare from the present work for the first 6000 seconds of the flare events. Integrating the impulsive phase from the start of the event to the peak for each flare results in a factor of $\sim$0.71 in flux delivered for the treatment in the present work treatment (solid blue) from Davenport et al. (2014), compared to results from the Segura et al. (2010) lightcurve (dashed red). Integrating each flare from start to end, however, results in the present treatment depositing approximately twice the overall flux when compared to the treatment in Segura et al. (2010). Integrating both curves across the FWHM results in a factor of $\sim$1.72 increase of the flux compared to the original treatment in Segura et al. (2010). The majority of the energy in the present work is delivered in the decay of the flare evolution. It is worth noting that for flare energies $<10^{34}$ erg, the FWHM, rise and decay times (and therefore total duration, as seen in Eq. 5.3) all occur at reduced scale with the decreased energies.

Timestep granularity has also been altered in our implementation to be more granular, from 20 flare points used in the 2010 work, now extended to 30 points (12 in the rise phase instead of 9, 18 in the decay phase instead of 11) to obtain proper coverage of temporal flare morphology. The resulting flare in Fig. 5.3 is $5.6\times$ the duration of the flare used in Segura et al. (2010) ($\sim$14,500 s versus $\sim$2,586 s) due to the long decay phase from the empirical template adopted from Davenport et al. (2014). This duration varies with the flare energy according to Eq. 5.3.

5.3.4 Proton Event Scaling and Impact Probability

We follow the same procedure to determine proton fluence in the present work that was used for the 10^{34} erg flare in Segura et al. (2010). The difference in the present work is the method is expanded to work for lower energies. We assume the spectral energy density in the 1-8 Å bandpass reported in Hawley and Pettersen (1991) scales directly with our relative flux amplitude relation in Eq. 5.1. The relationship between proton fluence and relative flux

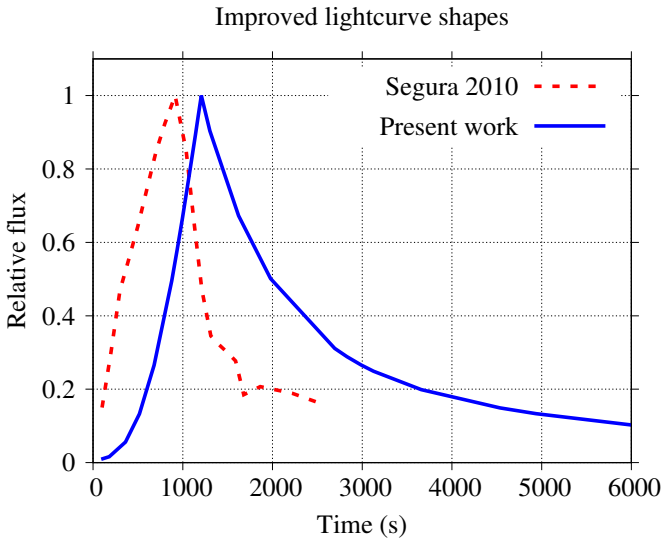

Figure 5.3 Comparison of lightcurve evolution from Segura et al. (2010) vs the method adopted in the present work, based on the observational results of Davenport et al. (2014).

or flare energy is shown in Fig. 5.4. The present work focuses on an unmagnetized planet, with no shielding from a global magnetic field. However, this does not necessarily imply that we should expect drastically different effects for a magnetized planet, with respect to the method applied to calculate the NO_x production, as discussed below. The effects of a global planetary magnetic field are considered in § 5.5.7, and are slated to be investigated in a companion paper.

Belov et al. (2005) showed a correlation between X-ray intensity and proton flux for solar events observed over three solar cycles, using the IMP-8 and GOES satellite instruments. The GOES satellites orbit at geosynchronous altitudes (∼6.6 RE, corresponding to magnetic foot point of ∼67° latitude - a nominally active location for auroral precipitation). This implies the GOES measurements of proton flux are typically taken from within the magnetosphere, except during strong flow due to a fast solar wind stream or the impact of a coronal mass ejection (CME). The increase in the dynamic ram pressure (ρv^2) of the solar wind compresses the magnetopause — possibly to a point where the satellite is exposed to the shocked or unshocked solar wind if there is a confluence of a solar event and

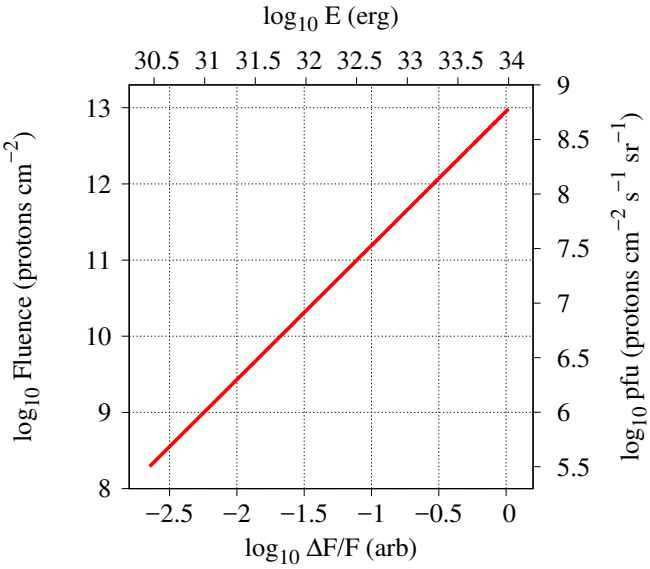

Figure 5.4 The relationship of proton fluence (left y-axis) and proton flux units (pfu, right y-axis) for the flares simulated in the present work, as function of relative flux increase (bottom x-axis) and total flare energy (top x-axis).

the satellite's orbital position is at the the sub-solar point or appropriate dayside location. One can estimate the magnetopause sub-solar distance (along a line from the planet to the star) from the pressure balance between the solar wind and Earth's magnetic field as (e.g., Schield, 1969):

$$R_{MP} = \left(\frac{B_{\oplus}^2}{2\mu_0 \rho v^2} \right)^{\frac{1}{6}}, \tag{5.4}$$

where R_{MP} is the magnetopause distance, $B_{\oplus}$ is the magnetic field strength of the Earth at the equator ($\sim$0.31 G), μ_0 is the vacuum permeability, ρ is the mass density of the solar wind, and v is the velocity of the solar wind. For the magnetopause to be compressed to a geosynchronous distance, and therefore expose the instrument outside the protection of the magnetosphere, the ram pressure is required to increase by a factor of $\geq$12.1 of the quiescent value. This is attainable in infrequent, highly energetic solar events such as CME/SEP as well as in fast stream stellar wind, and such wind conditions are potentially constant at an orbital distance of 0.16 AU around an active M dwarf like GJ1243.

The conditions in the solar wind, and indeed, during solar magnetic activity, are highly variable, and as such an average value is obtained for the present work. Magnetospheric dynamics are likewise unique for every potential geomagnetic response. Keeping this in mind, we compare here our proton event fluence scaling with a solar event that has been observed - a well-studied solar proton event of the Oct 19/20 1989 flare that is classified as a GOES X13 event, i.e., peak X-ray flux 1.3×10^{-3} W m^{-2} in the 1-8 Å bandpass as measured by the GOES-6/7 instruments (e.g. Jackman et al., 1993, 1995; Verronen et al., 2002). The GOES satellites measured a peak of ∼40,000 proton flux units (pfu, particles sr^{-1} cm^{-2} s^{-1}) for protons with energy ≥10 MeV during an event which had duration of ∼27 hours. This pfu measurement, then, takes into account the location of the satellite relative to the structure of the magnetosphere. This is an important point, as the magnetosphere deflects the stellar wind - and partially mitigates the impact of energetic proton events.

At the time of peak proton flux, at ∼1600 UTC on October 20, 1989, the IMP 8 satellite reported a solar wind ram pressure of 4.5 nPa - a factor of ∼3.2 over nominal solar wind conditions (5 protons cm^{-3}, 400 km s^{-1}); this pressure leads to a magnetospheric compression from a nominal 10-11 $R_{\oplus}$ planetward to 7.5 - 8.0 $R_{\oplus}$; this is still well sunward of geosynchronous orbital distance at 6.6 $R_{\oplus}$. GOES-6 and GOES-7 were shielded, well-behind the magnetopause, located on the dayside of the planet at local times of ∼07:00 and ∼09:30, respectively. We follow the scaling used in Segura et al. (2010) based on Belov et al. (2005), and find that an X13 flare would produce 24,611 pfu which seems reasonable (if a bit underscaled) when compared to the GOES-6/7 measurements of ∼40,000 pfu. Here, we are assuming all of our calculated flux reaches the upper atmosphere of the planet; for this single, energetic solar event, at least, the scaling matches well. To be sure, we must keep in mind that we are making many assumptions (e.g., M dwarf activity based on solar data, Earth-like geomagnetic field). More detailed discussion is found below in § 5.5.7, and more detailed work regarding the presence of a geomagnetic field will be forthcoming in a companion paper.

We therefore scale the proton events in the present work following the same method from Segura et al. (2010), calculating total proton fluence and pfu from the expected stellar flare X-ray flux for a given energy, as shown in Fig. 5.4. For the low end of our M dwarf flare

energy scale, the $10^{30.5}$ erg flare gives a $\geq$10 MeV proton flux of $\sim 3.25\times10^{5}$ pfu (fluence of $\sim 1.95\times10^{8}$ pr cm^{-2}), corresponding to a 1-8 Å bandpass flux of 1.25×10^{-2} W m^{-2} from our scaling method or a GOES X125 equivalent solar flare. The top end energy of 10^{34} erg scales to $\sim 6.20\times10^{8}$ pfu (fluence of $\sim 9.6\times10^{12}$, corresponding to 9.08 W m^{-2} in the 1-8 Å bandpass (approximately the same flux calculated in Segura et al. (2010)), or a GOES X94,000 solar flare. This is certainly a regime with much uncertainty, given no such events have ever been recorded for the sun.

With the above analysis in mind, we assume all stellar flare events modeled have a proton event associated. It has been reported that 100% of solar flare events of class GOES X2 or higher have energetic proton events (e.g., CME, SEP) associated with them (e.g. Yashiro et al., 2006; Hudson, 2011; Dierckxsens et al., 2015). That corresponds to an X-ray flux of 2×10^{-4} W m^{2} over the 1-8 Å bandpass. As mentioned above, following the assumptions made in Segura et al. (2010), the lowest energy flare in the present work would be roughly equivalent to a GOES X125 flare from the Sun — larger than any recorded event. Using this as proxy for the M dwarf events, it is not unrealistic to assume a one-to-one flare-CME frequency correlation for our work.

Since not all CMEs are guaranteed to be directed toward an orbiting planet, we want to take into account the geometries of emitted energetic proton events, (e.g., Khodachenko et al., 2007; Kay, Opher and Kornbleuth, 2016). Khodachenko et al. (2007) calculates the probability of a planet being hit by a flare related CME as:

$$P_{CME} = \frac{(\Delta_{CME} + \delta_{pl})\ \sin\left[(\Delta_{CME} + \delta_{pl})/2\right]}{2\pi \sin\Theta} \tag{5.5}$$

where Δ_{CME} is the angular size of the CME, δ_{pl} is the solid angle subtended by the planet, and Θ is the hemispheric latitude range of CME activity on the star. Here, we study two sets of values of $\Delta_{CME} = 5\pi/183$ ($\pi/2$) as a restrictive (permissive) estimate, and stellar magnetic latitude $\Theta = \pm\pi/4$ in both cases; $\delta_{pl} \approx 10^{-8}$ is negligible for an Earth-like planet at 0.16 AU; further, we assume zero orbital inclination. We also assume that CME activity expands similarly to solar geometry, instead of being trapped in the astrospheric current sheet. This gives a probability for every CME to hit our simulated planet of P_{CME}=0.083

(0.25) for the restrictive (permissive) CME angular size. In this work, we assume all particles in our calculated fluence impact and precipitate into the atmosphere of the planet, ignoring potential deflection from a planetary magnetic field. In § 5.5.7, we discuss the potential complications, and suggest directions for future work.

5.3.5 Optical-red flare continuum

In Segura et al. (2010), the flare spectrum used to drive the photochemistry included flux from the far UV to 4500 Å. During the 20 timesteps in the flare, flux from wavelengths greater than 4500 Å was not scaled to flare levels from the blackbody continuum associated with quiescence. In the present work, we extended all flare timesteps to include increased flux out to the near IR, to 8500 Å.

To use a more realistic spectrum, the optical-red continuum wavelengths longward of 4500 Å for each timestep were scaled to the relative flux value at 4500 Å, and then extended to 8500 Å by adding the modeled combined tails of two blackbody continuum curves with maximum temperatures of 5,000K and 10,000K to represent the increased optical-red spectrum from the flare the so-called "conundruum" following Kowalski et al. (2013). Fig. 5.5 shows the extended flare spectra during the impulsive, rising phase of the flare from 2000 - 8500 Å, with our extended, upscaled spectrum to the right of the vertical dashed red line at 4500 Å. The timesteps in the decay phase of the flare events were similarly scaled.

5.4 Results

The following subsections demonstrate the resulting effects of repeated stellar flares, with and without CME/SEP events, on the atmosphere and surface UV flux of an unmagnetized Earth-like planet at 0.16 AU.

The 1D photochemical model runs for each timestep throughout every simulation. For results in § 5.4.1 and 5.4.2, the timesteps during the flare are set by the energy scaling characteristics and lightcurve timing from GJ1243 (e.g. Hawley et al., 2014; Davenport et al., 2014), discussed above in § 5.3.3, and vary from order 10^0 to 10^3 seconds. For § 5.4.3 and 5.4.4, the entire flaring period for all durations were run with a 1 minute cadence; the coupled 1D radiative-convective model is run between flares, typically for intervals of

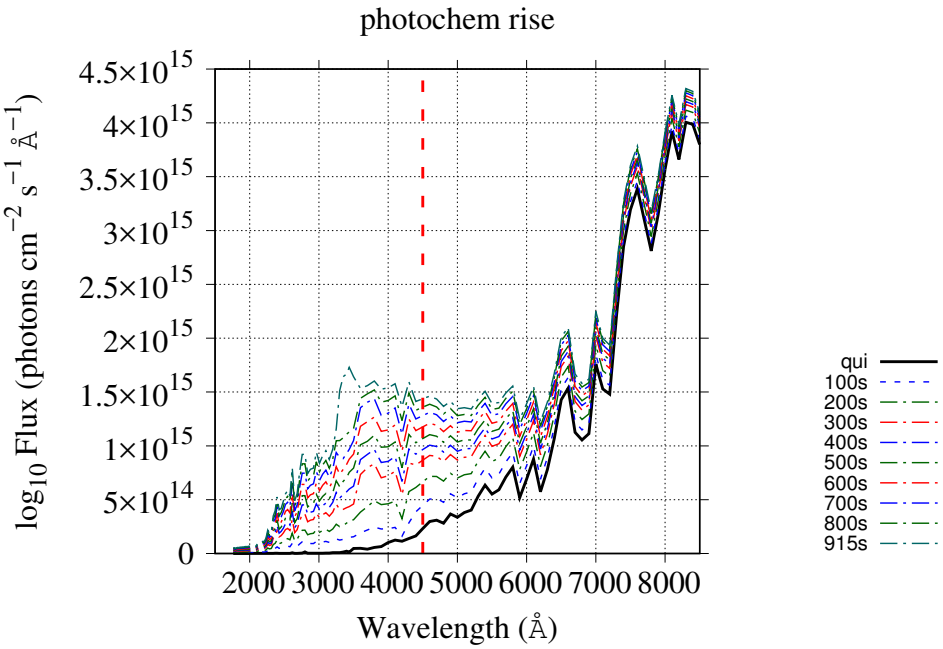

Figure 5.5 Full UV-visible spectrum for the impulsive phase of an AD Leonis great flare sized (10^{34} erg) event. The spectra to the right of the vertical dashed red line have been added in the present work.

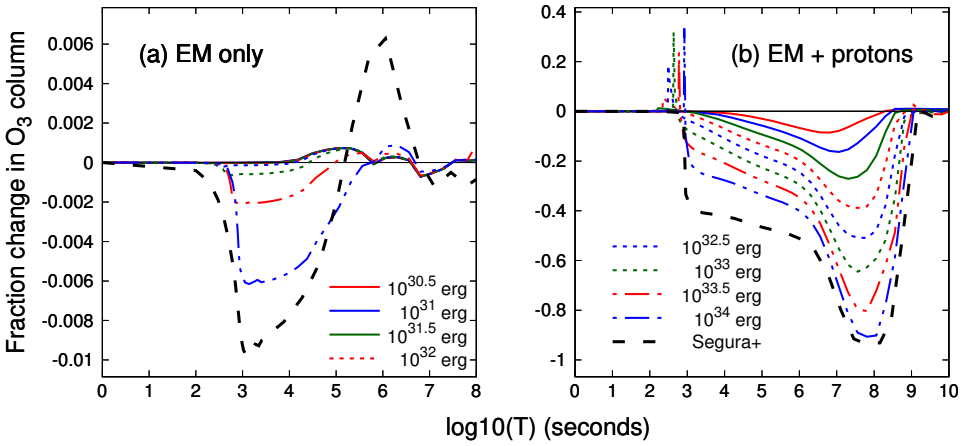

Figure 5.6 O_3 evolution for single-flare energy parameter comparison with Segura et al. (2010) for EM-only (left panel) and EM+protons (right panel) $10^{30.5}$ - 10^{34} erg flares.

order $\geq 10^3$ s both during interflare periods, and the post-flare recovery phase is run with a variable timestep, i.e., the method used in Segura et al. (2010). It is worthwhile to note here that due to the high frequency of flare activity, the atmosphere does not typically return to an equilibrated steady state between flare events, as would be the case for a planet orbiting such an active stellar host. The timescale to equilibrium for individual flare events can be seen in Fig. 5.6.

5.4.1 Energy parameter-space comparison with (Segura et al., 2010)

We simulated the atmospheric effects of an array of single-flare energies from the range covered by the GJ1243 FFD, and compared the results to the original ADLeo sized flare (10^{34} ergs) simulated in Segura et al. (2010). The effects of electromagnetic-only (EM-only) and electromagnetic with proton events (EM+protons) were both simulated; the proton flux and fluence for each flare (see Fig. 5.4) are correlated with the amplitude of the flare as given by the Kepler observational results as described in § 5.3.3, Eq. 5.1, and as discussed above in § 5.3.4.

Fig. 5.6 shows the single-flare effects on the ozone-column for EM-only and EM+protons in the left and right panels, respectively, as a function of time. The 10^{34} erg EM-only case in the left panel of Fig. 5.6 is a direct comparison of the new model (dash-dotted blue line, with

updates included from § 5.3.1) to the original flare simulated in Segura et al. (2010) (dashed black line). In the new treatment, the magnitude of O_3 column depletion is reduced, and the depressed column density recovers more gradually due to the long decay phase of the flare event. Applying the flare template from Davenport et al. (2014) to the flare spectral evolution discussed in § 5.3.3 (e.g., new treatment has wider FWHM, less impulsive, longer decay phase) is indicated in the overall impact on the O_3 column as seen in these single events. The results suggest that EM-only flare impulsivity has a strong impact on the O_3 column, when compared to the overall flux delivered to the atmosphere, whereas the atmospheric recovery time is more dependent on the flare duration or overall energy.

For EM-only lower energy flare events ($\leq 10^{32}$ erg), the overall effect is to initially decrease the O_3 column by a small amount (factor of 10^{-4}), and subsequently increase the ozone column by a fractional percentage ($< 1\%$). At lower flare energy, the flare duration is fairly short (e.g., 600 seconds for $10^{30.5}$ erg). The generation of ozone via free O atoms from photodissociation of other species (e.g., H_2O) occurs more rapidly than the direct photodissociation of O_3, resulting in the overall slight increase of the O_3 column. Once the energy of the modeled EM-only flares becomes sufficiently large ($>\sim 10^{32}$ erg), the overall O_3 photodissociation rates are significant enough to produce a notable net loss of ozone due to the flux input from a single flare event. The long-term effects of this slight increase in O_3 column depth by these low energy, high frequency EM-only events is discussed and shown below in § 5.4.3.

Fig. 5.6, right panel, shows the EM+protons cases, including a direct comparison of the new model (colored lines) with the results of Segura et al. (2010) (dashed black line). The most significant difference featured in runs from the present work is the rapid increase and subsequent decrease in the ozone column at the time of NO_x injection, and is driven by the mass-balancing addition of O at an equivalent rate to the NO injected as discussed in § 5.3.2. In these events, NO_x is injected at the peak of the flare, as in Segura et al. (2010), the timing of which increases with increasing overall flare energy, due to the related increase in both flare rise/decay times relative to flare durations (e.g. Hawley et al., 2014), as noted in Eq. 5.3. The immediate subsequent decrease of the O_3 generated by the injected O atoms is seen, e.g., due to the rapid action of NO_x destruction of O_3.

Comparing the two 10^{34} erg flares in panel (b) (present work - blue dash dotted line, Segura et al. (2010) - black dashed line) we find a difference between the two events, with a peak ozone loss of ∼90 (94)% occurring ∼2 years after the event for the present work (Segura et al. (2010)), and recovery taking ∼50 years in both cases. It is apparent that events with the highest impact on the atmosphere are those including stimulated NO_x-production through energetic proton flux into the upper atmosphere, as is evidenced by comparing the lowest EM+protons event at $10^{30.5}$ erg, which shows a factor of ∼14 greater O_3 column loss (∼8.4%) when compared to the highest EM-only 10^{34} erg flare in the left panel (0.6%). The proton flux, and therefore NO_x production, for all EM+protons events were scaled according to the method outlined in § 5.3.4, and seen in Fig. 5.4. This corresponds to a total fluence for the $10^{30.5}$ erg event of $\sim 1.95 \times 10^{8}$ protons cm^{-2}, or a factor of 2.03×10^{-5} of the simulated ADLeo event, and a factor of $\sim 1.33 \times 10^{-2}$ of the Carrington event of 1859 (Rodger et al., 2008). Taking into account this scaling for lower energy flare events, the ozone column is still significantly altered, with peak ozone column loss of ∼8.4% occurring ∼2.5 months after the event; for our simulation of a Carrington-sized proton events, peak O_3 loss of ∼36% equilibrium value occurs at ∼1.15 years after the flare.

Repeated impacts by proton events even at the lowest energies considered - could be particularly impactful on the ozone column of the Earth-like planet, depending on orbital parameters, as well as CME frequency and geometries. The resulting effect of multiple proton events on the O_3 column and surface UV flux are discussed below in § 5.4.2, 5.4.4, and 5.5.2.

5.4.2 Temporal spacing of flare activity, with and without protons

We simulated the effect of multiple flares with varying temporal spacing to parameterize the effect of flare frequency on atmospheric evolution, notably the O_3 column. Two sets of simulations were performed, EM-only and EM+proton events. The EM-only simulations were performed with 1000 flares, over five different cases that vary the interflare separation periods at two hours, one day, one week, one month and one year. Note that the spacing between flare events is measured from the final timestep of the initial flare event and the

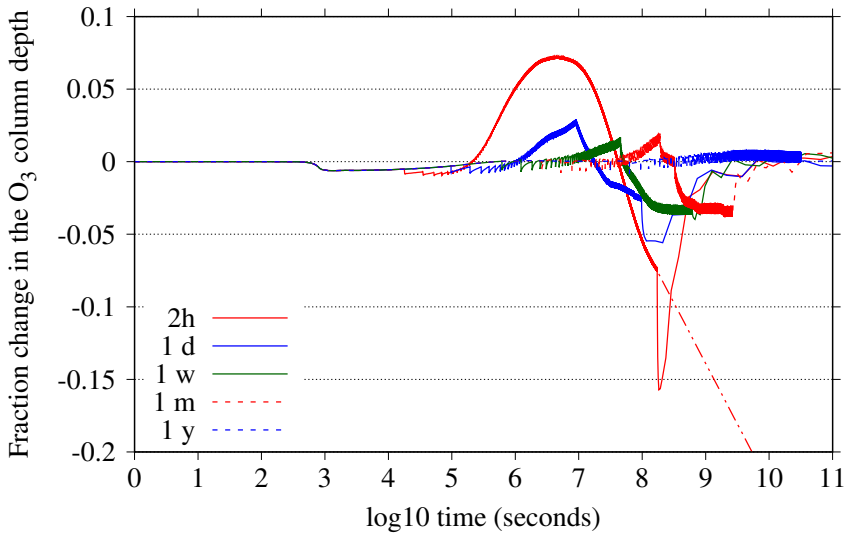

Figure 5.7 The effects on the O_3 column of EM-only, 10^{34} erg flares with varying interflare separations. Separations of 1 day, 1 week, 1 month and 1 year included simualtions of 10^3 flares, where the 2 hour separation included 10^4 flares to obtain extended effects for long-term prediction of O_3 column (dash-dotted red line).

first timestep of the following flare event. From Fig. 5.6(a), one can see that single lower energy flares do not significantly impact the ozone column, so the results shown in Fig. 5.7 to determine the effect of EM-only flare spacing were all performed with the ADLeo-like 10^{34} erg flare flux to generate the worst case effect of UV on the ozone column. In § 5.4.3 the effects of the lower energy EM-only events can be seen during the simulations generated from the GJ1243 FFD. Simple pairs of flare events were also simulated for both EM-only and EM+protons, but showed little deviation from single events and are not shown here.

Fig. 5.7 shows the results for the EM-only simulations, consisting solely of multiple 10^{34} erg flares. The results indicate that the electromagnetic events from active M dwarfs impact an atmosphere slowly, but perhaps over long enough time - significantly. The case with a one year interflare separation (dashed blue line) shows no appreciable change over the course of ∼1000 years, as the period of atmospheric recovery for a single 10^{34} erg event is ∼1 year (as seen in Fig. 5.6(a)); therefore, each flare is affecting a nearly re-equilibrated atmosphere,

leading to seemingly small change over periods of time of order 1000 years. It should be noted here that the active star used in the flare model - the ADLeo spectra applied to the atmosphere via the GJ1243 FFD and lightcurve - would experience a flare of this magnitude approximately once every 489 days, as seen in the stellar FFD in Fig. 5.1.

The cases run with interflare separation of one day, one week, and one month all suggest that extended periods of frequent events equivalent to the great flare of AD Leonis slowly erode the O_3 column over extended periods, but seem to reach a potential new equilibrium at ∼97% of the steady state value. This gives rise to some concern for a potentially habitable planet as M dwarfs stay active for well into their multi-Gyr lifetimes on the main sequence (e.g. Silvestri, Hawley and Oswalt, 2005). However, instead of focusing on the loss rate for those flaring frequencies, we will comment on the simulation with two hour interflare separation - the worst case scenario from a star much more active than ADLeo or GJ1243. In this case, 10^4 flares were run instead of 10^3, which corresponds to a period of ∼6.9 years. At that point, the O_3 column has been eroded by only ∼7.4% of the equilibrium value, albeit at a very steep rate of decline.

To estimate the continued loss rate if this high amount of flux continually impacts the planetary atmosphere, we extend the dot-dashed red trendline in Fig. 5.7, and find that even by the age of the current universe (∼4.3×10^{17} seconds) the O_3 column loss would only be ≈86.1%. This is less impactful than the full impact of a single proton event from a 10^{34} erg flare. This result is discussed primarily as an extreme thought experiment, as such conditions are highly unlikely to persist for a significant portion of planetary evolution: no M dwarf has been observed experiencing 12 AD Leonis great flare-sized events per day. It is possible that very young stars could exhibit such activity, though, so these results could be applied to very early evolution of an Earth-like atmosphere containing significant oxygen content.

The EM+protons simulations were performed with 100 flares - all proton events impacting the planetary system - for the same separation periods mentioned above. We chose to simulate energies of $10^{30.5}$ erg, the lowest energy included in this work, $10^{31.9}$ erg events with approximately equivalent proton fluence to the Carrington event, and 10^{34} erg, equivalent to the ADLeo flare. In Fig 5.8, we show the results from 100 proton events for three

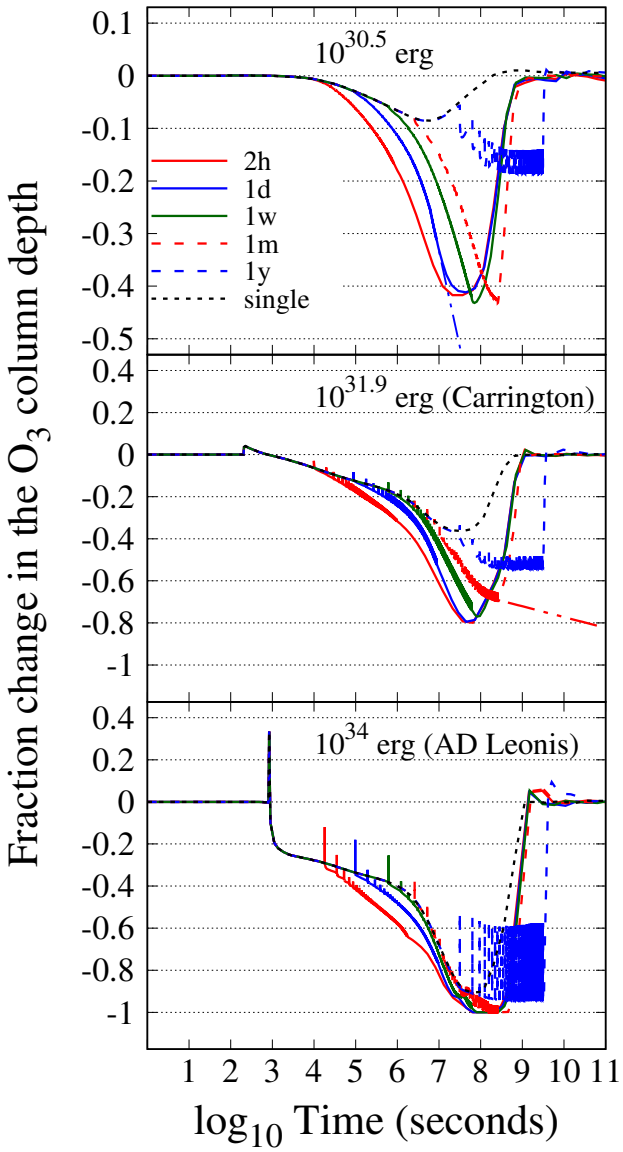

Figure 5.8 O_3 evolution driven by repeated proton events, 100 flare events for all cases. **Top:** $10^{30.5}$ erg flares+protons. The 1 d^{-1} period is likely to occur for a planet orbiting GJ1243; the dash-dotted blue line extrapolates the predicted O_3 loss rate. **Middle:** Carrington equivalent proton events at $10^{31.9}$ erg. The dash-dotted red line predicts O_3 evolution for the most likely frequency experienced at a GJ1243 orbiting planet. **Bottom:** AD Leonis equivalent proton events with 10^{34} erg.

different energies: $10^{30.5}$ - the lowest energy considered in the present work, $10^{31.9}$ - events with proton fluence similar to the Carrington event, and 10^{34} - events with proton fluence similar to the great flare of AD Leonis simulated in Fig. 5.6, respectively. The black dashed line in each panel shows the impact of a single proton event of each energy for reference. In these simulations, every event was assumed to directly impact the planet and fully affect the atmosphere. In reality, CME and SEP events could be glancing blows, or miss the planet entirely, as discussed in § 5.3.4. The interflare separations in each case are the same as those used in the EM-only simulations discussed above.

In general, the results suggest that even the lowest energy, most frequent flares from a star like GJ1243 - $10^{30.5}$ erg - can rapidly erode the O_3 column of an Earth-like planet for all interflare frequencies except the once-per-year case. Table 2 shows the time to destroy $\geq 99\%$ of the O_3 column for the cases in the middle (Carrington-like, $10^{31.9}$ erg) and bottom (ADLeo-like, 10^{34} erg) panels Fig. 5.8. To predict these time to loss values, we used a log fit to the O_3 column depth curve for the last $\approx$1000 points during the period of active flaring, and then extrapolated to find the intercept at 99%; the method assumes that the loss continues at the rate of the last 1000 or so points of O_3 column evolution during flare activity. Note that assuming the loss rate is maintained is possibly inaccurate, as one can see from the cases simulated for 10 year duration in Fig. 5.11 and discussed in § 5.4.4 — the response at long times tend to follow a separate fit, which declines more gradually. For this reason, we do not extrapolate from the $10^{30.5}$ erg results in the top panel of Fig. 5.8, instead we discuss the impact of these lower energy flares below, in § 5.4.4.

If every flare from a star as active as GJ1243 hits a planet, we might expect the rate of O_3 depletion to be quite rapid, similar to what is seen in the top panel of Fig. 5.8, for the two hour, one day, and one week interflare separations. One can see that for the one year interflare separation, the trend flattens out and the atmosphere reaches a new steady state at $\sim$86% of the original steady state column depth. Similarly, for the one month interflare simulations, the trend begins a flattening just before the end of the flare activity, likely reaching a new equilibrium around 50% of steady state.

Taking into account the CME/SEP geometries discussed in § 5.3.4, along with the FFD, the most likely case for a planet orbiting a star like GJ1243 to experience a Carrington-like

Table 2. Time estimation to $\geq$ 99% O_3 loss, by interflare separation

	$10^{31.9}$ erg	$10^{34.0}$ erg
2 hour sep	3.50×10^{7}	1.89×10^{7}
1 day sep	7.38×10^{7}	3.22×10^{7}
1 week sep	2.55×10^{8}	8.33×10^{7}
1 month sep	$\mathbf{2.64\times10^{14}}$	1.35×10^{8} **
Total fluence [prot cm^{-2}]	1.82×10^{12}	8.49×10^{14}

Note. — Time to $\geq$ 99% O_3 loss assuming continued flare activity beyond the 100 flares simulated as shown in Fig. 5.8. Power law fits to O_3 loss rate for last $\sim$20 flares in each case, and are shown for the most likely cases for a planet orbiting GJ1243. Times in bold represent the most likely time to loss for a planet orbiting GJ 1243 in the HZ for conservative CME/SEP geometries (see § 5.3.4).

** - For the 10^{34} erg flares with 1 month interflare separation, the system sustained O_3 losses $\geq$ 99% during the flaring period at this time above, no fit necessary.

event is in bold in Tab. 2. For the Carrington-like $10^{31.9}$ erg flares, one flare occurs every ∼3.7 days. Assuming the CME probability of 0.08, this implies one proton event hits the planet every ∼46 days. In this case, applying the power law fit suggests an O_3 lifetime of $\sim 2.64 \times 10^{14}$ seconds, or ∼8.4 Myr for a planet's O_3 column to be effectively destroyed with respect to surface UV shielding. Note that prolonged simulations may show a change in the trend as the atmosphere is able to recover from multiple flaring events such as these – see discussion in § 5.4.4.

In the case of the multiple 10^{34} erg flares, one can see in the bottom panel of Fig. 5.8 and in Tab. 2 that each interflare frequency simulated has the potential to effectively destroy the O_3 column to less than 99% in less than 3 years for all cases — except the two hour and one year interflare separations. While proton events impacting the planet with this frequency are unlikely for a host like GJ1243, a more active M dwarf, or very active early star could produce such events. A host like GJ1243 would experience one 10^{34} erg flare once every ∼489 days, so the once per year case (blue dashed line) is rough approximation to the expected atmospheric response if each of the events hit the planet. This case indicates that the O_3 column is roughly equilibrated at ∼94% loss. However, as the discussion in § 5.3.4 notes, approximately one in eight (or one in four) proton events of all energies hits the planet, depending on CME geometry.

For all of these EM+proton simulations, the results in Tab. 2 assume that only these proton events are impacting the planetary atmosphere, ignoring other less and more energetic proton events ejected by the stellar host as would be seen in a realistic flare distribution such as Fig. 5.2. The simulations including realistic flare distributions and proton event geometries are shown and discussed below in § 5.4.4.

5.4.3 EM-only FFD-generated flares

The results of Segura et al. (2010) and those in § 5.4.1 above indicate that single, EM-only flares do not significantly impact the atmosphere of the ozone column of an Earth-like planet at 0.16 AU. Results in § 5.4.2 suggest that even frequent 10^{34} erg EM-only events are not as impactful as a single, lower-energy proton event. However, given the flaring frequency

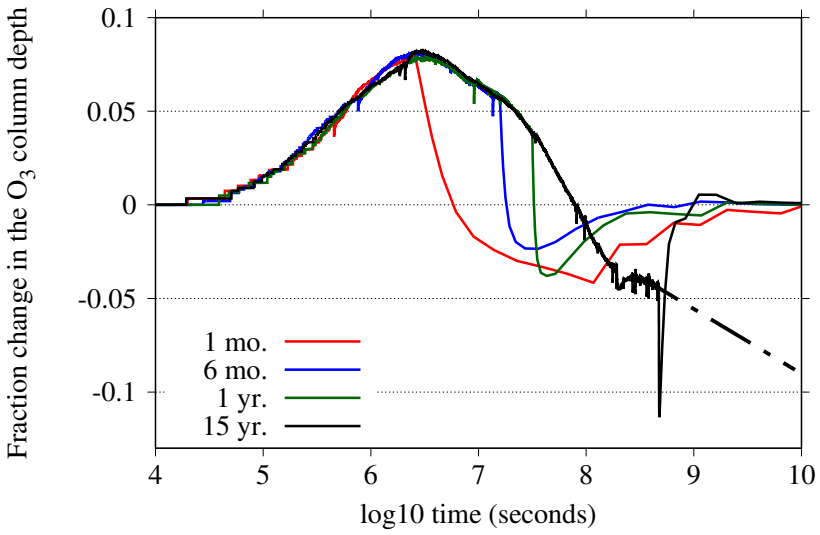

Figure 5.9 O_3 evolution for EM-only flare events generated from the GJ1243 FFD for periods of 1 month, 6 months, 1 year, and 15 years. The dash-dotted black line predicts continued effects of flaring beyond 15 years.

of active M dwarfs like GJ1243 (Hawley et al., 2014), terrestrial planetary atmospheres for planets orbiting these active hosts will be impacted by multiple flares per day at varying energies. Fig. 5.1 shows the GJ1243 FFD and amplitude for the stellar host's flare activity in our simulations, indicating that ∼7 flares per day of energy $10^{30.5}$ erg and above will impact the planetary atmosphere.

A six month (one year) example distribution of the generated flares are shown in the top (bottom) panel of Fig. 5.2, showing a generated timeline of 1277 (2555) flares over that 180 (360) day period. The flux for each flare was stacked additively, allowing for the effects of simulated complex flares as shown in the log-scale inset for the top panel of Fig.5.2; the inset is a zoom around the large flare event of amplitude ∼0.78 (∼$10^{33.84}$ erg) just prior to day 9. Four such individually generated distributions were created using the GJ1243 FFD and used to drive a more realistic atmospheric simulation response to EM-only flaring for periods of: one month, six months, one year, and 15 years. In the six month (one year) simulations shown in Fig. 5.2, the largest flare is of amplitude ∼0.972 (0.950) or 9.6(9.3)×10^{33} erg. An

average of seven flares occur per day in these distributions, most of low energy, and are not visible due to the scaling of the figure. The effects on the ozone column of the planet from the EM-only, multiple flaring distributions are shown in Fig. 5.9.

The simulations for each of the four distributions show that the early ozone evolution is dominated by the multitude of smaller flares. These smaller events increase the overall ozone column steadily and in predictable fashion despite each run being an independent distribution, most easily seen as the varied presence of larger flare events throughout the flaring period, as seen in Fig. 5.2. The larger flare events ($> 10^{33}$ erg) can be seen as negative spikes throughout the distributions. All runs reach a peak ozone increase of 8% around one month, and the longer runs then turn back toward equilibrium. The 15 year case runs long enough to drive the ozone column into the loss region, and from the trend for the range of 2-3$\times 10^8$ s, one can extend the rate of change to calculate that this level of maintained loss would result in O_3 column loss of $\sim$37% by the age of the universe; compared to the results shown in Fig. 5.7, the two hour interflare period for multiple 10^{34} erg flares drove more than twice the O_3 depletion in the same period. It is likely that the EM-only flaring can cause a slow change over 10s of billions of years, but even small, continuous proton events combined with the EM are significantly more destructive with respect to O_3 abundance.

Longer periods still need to be simulated to isolate the longer term effects of EM-only flaring, and are planned for future work. Given that M dwarf stars are active for significant portions of their long lives, these results suggest that the ozone column around these stellar hosts are likely to be depleted, quite significantly if proton events are involved, as shown in the next section.

5.4.4 EM+protons FFD-generated flares

To simulate a more realistic planetary atmospheric response to proton events from a stellar host with flare properties similar to GJ1243, we simulated several cases over one year of realistic flare activity generated from the FFD, shown in the bottom panel of Fig. 5.2. The 10 year simulations were run from a flare distribution (not shown) generated independently

from the GJ1243 FFD, and the distribution is separate from the six month and one year examples shown in Fig. 5.2. To gauge the effect of CME geometry discussed in § 5.3.4 and noted in Eq. 5.5, we ran two cases - one conservative case, with smaller CME solid angles ($\Delta_{CME} = 5\pi/18$) which gave each CME an ∼8.3% chance to hit the planet, and one more permissive case with larger CME solid angles ($\Delta_{CME} = \pi/2$), giving each CME a ∼25% chance to hit. In both cases the maximum stellar latitude of magnetic activity driving proton event ejections was constrained to be between $\Theta = \pm\pi/4$. With the combination of these two tools - FFD flare distribution from observation of GJ1243 and CME geometry - these results represent a more realistic representation of the effects of a proton event on the atmospheric evolution for an unmagnetized, Earth-like planet in the habitable zone at 0.16 AU around an active M dwarf host.

A representative frequency distribution of proton events impacting the planet is shown in Fig. 5.10; the events were taken from the 10 year duration simulation, the results of which are plotted in Fig. 5.11 and discussed below. In Fig. 5.10, the events plotted in green (magenta) represent the CME impact probability of P_{CME}=8% (P_{CME}=25%), as discussed above. Note there are a few events with less energy and fluence than $10^{30.5}$ erg shown here, as proton events were checked against P_{CME}, and simulated at one of three timesteps during each flare event in the simulation: either the peak of the flare, or the timestep to either side of the flare peak, which allowed the proton fluence to be scaled slightly downward for some events, e.g., to $10^{30.2}$ erg equivalent fluence. The proton events in each case were selected randomly in real-time during each simulation, and so the overall distribution of event energies and impact frequencies vary slightly in each of the four, one year simulations (the randomly selected distribution for the 10 year cases can be seen above in Fig. 5.10).

The influence on the O_3 column is shown in Fig. 5.11, with the conservative results ($\Delta_{CME} = 5\pi/18$, $P_{CME} = 8\%$) in the top panel, and the more permitted results (Δ_{CME}=$\pi/2$, $P_{CME} = 25\%$) in the lower panel. The vertical dashed lines correspond to the end of the flaring periods, i.e., one and 10 years. The number of impacting proton events in the conservative (more permissive) case in the top (bottom) panel was 199.25±17.23 (595.25±11.59) out of 2555 flares in the one year distribution (see bottom panel of Fig. 5.2), and 2045 (6301) events out of 25,550 impacted the atmosphere of the planet for the 10 year simulations, for

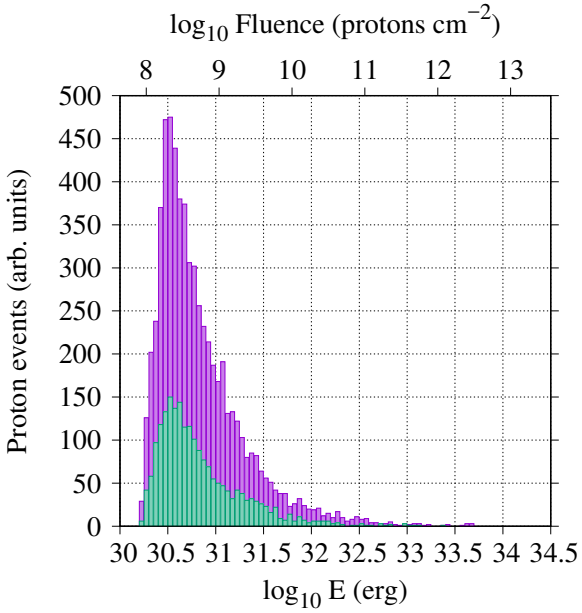

Figure 5.10 Distribution of proton events by flare event energy and proton fluence for the 10 year simulations. CME probability P = 0.25 (0.08) is shown in magenta (green).

P_{CME}=8% (25%).

The O_3 column responded similarly in each of the four one-year cases (shown as the average - black solid line, and the standard deviation - violet shaded region), for both restrictive and permissive CME geometries. There deviation seen in the one year simulations is due to the varying energies from the randomly selected impacting CME events (these can be seen as sudden increase of O_3 in each case similar to that discussed in $ 5.4.1). The more conservative CME geometry resulted in ∼74.10±2.54% O_3 column loss at the end of the year long simulations, and the more permissive geometry resulted in ∼80.07±4.03% loss.

To determine a more long term effect, one 10 year run was performed for each CME impact probability, and these are shown in red in both the top and bottom panels of Fig. 5.11. The 10 year flare distribution was generated separately from the one year distribution, and the proton event selection was random and could occur on either the timestep of the flare peak, or one timestep to either side. The O_3 column on the last timestep for the P_{CME}=0.08 (0.25) CME impact case is ∼10.2% (∼8%) of the steady-state equilibrium value. However,

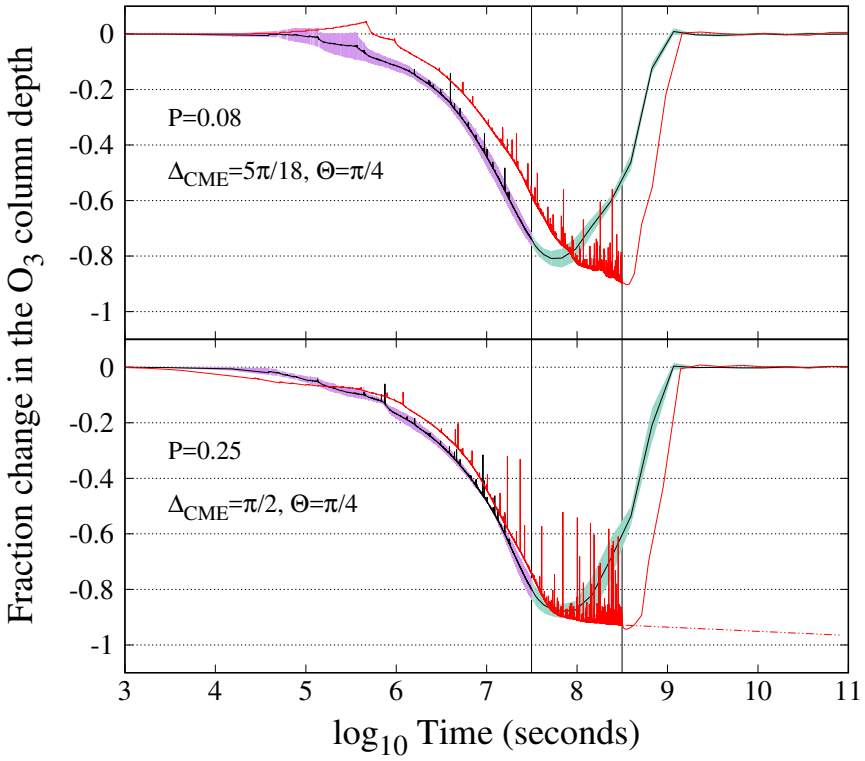

Figure 5.11 O_3 column depth response multiple proton events, generated by the GJ1243 FFD and taking into account CME geometries. The average (black line) and standard deviation (shaded violet/green regions) for one-year simulations, and one 10-year simulation (red line) are shown. **Top:** Events with more conservative CMEwith per-event probability for impact of P=0.083. **Bottom:** Events with more-permissive geometry with per-event impact probability of 0.25.

note that at the end of these simulations, both cases show a continuing trend of increasing loss. The P_{CME}=0.25 case, in particular, shows a consitent slope that predicts the time to 99% (99.9%) O_3 loss as 3.98×10^{12} s, or 126.7 kyr (1.59×10^{13}, or 502.9 kyr), assuming the same loss rate continues.

It is difficult to simulate the behavior at longer timescales, due to the balance maintained between the timestep granularity with which these events need to be simulated for accuracy, and the exponential timescales on which these processes occur, and could feasibly impact habitability.

5.5 Discussion

All of the results in the present work have been performed with a beginning point from an equilibrium Earth-like atmosphere, which by definition assumes an oxygen-rich state. This is worth keeping in mind during the below points of discussion. Future work is planned to investigate varying steady-state conditions for potentially habitable planets in different phases of atmospheric evolution, e.g., atmospheres with high CO_2, low O_2, or haze layers.

5.5.1 Multiple events, event frequency, stellar activity

Below a certain level of proton fluence, the response time of the atmosphere is sufficiently rapid to slow the rate of O_3 loss, or reach a new equilibrium. This effect can be seen in Fig. 5.8 as the flattening of the O_3 column response towards the later end of the simulations with larger interflare spacing. However, even for smaller flare energies with sufficient frequency - and therefore sustained proton flux - is it possible that O_3 recovery is insufficient to prevent a rate of sustained loss to levels $\leq$0.99% of steady-state equilibrium value.

The results for 100 10^{34} erg flare events at a frequency of once per year in the bottom panel of Fig. 5.8 show the O_3 column reaching equilibrium at a loss of $\sim$89% of the steady-state column depth. This outcome represents the approximate frequency of flaring at this energy level from an FFD like that of GJ 1243 (one 10^{34} erg event every $\sim$489 days), and is a loss of UV shielding similar to Segura et al. (2010) (which is important due to flaring with a depressed O_3 column as discussed below in § 5.5.2), but doesn't take into account the multiple smaller events, which as discussed in § 5.4.4 are very impactful. The results

of the more realistic case in Fig. 5.11, which is based on the FFD of GJ 1243, show a non-equilibrium, continual decrease in O_3 column depth to $\sim$94% O_3 loss after only 10 years, an order of magnitude smaller timeframe than the artificial 100 flares in 100 years above. This implies the continued, rapid deposition of proton events at the low end of the FFD energy range ($\sim$7 per day for energies $\geq 10^{30.5}$ erg) contributes significantly to the depletion of the O_3 column, despite a fluence that is less by a factor of $\sim 4\times10^4$ when comparing the two endpoint values in our adopted FFD ($10^{30.5}$ and 10^{34} erg); the frequency of the lower energy events is approximately three orders of magnitude higher.

This brings up the issue of whether proton event frequency or fluence dominates the O_3 column depletion, which has implications for atmospheric response for planets orbiting smaller, older, or less active stellar hosts. In effect, the average proton fluence delivered over a period of time from GJ1243-level activity is comparable to that of a single moderate flare from the same star. For example, in Fig. 5.11, the total proton fluence for the 10-year case with more restrictive CME geometry in the top panel was $\sim 9.9\times10^{12}$ protons cm^{-2}, roughly equivalent to one $10^{32.7}$ erg flare produced proton event per year; in the bottom panel, the fluence is roughly equal to one $10^{33.3}$ erg event per year. From Fig. 5.8, we can interpolate between the Carrington-sized events in the middle panel, and the AD Leo sized events in the bottom panel. Doing so, for fluence from single events per year, the values would equilibrate between roughly 70-75%, not the case we see in Fig. 5.11, where the 10 year simulations reach O_3 depletion $\geq$90%. For the delivery of proton fluence to the planet, it appears that the frequency of events is as important, if not more important, as the total fluence from the events. Note that it is likely that GJ1243, and other highly active M dwarfs, experience flare events with lower energy and higher frequency than we modeled here, but are challenging to measure due to observational constraints.

The total fluence delivered over the P=0.08 (P=0.25) single year simulations in Fig. 5.11 is $1.49\pm0.38\times10^{12}$ ($4.93\pm0.33\times10^{13}$). The size of a single Carrington event in the present paper is $1.1\sim10^{11}$ protons cm^{-2}, and occurs roughly once per 3.7 days. In comparison, for solar cycles 19-24, the total proton fluence from all measured proton events was of order 10^{10}-10^{11} over the 11-12 year periods (e.g., Shea and Smart, 1992; Mewaldt et al., 2005; Lario and Decker, 2011).

Planets orbiting active M dwarf stars are likely to experience, in a matter of months, massive O_3 depletion from proton flux that is multiple orders of magnitude higher than what Earth experiences over entire solar cycles; for planets in the nominal HZ around these hosts, the particle flux is further increased by a smaller orbital distance compared to Earth, scaling as $1/R^2$, assuming isotropic expansion. For more active fully-convective M3-M5 stars, or active binary systems such as GJ1245AB, one assumes the situation is even more extreme.

5.5.2 Impact on surface UV flux

Photo-dissociating and photo-ionizing short wavelength radiation is highly relevant to organic complexity, on one hand, it may be one of the drivers of prebiotic chemistry (e.g. Beckstead et al., 2016; Rapf and Vaida, 2016; Ranjan, Wordsworth and Sasselov, 2017). On the other hand, UV radiation is the responsible of mutations and degradation or transformation of biomolecules which may result in the loss of biological functions (e.g. De Mora, Demers and Vernet, 2000); therefore the shielding effects of an O_3 layer for any potentially habitable planet is beneficial the propagation of organisms in the planetary surface. For example, in Segura et al. (2010), the authors found that the surface UVC flux significantly increased from $< 10^{-14}$ up to 10^{-5} W m^{-2} during the peak and recovery phase after an AD Leonis-sized proton event. This is nine orders of magnitude increase over the quiescent value, and an UV dose rate for DNA damage of the order of 10% larger of such a planet.

In the present work, we focus on two aspects: 1) the overall effect of multiple flares on the O_3 column - and therefore UV shielding, and 2) the intensity of UV surface flux from flare activity on a planet with an atmosphere already depressed by multiple, prior proton events.

Regarding, point (1) above, we have shown that for stellar hosts with activity such as GJ1243, an O_3 column with the starting density of Earth can be reduced by an order of magnitude in only a few years. After this initial rapid loss, the atmosphere seems to move towards a new, lower O_3 equilibrium, with the loss rate slowing though not completely at equilibrium. For hosts less active than GJ1243, the situation could be analogous to the top

panel of Fig. 5.8, the atmosphere could reach a new equilibrium in a matter of decades.

Addressing point (2) above, the top panel of Fig. 5.12 represents the results of the O_3 depletion shown in both panels of Fig. 5.11. The vertical dashed blue lines denote the limits of UVC ($<$ 2800 Å), UVB (2800-3150 Å) and UVC (3150-4000 Å) regions. The quiescent UV flux is shown for initial steady-state at the top of the atmosphere (TOA, black dotted) and at the ground (black dash-dotted); also shown is the quiescent flux at the ground after the 10 year flaring period for CME impact probabilities of P=0.08 (dashed black) and P=0.25 (dashed red). UV flux for two flares near the ends of the 10 year runs are shown, at $10^{31.9}$ and $10^{33.6}$ erg for the P=0.25 run, with the O_3 column at $\sim$8% of steady-state equilibrium value. Top of atmosphere fluxes are shown for the flares as well, with the red-dotted line representing the more energetic flare, and the blue dotted line the lower.

The O_3 column at the end of the proton event simulations were $\sim$0.1 and $\sim$0.08 of the equilibrium values (as discussed above in § 5.4.4 for the P=0.08 and P=0.25 CME probabilities, respectively. Note, however, that the O_3 loss would likely continue with longer duration simulated flaring and proton fluence. Based on the simulations in Segura et al. (2010), one doesn't expect much UV-C flux to penetrate to the ground given those column O_3 abundances even at higher energies, as one can see in the surface UV for various conditions listed in Table 3. During quiescence, the value of UV-B and UV-C increase substantially for all simulated cases. At the end of the two 10 year runs in Fig. 5.11, the UV-C reaching the surface at the peak of representative flare events is $\sim$17-298 μW m^{-2}. While this $\sim$8-9 orders of magnitude over the steady-state, quiescent UV-C flux, still less than the UV-C flux calculated for Earth, 3.9 and 2 Ga ago (Table 6 Rugheimer et al., 2015). Based on Earth history this amount of UV-C radiation may not be asubstantial detriment to habitability. For a Carrington-sized flare during the period when the O_3 column is depressed to 8% of steady-state value, $\sim$17 μW m^{-2} UV-C reaches the surface. For a near ADLeo-sized flare, $10^{33.6}$ erg, $\sim$298 μW m^{-2} reaches the surface at the peak of the flare. An ADLeo sized flare at these O_3 levels would peak at $\sim$740 μW m^{-2}.

However, as discussed in § 5.3.3, the decay phase of the flare dominates the energy input. If one integrates over the temporal evolution applied in the present work, the total amount of UV-C energy delivered to the surface for the $10^{33.6}$ erg event (with 8% equilibrium O_3

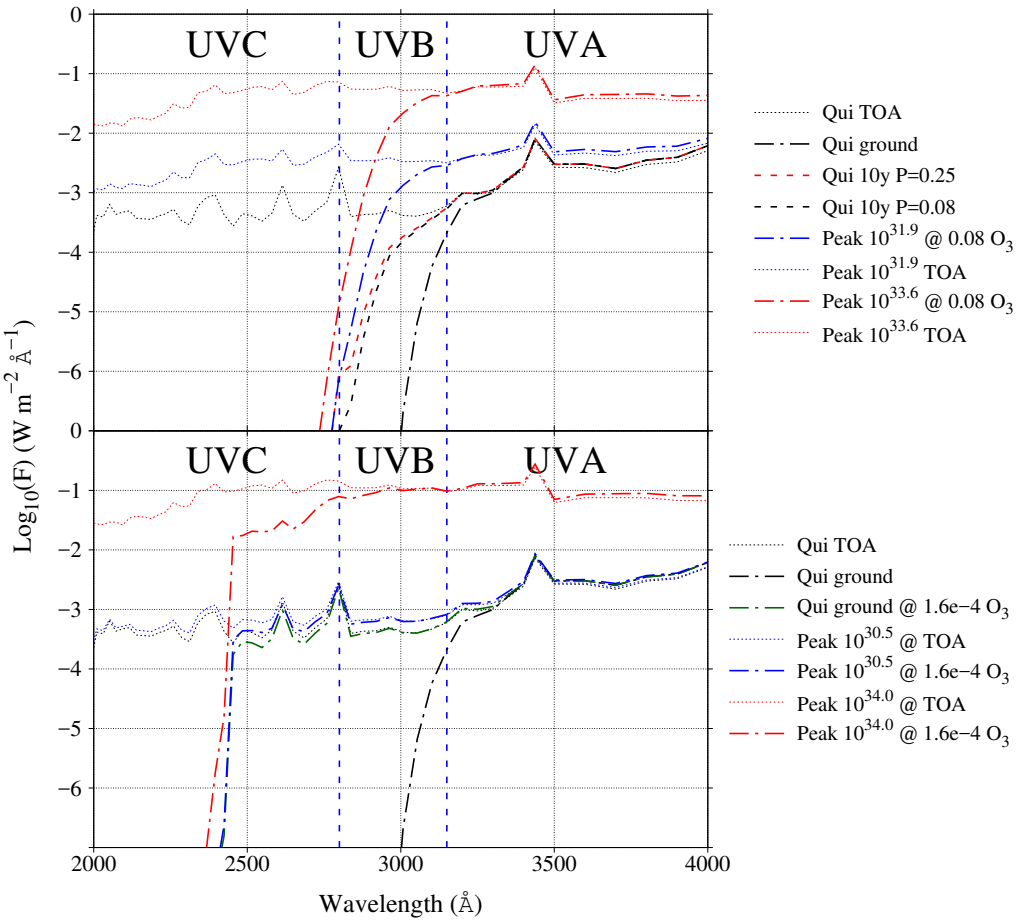

Figure 5.12 UV flux for **(top)** GJ1243 FFD generated flares, and **(bottom)** extreme O_3 loss. Steady-state O_3 column at the top of the atmosphere (TOA, dotted black line) and planetary surface (dash-dotted black line); conditions with depleted O_3 column at surface (green dash-dotted line); at top (bottom) conditions at the peak of a $10^{31.9}$ ($10^{30.5}$) erg flare at TOA (blue dotted line) and surface (blue dash-dotted line); conditions at the peak of a 10^{34} erg flare at TOA (red dotted line) and surface (red dash-dotted line). Integrated UVC flux values are given in Table 3.

Table 3. Integrated UVC flux (see Fig. 5.12)

	UVC @ TOA W m^{-2}	UVC @ Surface W m^{-2}	Integrated UVC J m^{-2}
Earth	6.73	2.13×10^{-14}	-
GJ1243 Planet			
Quiescence, full O_3	2.76	4.15×10^{-13}	-
Quiescence, 0.1 O_3	2.76	1.05×10^{-6}	-
Quiescence, 0.08 O_3	2.76	1.45×10^{-5}	-
Quiescence, 1.6×10^{-4} O_3	2.76	0.18	-
$10^{31.9}$ peak, 0.08 O_3	11.4	1.7×10^{-5}	4.5×10^{-3}
$10^{33.6}$, 0.08 O_3	180.4	2.98×10^{-4}	4.31×10^{-1}
$10^{30.5}$ peak, 1.6×10^{-4} O_3	3.63	0.24	3.53×10^{1}
10^{34} peak, 1.6×10^{-4} O_3	368.76	60.8	1.27×10^{5}

Note. — UVC flux (<2800 Å) in W m^{-2} - integrated over the examples in Fig. 5.12 - at the top of atmosphere (TOA) and the planetary surface for quiescent conditions with steady state O_3 column, quiescent conditions with depleted O_3 column (0.1, 0.08, and 1.6×10^{-4} of equilibrium value), and peak values for $10^{30.5}$, $10^{31.7}$, $10^{31.9}$, and 10^{34} erg flares with associated depleted O_3 values.

column) is 0.431 J m^{-2} over the $\sim10^4$ s event, giving an an average UV-C flux of ∼43.1 μW m^{-2}. For the ADLeo event, this figure would be a factor of ∼2.5 larger, due to the increased event amplitude and duration. Obtaining a 90% kill rate for a commonly studied, radiation resistant bacterial species, *Deinococcus Radiodurans*, requires a dose of ∼550 J m^{-2} (Gascón et al., 1995), which requires more than 1200 of such $10^{33.6}$ erg flare events at an 8% equilibrium O_3 level.

The average energy of all flare events for the 10 year distributions is $\sim10^{31.4}$ erg, each of which - when integrated - each provide a UV-C dose of only ∼0.13 mJ m^{-2} to the planetary surface with 8% of Earth's equilibrium O_3 column. One should consider effect to any underlying precursor organic molecules for which UV light may be a driver of complexity

(e.g. Beckstead et al., 2016; Rapf and Vaida, 2016; Ranjan, Wordsworth and Sasselov, 2017), however, when considering habitability. Another consideration is that the O_3 loss in these cases is still decreasing.

The bottom panel of Fig. 5.12 represents a worst-case scenario, where the O_3 column has been depleted to $\sim 10^{-4}$ of steady-state equilibrium value. This occurs in our simulations with repeated, extreme flaring with high proton fluence. In the present work such a state is reached after only $\sim$4.9 yr, given one ADLeo sized proton event per month - as seen in the bottom panel of Fig. 5.8. While such a flare frequency for that energy is not observed from GJ1243 at its current age, early stellar hosts and perhaps more highly active M dwarf hosts could exhibit such activity for millions of years. It is instructive to quantitatively consider these UV fluxes, as determining these values could offer insight to constraining the early development of complex organics or life on planetary surfaces - not the depths of any ocean, however.

Fig. 5.12, bottom panel, shows the UV flux in W m^{-2} $Å^{-1}$ for four different cases: 1) quiescent UV flux at the top of the atmosphere (TOA, black dotted line) and at the surface (black dash-dotted line), 2) quiescent flux with the O_3 column depleted by a factor of 1.6×10^{-4} at TOA (green dotted line) and surface (green dash-dotted line), 3) the peak flux of a $10^{30.5}$ erg flare with the highly depleted O_3 levels at TOA (blue dotted line) and surface (blue dash-dotted line), and 4) the peak flux of a 10^{34} erg flare with the highly depleted O_3 levels at TOA (red dotted line) and surface (red dash-dotted line).

The primary effect of the highly depleted O_3 layer is to allow more overall UV flux at the surface, but importantly the increased surface flux is in the UVB and UVC regions $\geq$2000 Å. Even at lower O_3 levels, any extremely lower wavelength flux is likely to be absorbed by the H_2O and CO_2 present in the atmosphere (e.g., Ranjan, Wordsworth and Sasselov, 2017). We have integrated UVC flux for each of the examples in Fig. 5.12, the results of which are displayed in Table 3. Note that when the O_3 is depleted by a factor of order 10^4, even the quiescent, background spectrum of the M dwarf is sufficient to deliver 0.18 W m^{-2} to the surface of the planet. Given the UV dose required for a germicidal dose, $\sim$10 J m^{-2}, this indicates that the surface would be sterilized within a few minutes, but likely before the O_3 column was depleted to this level. This level of flux does not take into account the

likely continuation of frequent flare activity during the high O_3 depletion.

During the flare of lowest energy in the present work - $10^{30.5}$ - peak UVC flux at the surface is ∼30% higher that during stellar quiescence, at ∼0.24 W m^{-2}. It is important to note here, that approximately seven of these flares occur daily on an active M dwarf like GJ1243, and have duration on the order of tens of minutes. However, even without the presence of these numerous, frequent, low-energy flares, the quiescent value alone is relatively high. During the peak of a large, AD Leonis like flare, 60.8 W m^{-2} bathes the planetary surface; over the course of the multi-hour flare, that value ranges from ∼1% of that flux up to the peak value. In particular, the rise and decay phases of our simulated flare lasts ∼4 hours, delivering ∼127 kJ m^{-2} of UVC to the surface during that time, compared to 35.3 J m^{-2} for the smaller $10^{30.5}$ erg flares that occur several times daily. In these cases, the survival of even the hardiest of known bacterial species is in question.

As pointed out by Ranjan, Wordsworth and Sasselov (2017), laboratory experiments are needed to evaluate how UV fluxes like the ones expected at planets in the habitable zone of M dwarfs may influence the construction of complex organic molecules. However if such UV fluxes are detrimental to build complex organic molecules, below approximately nine meters of sea-water, this photo-dissociating and photo-ionizing radiation will not penetrate, allowing such complexity to flourish where there is a sufficient free energy gradient and raw materials, e.g., around hydtrothermal vents.

5.5.3 The effect of flare-driven atmospheric evolution on observation

With missions on the horizon like the James Webb Space Telescope (JWST), and missions in planning such as LUVOIR, obtaining ever-increasing precision across the electromagnetic spectrum with transmission spectroscopy is certain - and of utmost importance to exoplanetary science and astrobiology. Given that we have a dataset of exactly one habitable planet, we need to develop understanding of how atmospheric evolution is driven by stellar activity to accurately interpret these spectra with respect to habitability and how atmospheres might be altered by the presence of life; of similar, related importance is correctly identifying abiotic false positive observations (Harman et al., 2015; Schwieterman et al., 2016).

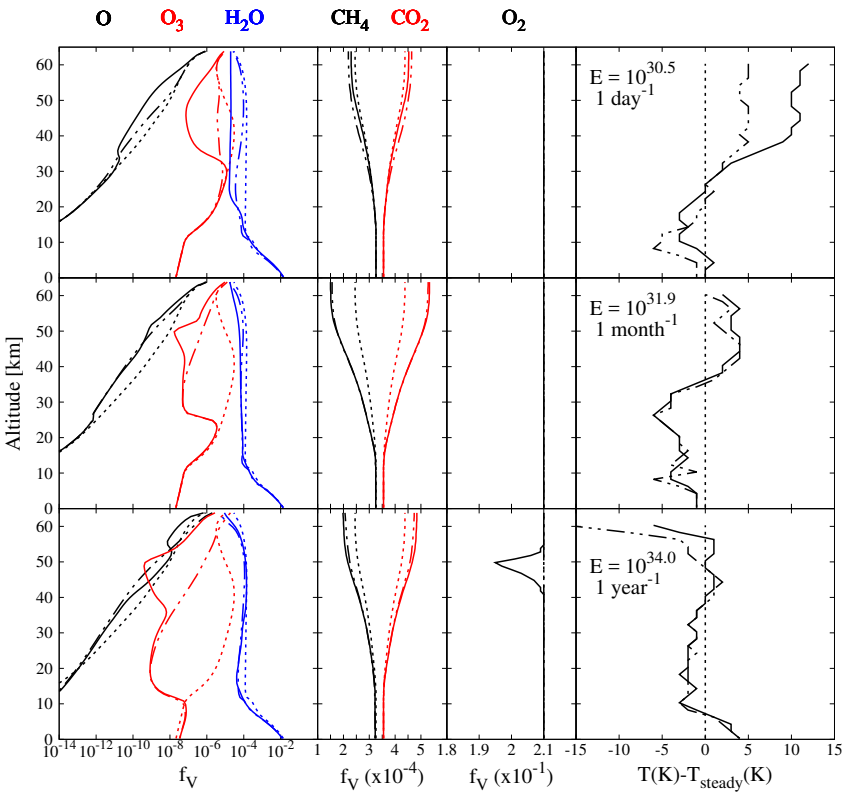

Figure 5.13 Atmospheric profiles for the three parameter studies of 100 flares of log(E) 30.5 at frequency of 1 per day (top row), 31.9 with frequency of 1 per month (middle row), and 34.0 with frequency 1 per year(bottom row). In all cases, the dashed line represents initial steady state, the dash-dotted line signifies the state at the end of the flaring (before recovery), and the solid line represents the state at peak ozone loss during recovery.

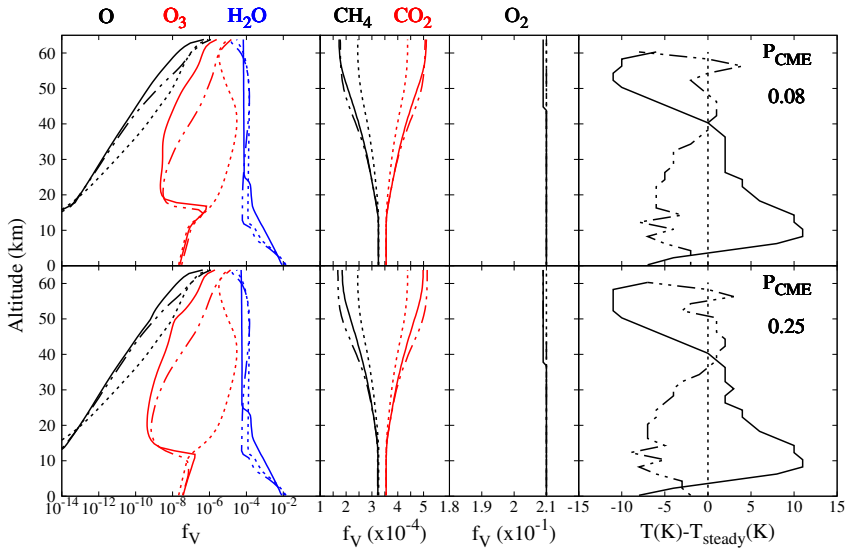

Figure 5.14 Atmospheric profiles for two 10-year periods of flare activity, generated from the GJ1243 flare frequency distribution. The top row is with a conservative CME impact probability of 0.08, and the bottom row is the more permissive probability of 0.25. In all cases, the dashed line represents initial steady state, the dash-dotted line signifies the state at the end of the flaring (before recovery), and the solid line represents the state at peak ozone loss during recovery.

One particular strong atmospheric signal pointing to biotic chemical disequilibrium on Earth is the co-existence of abundant N_2, O_2 and H_2O (Krissansen-Totton, Bergsman and Catling, 2016). In the present work, the levels of these particular species are not affected in either the 100 template flare simulations (from § 5.4.4, see Fig. 5.13) or the 10 year real-CME simulations (from § 5.4.4, see Fig. 5.14). However, it is noted that for our simulated starting point of an Earth-like planet, other species of interest that might be targeted by transmission spectroscopy can be altered significantly. For instance, the CO_2 in the upper atmosphere is notably increased by the photolysis of CH_4 driven by flaring activity, by $\geq$50 ppm at altitudes of 45 km and above, as seen in Figs. 5.13 & 5.14. Similarly, the CH_4 levels have been depleted by similar amounts. O_3 obviously experiences significant reduction, and H_2O is altered.

As the more realistic simulations in Fig. 5.14 are artificially cut off after a maximum of

10 years, we do not show the result of the anticipated millions of years of stellar activity on the atmospheric state. In the lower panels of Fig. 5.14 one can see that the O_2 levels have been slightly eroded, by ∼0.1%. While this is unlikely to produce significant alterations of spectral transit depth, continued reduction of O_2 over the periods of stellar activity exhibited by M dwarf hosts could potentially drive the signal below threshold for detection, giving a false indicator of the atmospheric state near the surface.

Our simulations indicate that a planet with an Earth-like atmosphere subjected to GJ1243 levels of flare and proton event activity is unlikely to be altered to the point of obscuring the strong N_2-O_2-H_2O chemical disequilibrium present. However, even on the short term of the present 10 year simulations, O_3 is rapidly eroded by multiple orders of magnitude, which indicates the possibility that no ozone layer may exist on such cases even if there is life producing oxygen, and there exists indication that O_2 could be further reduced by extended periods of M dwarf activity. Further work is required to explore the details of this particular consequence.

5.5.4 Other M dwarf hosts

We have focused here on M dwarf activity observed on GJ1243. M dwarf stellar activity is highly variant, however, with GJ1243 only a moderately-active star. Other active hosts, such as GJ876, display a drastically lower level of activity and anticipated total proton flux (e.g. Youngblood et al., 2017). Even with the lower levels of event-specific proton flux estimated for GJ876 (10^2 – 10^3 pfu compared to the events from 10^4 – 10^8 in the present work), one finds that the long-term stability of O_3 is reduced on a relatively quick timescale, to ∼80-90% of the equilibrium value after 40 months of flaring (see, e.g., Fig. 11 in Youngblood et al. (2017)). Extrapolating that rate of loss leads to ≥99% O_3 depletion after 10^9 – 10^{13} seconds (∼10^2 – 10^5 years), though as seen in Fig. 5.8, it is possible the atmosphere reaches a new equilibrium O_3 column.

Similarly, there are M dwarfs capable of much higher levels of activity, with very active M3-M5 stars observed displaying levels of activity from 1-2 orders of magnitude higher than what we have used in the present work (e.g., Hilton, 2011). Given the level of O_3 depletion

seen in the present work, it is likely that planets orbiting more active hosts show a more rapid, more thorough destruction of any potential O_3 layer.

5.5.5 Recently observed Earth-like planets

Recent observations have discovered potentially habitable worlds orbiting both Proxima Centauri and TRAPPIST-1, M6 and M8 stellar hosts, respectively (Anglada-Escudé, Amado, Barnes, Berdiñas, Butler, Coleman, de La Cueva, Dreizler, Endl, Giesers et al., 2016; Gillon et al., 2017). MOST observations have indicated that Proxima Centauri is highly active, with multiple flares per day at $10^{29.5}$ erg, up to a $10^{31.5}$ erg event every week (Davenport et al., 2016). This level of activity could drive significant loss of O_3 (see, e.g., middle panel of Fig. 5.8), especially given that the planet orbits at $\sim$0.0485 AU. The closer orbit increases the expected proton fluence and UV flux by an order of magnitude, compared to that in the present work — which assumes the planet orbits at 0.16 AU. Balancing this is the lower energy flare distribution, which is lower by about an order of magnitude, which by the scaling used in the present work, roughly produces similar fluences at the planet as the orbital and energy scaling cancel each other - though the UV flux would still increase from the isotropic scaling. Therefore, the estimates in Fig. 5.11 can loosely be ascribed to an Earth-like atmosphere on Proxima Centauri b, but detailed modeling is required to obtain accurate results.

TRAPPIST-1 seems to currently exhibit infrequent flaring activity by optical flux measurements. Vida et al. (2017) used K2 light curves to measure the flare activity of the star, and estimated events of order 10^{30}-10^{33} erg occur from once every few days for the lower energy events, and approximately once per 100 days on the high end of the energy range. OMalley-James and Kaltenegger (2017) showed that the surface habitability of the planets in TRAPPIST-1's habitable zone are constrained by the activity level of the star and oxic state of the atmosphere. There are currently no constraints on the biologically relevant UV flux for TRAPPIST-1, but from Lyman α chromospheric observations and the optical observations above, it is likely the star is active in that wavelength range.

If the surface habitability of these bodies, and those similar that are discovered in the

future, is to be assessed, the effect of M dwarf flaring on any present atmosphere must be explored. In the present work, we assumed the starting point of an Earth-like atmosphere, which presupposes a high O_2 content and chemical disequilibrium driven by life. However, it is likely that observed planets consist of varied compositions that will require detailed modeling based on observation from future missions such as JWST or LUVOIR.

5.5.6 Anoxic, Hazy Atmospheres

It is important to recognize that hazy layers or the relatively high population of aerosols could change these findings, as they are efficient absorbers of UV radiation. In an early-Earth type anoxic atmosphere, Arney et al. (2016) showed that the presence of haze can cut the incident UV-C radiation at the surface of the planet by a factor of $\sim$30 with a solar zenith angle of 60°. While we cannot observe the conditions of the early Earth, we do have a decent laboratory in the solar system for the formation and evolution of atmospheric hazes: Saturn's satellite Titan. It has been observed that energetic ions from Saturn's magnetosphere can drive significant changes in ionospheric upper atmospheric chemistry (e.g. Cravens et al., 2008); such activity is thought to significantly contribute to the formation of high-amu organic haze layers that can then precipitate and coalesce into tholins at the surface of the satellite (e.g. Waite et al., 2007; Lavvas et al., 2013).

Simulating the effects of stellar activity and proton chemistry on a terrestrial atmosphere after the development of photosynthesis but before the 'great oxidation event' could provide further insight into the shielding efficiency of aerosols and hazes during this early stage of the development of life, and therefore identify the amount of stress placed on an unshielded, early biosphere. Given increased activity during early solar evolution, and from M dwarfs in general, it is important to investigate how the presence of energetic proton precipitation would affect the formation and sustained chemistry of high altitude haze layers, and therefore their impact on UV-C radiation at the surface of a potentially habitable planet.

5.5.7 Unmagnetized Planet

There is uncertainty in the ability for a global magnetic field to protect against the erosion of terrestrial planetary atmospheres by a stellar wind. On one hand, the magnetized Earth has retained a relatively thick atmosphere while (mostly) unmagnetized Mars has not; on the other hand, unmagnetized Venus has a ∼93 bar atmosphere and experiences approximately twice the solar wind energy deposition per unit area as Earth due to its closer orbital distance.

Similarly, there is a question related to the present work on the ability of a planetary magnetic field to protect the atmosphere from energetic proton deposition by the stellar wind. One might naïvely assume that the lack of a global field allows the protons from the stellar wind free reign to penetrate deeply into the upper atmosphere of such a planet. However, photoionization of the upper atmosphere leads to a spherical, conducting shell (ionosphere) that deflects the magnetized stellar wind. It has been suggested that for Venus that solar wind penetration isn't expected to drive significant chemical or physical changes to the ionosphere or lower layers of the atmosphere (e.g., Gombosi et al., 1980). Interestingly, for planets without a global magnetic field that orbit close to their host stars, the increased XUV/EUV flux in the upper atmosphere are expected to produce an ionosphere of higher density and scale height, leading to deflection of the stellar wind at higher altitudes (e.g., Cohen et al., 2015). However, this expansion could lead to more rapid atmospheric erosion, which over time could reduce the strength of the ionospheric deflection. The penetration of energetic protons, like those from CME/SEP events, are still an open question for potentially habitable exoplanetary atmospheres.

For an undisturbed Earth-like geomagnetic field, protons require an energy of ≥10 GeV to penetrate directly into the subtropical to equatorial ionosphere (e.g., Rodger et al., 2006). While protons with these energies have been observed from high energy solar events, the indicate fluxes of ≥10 GeV protons are of factor ≥6 orders of magnitude lower than fluxes of protons of ∼100 MeV (e.g., Cliver and Dietrich, 2013). However, even if these particles don't penetrate completely to the upper atmosphere, they can become temporarily trapped in the geomagnetic field, and energized protons flowing within the magnetosphere are capable of

precipitation into the upper atmosphere, e.g., via pitch angle scattering.

The penetration energy requirement also declines with increasing magnetic latitude for a dipole magnetic field (e.g., Shea and Smart, 1992; Smart, Shea and Flückiger, 2000). There are open regions at the separation between open and closed magnetospheric field lines, i.e. the cusp regions, where energetic protons could flow directly from the stellar wind into the upper atmosphere. Further, it is worth noting the geometry, orientation and magnitude of a planetary field; an inclined dipole field could allow direct proton access to the upper atmosphere, and a strong quadrupole moment, for instance, has polar regions similar to the dipole field geometry of Earth, but also a circum-equatorial region with intersecting field lines where precipitation could occur.

The interactions between stellar wind, and energetic stellar outflows, are complex combinations of magnetic star-planet interactions that require further study. This begs the question of how effective magnetic fields are at deflecting (non-)relativistic proton events, shielding the planetary atmosphere. We plan to investigate and address these issues in Part 2, in an companion paper to the present work.

5.6 Concluding Remarks

- EM-only flaring for a stellar host like GJ1243 is unlikely to drive significant O_3 loss, with only ∼37% O_3 column loss by the present age of the universe for the modeled flaring activity. In contrast, the same loss can be achieved in a minimum ∼1.3 yr by weekly proton impacts from the lowest energy events simulated.

- O_3 column loss by more realistic flaring parameters from a host like GJ1243, as shown in Fig. 5.11, can drive ≥99.9% destruction of the O_3 column in as little as 0.5 Myr, with a trend of increasing loss that is unlikely to reverse.

- The impact of one ADLeo sized flare per month is sufficient to drive a loss of 99.99% of O_3 column within a ∼8 yr. In this case, the surface of a planet will experience *quiescent* UV-C flux of ∼0.18 W m^{-2}, with subsequent 10^{34} flares delivering ∼127 kJ m^{-2} of UV-C for a single event. Further experiments are needed to evaluate the

impact of these fluxes on the onset of complex organic chemistry and life.

- The model captures potential observational signatures of a flare-modified atmosphere. Mixing ratio vertical profiles change slightly for steady state conditions, particularly for CO_2 and CH_4, while activity can drive strong profile changes up to $\sim$100 ppm.

Chapter 6

CONSTRAINING THE MAGNETIC FIELD AND ATMOSPHERE OF PROXIMA CENTAURI B FROM AURORAL EMISSION

The detection of the oxygen auroral line at 5577Å would provide an important diagnostic for Proxima Centauri b's planetary properties. Its detection would not only serve as separate confirmation for discovery the planet, but would point to the presence of an atmosphere with abundant oxygen atoms, which is more likely to indicate a terrestrial body. Additionally, the detection of the line would yield a measurement of the radial velocity (RV) of the planet, which combined with the RV measurements of the star (Anglada-Escudé et al., 2016) would enable the measurement of the eccentricity and inclination of the orbit, ultimately yielding the mass of the planet (see, e.g., Lovis and Fischer, 2010). Detection of the oxygen auroral line would therefore provide several key planetary parameters that could be used to constrain Proxima Cen b's potential habitability (Barnes et al., 2016; Meadows et al., 2016).

It is possible that emission lines from other lines from gaseous species (e.g., N_2) could contribute to a detection, and the analysis that follows could be applied. Similarly, it is possible that the mass of Proxima Centauri b is sufficient to indicate a mini-Neptune instead of a terrestrial, in which case the atmosphere would be primarily H and H_2. This will be discussed briefly below.

This chapter is published as a subsection of Luger et al. (2017), and was written by the thesis author.

6.1 Overview - Auroral Signal Strength

Below, we quantitatively estimate the auroral intensity for steady-state stellar input. We assume the planet to be terrestrial with the orbital characteristics of Proxima Cen b (see Table 1) and calculate the auroral emission via two different methods. Method 1 (§6.4) involves a simple estimation of the emitted electromagnetic auroral power driven by the stellar wind power delivered at the magnetopause of the planet. Method 2 (§6.5) uses

Table 1. Proxima Centauri b properties

Property	Value†	1σ Interval
Distance from Earth (pc)	1.295	
Host spectral type	M5.5V	
Host mass, $M_\star$ ($M_\odot$)	0.120	[0.105 — 0.135]
Period, P (days)	11.186	[11.184 — 11.187]
Semi-major axis, a (AU)	0.0485	[0.0434 — 0.0526]
Minimum mass, $m_p \sin i$ ($M_\oplus$)	1.27	[1.10 — 1.46]
Radius, R_p ($R_\oplus$)	Unknown	[0.94 — 1.40]‡
Eccentricity, e	< 0.35	
Mean longitude, λ (°)	110	[102 — 118]
Inclination, i (°)	Unknown	[0 — 90]

Note. — † — Values from Anglada-Escudé et al. (2016) unless otherwise noted. ‡ — Plausible range from Brugger et al. (2016), assuming $m_p = 1.27 M_\oplus$.

the prediction of a magnetohydrodynamical (MHD) model that was tuned to calculate the auroral response at Earth, with modifications to the relevant inputs of the stellar wind of Proxima Centauri and assumed planetary parameters for Proxima Cen b (Anglada-Escudé et al., 2016).

The quantities we calculate include only the estimated, localized emissions caused by magnetospheric particle precipitation into a discrete auroral oval — not the diffuse, global phenomenon of airglow. On Earth, the 5577Å airglow can be visible to the naked eye and could be significant on Proxima Cen b, but is commonly driven by different physical processes (e.g., nightside recombination due to dayside photoionization) that are outside the scope of this analysis. Similarly, the 5577Å airglow has been observed at Venus (e.g. Slanger et al., 2001) and Mars (e.g. Seth, Haider and Oyama, 2002) — both having no present-day global magnetic field. For these reasons we cannot suggest basing the existence of or placing constraints on Proxima Cen b's planetary magnetic field based on the detection of this auroral line (see, for instance, Grießmeier, 2015). A search for radio emission from Proxima Cen b — which may be correlated with optical auroral emission, as it is on Earth and on Saturn (Kurth et al., 2005) — would likely be necessary to constrain the planetary magnetic field. However, it is worth noting that an Earth-like 1 kR (1 R = 1 Rayleigh $\equiv 10^6$ photons s^{-1} cm^{-2}) airglow across the entire planet would still emit $\sim$2 orders of magnitude less energy than the discrete polar aurora — see §6.8 below.

6.2 Stellar winds at Proxima Cen b

M dwarf mass-loss rates, and therefore stellar winds, are not well constrained due to observational sparsity and difficulty (e.g. Wood et al., 2004). To model the M dwarf winds for Proxima Centauri, we adopt the predictions from the modeling efforts of Cohen et al. (2014), who generated an MHD stellar wind model for the M3.5 star EV Lacertae based on available observations. There are two primary differences between EV Lac and Proxima Centauri that we should take into account when considering the stellar wind at our planet's location of interest: 1) the relative mass-loss rates, 2) the difference in rotation rates.

The first of these factors has been estimated by Wood et al. (2005), who find that the mass-loss per unit surface area for Proxima Centauri and EV Lacertae are quite similar.

This suggests comparable wind conditions at equal distances in units of their respective stellar radii.

The second factor, the rotation rate, affects the morphology of the stellar wind magnetic field by changing the Alfvén radius. The Alfvén radius, R_A, is defined as the point where the Alfvén Mach number is equal to unity — i.e., $M_A \equiv u_{sw}/v_A$=1, where u_{sw} is the stellar wind speed and v_A is the Alfvén speed. Interior to R_A (the sub-Alfvénic wind) the magnetic field of the star is mostly radial, and corotates at the angular rate of the star; exterior to R_A (the super-Alfvénic wind) the field begins to lag behind corotation as the magnetic tension is overcome by the flow of the wind. In the super-Alfvénic regime, the interplanetary magnetic field (IMF) exhibits the well-known Parker-spiral (Parker, 1958). The Alfvén point is an important boundary that modifies the energy transfer between the stellar wind and the planetary magnetosphere.

To correctly estimate the interactions, it is important to consider Proxima Cen b's orbital distance from its host star, for both the dynamic parameters (mass density, velocity) and the magnetic structure — i.e., we must consider where Proxima Cen b orbits relative to its Alfvén radius, R_A. We note that the rotational period of Proxima Centauri (82.6 days; Collins, Jones and Barnes, 2016) is ∼19 times slower than EV Lacertae (4.376 days; Testa, Drake and Peres, 2004). For our purposes, we estimate an average R_A for a simple stellar dipole moment:

$$R_A = \left(\frac{4\pi {\mathcal{M}_\star}^2}{\dot{M}_\star \omega_\star \mu_0} \right)^{\frac{1}{5}}, \tag{6.1}$$

where $\mathcal{M}_\star$ is the magnetic dipole moment for the star, $\dot{M}_\star$ is the mass-loss rate, $\omega_\star$ is the angular frequency of stellar rotation, and μ_0 is the vacuum permeability. For EV Lacertae and Proxima Centauri, R_A are ∼65.4 $R_\star$ (0.075 AU) and 115 $R_\star$ (0.192∼AU), respectively. This is the average value for a simple dipole moment, as we are not including magnetic topology, but nonetheless the value obtained for EV Lac agrees well with the approximate average for the more complicated magnetic treatment simulated in Cohen et al. (2014). The relative orbit for Proxima Cen b is therefore ∼0.76 R_A. Coincidentally, this corresponds well to the simulated Planet B at EV Lac in Cohen et al. (2014), which orbits at ∼0.79 R_A.

Recently, Garraffo, Drake and Cohen (2016) applied an MHD model of stellar winds

Table 2. Stellar wind conditions

Quantity	Sub-Alfvénic	Super-Alfvénic
n (cm^{-3})	433	12895
T (10^5 K)	3.42	4.77
u (km s^{-1})	(-630, -1, 30)	(-202, 102, 22)
B (nT)	(-804, 173, 63)	(-57, 223, 92)
M_A	0.73	4.76

Note. — Stellar wind conditions from Cohen et al. (2014), at EV Lacertae for a∼51.98 R$_*$ (0.073 AU). n is the stellar wind number density, T is the ion temperature, **u** is the velocity, **B** is the interplanetary magnetic field (IMF), and M_A is the Alfvén mach number.

based on the Zeeman-Doppler Imaging (ZDI) of GJ51, and scaled the magnitude of the surface field to match the anticipated value of 600 G for Proxima Centauri. Their results from the assumed magnetic environment are in line with the values we adopt from Table 1, and our value calculated for the magnetopause distance using Eq. 6.3 below is within the range of their calculations for magnetopause distance for Proxima Cen b. However, the structure of the magnetic topology in the simulation of Garraffo, Drake and Cohen (2016) places Proxima Cen b primarily in the super-Alfvénic wind, contrary to both the simple method above and the bulk of the structure found by Cohen et al. (2014).

Our estimate of R_A does not take into account the complicated magnetic topology of a realistic stellar magnetic field, which could indicate the planet likely orbits primarily through sub-Alfvénic conditions (e.g., Fig. 1 of Cohen et al., 2014) or through primarily super-Alfvénic conditions (Fig. 2 from Garraffo, Drake and Cohen, 2016). Therefore, we consider both super- and sub-Alfvénic conditions for the steady-state stellar wind, using the reported parameters at Planet B from Cohen et al. (2014); see Table 1.

6.3 Magnetic dipole moment of Proxima Cen b

Tidal locking is likely for the expected orbital parameters of Proxima Cen b and the age of the system. We therefore expect a rotational period equal to the orbital period, 11.186 days, or 8.94% of the Earth's rotational frequency. Following the magnetic moment scaling of Stevenson (1983) and Mizutani, Yamamoto and Fujimura (1992), we assume the upper limit of the rotationally-driven planetary dynamo as $\mathcal{M} \propto \omega^{1/2} r_c^3$, where $\mathcal{M}$ is the magnetic moment, ω is the rotation rate of the planet, and r_c is the core radius (which we assume to be proportional to the planetary radius). This suggests a magnetic moment for an Earth-radius Proxima Cen b of $\sim 0.3 \mathcal{M}_{\oplus}$. Taking the upper limit of the expected radius of Proxima Cen b, 1.4 $R_{\oplus}$, this gives a magnetic moment of $\sim 0.8 \mathcal{M}_{\oplus}$, which agrees with the upper limit of Zuluaga and Bustamante (2016). However, Driscoll and Barnes (2015) showed that for an Earth-like terrestrial planet orbiting a star of 0.1 $M_{\odot}$ with high initial eccentricity ($e \geq 0.1$) within 0.07 AU, the planet will circularize before 10 Gyr. On this timescale, the orbital energy dissipated as tidal heating is sufficient to drive a strong convective flow in the planetary interior that could generate a magnetic moment in the range of $\sim 0.8 - 2.0 \mathcal{M}_{\oplus}$ during the process of circularization. Given the above, we consider the situation of an Earth magnitude magnetic field for Proxima Cen b, but discuss how each of the methods below can be scaled to various magnetic dipole moments.

6.4 Stellar wind ram pressure power scaling

Desch and Kaiser (1984) suggested a correlation between incident stellar wind power and the power of planetary radio emissions in the solar system, a so-called "radiometric Bode's law." Zarka (2006, 2007) extended the work to modern solar system measurements as well as potential exoplanetary systems, and further suggested that a similar "auroral UV-magnetic Bode's law" could exist, though the author notes such scaling would be less generally applicable than the radio case across planetary systems due to the complexities of UV auroral generation for differing planetary atmospheres and magnetospheric dynamics. The calculations in this section can be thought of similarly as a "visible-kinetic Bode's law" for the specific case of exoplanets with an Earth-like atmosphere. A similar relation may also be

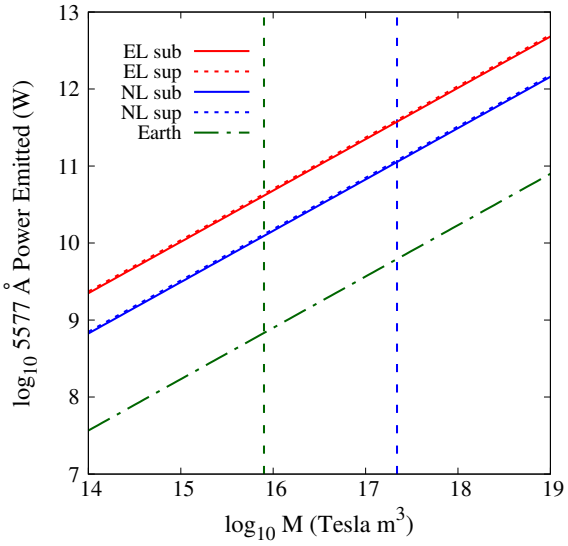

Figure 6.1 Predicted 5577Å auroral power as a function of planetary magnetic dipole moment calculated using the stellar wind scaling method from §6.4. The solid (dotted) red line corresponds to the sub-(super-) Alfvénic stellar wind conditions at Proxima Cen b. The black dash-dotted line corresponds to Earth in its natural orbit around the Sun, and the black Earth symbol corresponds to the method's calculation for Earth. The dashed vertical black line indicates an Earth-equivalent magnetic dipole moment.

derived for the magnetic stellar wind interaction (e.g., a "visible-magnetic Bode's law"; details below).

The stellar wind kinetic power delivered to the magnetosphere of the planet can be expressed as:

$$P_U = \rho\, v^3\, \pi\, R_{MP}^2, \tag{6.2}$$

where ρ and v are the stellar wind mass density and velocity relative to planetary motion ($\sim$48 km/s), respectively, and R_{MP} is the magnetopause distance along the line connecting the star and planet (sub-stellar point). The latter can be estimated through magnetospheric pressure balance with the stellar wind dynamic ram pressure (e.g. Schield, 1969):

$$\frac{2\,\mathcal{M}^2}{K_{SW}\,\mu_0\,R_{MP}^6} = p_{ram}, \tag{6.3}$$

where $\mathcal{M}$ represents the magnitude of the magnetic dipole moment, K_{SW} is related to particle reflection at the magnetopause (herein the interaction is assumed to consist of

inelastic collisions, or K_{SW}=1), and R_{MP} is the distance from the planet at which the magnetic pressure of the planet balances the pressure of the stellar wind. The RHS of Eq. 6.3 represents the dynamic ram ($p_{ram} = \rho v^2$) pressure of the stellar wind, calculated from the values in Table 1.

We consider an Earth-strength magnetic dipole moment of $\mathcal{M} = 8.0{\times}10^{15}$ Tesla m^3. Solving for R_{MP} in Eq. 6.3 and inserting into Eq. 6.2 provides an estimate of the stellar wind power incident on the planetary magnetopause. Externally-driven planetary auroral systems are not typically 100% efficient at converting the incident stellar wind power into electromagnetic auroral emission, and range from ∼0.3% at Neptune, ∼1% at Earth, and up to almost 100% at Jupiter (e.g. Cheng, 1990; Bhardwaj and Gladstone, 2000). For reference, at Earth, this method gives us a reasonable estimate of the total emitted electromagnetic auroral power of ∼30 GW for nominal solar wind conditions (4 cm^{-3}, 400 km s^{-1}), which is consistent with the anticipated power of 1-100 GW, depending on solar and magnetospheric activity. While the intensities of various emissions vary widely with activity and atmospheric conditions, we assume an averaged auroral emission. In order to estimate the emitted power of the OI 5577Å line, we assume it represents 2% of all emitted electromagnetic power (Chamberlain, 2016; Kivelson and Russell, 1995), as calculated by Eq. 6.2 We note that this assumes an Earth-like atmosphere for the planet; we briefly discuss the effect of a Neptune-like, H/H_2 dominated atmospheric composition in §6.7.

Fig. 6.1 shows the predicted emitted power of the 5577Å line based on Eq. 6.2 and multiplied by the 2% factor mentioned above and by the conversion efficiency of 1%. For the Earth, this method predicts a power of $\phi_{\pm}^{\circ}$ ∼0.68 GW in the 5577Å line. Assuming a 5° latitudinal width starting at ∼18° co-latitude and extending equatorward, this corresponds to a photon flux of ∼13.7 kR. This is in agreement with moderate auroral activity (IBC II[1], 10 kR 5577Å emission; see Table II.1 in Chamberlain, 2016), and within a factor of 2–5 of observations during moderate geomagnetic disturbance (2.5–6 kR 5577 Å emission, e.g. Steele and McEwen, 1990).

Power estimates for the 5577Å line for a 0.05 AU orbit around Proxima Centauri are

[1]IBC = International Brightness Coefficients, a standardized scale for quantifying auroral intensities (see, e.g., Hunten, 1955).

shown in Table 3. The calculated power is ∼75.3 (54.7) times $\phi_{\overset{+}{\odot}}$, in the sub-(super-) Alfvénic stellar wind. These are the estimates for a steady-state stellar wind, for a terrestrial planet with an Earth-like magnetic dipole moment. Note that by inspection of Eqs. 6.2 and 6.3, one can see that the expected power scales as $\mathcal{M}^{2/3}$, and so can easily be extended to different planetary dipole moments.

The method above has a weakness in that it completely ignores the incident Poynting flux from the IMF, and potential direct magnetic interactions between the stellar wind and planetary magnetic field, e.g. flux merging or reconnection. These interactions can produce a significant amount of magnetospheric energy input, and so they are important to consider. Similar to Eq. 6.2, a scaling relation between power emitted at the 5577 Å line and incident magnetic flux in the stellar wind, akin to a visible-magnetic Bode's law, can be given as (e.g., Zarka, 2006, 2007; Grießmeier, Zarka and Spreeuw, 2007):

$$P_B = \epsilon\, K \left(\frac{v\, B_\perp^2}{\mu_0} \right) \pi\, R_{MP}^2 \tag{6.4}$$

where ϵ is the efficiency of reconnection (typically of order 0.1–0.2), K is related to the "openness" of the magnetosphere, and for an Earth-like dipole is $K = \sin^4(\theta/2)$ where θ is the angle between the perpendicular IMF and planetary dipole field, $B_\perp$ is the perpendicular IMF ($\sqrt{B_Y^2 + B_Z^2}$), μ_0 is the vacuum permeability, and R_{MP} is the magnetopause sub-stellar point discussed above. We can estimate the magnetic interaction at Proxima Cen b using our stellar wind conditions by taking the ratio of Eqs. 6.4 and 6.2:

$$\frac{P_B}{P_U} = \frac{\epsilon\, K\, B_\perp^2}{\mu_0\, \rho\, v^2}, \tag{6.5}$$

which is essentially the ratio of the perpendicular IMF magnetic pressure to the ram pressure, modulated by magnetic field orientation and reconnection efficiency. In the best case scenario, K is equal to 1 (indicating $\theta{=}\pi$, driving strong reconnection at the magnetopause), and ϵ is of order 0.2 or so. Assuming this best case, and inserting the values from Table 1 for the sub- and super-Alfvénic cases, one obtains a ratio of ∼0.019 and 0.0084 for the sub- and super-Alfvénic cases, respectively. For the particular stellar wind parameters we have chosen, the kinetic power dominates the anticipated auroral output for Proxima Cen b. It is worth noting, however, that the magnetic environment (both planet and star) is largely unconstrained, and highly dynamic—particularly near active M dwarfs.

Table 3. Calculated 5577Å auroral power, by method

Case	Meth. 1 [TW]	Meth. 2 (quiet) [TW]	Meth. 2 (SS) [TW]	Meth. 2 (CME) [TW]	Meth. 2 (CME+SS) [TW]
Prox Cen b (Sub)	0.051	0.09	0.24	8.103	21.42
Prox Cen b (Sup)	0.038	0.049	0.14	4.41	12.10
Earth/Sun	6.7×10^{-4}	7.5×10^{-4}	1.5×10^{-3}	0.068	0.1317

Note. — Power emitted for the OI 5577Å line in terrawatts (TW) for an Earth-strength magnetic dipole on Proxima Cen b in the sub-Alfvénic (Sub) and super-Alfvénic (Sup) stellar winds. For method 2: column 2 assumes no significant stellar activity and a quiet magnetosphere; column 3 assumes geomagnetic substorm (SS) activity; column 4 assumes CME conditions in the stellar winds, but no magnetospheric disturbance; column 5 assumes both CME conditions and substorm activity.

6.5 3D MHD empirical energy coupling

Eqs. 6.2 & 6.4 above are decent first approximations, but involve significant uncertainties concerning the energy dissipation in physical phenomena throughout the magnetosphere (i.e., auroral activity) (Perreault and Akasofu, 1978; Akasofu, 1981). Wang et al. (2014) developed a global, 3D MHD model to obtain a fit for the energy coupling between the solar wind and Earth's magnetosphere to estimate the energy transferred directly from the wind into the magnetosphere and auroral precipitation (see their Eq. 13, and below). The simulations were performed over 240 iterations across their solar wind parameter space, and the resulting nonlinear fit for the energy transfer to the terrestrial magnetosphere was found to be:

$$P_{trans} = K_1\, n_{sw}^{0.24}\, v_{sw}^{1.47}\, B_T^{0.86}\, \left[\sin^{2.7}(\theta/2) + 0.25\right], \tag{6.6}$$

where $K_1 = 3.78 \times 10^7$ is a coupling constant, n_{sw} and v_{sw} are the stellar wind number density (in cm^{-3}) and velocity relative to planetary motion (in km s^{-1}), respectively, B_T is the magnitude of the transverse component of the Sun's IMF ($B_T = \sqrt{B_X^2 + B_Y^2}$) in nT,

and θ is the so-called IMF clock angle ($\tan\theta = B_Y/B_Z$). The coordinate system used is the geocentric solar magnetospheric (GSM) system, with $\hat{X}$ pointing from the planet to the star, $\hat{Z}$ aligned with the magnetic dipole axis of the planet (here assumed to be perpendicular to the ecliptic), and $\hat{Y}$ completing a right-handed coordinate system.

Wang et al. (2014) were focused solely on the Earth's magnetosphere, but one can scale to any dipole moment by noting that Eq. 6.6 scales just as in §6.4: the dipole moment term is implicitly included in the coupling constant K_1 above and scales with the planetary magnetic dipole magnitude as $\mathcal{M}_P^{2/3}$ (Vasyliunas et al., 1982, also Eqs. 6.2 & 6.3 above).

Eq. 6.6 is the total power delivered by the stellar wind to the magnetosphere, which Wang et al. (2014) estimate is ∼13% of the total incident stellar wind energy. They further estimate that 12% of that energy is dissipated by particle precipitation into the auroral regions, yielding a total solar wind/auroral coupling efficiency of ∼1.56% – very similar to the efficiency value of 1% assumed for Earth and Proxima Cen b in §6.4. As simple validation for our purposes, we use this method to predict a maximum coupling of auroral particle precipitation (with IMF clock angle $\theta = \pi$, driving reconnection and likely substorm activity) at Earth of ∼0.17 TW. This is in agreement with terrestrial plasma observations during periods of geomagnetic disturbance (e.g. Hubert et al., 2002). This method is useful in that it provides a direct relationship between the power delivered as auroral particle precipitation and incident stellar wind conditions.

For Proxima Cen b subjected to the stellar winds from Table 1, this method predicts a total power of auroral particle precipitation of ∼10.7 (5.8) TW for the sub-(super-)Alfvénic stellar wind. The stellar wind parameters in Table 1, however, are a snapshot and not indicative of the highly variable conditions likely experienced at Proxima Cen b.

Magnetospheric substorms, related to transient populations of energized particles driven by magnetic reconnection in the magnetotail, can drive strong increases in auroral particle precipitation. Though not a one-to-one indicator, substorm activity can be associated with periods of strong reconnection at the magnetopause—correlated with a significant negative B_Z component in the IMF. In the present work, we assume θ=π, or B_Y=0, to obtain an upper limit to substorm influence under our model. Although this is not a strict definition, Wang et al. (2014) calibrated the model used here to include periods of substorm activity

and high hemispheric energy input. Assuming with this strong negative B_Z that a substorm is driven at Proxima Cen b, we predict an energy input of ∼28.3 (15.9) TW for the sub-(super-)Alfvénic wind. To compare directly to the 5577Å line auroral power output such as that calculated in §6.4, we must link these values to the aurora by including the efficiency of precipitating charged particles in the production of auroral emission for the 5577Å line, which will be done below.

To calculate the auroral 5577Å photon flux, we use the precipitating auroral particle powers above obtained from Eq. 6.6, and combine with the anticipated size of the auroral oval and an observed conversion efficiency for electron precipitation to 5577Å emission. This gives the photon flux in kR, ϕ_{5577}:

$$\phi_{5577} = P_{in}\, A_{mag}^{-1}\, \epsilon_e, \tag{6.7}$$

where P_{in} is 12% (discussed above) of P_{trans} from Eq. 6.6, A_{mag} is the summed area of both the northern and southern auroral ovals (we assume N-S symmetry), and ϵ_e is the efficiency with which magnetospheric electrons are converted to auroral emission of the 5577Å oxygen line. We use the reported values from Steele and McEwen (1990) (noted below), who used ground-based observations of auroral line intensities and the related satellite observations of energetic electron flux to draw a relation between electron precipitation and auroral photon flux. We then integrate the resulting flux over a nominal 5° auroral oval (for each hemisphere), the colatitude of which is dependent on the sub-stellar magnetopause distance (discussed below).

It should be noted that proton-driven aurora (separately categorized events) are highly correlated with 5577Å flux as well. Indeed, the precise aeronomy of the 5577Å emission (and others) is still a subject of much study (e.g. Solomon, 1991; Omholt, 2012, and references therein).

Steele and McEwen (1990) reported the conversion efficiency for the 5577Å OI line as 1.73±0.51 (1.23±0.44) kR/(erg cm^{-2} s^{-1}) for a magnetospheric Maxwellian electron population of characteristic temperature 1.8 (3.1) keV. In the present work, we take the average values for these populations, ∼1.48 kR/(erg cm^{-2} s^{-1}). We assume the fraction of

total hemispheric power (P_{in}) delivered by electrons to be 0.8 (Hubert et al., 2002), so this factor is included in the P_{in} factor.

The magnetopause distance we calculate via Eq. 6.3 for the Earth-like magnetic dipole moment is ∼4.2 (3.3) R_P for the (sub-)super-Alfvénic conditions. From these values, we can provide a simple estimate of the total auroral oval coverage. The magnetic co-latitude of the boundary between open and closed flux for our assumed ideal planetary dipole geometry (i.e., the co-latitude where the field structure no longer intersects the planetary surface) is $\sin^{-1}(1/\sqrt{R_{MP}})$ (Kivelson and Russell, 1995). Discrete auroral activity occurs primarily due to energized plasma originating from closed field structure stretched out behind the planet in the stellar wind, i.e., the magnetotail. This field structure intersects the planet equatorward of the open/closed boundary co-latitude. If we assume a nominal 5° auroral oval width beginning at the co-latitude obtained, and extending equatorward, we calculate a single-hemisphere coverage of $\sim 1.17\times10^{17}$ cm^2 for the auroral oval under sub-Alfvénic conditions, and $\sim 1.30\times10^{17}$ cm^2 under super-Alfvénic conditions.

Following the above, we obtain a photon flux value of ϕ_{5577} ∼2.26 (1.16) MR for the sub-(super-)Alfvénic wind conditions. This corresponds to our predicted emission power in Table 3, method 2 (quiet) of ∼0.090 (0.049) TW under steady-state sub-(super-)Alfvénic conditions. For the maximum emission during a magnetospheric substorm, we obtain values of ∼0.24 (0.14) TW for sub-(super-)Alfvénic winds.

There is another case of interactions that we should consider that involves stellar activity — flaring and coronal mass ejections (CME). During these events, stellar wind densities could increase by a factor of ∼10, velocities by a factor of ∼3, and IMF magnitude by a factor of $\sim 10 - 20$ (Khodachenko et al., 2007; Gopalswamy et al., 2009). Inserting such ratios in the 3D MHD-fit predicted power in from Eq. 6.6, we predict transient maximum 5577Å emissions of ∼8.10 (4.40) TW for the sub-(super-)Alfvénic CME conditions. For the maximum emission during a magnetospheric substorm under CME conditions, we obtain values of ∼21.42 (12.10) TW for sub-(super-)Alfvénic winds. These transient CME conditions can have timescales of $\sim 10 - 10^3$ minutes per event, with multiple, consecutive events possible. Given that Davenport et al. (2016) report such high stellar activity for Proxima Centauri, Proxima Cen b could experience CME impacts for a large percentage of its orbital

phase (e.g., Khodachenko et al., 2007).

6.6 Unmagnetized planet

The above results all assume a large, Earth-like planetary magnetic dipole moment for Proxima Cen b. If, in fact, the planet does not sustain a global dynamo, it will only be protected by a relatively thin spherical shell (∼1000 km) of plasma in the upper atmosphere - similar to Earth's ionosphere.

For the sub-Alfvénic case, the interaction is a unipolar interaction similar to the Jupiter-Io interaction (Zarka, 2007). In this case, the power dissipated by the wind is similar to the form of Eq. 6.4, where ϵ and K are replaced by a single parameter indicating the fraction of magnetic flux convected onto the "obstacle" (the ionosphere), and R_{MP} becomes the size of the "obstacle" — for an Earth-like ionosphere, ∼1.16 planetary radii. While there is no dipolar focusing mechanism for the particle precipitation in this case, it is worth considering the energized particles flowing on the flux tube connecting the unmagnetized planet with the star, producing maxima on the unmagnetized body in the plane perpendicular to the IMF (see, e.g., Saur et al., 2000, 2004).

Assuming 100% of incident magnetic energy flux is convected onto the planet and ionosphere, the expected 5577Å auroral power becomes 5.9×10^{-4} TW for the sub-Alfvénic stellar wind conditions in Table 1. This interaction is likely insignificant in the context of remote sensing.

For the super-Alfvénic flow, this could be considered as analogous to Venus' situation, which sustains no global magnetic field. In this case, the discrete aurora would obviously not be expected due to a lack of magnetic structure, though induced airglow is still a consideration. Lacking a planetary magnetosphere, the magnetic structure fails to focus precipitating particles into the upper atmosphere of such a planet, though there is still magnetic interaction at the planet. The ionosphere is a spherical, conducting shell, and so interacts with the magnetic flux from the IMF as it drapes over and around the planet. Energized particles in the impacting stellar wind magnetic flux could still dip down into the upper atmosphere, depositing sufficient energy to produce airglow - this is especially true for the strong flows from CME activity, or fast stellar wind flow.

A study of the intensity of 5577Å oxygen emission at Venus, relative to Earth, for CME/flare events from the Sun was performed by Gray et al. (2014). The results indicated that the airglow was relatively on par with that of Earth's upper atmosphere, varying between 10 and a few hundred Rayleigh, which, if integrated over an entire hemisphere of an Earth-like planet, gives a value less than 1% of the discrete values given in Table 3. For the super-Alfvénic flow in Table 1, the number density is ∼1500 times greater than the average at Venus, and the velocity is a factor of ∼0.5 that at Venus or Earth. Given the power scales as $\rho\, v^3$, this is a factor of ∼200 greater power delivered to the planet. Assuming that airglow at an unmagnetized Proxima Cen b scales linearly with the incident power, this would give a brightness of ∼2-60 kR, which is at most a factor of ∼5 times the value for Earth using Method 1 and 2 in Table 3, or on the order of 10^{-3} TW. It is not likely this signal could be detected with either current or upcoming missions, further discussion can be found in the published version of this work (Luger et al., 2017).

6.7 Super-Earth or Neptune-like Planet

Alternatively, Proxima Cen b could be terrestrial but be significantly larger than the Earth, with mass as high as $\sim 4 M_\oplus$ and radius $\sim 1.5 R_\oplus$. Since the scaling methods used in §6.1 implicitly assume Proxima Centauri b is similar to Earth in size, the auroral strength could be different than the above estimate. It should be noted, however, a super-Earth doesn't necessarily imply a stronger magnetic dipole moment, as dynamo-generating convective thermal evolution is not well understood, and the presence of water is likely required to drive plate tectonics for large terrestrial bodies (e.g. Foley, Bercovici and Landuyt, 2012; Miyagoshi et al., 2013; Korenaga, 2016).

For the purpose of discussion, we assume a global magnetic field at a super-Earth terrestrial planet. A larger planetary radius (and therefore dynamo-generating core radius) could result in a stronger magnetic dipole, increasing the magnetospheric cross-section to the stellar wind, leading to an increase in the emitted power. Furthermore, assuming an Earth-like atmospheric composition, the higher surface gravity would decrease the ionospheric scale height, which could lead to larger magnetic field parallel potential drops in auroral acceleration regions. This would increase the upward flowing current and therefore

the downward accelerated electron beams into the upper atmosphere, which could also enhance the auroral signal. Moreover, an increased atmospheric density at the depth where precipitating electrons deposit their energy could also change recombination rates and alter the energy level distribution of the O atoms, which would in turn affect the auroral strength in different lines. A quantitative estimate of these effects is beyond the scope of this discussion, as it would require both modeling the changes to the atmospheric structure and solving the Boltzmann kinetic transport equation. Future work is planned to investigate these effects.

If Proxima Cen b is, instead, a planet of Neptune mass and radius on a close to face-on orbit, it will have an upper atmosphere dominated by en envelope of H/H_2. Therefore the above calculations for O_2 scaling are not applicable, and we should consider FUV emission in lieu of the OI line. Voyager UV observations reported by Sandel et al. (1990) estimated the localized FUV (967-1115 Å) auroral photon flux as ∼5 R. Mauk, Krimigis and Acua (1994) found that the electron flux to drive the observed UV aurora at Neptune was $\sim 10^{-3}$ erg cm^{-2} s^{-2}. Therefore we infer a conversion efficiency for Neptune's aurora in the 967-1115 Å bandpass to be ∼5 kR/(erg cm^{-2} s^{-1}), corresponding to ∼9.9%. This gives us a scaled FUV photon flux of ∼3.84 (2.13) MR for the sub-(super-) Alfvénic stellar wind conditions for the Neptune size Proxima Cen b, or 14.88 (8.1) TW over the 967-1115 Å band (assuming the average photon energy at 1041 Å, the center of the band). While this is significantly stronger than the OI emission of an Earth-like planet, it may be harder to detect given both the width of this band and the fact that if Proxima Cen b is Neptune-like, its orbital inclination must be $\lesssim 5°$, making deconvolution from stellar lines (from a highly active star) more difficult (see Luger et al. (2017)). Note that Neptune's magnetic field is highly inclined, rotationally offset, and relatively complex with significant quadrupole/octupole moments that have similar or higher magnitude than the dipole moment; in the present work, we have assumed a simple, untilted dipole field, with a magnetic moment equal to that reported by Voyager 1 observations (e.g. Connerney, Acua and Ness, 1991; Mauk and Bagenal, 2012).

6.8 Signal Summary

The preceding estimates are mostly conservative. It is possible that all the auroral numbers reported for the sub-Alfvénic cases above could be a factor of 4–5 (or more) larger. We are assuming a simple dipolar interaction with the stellar wind, which isn't specifically the case for a planetary dipole in the sub-Alfvénic stellar wind; these interactions are more akin to the interactions of Ganymede and Io with the corotating magnetosphere of Jupiter, with the formation of Alfvén wings. Modeling efforts by Preusse et al. (2007) showed that for a giant planet with a dipole magnetic moment, field-aligned currents (which are associated with auroral activity) are significantly stronger for planets orbiting inside the Alfvén radius of their stellar host. Our estimates, therefore, could be viewed as lower limits. It is also worth noting that Cohen et al. (2014) suggested that a transition between the sub- and super-Alfvénic conditions would likely produce enhanced magnetospheric activity and therefore could lead to a periodicity in the auroral activity depending on combined planetary orbital and stellar rotational phases.

For planets in the solar system, only Mars and Earth exhibit observed, significant 5577Å emission for both diffuse airglow and discrete aurora. Mars does not presently have a global magnetic field, but there are crustal regions containing the remnants of previous magnetization that exist and focus particles into the upper atmosphere to produce a relatively weak (inferred ∼30 R at 5577Å) discrete aurora that is ∼10 times the strength of the nominal airglow (e.g. Acuña et al., 2001; Bertaux et al., 2005; Lilensten et al., 2015). On Earth, the airglow and aurora are typically in the range 0.01–1 kR and 1–1000 kR, respectively. During transient periods of minimal auroral activity and maximum airglow emission, emissions can be roughly equivalent, but the average ratio of airglow emission to auroral emission is ≤1% (e.g. Chamberlain, 2016; Greer et al., 1986). Even for a constant, planet-wide 1 kR airglow on an Earth-sized planet at Proxima Cen b (R_P ∼6371 km), the total signal from the observer-facing hemisphere would be ∼4.54×10^8W, which is ∼1% of the lowest signal from Table 3 and would not be detectable.

Nevertheless, it is important to note that the FUV flux from Proxima Centauri is nearly two orders of magnitude higher than that of the Sun (Meadows et al., 2016). Airglow

stemming from recombination of photodissociated O_2 and CO_2 could thus be significantly stronger on Proxima Cen b than on Earth. Barthelemy and Cessateur (2014) stress the importance of stellar UV/FUV emissions on the production of UV and visible aurorae, and note that, e.g., Lyman-α flux can contribute up to 25% to the production of the O(^1D) red-line. However, even if Proxima Cen b had a sustained 100 kR airglow—one hundred times the maximum Earth airglow—its emission would be comparable to the lowest estimate of auroral emission in Table 3, which is still unlikely to be detectable (see Luger et al. (2017)). We therefore ignore this potential contribution in the present work, noting that a detailed photochemical treatment would be required to pin down the expected airglow emission at Proxima Cen b.

In summary, we predict a steady-state auroral emission at 5577Å from Proxima Cen b that is of order 100 times stronger than seen on Earth for a quiet magnetosphere, corresponding to an emitted auroral power for the OI line on the order of ∼0.090 (0.049) TW for the sub-(super-)Alfvénic winds using method 2 (§6.5). We believe that this method yields more realistic results than the purely kinetic power estimate in method 1 (§6.4), due to the inclusion of magnetic interactions in method 2 - though the magnitudes are similar to within a factor of 2. Assuming Proxima Cen b is an Earth-like terrestrial planet, our maximum transient power estimate for the 5577Å line for CME conditions that drive a magnetospheric substorm is ∼21.42∼TW, or ∼30,000 times stronger than on Earth under nominal solar wind conditions. The actual values for Proxima Cen b will naturally change based on planetary parameters (e.g., magnetic dipole moment, magnetospheric particle energy distributions, substorm onset, atmospheric Joule heating) and stellar activity. By our analysis, a $\sim 10^3$ (or higher) enhancement compared to Earth as suggested by OMalley-James and Kaltenegger (2016) is only possible due to one or more of the following: transient magnetospheric conditions driven by either CME or substorm activity, a magnetic dipole significantly stronger than Earth's, or higher stellar mass-loss than predicted (Wood et al., 2005; Cohen et al., 2014).

6.8.1 Auroral Radio Characterization

I consider here non-thermal radio emission as a means to characterize the magnetic environment of Proxima Centauri b as it could indicate the presence of a planetary magnetic field, assuming the signal is separable from stellar radio emissions. Electron cyclotron maser instability (ECMI) is the most significant contributor to planetary non-thermal radio emission throughout the solar system. Assuming an equatorial magnetic dipole of strength 1-3$\times 10^{-5}$ T (approximately one-third to one times of the dipole moment of Earth), as given, e.g., by Driscoll and Barnes (2015); Zuluaga and Bustamante (2016), we can consider the frequency of emission for ECMI-produced radio at high latitudes (auroral regions), and at a distance of few planetary radii (e.g., Zarka, 1998).

Given the assumed compression of the magnetosphere as reported in Garraffo, Drake and Cohen (2016), one might expect a strong forcing that could drive very bright radio emission for the star-planet system. However, the magnetospheric geometry of an Earth-like magnetosphere driven by such stellar winds would necessitate that ECMI-driven radio emission could still occur at distances comparable to Earth; here we follow Zarka (1998) for emission distances of 1.3-4 planetary radii. The magnitude of a dipole planetary field scales as $1/\mathrm{R}^3$, which would reduce the B-field magnitude by a factor of 2.2-64 from the equatorial value; however the dipole field also increases with latitude as $\sqrt{1+3\sin^2(\theta)}$, by a maximum factor of two at the magnetic poles. For typical radio auroral latitudes at Earth (60-80 degrees), the field strength increase of factor $\sim$1.91 at 70° latitude would partially offset the radial distance reduction. Note that due to the geometric compression of the field, auroral regions might be farther equatorward (lowering the factor 1.91 above). Earth's emission peaks at $\sim$250kHz (e.g., at $\sim$1.88 R_P and 70° latitude), and extends to $\sim$800 kHz (e.g., at $\sim$1.3 R_P and 70°). The magnetic dipole moment of Proxima Centauri b is unconstrained, however, and could the emission could shift to lower or higher frequencies, and different locations in the magnetosphere depending on the balance with the stellar wind and overall dynamics.

For these frequencies, the power emitted does not matter if the radiation cannot escape, even if driven by a stronger stellar wind/IMF from the host star. Here, there are three

issues for near-Earth, space-based detection of radio emission from Proxima Centauri b:

1. Given the high EUV/XUV flux and activity of Proxima Centauri b (and most M dwarfs) (e.g., Davenport et al., 2016), the ionosphere of an Earth-like planet could be both radially extended from the upper atmospheric heating from the constant stellar activity, and have high plasma density from increased rates of ionization. Detailed modeling is required to determine the limits, but this could effectively lock higher frequency emissions in the upper ionosphere; i.e., if the density is ∼8000 cm^{-3}, the electron plasma frequency is ∼800 kHz, leading to absorption of all frequencies equal and below that level. For lower ionospheric densities, and throughout the planetary magnetosphere, there remains the question of attenuation if they do happen to escape. This is a similar situation to the results found for Mercury by Varela et al. (2016).

2. Next, we have to consider the stellar wind and astrosphere. The stellar wind density values from Garraffo, Drake and Cohen (2016) gives a lower end estimate for an average stellar wind density of 1000 cm^{-3} at the orbit of Proxima Centauri b - ∼0.16 AU. The electron plasma frequency of oscillation for that density is ∼0.285 MHz. While variable with the stellar activity, this could effectively block the lower end - and potentially the peak - of the spectrum, while providing strong dispersion throughout the astrosphere which has extent of ∼50 AU (Wood, 2004).

3. Lastly, as stressed in Burkhart and Loeb (2017) one should consider the contributions from the local interstellar material (LISM) between the Proxima Centauri system and the solar system. Observations and modeling have suggested that LISM electron density is 0.1-0.3 cm^{-3}, with temperatures 7000-9500 K (e.g., Wood and Linsky, 1997). Free-free absorption scales as (e.g., Rybicki and Lightman, 2008):

$$k_{ff} = 0.018\, T^{-1.5}\, \nu^{-2}\, n^2\, cm^{-1} \tag{6.8}$$

where T is the temperature of the LISM electrons, ν is the frequency of propagating radiation, and n is the LISM electron density. Fig. 6.2 shows the optical depth as a

function of LISM electron density for propagating radio emission for 50, 100, and 300 kHz for both 7000 and 9000 K LISM electrons. It looks as though there will be some attenuation of any emitted power for most frequencies, and absorption is likely for lower frequencies. Including attenuation from Proxima Centauri b's magnetosphere, ProxCen's astrosphere, and the heliosphere - any signal reaching Earth would be reduced significantly.

Given the compression of the magnetic field to ∼2.5 planetary radii at Proxima Centauri b (as shown in Garraffo et al. 2016), the regions of auroral emission would likely occur at lower latitudes, as the separation between open and closed field lines would be located at a latitude of ∼50 degrees. This would reduce the latitudinal scaling factor given above by about 10% to ∼1.66, further decreasing the emitted radio frequencies. The compression also brings up a further issue of directionality. The emission geometry at Earth is highly localized into a two-lobe, narrow beam, so the orbital characteristics must be aligned just right with respect to observational line of sight. If, instead, the beaming has larger geometry, such as the hollow-cone emission like Saturn or Jupiter, then there is a higher probability that reasonable fraction of power could be emitted towards Earth (see, e.g., Fig. 3.5 in § 3.9).

A stronger planetary field could be considered, up to a value of 1 G or three times an Earth-magnitude dipole. The probability of such a field strength is questionable given the likely tidally locked nature of Proxima Centauri b, though a generation of such dipole strength might occur, but is likely to be transient over the evolution of the system (e.g., Driscoll and Barnes, 2015).

6.9 Concluding Remarks

The concept of detecting auroral signatures from Proxima Centauri b is enticing, as such observations could offer planetary characterization unobtainable by other means, and would offer constraints on and verification of more traditional observational techniques (e.g., radial velocity, transit spectroscopy). For an Earth-like atmosphere, future instrumentation such as LUVIOR and the Thirty Meter Telescope could see the predicted 5577 Å auroral emission within a matter of days. Radio, however, is less likely due to free-free absorption in the plane-

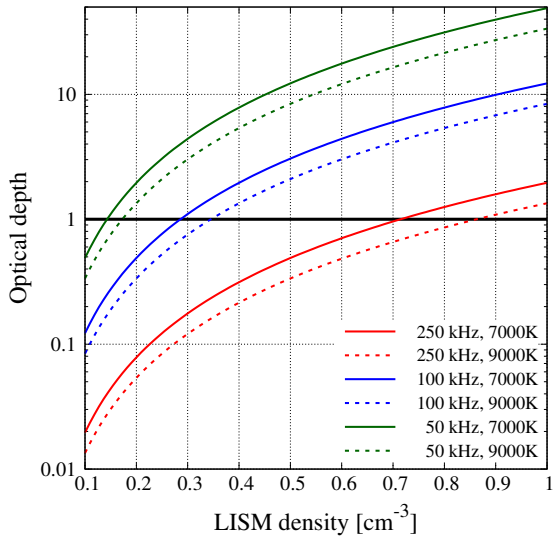

Figure 6.2 Optical depth of radio emission by the interstellar medium as function of LISM density.

tary magnetosphere, the stellar host's astrosphere, and LISM material between the Proxima Centauri system and our own. The problem is complex, and more detailed simulations in the realms of stellar activity, atmospheric photochemistry, ionosphere-magnetospheric coupling, and planetary interiors must be employed.

Chapter 7

SUMMARY AND FUTURE WORK

7.1 Summary of Major Findings

The goal of this dissertation was to explore the dynamics and effects of the presence or absence of a planetary magnetic field on potentially habitable environments, both planetary and natural satellites (moons), and to model the effect of plasma pressure anisotropy at Saturn. The findings suggest that a present magnetic field can bring potential detection signatures, and provide a shield from stellar wind as well as an input source of energized magnetospheric particles for potentially habitable exomoons. The absence of such a field can be detrimental to the development of organic complexity on the surface of a terrestrial planet orbiting an active M dwarf due to the lack of deflection of energized protons from stellar flare events. Below is a brief summary of each chapter, followed by some directions planned for future work.

7.1.1 Exogiant response to increased stellar wind forcing

Chapter 3 showed that increased stellar forcing has dramatic effect on an exo-Saturn like planet. The planet was simulated from 10 to 0.2 AU from a G dwarf, Sun-like star. The interchange instability for the system, which is the primary means of mass loss at Saturn and Jupiter, was shown to be inhibited by the compression of the magnetosphere. Field aligned currents were shown to be dramatically increased in intensity as well as latitudinal coverage, which implies a much stronger radio signal with broader celestial projection from such a forced exoplanet. Combined with the compression of the magnetosphere, hollow cone type radio emissions likely will be focused towards the polar regions of the celestial sphere around the planet. Also, it was shown that even at 0.2 AU, the plasma density at the bow shock could be sufficient to generate transit depth modifications in the UV. More importantly, a moon-generated plasma torus was shown to be a potentially stronger effect

which should be explored in more detail.

7.1.2 Effects of plasma pressure anisotropy at Saturn

In Chapter 4, I explored the effects of plasma pressure anisotropy at Saturn using an improved version of the multifluid plasma model. The model captured the perpendicular plasma pressure anisotropy from the orbit of Enceladus out to the magnetopause, as was seen (at least on the dayside) by Cassini. The presence of anisotropic plasma, in this case strongly perpendicular, confined plasma to the equatorial plane, which produced a stronger centrifugal body force on the system. Combined with pressure gradients and increased curvature effects driven by anisotropy, the overall force balance of the magnetodisc was shown to require a higher azimuthal equatorial current to balance the outflow forces on the plasma. The interchange instability was also shown to be influenced by the presence of pressure anisotropy in the equatorial plane, with the more consistent well-defined injection/outflow signatures observed by Cassini throughout the magnetosphere; in particular, in the nightside where the isotropic model failed to capture such structures, while the anisotropic model showed the alternating pattern of dense, cool outflowing plasma and tenuous, hot inflowing plasma. Overall mass flow at the planet was shown to be more consistent with Cassini observation, with corotation enforcement in the nightside tail region suppressed in the anisotropic model by strong parallel anisotropy in the lobe regions of the magnetosphere - which cause a less efficient communication with the planetary ionosphere by inhibiting the Alfvén speed, and therefore the field-aligned currents, in the lobe regions. Scale heights in the plasma sheet also agreed with Cassini data more closely, with the anisotropic model capturing more realistic values with its ability to capture parallel temperatures in the equatorial plane. Preliminary work looks as though the overall magnetic structure and dynamics, as well as the corotational and field-aligned current systems are also impacted.

All of these observations in the dynamic and structural differences in Saturn's magnetosphere are due to the increased physics captured in the model. This implies that the inclusion of pressure anisotropy into the multifluid model provides a more accurate rep-

resentation of the magnetospheric environment, which is pivotal if the realistic inputs to (exo)moon atmospheres and surface conditions are to be simulated.

7.1.3 Atmospheric effects of repeated M dwarf flaring on unmagnetized, Earth-like planet

Moving to a terrestrial planetary system, Chapter 5 discussed the effects of M dwarf flaring on the atmosphere of an Earth-like planet orbiting in the nominal habitable zone. The work explored the effects of both EM-only (e.g., x-ray, UV) radiation on the atmospheric chemistry, as well as the inclusion of EM + particle radiation, in the form of NO_x produced by the precipitation energetic protons from stellar events. It was shown that EM-only flaring has a weak effect on the evolution of the protective O_3 column of the planet, with a projected value of 15-20% of the equilibrium column surviving after ∼15 Gyr. Repeated EM + proton events, however, were highly detrimental - with O_3 column loss by 99.9% after only ∼0.5 Myr in the worse case, with a downward trend continuing. Though not yet observed in nature, an extremely active star producing one AD Leo great flare event with energized protons per month could reduce the O_3 column by 4 orders of magnitude within a decade. With such low values of O_3, the surface conditions of the planet are no longer the stable and clement environment required for the long term development of organic complexity. The UV-C flux can reach up to 0.18 W m^{-2} during quiescent times, with the AD Leo large flares bathing the surface of such a planet in 127 kJ m^{-2} over a single ∼3 hour event - these values are germicidal, sufficiently equivalent to lamps used in laboratories worldwide. Life and organic complexity can likely still form under the cover of an H_2O ocean, however, as any amount of UV-C is attenuated by ∼9 m depth.

These results require the investigation of how well a magnetized planet could actually deflect such incoming proton events from such an active star, with stellar winds that compress the planetary magnetosphere to ∼10% the size of the Earth's. The polar cap regions in such a compressed magnetosphere are also more open, potentially allowing the precipitation of more energized particles as well. Future work is planned along these lines.

7.1.4 Detecting auroral signals at Proxima Centauri b

Chapter 6 explores the possibility for characterization of terrestrial planets via their auroral signals, in particular for the example of Proxima Centauri b. The atomic O 5577 Åauroral line would be a strong signal that constrains the presence of an oxygen bearing atmosphere on the planet, though it could be a poor predictor of the presence of a magnetic field since a strong photochemical airglow could ostensibly produce a comparable signal, though not one as sensitive to the stellar wind of the host. It was shown that the signal for an Earth-like Proxima Centauri b would likely produce a signal 2 - 4 orders of magnitude brighter than that produce at Earth under moderately active conditions. While this signal is not observable with today's instrumentation, observational platforms coming online in the near future could detect such a signal in a matter of hours of integrated observational time. Radio emission from the planet was also considered, but even at the relatively close distance between Earth and our nearest planetary neighbor, there are several obstacles to overcome. A space-based observational platform is required due to the low frequency of the emissions and presence of Earth's ionosphere. Similarly, both the dense astrosphere of Proxima Centauri and the amount of free-free scattering in the LISM could prove problematic, and could significantly attenuate the signal before reaching Earth. However, if the signal can make it through such a difficult medium, the coherence and stability of such a signal (along with reactions to stellar activity) would directly confirm the presence of a magnetic field on the planet which would be extraordinary.

There is much work to be performed, still, to answer questions regarding magnetic fields and the habitability and detection of extrasolar planets. Such a dynamic, complex system - the propagation of EM and particle radiation from the surface of stars, through the magnetic medium to the atmospheres and surfaces of planets - is one for which it proves extremely difficult to develop a global predictive capability. There is much to be learned and developed, still, if we are to answer the question: Does a magnetic field matter for habitability?

7.2 Directions for Future Work

7.2.1 Plasma Tori: Exomoon Detectability and Characterization

To date, using direct detection of exomoons using Kepler/K2 via transit signals, there has been only one reported exomoon candidate discovery (Teachey, Kipping and Schmitt, 2017), despite a large amount of effort (e.g., Kipping, 2009; Kipping, Fossey and Campanella, 2009; Kipping et al., 2013; Heller, 2014; Hippke, 2015). Planetary disk models have replicated solar system satellite formation for Saturn and Jupiter, and the findings suggest that in situ formation of massive satellites ($\sim$1 $M_{\male}$) orbiting extrasolar gas giants can generally form from the circumplanetary disk at orbital distances amenable to likely detection through the transit method (e.g., Canup and Ward, 2006; Sasaki, Stewart and Ida, 2010). Similarly, the capture of exomoons by gas giant exoplanets is also a potential pathway for observable satellites (Williams, 2013). Orbital stability must also be a consideration for an exomoon around a warm or hot planet, but extant satellites are still possible (Barnes and Obrien, 2002; Sasaki, Barnes and O'Brien, 2012).

Given that a massive satellite approximately the size of Mars can potentially form or be captured around planets with orbital distances at which transit methods are sensitive, it is probable that such a moon could be directly detectable in a future transit mission. Earth-sized moons can potentially be teased out from the Kepler data using clever analysis (e.g., Heller, 2014; Hippke, 2015). Smaller bodies, however, are likely to be more numerous yet not resolved directly by transit.

It is likely that many extrasolar planets have natural satellites, and that some of these bodies could be habitable. These worlds will prove quite difficult to detect and characterize with current methods. Tidal interactions and other internally driven processes, however, can drive the generation of a relatively optically thin torus of material over a large area in a planetary magnetosphere to drive the indirect detection of an exomoon presence (e.g., Ben-Jaffel and Ballester, 2014).

In Fig. 7.1 (A), one can see an orbital sampling effect (OSE) that would offer a transit signature over multiple observations, with high sufficiently precise instrumentation. In the lower panel, (B), the figure shows the column depth of $q/m = 16$ ions generated by an

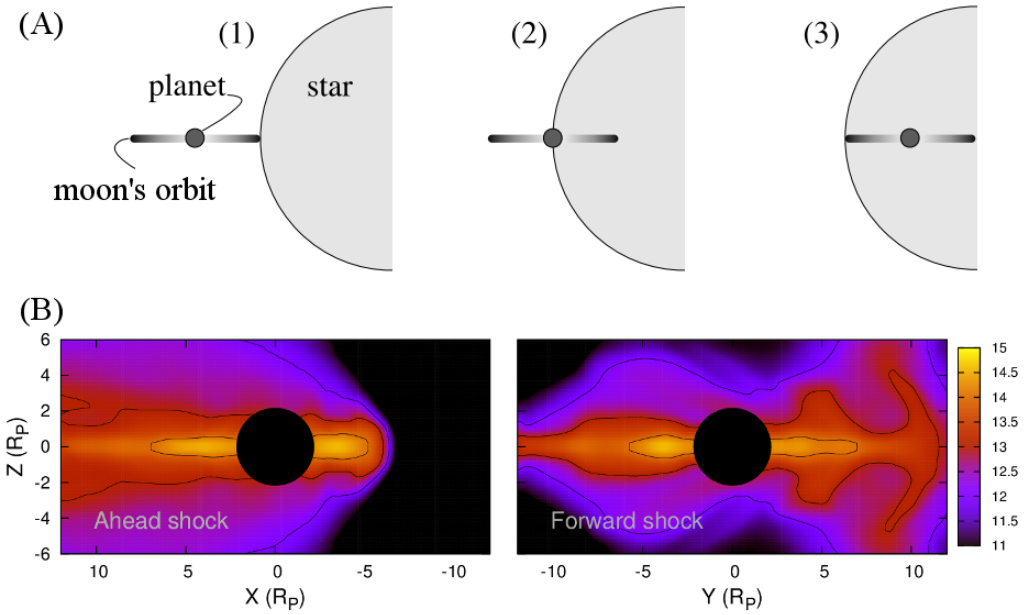

Figure 7.1 (A) An orbital sampling effect (OSE) from multiple observations of an exomoon with varying phase (adapted from Heller (2014)). (B) Log10 column density in cm^{-2} for $m/q = 16$ ions (e.g., O^+ ions) injected at 4 R_P for gas giant at 0.2 AU for forward (left) and ahead (right) shock orientations generated by the multifluid model (see Chapter 3).

exomoon at 4 R_P, orbiting a gas giant at 0.2 AU around a G dwarf. The signatures in the wavelength filters where the tori absorb could have a similar effect as the OSE in (A). There are some different issues to take into account, however. The tori is diffuse, and is not 100% opaque, but it is centrifugally expanded, out to 5-10 R_P with a scale height on the order of R_P which could offset some of the opacity concern given the cross sectional area. While a gas giant the size of Jupiter or Saturn could cover ∼1% of a G dwarf, and therefore generate a 1% transit signal, and the Earth ∼0.0084%, a Luna-sized exomoon would cover just six parts per million of the flux. Amongst the systematic and stellar noise, this is likely to be very difficult to observe. For the purpose of this discussion, assume the plasma torus generated by such a moon covers an area ∼15 R_P × 3 R_P, or ∼45 × that of the planetary disk (for the left panel in (B)); in this case, even an optically thin torus could produce transit signal.

As a quick calculation for the $m/q = 16$ torus shown in Fig. 7.1 for atomic species with similar m/q ratios, e.g., O II, S III, we can approximate transit effects. Assume an approximate average column density of $10^{14.3}$ cm^{-2} over the area above. The cross section for some of the stronger absorption lines for O II is $\sigma \approx 10^{-16}$ (Nahar, 1999), and combining the two gives an optical depth of $\tau \approx 10^{-1.7}$ or an attenuation of $\sim e^{-\tau} \approx 2\%$. Combined with the fraction of the star covered above ∼0.45, assuming low impact parameter, and we obtain a rough transit depth of ∼0.9% - comparable to the planet itself.

Not only the magnitude of the transit signal could be modified, but also the signature shape itself. Unlike the OSE effects in Fig. 7.1 (A) which requires the folding of multiple observations to get a signal, each transit would show this absorption signature. Some variablility due to exomoon outflow and stellar events could be expected. Fig. 7.2 is a cartoon depicting potential signals during ingress and egress generated by the plasma torus in the appropriate filters. The dashed line depicts the transit of a clean, planetary disk. The orange (purple) lines depict the modifications from an geometrically asymmetric (symmetric) torus, which could be roughly ascribed to the left (right) panel in Fig. 7.1 (B).

Granted, there are some issues with this method to take into account: the modifications are only applicable at the absorption wavelengths, so the number of photons emitted by the host star that pass through the plasma must be sufficient; the ions could be fairly hot

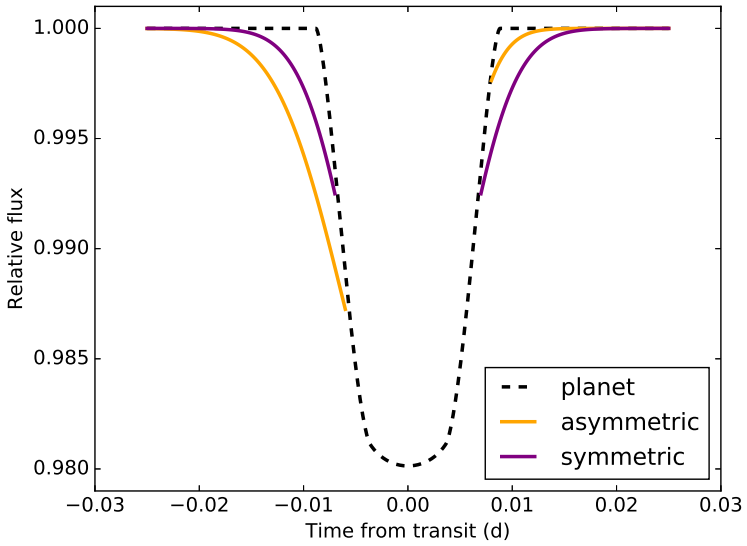

Figure 7.2 An illustration of potential 'wings' formed in the transit ingress and egress, by the attenuation by a plasma torus.

(100-1000 eV) which could impact line width broadening; variability of outflow could create an inconsistent signal; how does one separate the signal from the plasma torus from the transmission through the upper atmosphere of the planet? The upside is that if the signal is detected, it gives direct insight into the species in the outflow of the exomoon, which could point to characterizing the surface conditions and whether the bModeling effecody has an atmosphere or ocean.

When future missions like JWST and LUVOIR come online, the increase in sensitivity and spectral coverage will greatly improve incoming spectroscopic data from planets targeted by Kepler and TESS; it is likely that neutrals and ionic species from active exomoons associated with targeted planets will be a source of noise in the planets spectrum, and of interest to determining both the existence and details about the moon itself.

7.3 Anisotropic multifluid simulations of Proxima Centauri b

Here, I discuss some preliminary work on the multifluid modeling of Proxima Centauri b, which is a starting point for the Part II follow-up to § 5. Observations have measured

the estimated mass loss rate from Proxima Centauri using astrospheric Lyα measurements (e.g. Wood et al., 2001) and more recently, MHD models have estimated the structure of the stellar wind of Proxima Centauri (Garraffo, Drake and Cohen, 2016), and its effect on a simple pressure balance model of an Earth-like planet's magnetopause distance (see, e.g., Figs. 4 and 5 in Garraffo, Drake and Cohen (2016)). Potential atmospheric loss from the planet (e.g., Airapetian et al., 2017; Dong et al., 2017) has been studied for varying cases of stellar wind dynamic pressure, planetary magnetic field strength and atmospheric initialization.

The results presented here were performed for an Earth magnitude magnetic moment (not unlikely even if the planet is synchronously locked, see Driscoll and Barnes (e.g. 2015); Zuluaga and Bustamante (e.g. 2016)), with density $\sim 10^4$ cm^{-3} each of O^+ and H^+ ions at the inner boundary of 1.6 R_E, with ion temperature of $\sim$0.7 eV. Densities and temperature were set according to Earth values (assuming Earth-like planetary atmosphere), scaled up by the increase in proximity to Proxima Centauri; the exoplanet orbits a factor of 20 closer at $\sim$0.05 AU, so $\sim 400\times$ via isotropic, $1/R^2$ scaling and with the further assumption that the ionizing radiation $<\sim$180 nm is increased at the M dwarf. Stellar wind parameters were approximately in the middle of the ranges estimated in Garraffo, Drake and Cohen (2016). Solar wind velocity was set to 1080 km s^{-1}, with a H^+ density of 2500 cm^{-3}, generating a dynamic ram pressure of $\sim 2000\times$ that of the nominal solar wind at Earth (5 cm$-$3, 400 km s$-$1). The IMF magnitude was set to $\sim$500 nT with a parallel B_z of $\sim$120 nT, and approximately 45° azimuthal angle. All plasma was initialized with isotropic pressure and allowed to evolve according to the controlling pressure evolution.

Fig. 7.3 shows meridional slices of the simulation for both the anisotropic (first two of first row, and entire middle row) and isotropic (last of top row, entire bottom row) implementations. The top left panel shows the measure of pressure/temperature anisotropy present for the O^+ ions in the system, the primary sources of which are ionospheric. One can see that of the O^+ that have entered the magnetosheath, there is a strong perpendicular anisotropic component as the ions are heated in the compression and pile up of the stellar wind. The darker, purple areas in the northern and southern tail lobes are more strongly parallel, and are associated with the outflow of O^+ ions discussed below.

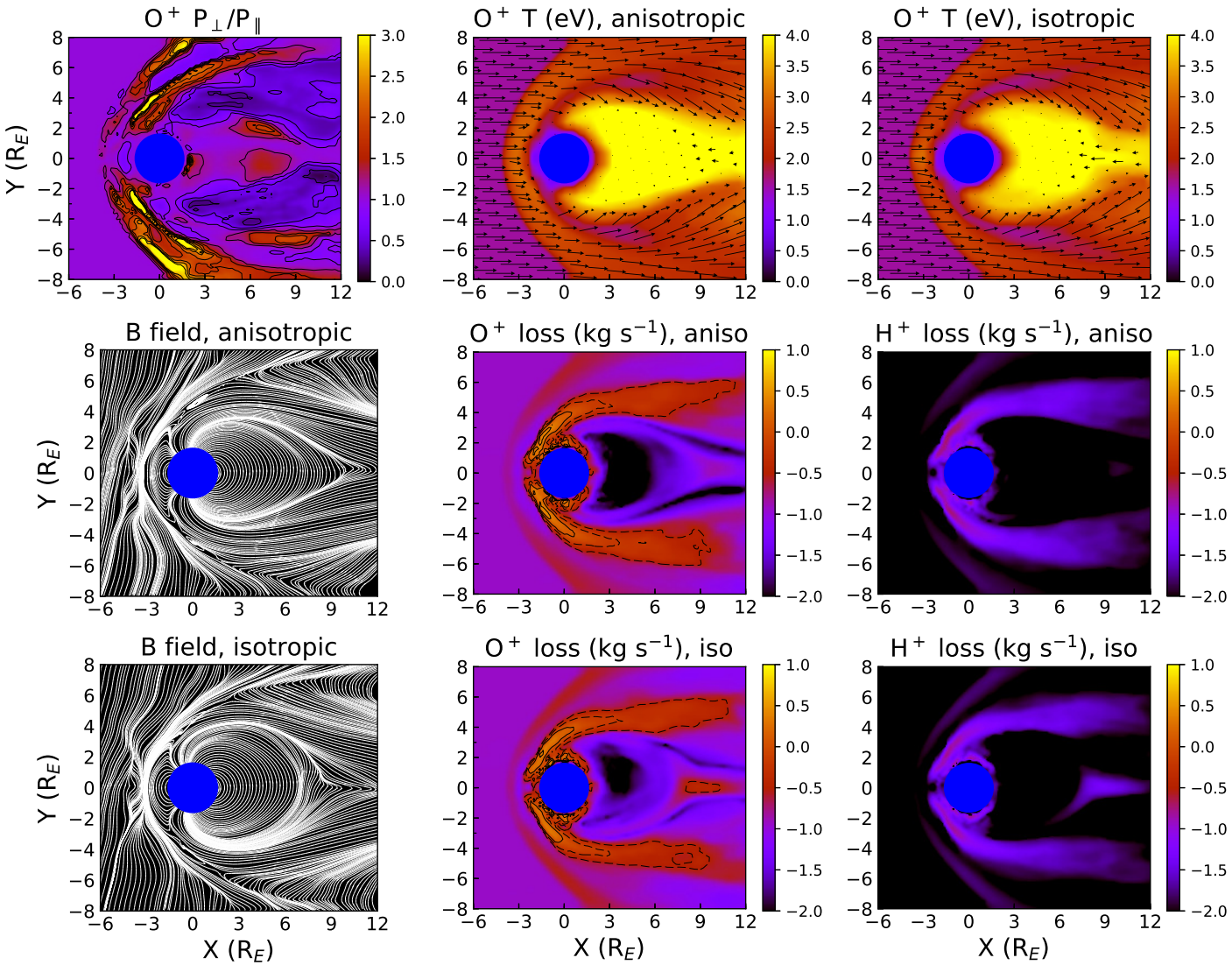

Figure 7.3 **All:** Meridional slices of the space weather environnment at Proxima Centauri b. **Top left:** O^+ anisotropy. **Top middle and right:** Log_{10} O^+ temperature for the anisotropic (middle) and isotropic (right) simulations. **Middle and bottom rows:** For the anisotropic (middle row) and isotropic (bottom row) simulations, magnetic field structure (left), O^+ mass flux (middle), and H^+ mass flux (right).

The middle and right panels in the top row show the $\log_{10}O^+$ temperature (eV) in the color palette for the anisotropic, and isotropic simulations, respectively. The vector field represents the flow of O^+ ions in the system. Ions outflowing from the cusp regions (see middle panels, middle and bottom row) are hotter by a factor of ∼2 in the anisotropic simulation (∼80 eV vs. ∼40 eV), due to energization along the direction of the magnetic field in the outflow. One difference in flow comparison, keeping in mind this is a snapshot in time, is that the isotropic simulation displays stronger return flow from the tail than the anisotropic simulation. This is likely related to suppression of tail reconnection from the slightly perpendicular anisotropy seen in the top left panel.

The first panel of the middle and bottom rows show the magnetic field structure of the system which is highly compressed by the incoming Proxima Centauri stellar wind. The structures look similar in that both are showing steady-state magnetic reconnection in the cusps (e.g., note the cross-sectional flux rope in the southern cusp of the anisotropic simulation and field structure as one moves in the +X direction - left panel, middle row), and the magnetopause distances are similar at ∼3 R_E, with slightly more compression in the isotropic case. This distance agrees well with the simulations performed in Garraffo, Drake and Cohen (2016).

In the middle (right) panels of the middle and bottom row, we see the difference in O^+ (H^+) mass flux, with strong escape from the dayside cusp regions. Comparing to the flow and magnetic field structures, most of the mass is lost as it escapes through the cusp region, and is then carried tailward into the outflowing stellar wind, on convecting reconnected magnetic flux. The anisotropic model shows higher mass flux out of the cusps at ∼15.01 (1.28) kg s^{-1}, compared to ∼13.45 (1.05) kg s^{-1} in the isotropic model. Some of that is seen returning planetward from the tail equatorial region, and for this snapshot this return is stronger in the isotropic model.

These total mass loss rates are in line with estimates from 1D polar wind models that include much more detailed atmospheric characteristics than our simple inner boundary. Fig. 7.4 from Garcia-Sage et al. (2017) shows mass loss from the Goddard polar wind model, PWOM, for four different multiples of Earth ionospheric temperatures, as a function of the closed/open field line boundary (∼50.8° latitude for both multifluid simulations). The red

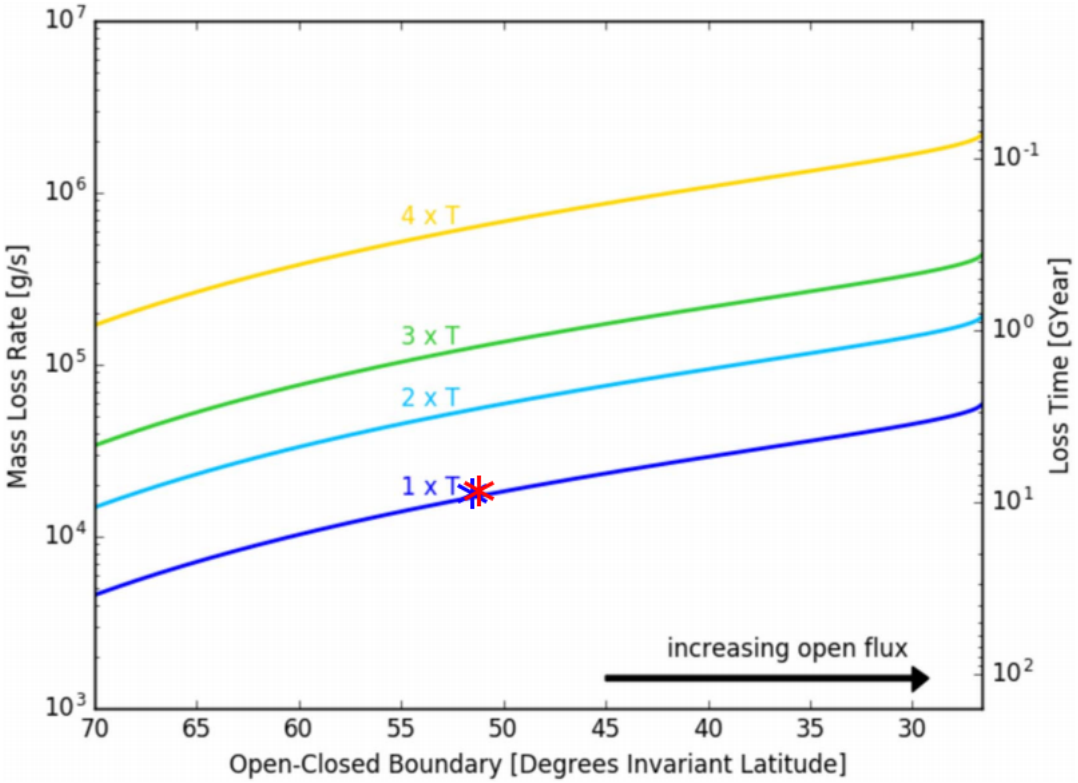

Figure 7.4 Results from 1D polar wind model of total mass loss from the atmosphere of Proxima Centauri b for varying multiples (1-4) of Earth ionospheric temperatures as a function of separatrix location. The multifluid models are noted, anisotropic model (red asterisk) and isotropic model (blue asterisk) (adapted from Garcia-Sage et al. (2017)).

and blue asterisks represent the anisotropic and isotropic mass loss, which is in line with the 1×T in the model of Garcia-Sage et al. (2017), which suggests 850 Myr to total loss. The values for mass loss captured in the multifluid model in Fig. 7.4 also agree well with the estimates from Dong et al. (2017), wherein it was predicted that 0.59-7.3×10^{26} O^+ ions s^{-1} would escape under varying stellar wind conditions, where the anisotropic (isotropic) multifluid model shows escape rates of 5.6 (5.0)×10^{26} ions s^{-1} for O^+ ions. A few significant differences exist between the preliminary multifluid results and those of Dong et al. (2017): 1) the present work used a 1 $\mathcal{M}_E$ magnetic moment, where those of Dong et al. (2017) used 0.33 $\mathcal{M}_E$, 2) the Dong et al. (2017) results also simulated the system down to the auroral regions, ∼100 km, where our inner boundary is ∼1.6 R_E, which requires some simplification of the ionospheric parameters in the present preliminary work, and 3) the present work used an Earth-like atmosphere, where the work from Dong et al. (2017) simulated a dominant neutral CO_2 constituent as opposed to N_2.

7.4 Anisotropic contributions to orbital plasma environment at Titan

The accurate prediction for plasma flux at the orbital positions of moons like Titan, Europa and Enceladus is of primary importance if our understanding of magnetospheric effects on atmospheric and surface chemical evolution of these bodies is to be investigated. As seen in Chapter 4, the plasma characteristics and structure of Saturn's magnetosphere is altered significantly through the inclusion of plasma pressure anisotropy. If we want to develop a ground truth for exoplanetary environments, it seems that anisotropy is important to include.

Fig. 7.5 shows synthetic spectra for $\log_{10}$ flux of both H^+ (top row) and W^+ (bottom row) ions at 20 R_S as a function of local time, for the isotropic (left column) and anisotropic (right column) simulations in units of eV^{-1} cm^{-2} s^{-1}. The isotropic version shows a marked difference in H^+ flux, with higher values throughout the azimuthal extent. The energies seen are similar, but the average is higher in the anisotropic flux of H^+ throughout the magnetosphere, but the dayside in particular, as the magnetopause is more compressed for the anisotropic simulation, and therefore some sampling of the hotter ions near the magnetosheath is performed.

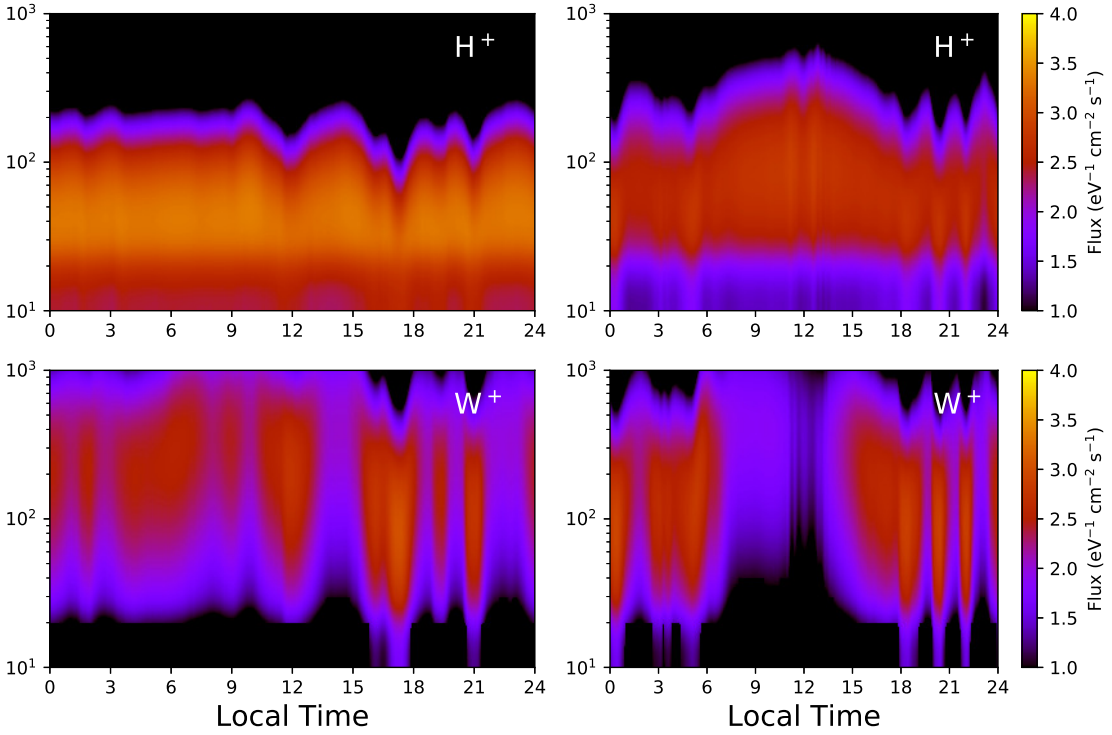

Figure 7.5 Synthetic spectra of $\log_{10}$ flux of H^+ (top row) and W^+ (bottom row) ions at 20 R_S, for the isotropic (left column) and anisotropic (right column) simulations in units of eV^{-1} cm^{-2} s^{-1}.

The W^+ ions show that the nightside (2100-0300 LT) exhibits a lack of high flux, lower energy W^+ fingers in the isotropic code, but there are distinct interchange structures in the anisotropic code, as discussed above in Chapter 4. The average energies are similar (aside from the dayside extension into the magnetosheath in the anisotropic code), and flux values are also approximately equal.

The ion fluxes and energetic populations have a distinct effect at Titan, contributing to the formation of complex organic haze layers and the eventual rainout of so-called 'tholins' to the surface of the moon (Sagan et al., 1993; Coates et al., 2007). A more extensive study of the effects of plasma flux for varying magnetospheric paramterizations could prove enlightening towards the eventual characterization of potentially habitable (exo)moon environments.

Appendix A

DERIVATION OF ANISOTROPIC PRESSURE TREATMENT IN THE MULTIFLUID MODEL

We note the definition of the 0^{th} and 1^{st} moments of the multifluid equations as:

$$\int f(\mathbf{x},\mathbf{v},t)\,d^3v = n(\mathbf{x},t) \;\; \textbf{and} \;\; \int \mathbf{v}\, f(\mathbf{x},\mathbf{v},t)\,d^3v = u(\mathbf{x},t)n(\mathbf{x},t), \tag{A.1}$$

where $f(\mathbf{x},\mathbf{v},t)$ is the distribution function of a particle species, and $n(\mathbf{x},t)$ and $u(\mathbf{x},t)$ are the fluid number densities and bulk velocities which are tracked individually for each species. Similarly, we define the total velocity of the fluids as $\mathbf{v}(\mathbf{x},t)$, and thermal (non-kinetic) fluid velocity as $\mathbf{w}(\mathbf{x},t)$ such that:

$$\mathbf{v} \equiv \mathbf{w} + \mathbf{u} \text{ and equivalently, } \mathbf{w} = \mathbf{v} - \mathbf{u}. \tag{A.2}$$

follows.[1]

We then can define (using the definition of the first moment and and A.2 above):

$$\int \mathbf{w}\, f\, d^3v = \int (\mathbf{v}-\mathbf{u})\, f\, d^3v = \int \mathbf{v}\, f\, d^3v - \mathbf{u}\int f\, d^3v = 0 \tag{A.3}$$

The 2^{nd} moment of the multifluid equations is defined as:

$$\int w_i\, w_j\, f\, d^3v = P_{ij}(x,t), \tag{A.4}$$

[1]It is worth noting here that in the multifluid regime, we do not track all species in a single fluid, rather each species is tracked independently; therefore any center of mass velocity in a particular fluid is identical to the bulk velocity (as opposed to, e.g., Shkarofsky, Johnston and Bachynski (1966)). For this reason, we note the definition of the average intrinsic (thermal) fluid velocity, w, in Eq. A.3.

where $w_{i,j}$ is the i/jth component of the thermal velocity. The conservative form of the anisotropic pressure evolution is derived by applying the second moment to the Vlasov equations, i.e.:

$$\int w_i\, w_j \left[\frac{\partial f}{\partial t} + \mathbf{v}\cdot\nabla_{\mathbf{x}} f + \mathbf{a}\cdot\nabla_{\mathbf{v}} f\right] d^3v = 0 \tag{A.5}$$

where we assume regimes where collisional effects are negligible (thus the RHS $\rightarrow$ 0), and $\mathbf{a} = \frac{q}{m}[\mathbf{E}\times\mathbf{B}]$.

We will split Eq. A.5 into three terms, with a derivative in each term. Namely:

$$T^1_{ij} = \int w_i\, w_j \frac{\partial f}{\partial t}\, d^3v \tag{A.6}$$

$$T^2_{ij} = \int w_i\, w_j\, \mathbf{v}\cdot\nabla_{\mathbf{x}} f\, d^3v \tag{A.7}$$

$$T^3_{ij} = \int w_i\, w_j\, \mathbf{a}\cdot\nabla_{\mathbf{v}} f\, d^3v \tag{A.8}$$

For Term 1 in Eq. A.6, we can note that since $\mathbf{v}$ is an independent variable, we can pull the partial integration outside the integral , leaving the definition of the second moment as defined in Eq. A.4, or:

$$T^1_{ij} = \frac{\partial P_{ij}}{\partial t} \tag{A.9}$$

Term 2 in Eq. A.7 can be redefined using the vector calculus identity $\nabla\cdot(f\mathbf{A}) = \mathbf{A}\cdot\nabla f + f\nabla\cdot\mathbf{A}$, giving:

$$T^2_{ij} = \int \nabla_{\mathbf{x}}\cdot(w_i\, w_j\, \mathbf{v} f) d^3v - \int f\nabla_{\mathbf{x}}\cdot(w_i w_j \mathbf{v}) d^3v \tag{A.10}$$

Applying the product rule to the right hand side of Eq. A.10 gives an equation where the last term vanishes ($\mathbf{v}$ is the independent variable.) Noting the assumptions in Eq. A.2, and substituting in the first term of Eq. A.10 for $\mathbf{v}$, and for $\mathbf{w}$ in second term (noting that the $\mathbf{v}$ terms go to zero if the derivative is applied) we see:

$$T_{ij}^{2} = \nabla_{\mathbf{x}} \cdot \int w_i w_j w_k f d^3v - \nabla_{\mathbf{x}} \cdot \int w_i w_j u f d^3v + \int w_i \mathbf{v} \cdot \nabla_{\mathbf{x}} u_j f d^3v + \int w_j \mathbf{v} \cdot \nabla_{\mathbf{x}} u_i f d^3v \tag{A.11}$$

and we find term 2.1 is the divergence of the 3^{rd} fluid moment - the heat flux, $\overline{\overline{\overline{\mathbf{Q}}}}$:

$$T_{ij}^{2.1} = \nabla_{\mathbf{x}} \cdot \overline{\overline{\overline{\mathbf{Q}}}}. \tag{A.12}$$

We apply Eq. A.4, the moment definition of pressure, to term 2.2, and find the divergence of the pressure flux:

$$T_{ij}^{2.2} = \nabla_{\mathbf{x}} \cdot (\mathbf{u} P_{ij}). \tag{A.13}$$

Terms 2.3 and 2.4 involve the velocity shear contribution to the pressure anisotropy. Now expanding the velocity term via Eq. A.2, and noting Eq. A.3, we find these terms are symmetric around the i- and j- indices:

$$T_{ij}^{2.3} = P_{ik} \cdot \nabla_{x_k} u_j \tag{A.14}$$

$$T_{ij}^{2.4} = P_{jk} \cdot \nabla_{x_k} u_i. \tag{A.15}$$

Noting that we close our system by assuming the heat flux is negligible (a valid assumption in the regime of convection-dominated collisionless space plasmas), this second term can be written:

$$T_{ij}^{2} = \nabla_{\mathbf{x}} \cdot (\mathbf{u} P_{ij}) + P_{ik} \cdot \nabla_{x_k} u_j + P_{jk} \cdot \nabla_{x_k} u_i. \tag{A.16}$$

The third term is noted as:

$$T_{ij}^{3} = \int w_i w_j \mathbf{a} \cdot \nabla_{\mathbf{v}} f d^3v \tag{A.17}$$

where **a** is the acceleration from the Lorenz force. We can then write Eq. A.17 as:

$$T_{ij}^{3} = \frac{q}{m}\left[\int w_i w_j \mathbf{E}\cdot\nabla_{\mathbf{v}} f d^3v + \int w_i w_j \mathbf{v}\times\mathbf{B}\cdot\nabla_{\mathbf{v}} f d^3v\right] \tag{A.18}$$

We can rewrite the above using the vector product rule, once again, for the first and second terms in Eq. A.18 and obtain four terms:

$$T_{ij}^{3.1} = \frac{q}{m}\int \nabla_{\mathbf{v}}\cdot(w_i w_j \mathbf{E}\, f)\, d^3v \tag{A.19}$$

$$T_{ij}^{3.2} = -\frac{q}{m}\int f\,\nabla_{\mathbf{v}}\cdot(w_i w_j \mathbf{E})\, d^3v \tag{A.20}$$

$$T_{ij}^{3.3} = \frac{q}{m}\int \nabla_{\mathbf{v}}\cdot(w_i w_j \mathbf{v}\times\mathbf{B}\, f)\, d^3v \tag{A.21}$$

$$T_{ij}^{3.4} = -\frac{q}{m}\int f\,\nabla_{\mathbf{v}}\cdot(w_i w_j \mathbf{v}\times\mathbf{B})\, d^3v \tag{A.22}$$

$$\tag{A.23}$$

Applying the divergence theorem causes terms 3.1 and 3.3 to go to zero (since $f \to 0$ as $v \to \infty$). We distribute the divergence operator on the quantities in 3.2, again expanding **w** as was done above in Eqs. A.10 and A.11, using Eq. A.3, and noting that **u** and **E** are functions of x and t only, and all terms in 3.2 to go zero:

$$T_{ij}^{3.2} = -\frac{q}{m}\,\mathbf{E}\left(\cancelto{0}{\int f w_j d^3v} + \cancelto{0}{\int f w_i d^3v}\right) + \cancelto{0}{\int f\, w_i w_j \nabla_{\mathbf{v}}\cdot\mathbf{E} d^3v} = 0 \tag{A.24}$$

Term 3.4 expands as follows:

$$T_{ij}^{3.4} = -\frac{q}{m}\int f\ (w_j \mathbf{v}\times\mathbf{B} + w_i \mathbf{v}\times\mathbf{B} + w_i w_j \nabla_{\mathbf{v}}\cdot\mathbf{v}\times\mathbf{B})\, d^3v \tag{A.25}$$

B is a function of x and t only, so we can integrate across the cross product, and only consider the **v** term:

$$T_{ij}^{3.4} = -\frac{q}{m}\left(\int f\, w_j \mathbf{v} d^3v + \int f\, w_i \mathbf{v} d^3v\right)\times\mathbf{B} + \int f\, w_i w_j \nabla_{\mathbf{v}}\cdot(\mathbf{v}\times\mathbf{B})\, d^3v, \tag{A.26}$$

where the last term goes to zero since the cross product is orthogonal to $\mathbf{v}$-space:

$$\nabla_{\mathbf{v}} \cdot (\mathbf{v} \times \mathbf{B}) = \mathbf{B} \cdot \cancelto{0}{(\nabla_{\mathbf{v}} \times \mathbf{v})} - \mathbf{v} \cdot \cancelto{0}{(\nabla_{\mathbf{v}} \times \mathbf{B})} = 0. \tag{A.27}$$

Expanding $\mathbf{v}$, noting Eq. A.3, and applying the definition of the 2^{nd} moment gives us the final 3^{rd} term:

$$T^3_{ij} = -\frac{q}{m}\left[\overline{\overline{\mathbf{P}}} \times \mathbf{B} + [\overline{\overline{\mathbf{P}}} \times \mathbf{B}]^{\mathbf{T}}\right] \tag{A.28}$$

Now we combine Eqs. A.9, A.16, and A.28 to obtain the pressure evolution equation with full pressure anisotropy (tensor notation):

$$\frac{\partial \overline{\overline{\mathbf{P}}}}{\partial t} + \nabla_{\mathbf{x}} \cdot (\mathbf{u}\overline{\overline{\mathbf{P}}}) + \nabla_{\mathbf{x}}\mathbf{u} \cdot \overline{\overline{\mathbf{P}}} + \left(\nabla_{\mathbf{x}}\mathbf{u} \cdot \overline{\overline{\mathbf{P}}}\right)^{\mathbf{T}} - \frac{q}{m}\left[\overline{\overline{\mathbf{P}}} \times \mathbf{B} + \left(\overline{\overline{\mathbf{P}}} \times \mathbf{B}\right)^{\mathbf{T}}\right] = 0. \tag{A.29}$$

Appendix B

SIMPLIFIED RADIO PROJECTION MODEL

A zeroth order model was developed to estimate the projection of auroral radio emissions on a celestial sphere surrounding the Saturn-like planet as shown in Fig. 3.5. The model was developed by using the field-aligned current (FAC) latitudes given by the multifluid model as in Fig. 3.4 and Cassini observations of Saturnian Kilometric Radiation (SKR) as reported by Cecconi et al. (2009) - including beaming angle and longitudinal measurements.

A common visualization of radio emission is seen in Fig. B.1. The red cone represents the typical geometry of emission that has been measured by satellite instrumentation at Saturn. B labels a dipole magnetic field line extending from the planet in the lower left. The beaming angle, or aperture angle, of emission is labeled by β and defined as the angle of emission relative to the magnetic field at the point of origin - illustrated by the dashed red lines. δ denotes the 'soft' beaming angle, shown by the shaded area, that corresponds to power scaling relative to the particle trajectory, or 'on-cone' emission, for particle generated electromagnetic emissions (e.g. Rybicki and Lightman, 2008).

The following assumptions were made in our model:

1. The surface of the projected sphere plotted in Fig. 3.5 was located at a distance $\gg \mathcal{O}(\mathrm{R}_P)$.

2. Planetary shadowing (projected emission intersecting with and blocked by the planet) was ignored.

3. Two values were chosen for β in both northern and southern hemispheres according to the extreme values given by Cassini observations (Cecconi et al., 2009). As shown in Fig. 3.5, the left column corresponds to β=$90^o(60^o)$ in the northern(southern) hemisphere, and the right column corresponds to β=$65^o(45^o)$ in the northern(southern) hemisphere.

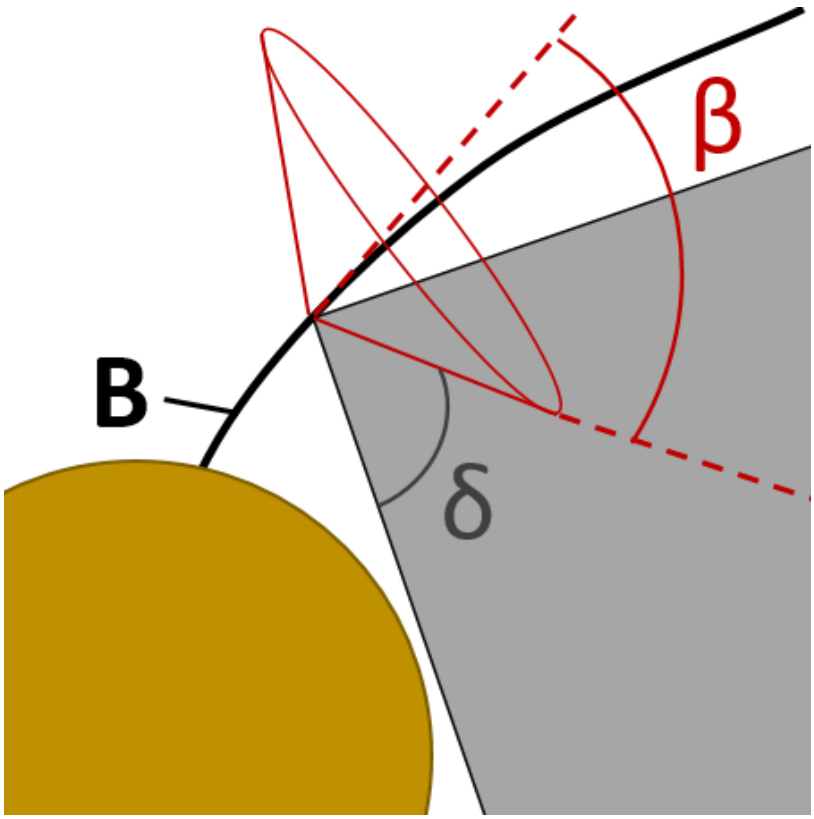

Figure B.1 Visualization of radio emission geometry generated along magnetic field line, B, with beaming angle, β, and soft beaming angle, δ.

4. Absolute emitted spectral flux densities (e.g. in units of Jy) are ignored, as this is simply a visualization of radio power projected around the planet as a function of magnetospheric morphology and dynamics. 'On-cone' emission power (along the red dashed lines in Fig. B.1) was assigned a normalized value of 1, scaling by $\sin^2(\theta)$ out to an angle of δ. Angles larger than δ were not included.

5. δ was set to 45^o which corresponds to a value of 1/2 maximum power emitted 'on-cone', as power emitted is given by P $\propto \sin^2(\theta)$, where θ is the angle between 'on-cone' emission and point of observation.

6. Emissions were modeled as being generated between the latitude endpoints given in Fig. 3.4 for the 10 AU and 0.2 AU cases, and between longitudes correlated with Saturn Local Times (SLT) 04:00 and 16:00 (Cecconi et al., 2009) - essentially a 180^o coverage in longitude.

Emission cones were modeled on a planetary long-lat grid corresponding to the longitude and latitude boundaries given above, with a spacing of 1^o for latitude, and 1.5^o for longitude. The celestial sphere consisted of a grid in celestial long-lat pairs, with spacing of $\sim 15.7^o$ for celestial latitude, and $\sim 31.4^o$ for celestial longitude. For each point in the celestial long-lat projection, the contribution of all emission cones from each planetary long-lat pair were summed and averaged over the total number of cones modeled. This process resulted in each point on the celestial long-lat map representing the projected radio emission relative to the maximum potential of 1.0 - if all emission cones were oriented identically, giving a type of 'heat map' for planetary radio emission.

BIBLIOGRAPHY

Achilleos, Nick, P Guio and Chris S Arridge. 2010. "A model of force balance in Saturn's magnetodisc." *Monthly Notices of the Royal Astronomical Society* 401(4):2349–2371.

Acuña, MH, JEP Connerney, P Wasilewski, RP Lin, D Mitchell, KA Anderson, CW Carlson, J McFadden, H Rème, C Mazelle et al. 2001. "Magnetic field of Mars: Summary of results from the aerobraking and mapping orbits." *Journal of Geophysical Research: Planets* 106(E10):23403–23417.

Airapetian, Vladimir S, Alex Glocer, George V Khazanov, Robert O Parke Loyd, Kevin France, Jan Sojka, William C Danchi and Michael W Liemohn. 2017. "How hospitable are space weather affected habitable zones? The role of ion escape." *The Astrophysical Journal Letters* 836(1):L3.

Akasofu, S-I. 1981. "Energy coupling between the solar wind and the magnetosphere." *Space Science Reviews* 28(2):121–190.

Alexander, RD, Graham A Wynn, H Mohammed, Jonathan D Nichols and B Ercolano. 2015. "Magnetospheres of hot Jupiters: hydrodynamic models and ultraviolet absorption." *Monthly Notices of the Royal Astronomical Society* 456(3):2766–2778.

Alfvén, Hannes. 1977. "Electric currents in cosmic plasmas." *Reviews of Geophysics* 15(3):271–284.

André, N, MK Dougherty, CT Russell, JS Leisner and KK Khurana. 2005. "Dynamics of the Saturnian inner magnetosphere: First inferences from the Cassini magnetometers about small-scale plasma transport in the magnetosphere." *Geophysical research letters* 32(14).

Anglada-Escudé, G. et al. 2016. "A terrestrial planet candidate in a temperate orbit around Proxima Centauri." *Nature* 536:437–440.

Anglada-Escudé, Guillem, Pedro J Amado, John Barnes, Zaira M Berdiñas, R Paul Butler, Gavin AL Coleman, Ignacio de La Cueva, Stefan Dreizler, Michael Endl, Benjamin Giesers et al. 2016. "A terrestrial planet candidate in a temperate orbit around Proxima Centauri." *Nature* 536(7617):437–440.

Arney, Giada, Shawn D Domagal-Goldman, Victoria S Meadows, Eric T Wolf, Edward Schwieterman, Benjamin Charnay, Mark Claire, Eric Hébrard and Melissa G Trainer. 2016. "The pale orange dot: the spectrum and habitability of hazy Archean Earth." *Astrobiology* 16(11):873–899.

Axford, W Ian and Colin O Hines. 1961. "A unifying theory of high-latitude geophysical phenomena and geomagnetic storms." *Canadian Journal of Physics* 39(10):1433–1464.

Bagenal, F, M Horányi, DJ McComas, RL McNutt, HA Elliott, ME Hill, LE Brown, PA Delamere, P Kollmann, SM Krimigis et al. 2016. "Plutos interaction with its space environment: Solar wind, energetic particles, and dust." *Science* 351(6279):aad9045.

Bagenal, Fran. 2007. "The magnetosphere of Jupiter: Coupling the equator to the poles." *Journal of Atmospheric and Solar-Terrestrial Physics* 69(3):387–402.

Bagenal, Fran and Peter A Delamere. 2011. "Flow of mass and energy in the magnetospheres of Jupiter and Saturn." *Journal of Geophysical Research: Space Physics* 116(A5).

Barnes, Jason W and DP Obrien. 2002. "Stability of satellites around close-in extrasolar giant planets." *The Astrophysical Journal* 575(2):1087.

Barnes, R., R. Deitrick, R. Luger, P. E. Driscoll, T. R. Quinn, D. P. Fleming, B. Guyer, D. V. McDonald, V. S. Meadows, G. Arney, D. Crisp, S. D. Domagal-Goldman, A. Lincowski, J. Lustig-Yaeger and E. Schwieterman. 2016. "The Habitability of Proxima Centauri b I: Evolutionary Scenarios." *ArXiv e-prints, arXiv:1608.06919* .

Barnes, Rory, Kristina Mullins, Colin Goldblatt, Victoria S Meadows, James F Kasting and René Heller. 2013. "Tidal Venuses: triggering a climate catastrophe via tidal heating." *Astrobiology* 13(3):225–250.

Barthelemy, Mathieu and Gaël Cessateur. 2014. "Sensitivity of upper atmospheric emissions calculations to solar/stellar UV flux." *Journal of Space Weather and Space Climate* 4:A35.

Beckstead, Ashley A, Yuyuan Zhang, Mattanjah S de Vries and Bern Kohler. 2016. "Life in the light: nucleic acid photoproperties as a legacy of chemical evolution." *Physical Chemistry Chemical Physics* 18(35):24228–24238.

Belcher, JW, AJ Lazarus, RL McNutt and GS Gordon. 1993. "Large-scale density structures in the outer heliosphere." *Advances in Space Research* 13(6):41–46.

Belov, A, H Garcia, V Kurt, H Mavromichalaki and M Gerontidou. 2005. "Proton enhancements and their relation to the X-ray flares during the three last solar cycles." *Solar Physics* 229(1):135–159.

Ben-Jaffel, Lotfi and Gilda E Ballester. 2014. "Transit of exomoon plasma tori: new diagnosis." *The Astrophysical Journal Letters* 785(2):L30.

Bertaux, Jean-Loup, François Leblanc, Olivier Witasse, Eric Quemerais, Jean Lilensten, SA Stern, B Sandel and Oleg Korablev. 2005. "Discovery of an aurora on Mars." *Nature* 435(7043):790–794.

Bhardwaj, Anil and G. Randall Gladstone. 2000. "Auroral emissions of the giant planets." *Reviews of Geophysics* 38(3):295–353.
URL: *http://dx.doi.org/10.1029/1998RG000046*

Borovikov, SN and NV Pogorelov. 2014. "Voyager 1 near the heliopause." *The Astrophysical Journal Letters* 783(1):L16.

Brice, Neil M and George A Ioannidis. 1970. "The magnetospheres of Jupiter and Earth." *Icarus* 13(2):173–183.

Brown, Robert, Jean Pierre Lebreton and Jack Waite. 2009. *Titan from Cassini-Huygens*. Springer Science & Business Media.

Brugger, B., O. Mousis, M. Deleuil and J. I. Lunine. 2016. "Possible Internal Structures and Compositions of Proxima Centauri b." *The Astrophysical Journal Letters* 831:L16.

Bunce, EJ, SWH Cowley, DM Wright, AJ Coates, MK Dougherty, N Krupp, WS Kurth and AM Rymer. 2005. "In situ observations of a solar wind compression-induced hot plasma injection in Saturn's tail." *Geophysical research letters* 32(20).

Burch, J. L., J. Goldstein, T. W. Hill, D. T. Young, F. J. Crary, A. J. Coates, N. Andr, W. S. Kurth and E. C. Sittler. 2005. "Properties of local plasma injections in Saturn's magnetosphere." *Geophysical Research Letters* 32(14). L14S02.

Burke, BF and KL Franklin. 1955. "Observations of a variable radio source associated with the planet Jupiter." *Journal of Geophysical Research* 60(2):213–217.

Burkhart, Blakesley and Abraham Loeb. 2017. "The Detectability of Radio Auroral Emission from Proxima B." *arXiv preprint arXiv:1706.07038* .

Canup, Robin M and William R Ward. 2006. "A common mass scaling for satellite systems of gaseous planets." *Nature* 441(7095):834.

Cecconi, B, L Lamy, P Zarka, R Prangé, WS Kurth and P Louarn. 2009. "Goniopolarimetric study of the revolution 29 perikrone using the Cassini Radio and Plasma Wave Science instrument high-frequency radio receiver." *Journal of Geophysical Research: Space Physics* 114(A3).

Chamberlain, Joseph W. 2016. *Physics of the Aurora and Airglow: International Geophysics Series*. Vol. 2 Elsevier.

Chapman, S and VCA Ferraro. 1940. "The theory of the first phase of a geomagnetic storm." *Journal of Geophysical Research* 45(3):245–268.

Chapman, Sidney and Vincent CA Ferraro. 1930. "A new theory of magnetic storms." *Nature* 126(3169):129–130.

Chapman, Sydney and Thomas George Cowling. 1970. *The mathematical theory of non-uniform gases: an account of the kinetic theory of viscosity, thermal conduction and diffusion in gases*. Cambridge university press.

Charbonneau, David, Timothy M Brown, David W Latham and Michel Mayor. 1999. "Detection of planetary transits across a sun-like star." *The Astrophysical Journal Letters* 529(1):L45.

Chen, Y, TW Hill, AM Rymer and RJ Wilson. 2010. "Rate of radial transport of plasma in Saturn's inner magnetosphere." *Journal of Geophysical Research: Space Physics* 115(A10).

Cheng, Andrew F. 1990. "Triton torus and Neptune aurora." *Geophysical Research Letters* 17(10):1669–1672.
URL: *http://dx.doi.org/10.1029/GL017i010p01669*

Chew, GF, ML Goldberger and FE Low. 1956. The Boltzmann equation and the one-fluid hydromagnetic equations in the absence of particle collisions. In *Proceedings of the Royal Society of London A: Mathematical, Physical and Engineering Sciences*. Vol. 236 (1204) The Royal Society pp. 112–118.

Chyba, Christopher F. 2000. "Energy for microbial life on Europa." *Nature* 403(6768):381–383.

Cliver, Edward W and William F Dietrich. 2013. "The 1859 space weather event revisited: limits of extreme activity." *Journal of Space Weather and Space Climate* 3:A31.

Coates, AJ, FJ Crary, GR Lewis, DT Young, JH Waite and EC Sittler. 2007. "Discovery of heavy negative ions in Titan's ionosphere." *Geophysical Research Letters* 34(22).

Cohen, O., J. J. Drake, A. Glocer, C. Garraffo, K. Poppenhaeger, J. M. Bell, A. J. Ridley and T. I. Gombosi. 2014. "Magnetospheric Structure and Atmospheric Joule Heating of Habitable Planets Orbiting M-dwarf Stars." *The Astrophysical Journal* 790:57.

Cohen, O, VL Kashyap, JJ Drake, IV Sokolov and TI Gombosi. 2011. "The dynamics of stellar coronae harboring hot Jupiters. II. A space weather event on a hot Jupiter." *The Astrophysical Journal* 738(2):166.

Cohen, O, Y Ma, JJ Drake, A Glocer, C Garraffo, JM Bell and TI Gombosi. 2015. "The interaction of Venus-like, M-dwarf planets with the stellar wind of their host star." *The Astrophysical Journal* 806(1):41.

Cohen, Ofer, VL Kashyap, JJ Drake, IV Sokolov, Cecilia Garraffo and TI Gombosi. 2011. "The Dynamics of Stellar Coronae Harboring Hot Jupiters. I. A Time-dependent Magnetohydrodynamic Simulation of the Interplanetary Environment in the HD 189733 Planetary System." *The Astrophysical Journal* 733(1):67.

Collins, John M, Hugh RA Jones and John R Barnes. 2016. "Calculations of periodicity from H {\ alpha} profiles of Proxima Centauri." *ArXiv e-prints, arXiv:1608.07834* .

Connerney, J. E. P., Mario H. Acua and Norman F. Ness. 1991. "The magnetic field of Neptune." *Journal of Geophysical Research: Space Physics* 96(S01):19023–19042.
URL: *http://dx.doi.org/10.1029/91JA01165*

Cowley, SWH, Sarah V Badman, EJ Bunce, JT Clarke, J-C Gérard, Denis Grodent, Caitriona M Jackman, Steve E Milan and Tim K Yeoman. 2005. "Reconnection in a rotation-dominated magnetosphere and its relation to Saturn's auroral dynamics." *Journal of Geophysical Research: Space Physics* 110(A2).

Cox, Donald P and Ronald J Reynolds. 1987. "The local interstellar medium." *Annual Review of Astronomy and Astrophysics* 25(1):303–344.

Cravens, TE, IP Robertson, SA Ledvina, D Mitchell, SM Krimigis and JH Waite. 2008. "Energetic ion precipitation at Titan." *Geophysical Research Letters* 35(3).

Crosby, Norma B, Markus J Aschwanden and Brian R Dennis. 1993. "Frequency distributions and correlations of solar X-ray flare parameters." *Solar Physics* 143(2):275–299.

Davenport, James RA, David M Kipping, Dimitar Sasselov, Jaymie M Matthews and Chris Cameron. 2016. "MOST Observations of our Nearest Neighbor: Flares on Proxima Centauri." *The Astrophysical Journal Letters* 829(2):L31.

Davenport, James RA, Suzanne L Hawley, Leslie Hebb, John P Wisniewski, Adam F Kowalski, Emily C Johnson, Michael Malatesta, Jesus Peraza, Marcus Keil, Steven M Silverberg et al. 2014. "Kepler Flares. II. The Temporal Morphology of White-light Flares on GJ 1243." *The Astrophysical Journal* 797(2):122.

De Mora, Stephen, Serge Demers and Maria Vernet. 2000. *The effects of UV radiation in the marine environment*. Vol. 10 Cambridge University Press.

Del Sarto, Daniele, Francesco Pegoraro and Francesco Califano. 2016. "Pressure anisotropy and small spatial scales induced by velocity shear." *Physical Review E* 93(5):053203.

Delamere, PA and F Bagenal. 2010. "Solar wind interaction with Jupiter's magnetosphere." *Journal of Geophysical Research: Space Physics* 115(A10).

Delamere, PA, F Bagenal, V Dols and LC Ray. 2007. "Saturn's neutral torus versus Jupiter's plasma torus." *Geophysical research letters* 34(9).

Desch, MD and HO Rucker. 1983. "The relationship between Saturn kilometric radiation and the solar wind." *Journal of Geophysical Research: Space Physics* 88(A11):8999–9006.

Desch, MD and ML Kaiser. 1984. "Predictions for Uranus from a radiometric Bode's law." *Nature* 310(5980):755–757.

Desch, Michael D. 1982. "Evidence for solar wind control of Saturn radio emission." *Journal of Geophysical Research: Space Physics* 87(A6):4549–4554.

Dessler, Alexander J. 2002. *Physics of the Jovian magnetosphere*. Vol. 3 Cambridge University Press.

Dierckxsens, M, K Tziotziou, Silvia Dalla, I Patsou, MS Marsh, NB Crosby, O Malandraki and G Tsiropoula. 2015. "Relationship between solar energetic particles and properties of flares and CMEs: statistical analysis of solar cycle 23 events." *Solar Physics* 290(3):841–874.

Dole, S. H. 1964. *Habitable planets for man*. New York: Blaisdell Pub. Co. [1964] [1st ed.].

Dong, Chuanfei, Meng Jin, Manasvi Lingam, Vladimir S Airapetian, Yingjuan Ma and Bart van der Holst. 2017. "Atmospheric escape from the TRAPPIST-1 planets and implications for habitability." *arXiv preprint arXiv:1705.05535* .

Dougherty, Michele, Larry Esposito and Stamatios Krimigis. 2009. *Saturn from Cassini-Huygens*. Springer Science & Business Media.

Driscoll, PE and Rory Barnes. 2015. "Tidal heating of Earth-like exoplanets around M stars: thermal, magnetic, and orbital evolutions." *Astrobiology* 15(9):739–760.

Dungey, James W. 1961. "Interplanetary magnetic field and the auroral zones." *Physical Review Letters* 6(2):47.

Estrela, Raissa and Adriana Valio. 2017. "Superflare UV flashes impact on Kepler-96 system: a glimpse of habitability when the ozone layer first formed on Earth." *arXiv preprint arXiv:1708.05400* .

Farrell, WM, MD Desch and P Zarka. 1999. "On the possibility of coherent cyclotron emission from extrasolar planets." *Journal of Geophysical Research: Planets* 104(E6):14025–14032.

Fleshman, BL, PA Delamere and F Bagenal. 2010. "A sensitivity study of the Enceladus torus." *Journal of Geophysical Research: Planets* 115(E4).

Foley, Bradford J, David Bercovici and William Landuyt. 2012. "The conditions for plate tectonics on super-Earths: inferences from convection models with damage." *Earth and Planetary Science Letters* 331:281–290.

Fossati, L, CA Haswell, CS Froning, L Hebb, S Holmes, U Kolb, Ch Helling, A Carter, P Wheatley, A Collier Cameron et al. 2010. "Metals in the exosphere of the highly irradiated planet WASP-12b." *The Astrophysical Journal Letters* 714(2):L222.

France, Kevin, Cynthia S Froning, Jeffrey L Linsky, Aki Roberge, John T Stocke, Feng Tian, Rachel Bushinsky, Jean-Michel Désert, Pablo Mauas, Mariela Vieytes et al. 2013.

"The ultraviolet radiation environment around M dwarf exoplanet host stars." *The Astrophysical Journal* 763(2):149.

France, Kevin, Jeffrey L Linsky, Feng Tian, Cynthia S Froning and Aki Roberge. 2012. "Time-resolved ultraviolet spectroscopy of the M-dwarf GJ 876 exoplanetary system." *The Astrophysical Journal Letters* 750(2):L32.

Garcia-Sage, K, A Glocer, JJ Drake, G Gronoff and O Cohen. 2017. "On the Magnetic Protection of the Atmosphere of Proxima Centauri b." *ASTROPHYSICAL JOURNAL LETTERS* 844(1).

Garraffo, Cecilia, Jeremy J Drake and Ofer Cohen. 2016. "The Space Weather of Proxima Centauri b." *The Astrophysical Journal Letters* 833(1):L4.

Garraffo, Cecilia, Jeremy J Drake, Ofer Cohen, Julian D Alvarado-Gomez and Sofia P Moschou. 2017. "The Threatening Environment of the TRAPPIST-1 Planets." *arXiv preprint arXiv:1706.04617* .

Gary, S Peter. 1992. "The mirror and ion cyclotron anisotropy instabilities." *Journal of Geophysical Research: Space Physics* 97(A6):8519–8529.

Gascón, Jordi, Anna Oubiña, Ana Pérez-Lezaun and Jordi Urmeneta. 1995. "Sensitivity of selected bacterial species to UV radiation." *Current microbiology* 30(3):177–182.

Gillmor, Stewart and John R Sprieter. 1997. *Discovery of the Magnetosphere (History of Geophysics)*. American Geophysical Union.

Gillon, Michaël, Amaury HMJ Triaud, Brice-Olivier Demory, Emmanuël Jehin, Eric Agol, Katherine M Deck, Susan M Lederer, Julien De Wit, Artem Burdanov, James G Ingalls et al. 2017. "Seven temperate terrestrial planets around the nearby ultracool dwarf star TRAPPIST-1." *Nature* 542(7642):456–460.

Gold, Thomas. 1959. "Motions in the magnetosphere of the Earth." *Journal of Geophysical Research* 64(9):1219–1224.

Gombosi, TI, TE Cravens, AF Nagy, RC Elphic and CT Russell. 1980. "Solar wind absorption by Venus." *Journal of Geophysical Research: Space Physics* 85(A13):7747–7753.

Gopalswamy, N, S Yashiro, G Michalek, G Stenborg, A Vourlidas, S Freeland and R Howard. 2009. "The soho/lasco cme catalog." *Earth, Moon, and Planets* 104(1-4):295–313.

Gray, CL, NJ Chanover, TG Slanger and K Molaverdikhani. 2014. "The effect of solar flares, coronal mass ejections, and solar wind streams on Venus 5577Å oxygen green line." *Icarus* 233:342–347.

Greer, RGH, DP Murtagh, IC McDade, PHG Dickinson, L Thomas, DB Jenkins, J Stegman, EJ Llewellyn, G Witt, DJ Mackinnon et al. 1986. "ETON 1: A data base pertinent to the study of energy transfer in the oxygen nightglow." *Planetary and space science* 34(9):771–788.

Grevesse, N, Martin Asplund and AJ Sauval. 2007. The solar chemical composition. In *The Composition of Matter*. Springer pp. 105–114.

Grießmeier, J.-M., P. Zarka and H. Spreeuw. 2007. "Predicting low-frequency radio fluxes of known extrasolar planets." *Astronomy and Astrophysics* 475:359–368.

Grießmeier, Jean-Mathias. 2015. Detection methods and relevance of exoplanetary magnetic fields. In *Characterizing stellar and exoplanetary environments*. Springer pp. 213–237.

Han, Eunkyu, Sharon X Wang, Jason T Wright, Y Katherina Feng, Ming Zhao, Onsi Fakhouri, Jacob I Brown and Colin Hancock. 2014. "Exoplanet orbit database. II. Updates to exoplanets. org." *Publications of the Astronomical Society of the Pacific* 126(943):827.

Hand, Kevin P, Robert W Carlson and Christopher F Chyba. 2007. "Energy, chemical disequilibrium, and geological constraints on Europa." *Astrobiology* 7(6):1006–1022.

Harman, CE, EW Schwieterman, JC Schottelkotte and JF Kasting. 2015. "Abiotic O2 levels on planets around F, G, K, and M stars: possible false positives for life?" *The Astrophysical Journal* 812(2):137.

Harnett, EM, RM Winglee and T Lerud. 2010. "Multiscale-multifluid simulations of the 26 February 2008 substorm: Evidence for internal triggering of a substorm." *Journal of Geophysical Research: Space Physics* 115(A12).

Harvey, Brian. 2007. *Russian planetary exploration: history, development, legacy and prospects*. Springer Science & Business Media.

Haswell, CA, L Fossati, T Ayres, K France, CS Froning, S Holmes, UC Kolb, R Busuttil, RA Street, L Hebb et al. 2012. "Near-ultraviolet absorption, chromospheric activity, and star-planet interactions in the WASP-12 system." *The Astrophysical Journal* 760(1):79.

Hawley, Suzanne L and Bjorn R Pettersen. 1991. "The great flare of 1985 April 12 on AD Leonis." *The Astrophysical Journal* 378:725–741.

Hawley, Suzanne L, James RA Davenport, Adam F Kowalski, John P Wisniewski, Leslie Hebb, Russell Deitrick and Eric J Hilton. 2014. "Kepler flares. I. Active and inactive M dwarfs." *The Astrophysical Journal* 797(2):121.

Hays, L, L Archenbach, J Bailey, R Barnes, J Barros, C Bertka, P Boston, E Boyd, M Cable, I Chen et al. 2015. "NASA Astrobiology strategy.".

Heller, René. 2014. "Detecting extrasolar moons akin to solar system satellites with an orbital sampling effect." *The Astrophysical Journal* 787(1):14.

Heller, René, Darren Williams, David Kipping, Mary Anne Limbach, Edwin Turner, Richard Greenberg, Takanori Sasaki, Émeline Bolmont, Olivier Grasset, Karen Lewis et al. 2014. "Formation, habitability, and detection of extrasolar moons." *Astrobiology* 14(9):798–835.

Heller, René and Rory Barnes. 2013. "Exomoon habitability constrained by illumination and tidal heating." *Astrobiology* 13(1):18–46.

Hill, TW. 1976. "Interchange stability of a rapidly rotating magnetosphere." *Planetary and Space Science* 24(12):1151–1154.

Hill, TW. 1983. Solar-wind magnetosphere coupling. In *Solar-Terrestrial Physics*. Springer pp. 261–302.

Hilton, E.J. 2011. The Galactic M Dwarf Flare Rate PhD thesis University of Washington.

Hippke, Michael. 2015. "On the detection of exomoons: A search in Kepler data for the orbital sampling effect and the Scatter Peak." *The Astrophysical Journal* 806(1):51.

Hirabayashi, K and M Hoshino. 2013. "Magnetic reconnection under anisotropic magnetohydrodynamic approximation." *Physics of Plasmas* 20(11):112111.

Hubert, B., J.-C. Grard, D. S. Evans, M. Meurant, S. B. Mende, H. U. Frey and T. J. Immel. 2002. "Total electron and proton energy input during auroral substorms: Remote sensing with IMAGE-FUV." *Journal of Geophysical Research: Space Physics* 107(A8):SMP 15–1–SMP 15–12.
URL: *http://dx.doi.org/10.1029/2001JA009229*

Hudson, Hugh S. 2011. "Global properties of solar flares." *Space Science Reviews* 158(1):5–41.

Hunten, D. M. 1955. "Some photometric observations of auroral spectra." *Journal of Atmospheric and Terrestrial Physics* 7:141–151.

Jackman, Caitriona M, JA Slavin, MG Kivelson, DJ Southwood, Nick Achilleos, MF Thomsen, GA DiBraccio, JP Eastwood, MP Freeman, MK Dougherty et al. 2014. "Saturn's dynamic magnetotail: A comprehensive magnetic field and plasma survey of plasmoids and traveling compression regions and their role in global magnetospheric dynamics." *Journal of Geophysical Research: Space Physics* 119(7):5465–5494.

Jackman, Charles H, J Eric Nielsen, Dale J Allen, Mark C Cerniglia, Richard D McPeters, Anne R Douglass and Richard B Rood. 1993. "The effects of the October 1989 solar proton events on the stratosphere as computed using a three-dimensional model." *Geophysical research letters* 20(6):459–462.

Jackman, Charles H, Mark C Cerniglia, J Eric Nielsen, Dale J Allen, Joseph M Zawodny, Richard D McPeters, Anne R Douglass, Joan E Rosenfield and Richard B Rood. 1995.

"Two-dimensional and three-dimensional model simulations, measurements, and interpretation of the influence of the October 1989 solar proton events on the middle atmosphere." *Journal of Geophysical Research: Atmospheres* 100(D6):11641–11660.

Johnson, John Asher, Geoffrey W Marcy, Debra A Fischer, Gregory Laughlin, R Paul Butler, Gregory W Henry, Jeff A Valenti, Eric B Ford, Steven S Vogt and Jason T Wright. 2006. "The N2K consortium. VI. Doppler shifts without templates and three new short-period planets." *The Astrophysical Journal* 647(1):600.

Joshi, Manoj. 2003. "Climate model studies of synchronously rotating planets." *Astrobiology* 3(2):415–427.

Joshi, M.M., R.M. Haberle and R.T. Reynolds. 1997. "Simulations of the Atmospheres of Synchronously Rotating Terrestrial Planets Orbiting M Dwarfs: Conditions for Atmospheric Collapse and the Implications for Habitability." *Icarus* 129(2):450 – 465.
URL: *http://www.sciencedirect.com/science/article/pii/S0019103597957936*

Kane, M, DG Mitchell, JF Carbary and SM Krimigis. 2014. "Plasma convection in the nightside magnetosphere of Saturn determined from energetic ion anisotropies." *Planetary and Space Science* 91:1–13.

Kane, M, DG Mitchell, JF Carbary, SM Krimigis and FJ Crary. 2008. "Plasma convection in Saturn's outer magnetosphere determined from ions detected by the Cassini INCA experiment." *Geophysical Research Letters* 35(4).

Kasting, James F and Thomas P Ackerman. 1986. "Climatic consequences of very high carbon dioxide levels in the Earth's early atmosphere." *Science* 234:1383–1386.

Kay, C, M Opher and M Kornbleuth. 2016. "Probability of CME Impact on Exoplanets Orbiting M Dwarfs and Solar-Like Stars." *The Astrophysical Journal* 826(2):195.

Khodachenko, Maxim L, Ignasi Ribas, Helmut Lammer, Jean-Mathias Grießmeier, Martin Leitner, Franck Selsis, Carlos Eiroa, Arnold Hanslmeier, Helfried K Biernat, Charles J Farrugia et al. 2007. "Coronal mass ejection (CME) activity of low mass M stars as

an important factor for the habitability of terrestrial exoplanets. I. CME impact on expected magnetospheres of Earth-like exoplanets in close-in habitable zones." *Astrobiology* 7(1):167–184.

Kidder, A, RM Winglee and EM Harnett. 2009. "Regulation of the centrifugal interchange cycle in Saturn's inner magnetosphere." *Journal of Geophysical Research: Space Physics* 114(A2).

Kidder, Ariah R. 2011. *Dynamic Heavy Ions and Magnetic Reconnection at Mercury and Saturn*. University of Washington.

Kimura, Tomoki, L Lamy, Chihiro Tao, Sarah V Badman, Satoshi Kasahara, B Cecconi, P Zarka, A Morioka, Y Miyoshi, Daichi Maruno et al. 2013. "Long-term modulations of Saturn's auroral radio emissions by the solar wind and seasonal variations controlled by the solar ultraviolet flux." *Journal of Geophysical Research: Space Physics* 118(11):7019–7035.

Kipping, David M. 2009. "Transit timing effects due to an exomoon–II." *Monthly Notices of the Royal Astronomical Society* 396(3):1797–1804.

Kipping, David M, Duncan Forgan, Joel Hartman, D Nesvornỳ, Gáspár Á Bakos, A Schmitt and L Buchhave. 2013. "The hunt for exomoons with Kepler (HEK). III. The first search for an exomoon around a habitable-zone planet." *The Astrophysical Journal* 777(2):134.

Kipping, David M, Stephen J Fossey and Giammarco Campanella. 2009. "On the detectability of habitable exomoons with Kepler-class photometry." *Monthly Notices of the Royal Astronomical Society* 400(1):398–405.

Kivelson, Margaret G and Christopher T Russell. 1995. *Introduction to space physics*. Cambridge university press.

Kivelson, Margaret Galland. 2015. "Planetary magnetodiscs: Some unanswered questions." *Space Science Reviews* 187(1-4):5–21.

Kivelson, MG and DJ Southwood. 2005. "Dynamical consequences of two modes of centrifugal instability in Jupiter's outer magnetosphere." *Journal of Geophysical Research: Space Physics* 110(A12).

Korenaga, Jun. 2016. "Can mantle convection be self-regulated?" *Science advances* 2(8):e1601168.

Kowalski, Adam F, Suzanne L Hawley, John P Wisniewski, Rachel A Osten, Eric J Hilton, Jon A Holtzman, Sarah J Schmidt and James RA Davenport. 2013. "TIME-RESOLVED PROPERTIES AND GLOBAL TRENDS IN dMe FLARES FROM SIMULTANEOUS PHOTOMETRY AND SPECTRABased on observations obtained with the Apache Point Observatory 3.5 m telescope, which is owned and operated by the Astrophysical Research Consortium." *The Astrophysical Journal Supplement Series* 207(1):15.

Kreidberg, Laura, Jacob L Bean, Jean-Michel Désert, Michael R Line, Jonathan J Fortney, Nikku Madhusudhan, Kevin B Stevenson, Adam P Showman, David Charbonneau, Peter R McCullough et al. 2014. "A precise water abundance measurement for the hot Jupiter WASP-43b." *The Astrophysical Journal Letters* 793(2):L27.

Krissansen-Totton, Joshua, David S Bergsman and David C Catling. 2016. "On detecting biospheres from chemical thermodynamic disequilibrium in planetary atmospheres." *Astrobiology* 16(1):39–67.

Kurth, W. S., D. A. Gurnett, J. T. Clarke, P. Zarka, M. D. Desch, M. L. Kaiser, B. Cecconi, A. Lecacheux, W. M. Farrell, P. Galopeau, J.-C. Gérard, D. Grodent, R. Prangé, M. K. Dougherty and F. J. Crary. 2005. "An Earth-like correspondence between Saturn's auroral features and radio emission." *Nature* 433:722–725.

Lai, Dong, Ch Helling and EPJ Van den Heuvel. 2010. "Mass transfer, transiting stream, and magnetopause in close-in exoplanetary systems with applications to WASP-12." *The Astrophysical Journal* 721(2):923.

Lammer, H., F. Selsis, I. Ribas, E. F. Guinan, S. J. Bauer and W. W. Weiss. 2003. "Atmospheric Loss of Exoplanets Resulting from Stellar X-Ray and Extreme-Ultraviolet Heat-

ing." *The Astrophysical Journal Letters* 598(2):L121.
URL: *http://stacks.iop.org/1538-4357/598/i=2/a=L121*

Lario, D and RB Decker. 2011. "Estimation of solar energetic proton mission-integrated fluences and peak intensities for missions traveling close to the Sun." *Space Weather* 9(11).

Lavvas, Panayotis, Roger V Yelle, Tommi Koskinen, Axel Bazin, Véronique Vuitton, Erik Vigren, Marina Galand, Anne Wellbrock, Andrew J Coates, Jan-Erik Wahlund et al. 2013. "Aerosol growth in Titans ionosphere." *Proceedings of the National Academy of Sciences* 110(8):2729–2734.

Lilensten, J., D. Bernard, M. Barthélémy, G. Gronoff, C. Simon Wedlund and A. Opitz. 2015. "Prediction of blue, red and green aurorae at Mars." *Planetary and Space Science* 115:48–56.

Llama, J, AA Vidotto, M Jardine, K Wood, R Fares and TI Gombosi. 2013. "Exoplanet transit variability: bow shocks and winds around HD 189733b." *Monthly Notices of the Royal Astronomical Society* 436(3):2179–2187.

Llama, Joe, Kenny Wood, M Jardine, AA Vidotto, Ch Helling, L Fossati and CA Haswell. 2011. "The shocking transit of WASP-12b: modelling the observed early ingress in the near-ultraviolet." *Monthly Notices of the Royal Astronomical Society: Letters* 416(1):L41–L44.

Lovis, Christophe and D Fischer. 2010. *Radial velocity techniques for exoplanets*. University of Arizona Press pp. 27–53.

Luger, Rodrigo, Jacob Lustig-Yaeger, David P Fleming, Matt A Tilley, Eric Agol, Victoria S Meadows, Russell Deitrick and Rory Barnes. 2017. "The Pale Green Dot: A Method to Characterize Proxima Centauri b Using Exo-Aurorae." *The Astrophysical Journal* 837(1):63.

Luger, Rodrigo and Rory Barnes. 2015. "Extreme water loss and abiotic O2 buildup on planets throughout the habitable zones of M dwarfs." *Astrobiology* 15(2):119–143.

Marsch, Eckart. 2012. "Helios: Evolution of distribution functions 0.3–1 AU." *Space science reviews* 172(1):23–39.

Masters, Adam, MF Thomsen, SV Badman, Chris S Arridge, DT Young, Andrew J Coates and MK Dougherty. 2011. "Supercorotating return flow from reconnection in Saturn's magnetotail." *Geophysical Research Letters* 38(3).

Mauk, B. and F. Bagenal. 2012. "Comparative Auroral Physics: Earth and Other Planets." *Washington DC American Geophysical Union Geophysical Monograph Series* 197.

Mauk, B. H., S. M. Krimigis and M. H. Acua. 1994. "Neptune's inner magnetosphere and aurora: Energetic particle constraints." *Journal of Geophysical Research: Space Physics* 99(A8):14781–14788.
URL: *http://dx.doi.org/10.1029/94JA00735*

Mauk, BH, DC Hamilton, TW Hill, GB Hospodarsky, RE Johnson, C Paranicas, E Roussos, CT Russell, DE Shemansky, EC Sittler Jr et al. 2009. Fundamental plasma processes in Saturn's magnetosphere. In *Saturn from Cassini-Huygens*. Springer pp. 281–331.

Mauk, BH, J Saur, DG Mitchell, EC Roelof, PC Brandt, TP Armstrong, DC Hamilton, SM Krimigis, N Krupp, SA Livi et al. 2005. "Energetic particle injections in Saturn's magnetosphere." *Geophysical research letters* 32(14).

Mcandrews, Hazel J, Michelle F Thomsen, Chris S Arridge, CM Jackman, RJ Wilson, MG Henderson, RL Tokar, Krishan K Khurana, Edward C Sittler, Andrew J Coates et al. 2009. "Plasma in Saturn's nightside magnetosphere and the implications for global circulation." *Planetary and Space Science* 57(14):1714–1722.

Meadows, V. S., G. N. Arney, E. W. Schwieterman, J. Lustig-Yaeger, A. P. Lincowski, T. Robinson, S. D. Domagal-Goldman, R. K. Barnes, D. P. Fleming, R. Deitrick, R. Luger, P. E. Driscoll, T. R. Quinn and D. Crisp. 2016. "The Habitability of Proxima Centauri b: II: Environmental States and Observational Discriminants." *ArXiv e-prints, arXiv:1608.08620* .

Meng, X, G Toth, A Glocer, M-C Fok and TI Gombosi. 2013. "Pressure anisotropy in global magnetospheric simulations: Coupling with ring current models." *Journal of Geophysical Research: Space Physics* 118(9):5639–5658.

Meng, X, G Tóth, MW Liemohn, TI Gombosi and A Runov. 2012. "Pressure anisotropy in global magnetospheric simulations: A magnetohydrodynamics model." *Journal of Geophysical Research: Space Physics* 117(A8).

Mewaldt, RA, CMS Cohen, AW Labrador, RA Leske, GM Mason, MI Desai, MD Looper, JE Mazur, RS Selesnick and DK Haggerty. 2005. "Proton, helium, and electron spectra during the large solar particle events of October–November 2003." *Journal of Geophysical Research: Space Physics* 110(A9).

Mitchell, DG, PC Brandt, EC Roelof, J Dandouras, SM Krimigis, BH Mauk, CP Paranicas, N Krupp, DC Hamilton, WS Kurth et al. 2005. "Energetic ion acceleration in Saturn's magnetotail: Substorms at Saturn?" *Geophysical research letters* 32(20).

Mitra-Kraev, U, LK Harra, M Güdel, M Audard, G Branduardi-Raymont, HRM Kay, R Mewe, AJJ Raassen and L van Driel-Gesztelyi. 2005. "Relationship between X-ray and ultraviolet emission of flares from dMe stars observed by XMM-Newton." *Astronomy & Astrophysics* 431(2):679–686.

Miyagoshi, Takehiro, Chihiro Tachinami, Masanori Kameyama and Masaki Ogawa. 2013. "On the vigor of mantle convection in super-Earths." *The Astrophysical Journal Letters* 780(1):L8.

Mizutani, Hitoshi, Tetsuo Yamamoto and Akio Fujimura. 1992. "A new scaling law of the planetary magnetic fields." *Advances in Space Research* 12(8):265–279.

Morton, Timothy D and Jonathan Swift. 2014. "The radius distribution of planets around cool stars." *The Astrophysical Journal* 791(1):10.

Morton, Timothy D, Stephen T Bryson, Jeffrey L Coughlin, Jason F Rowe, Ganesh Ravichandran, Erik A Petigura, Michael R Haas and Natalie M Batalha. 2016. "False

positive probabilities for all Kepler objects of interest: 1284 newly validated planets and 428 likely false positives." *The Astrophysical Journal* 822(2):86.

Nahar, Sultana N. 1999. "Electron-ion recombination rate coefficients, photoionization cross sections, and ionization fractions for astrophysically abundant elements. II. Oxygen ions." *The Astrophysical Journal Supplement Series* 120(1):131.

NASA. 2018. "New Worlds Atlas.".
URL: *https://exoplanets.nasa.gov/newworldsatlas/*

Nichols, JD. 2012. "Candidates for detecting exoplanetary radio emissions generated by magnetosphereionosphere coupling." *Monthly Notices of the Royal Astronomical Society: Letters* 427(1):L75–L79.

Nichols, Jonathan D. 2011. "Magnetosphere–ionosphere coupling at Jupiter-like exoplanets with internal plasma sources: implications for detectability of auroral radio emissions." *Monthly Notices of the Royal Astronomical Society* 414(3):2125–2138.

Nichols, Jonathan D, Graham A Wynn, M Goad, Richard D Alexander, Sarah L Casewell, SW H Cowley, Matt R Burleigh, JT Clarke and D Bisikalo. 2015. "Hubble Space Telescope Observations of the NUV Transit of WASP-12b." *The Astrophysical Journal* 803(1):9.

Nichols, Jonathan D, N Achilleos and Stanley WH Cowley. 2015. "A model of force balance in Jupiter's magnetodisc including hot plasma pressure anisotropy." *Journal of Geophysical Research: Space Physics* 120(12).

Northrop, TG and TJ Birmingham. 1982. "Adiabatic charged particle motion in rapidly rotating magnetospheres." *Journal of Geophysical Research: Space Physics* 87(A2):661–669.

Noyola, JP, S Satyal and ZE Musielak. 2016. "On the radio detection of multiple-exomoon systems due to plasma torus sharing." *The Astrophysical Journal* 821(2):97.

OMalley-James, J. T. and L. Kaltenegger. 2016. "Biofluorescent Worlds: Biological fluores-

cence as a temporal biosignature for flare star worlds." *ArXiv e-prints, arXiv:1608.06930* .

Omholt, Anders. 2012. *The optical aurora.* Vol. 4 Springer Science & Business Media.

OMalley-James, Jack T and L Kaltenegger. 2017. "UV surface habitability of the TRAPPIST-1 system." *Monthly Notices of the Royal Astronomical Society: Letters* 469(1):L26–L30.

Parker, Eugene N. 1958. "Dynamics of the Interplanetary Gas and Magnetic Fields." *The Astrophysical Journal* 128:664.

Parks, George K. 1991. "Physics of space plasmas-an introduction.".

Pavlov, Alexander A, James F Kasting, Lisa L Brown, Kathy A Rages and Richard Freedman. 2000. "Greenhouse warming by CH4 in the atmosphere of early Earth." *Journal of Geophysical Research: Planets* 105(E5):11981–11990.

Perreault, Paul and SI Akasofu. 1978. "A study of geomagnetic storms." *Geophysical Journal International* 54(3):547–573.

Persoon, AM, DA Gurnett, O Santolik, WS Kurth, JB Faden, JB Groene, GR Lewis, AJ Coates, RJ Wilson, RL Tokar et al. 2009. "A diffusive equilibrium model for the plasma density in Saturn's magnetosphere." *Journal of Geophysical Research: Space Physics* 114(A4).

Persoon, AM, DA Gurnett, WS Kurth, GB Hospodarsky, JB Groene, P Canu and MK Dougherty. 2005. "Equatorial electron density measurements in Saturn's inner magnetosphere." *Geophysical research letters* 32(23).

Pilkington, Nathan M, Nicholas Achilleos, Christopher Stephen Arridge, Patrick Guio, Adam Masters, LC Ray, Nicholas Sergis, Michelle F Thomsen, AJ Coates and MK Dougherty. 2015. "Internally driven large-scale changes in the size of Saturn's magnetosphere." *Journal of Geophysical Research: Space Physics* 120(9):7289–7306.

Porter, HS, CH Jackman and AES Green. 1976. "Efficiencies for production of atomic nitrogen and oxygen by relativistic proton impact in air." *The Journal of Chemical Physics* 65(1):154–167.

Prajapati, RP and RK Chhajlani. 2010. "Effect of pressure anisotropy and flow velocity on Kelvin–Helmholtz instability of anisotropic magnetized plasma using generalized polytrope laws." *Physics of Plasmas* 17(11):112108.

Preusse, S, A Kopp, J Büchner and U Motschmann. 2005. "Stellar wind regimes of close-in extrasolar planets." *Astronomy & Astrophysics* 434(3):1191–1200.

Preusse, S, A Kopp, J Büchner and U Motschmann. 2007. "MHD simulation scenarios of the stellar wind interaction with Hot Jupiter magnetospheres." *Planetary and Space Science* 55(5):589–597.

Ranjan, S., R. Wordsworth and D. D. Sasselov. 2017. "The Surface UV Environment on Planets Orbiting M Dwarfs: Implications for Prebiotic Chemistry and the Need for Experimental Follow-up." *The Astrophysical Journal* 843:110.

Rapf, Rebecca J and Veronica Vaida. 2016. "Sunlight as an energetic driver in the synthesis of molecules necessary for life." *Physical Chemistry Chemical Physics* 18(30):20067–20084.

Redfield, Seth, Michael Endl, William D Cochran and Lars Koesterke. 2008. "Sodium absorption from the exoplanetary atmosphere of HD 189733b detected in the optical transmission spectrum." *The Astrophysical Journal Letters* 673(1):L87.

Ribas, Ignasi, Emeline Bolmont, Franck Selsis, Ansgar Reiners, Jérémy Leconte, Sean N Raymond, Scott G Engle, Edward F Guinan, Julien Morin, Martin Turbet et al. 2016. "The habitability of Proxima Centauri b-I. Irradiation, rotation and volatile inventory from formation to the present." *Astronomy & Astrophysics* 596:A111.

Richardson, John D. 1998. "Thermal plasma and neutral gas in Saturn's magnetosphere." *Reviews of Geophysics* 36(4):501–524.

Richardson, John D and Charles W Smith. 2003. "The radial temperature profile of the solar wind." *Geophysical research letters* 30(5).

Rodger, Craig J, Mark A Clilverd, Pekka T Verronen, Thomas Ulich, Martin J Jarvis and Esa Turunen. 2006. "Dynamic geomagnetic rigidity cutoff variations during a solar proton event." *Journal of Geophysical Research: Space Physics* 111(A4).

Rodger, Craig J, Pekka T Verronen, Mark A Clilverd, Annika Seppälä and Esa Turunen. 2008. "Atmospheric impact of the Carrington event solar protons." *Journal of Geophysical Research: Atmospheres* 113(D23).

Rugheimer, S, A Segura, L Kaltenegger and D Sasselov. 2015. "UV surface environment of Earth-like planets orbiting FGKM stars through geological evolution." *The Astrophysical Journal* 806(1):137.

Rusch, DW, J-C Gerard, Solomon Solomon, PJ Crutzen and GC Reid. 1981. "The effect of particle precipitation events on the neutral and ion chemistry of the middle atmosphereI. Odd nitrogen." *Planetary and Space Science* 29(7):767–774.

Rybicki, George B and Alan P Lightman. 2008. *Radiative processes in astrophysics*. John Wiley & Sons.

Sagan, Carl, BN Khare, WR Thompson, GD McDonald, Michael R Wing, Jeffrey L Bada, Tuan Vo-Dinh and ET Arakawa. 1993. "Polycyclic aromatic hydrocarbons in the atmospheres of Titan and Jupiter." *The Astrophysical Journal* 414:399–405.

Sánchez-Lavega, A. 2004. "The magnetic field in giant extrasolar planets." *The Astrophysical Journal Letters* 609(2):L87.

Sandel, B. R., F. Herbert, A. J. Dessler and T. W. Hill. 1990. "Aurora and airglow on the night side of Neptune." *Geophysical Research Letters* 17(10):1693–1696.
URL: *http://dx.doi.org/10.1029/GL017i010p01693*

Sasaki, Takanori, Glen R Stewart and Shigeru Ida. 2010. "Origin of the different ar-

chitectures of the jovian and saturnian satellite systems." *The Astrophysical Journal* 714(2):1052.

Sasaki, Takashi, Jason W Barnes and David P O'Brien. 2012. "Outcomes and duration of tidal evolution in a star-planet-moon system." *The Astrophysical Journal* 754(1):51.

Saur, Joachim, Fritz M Neubauer, Darrell F Strobel and Michael E Summers. 2000. "Io's ultraviolet aurora: Remote sensing of Io's interaction." *Geophysical research letters* 27(18):2893–2896.

Saur, Joachim, Fritz M Neubauer, JEP Connerney, Philippe Zarka and Margaret G Kivelson. 2004. "Plasma interaction of Io with its plasma torus." *Jupiter: The Planet, Satellites and Magnetosphere* 1:537–560.

Scalo, J., L. Kaltenegger, A. G. Segura, M. Fridlund, I. Ribas, Y. N. Kulikov, J. L. Grenfell, H. Rauer, P. Odert, M. Leitzinger, F. Selsis, M. L. Khodachenko, C. Eiroa, J. Kasting and H. Lammer. 2007. "M Stars as Targets for Terrestrial Exoplanet Searches And Biosignature Detection." *Astrobiology* 7:85–166.

Schield, MA. 1969. "Pressure balance between solar wind and magnetosphere." *Journal of Geophysical Research* 74(5):1275–1286.

Schubert, G and KM Soderlund. 2011. "Planetary magnetic fields: Observations and models." *Physics of the Earth and Planetary Interiors* 187(3-4):92–108.

Schwieterman, Edward W, Victoria S Meadows, Shawn D Domagal-Goldman, Drake Deming, Giada N Arney, Rodrigo Luger, Chester E Harman, Amit Misra and Rory Barnes. 2016. "Identifying planetary biosignature impostors: spectral features of CO and O4 resulting from abiotic O2/O3 production." *The Astrophysical Journal Letters* 819(1):L13.

Segura, Antigona, James F Kasting, Victoria Meadows, Martin Cohen, John Scalo, David Crisp, Rebecca AH Butler and Giovanna Tinetti. 2005. "Biosignatures from Earth-like planets around M dwarfs." *Astrobiology* 5(6):706–725.

Segura, Antígona, Kara Krelove, James F Kasting, Darrell Sommerlatt, Victoria Meadows, David Crisp, Martin Cohen and Eli Mlawer. 2003. "Ozone concentrations and ultraviolet fluxes on Earth-like planets around other stars." *Astrobiology* 3(4):689–708.

Segura, Antígona, Lucianne M Walkowicz, Victoria Meadows, James Kasting and Suzanne Hawley. 2010. "The effect of a strong stellar flare on the atmospheric chemistry of an Earth-like planet orbiting an M dwarf." *Astrobiology* 10(7):751–771.

Sergis, N, CM Jackman, MF Thomsen, SM Krimigis, DG Mitchell, DC Hamilton, MK Dougherty, N Krupp and RJ Wilson. 2017. "Radial and local time structure of the Saturnian ring current, revealed by Cassini." *Journal of Geophysical Research: Space Physics* 122(2):1803–1815.

Sergis, N, SM Krimigis, EC Roelof, Chris S Arridge, AM Rymer, DG Mitchell, DC Hamilton, N Krupp, MF Thomsen, MK Dougherty et al. 2010. "Particle pressure, inertial force, and ring current density profiles in the magnetosphere of Saturn, based on Cassini measurements." *Geophysical Research Letters* 37(2).

Seth, SP, SA Haider and KI Oyama. 2002. "Photoelectron flux and nightglow emissions of 5577 and 6300 Å due to solar wind electron precipitation in Martian atmosphere." *Journal of Geophysical Research: Space Physics* 107(A10).

Shea, MA and DF Smart. 1992. "Recent and historical solar proton events." *Radiocarbon* 34(2):255–262.

Shields, A. L., S. Ballard and J. A. Johnson. 2016. "The habitability of planets orbiting M-dwarf stars." *Physics Report* 663(7):1–38.

Shkarofsky, Issie Peter, Tudor Wyatt Johnston and Morrel Paul Bachynski. 1966. *The particle kinetics of plasmas*. Reading, Mass.: Addison-Wesley Publishing Company.

Shkolnik, Evgenya, David A Bohlender, Gordon AH Walker and Andrew Collier Cameron. 2008. "The on/off nature of star-planet interactions." *The Astrophysical Journal* 676(1):628.

Shkolnik, Evgenya, Gordon AH Walker and David A Bohlender. 2003. "Evidence for planet-induced chromospheric activity on HD 179949." *The Astrophysical Journal* 597(2):1092.

Silvestri, Nicole M, Suzanne L Hawley and Terry D Oswalt. 2005. "The chromospheric activity and ages of M dwarf stars in wide binary systems." *The Astronomical Journal* 129(5):2428.

Siscoe, George L. 1983. Solar system magnetohydrodynamics. In *Solar-terrestrial physics*. Springer pp. 11–100.

Sittler, EC, MF Blanc and JD Richardson. 2006. "Proposed model for Saturn's auroral response to the solar wind: Centrifugal instability model." *Journal of Geophysical Research: Space Physics* 111(A6).

Sittler, EC, N Andre, M Blanc, M Burger, RE Johnson, A Coates, A Rymer, D Reisenfeld, MF Thomsen, A Persoon et al. 2008. "Ion and neutral sources and sinks within Saturn's inner magnetosphere: Cassini results." *Planetary and Space Science* 56(1):3–18.

Slanger, T. G., P. C. Cosby, D. L. Huestis and T. A. Bida. 2001. "Discovery of the Atomic Oxygen Green Line in the Venus Night Airglow." *Science* 291:463–465.

Smart, DF, MA Shea and EO Flückiger. 2000. Magnetospheric models and trajectory computations. In *Cosmic Rays and Earth*. Springer pp. 305–333.

Snowden, D, R Winglee and A Kidder. 2011. "Titan at the edge: 1. Titan's interaction with Saturn's magnetosphere in the prenoon sector." *Journal of Geophysical Research: Space Physics* 116(A8).

Solomon, Stanley C. 1991. "Optical aeronomy." *Reviews of Geophysics Supplement* 29:1089–1109.

Sorba, AM, NA Achilleos, Patrick Guio, Christopher Stephen Arridge, NM Pilkington, Adam Masters, Nicholas Sergis, Andrew J Coates and MK Dougherty. 2017. "Modeling the compressibility of Saturn's magnetosphere in response to internal and external influences." *Journal of Geophysical Research: Space Physics* 122(2):1572–1589.

Steele, D. P. and D. J. McEwen. 1990. "Electron auroral excitation efficiencies and intensity ratios." *Journal of Geophysical Research: Space Physics* 95(A7):10321–10336.
URL: *http://dx.doi.org/10.1029/JA095iA07p10321*

Steffl, Andrew J, Fran Bagenal and A Ian F Stewart. 2004. "Cassini UVIS observations of the Io plasma torus: II. Radial variations." *Icarus* 172(1):91–103.

Stevenson, DJ. 1983. "Planetary magnetic fields." *Reports on Progress in Physics* 46(5):555.

Tachinami, Chihiro, H Senshu and S Ida. 2011. "Thermal evolution and lifetime of intrinsic magnetic fields of super-Earths in habitable zones." *Astrophysical Journal* 726(2):70.

Talboys, DL, CS Arridge, EJ Bunce, AJ Coates, SWH Cowley and MK Dougherty. 2009. "Characterization of auroral current systems in Saturn's magnetosphere: High-latitude Cassini observations." *Journal of Geophysical Research: Space Physics* 114(A6).

Talboys, DL, EJ Bunce, Stanley WH Cowley, Chris S Arridge, Andrew J Coates and MK Dougherty. 2011. "Statistical characteristics of field-aligned currents in Saturn's nightside magnetosphere." *Journal of Geophysical Research: Space Physics* 116(A4).

Tarter, J. C., P. R. Backus, R. L. Mancinelli, J. M. Aurnou, D. E. Backman, G. S. Basri, A. P. Boss, A. Clarke, D. Deming, L. R. Doyle, E. D. Feigelson, F. Freund, D. H. Grinspoon, R. M. Haberle, S. A. Hauck, II, M. J. Heath, T. J. Henry, J. L. Hollingsworth, M. M. Joshi, S. Kilston, M. C. Liu, E. Meikle, I. N. Reid, L. J. Rothschild, J. Scalo, A. Segura, C. M. Tang, J. M. Tiedje, M. C. Turnbull, L. M. Walkowicz, A. L. Weber and R. E. Young. 2007. "A Reappraisal of The Habitability of Planets around M Dwarf Stars." *Astrobiology* 7:30–65.

Teachey, Alex, David M Kipping and Allan R Schmitt. 2017. "HEK VI: On the Dearth of Galilean Analogs in Kepler and the Exomoon Candidate Kepler-1625b I." *arXiv preprint arXiv:1707.08563* .

Testa, Paola, Jeremy J Drake and Giovanni Peres. 2004. "The density of coronal plasma in active stellar coronae." *The Astrophysical Journal* 617(1):508.

Thomsen, MF. 2013. "Saturn's magnetospheric dynamics." *Geophysical Research Letters* 40(20):5337–5344.

Thomsen, MF, DB Reisenfeld, DM Delapp, RL Tokar, DT Young, FJ Crary, EC Sittler, MA McGraw and JD Williams. 2010. "Survey of ion plasma parameters in Saturn's magnetosphere." *Journal of Geophysical Research: Space Physics* 115(A10).

Tilley, Matt A., Antígona Segura, Victoria Meadows, Suzanne Hawley and James Davenport. 2017. "Modeling Repeated M-dwarf Flaring at an Earth-like Planet in the Habitable Zone: I. Atmospheric Effects for an Unmagnetized Planet." *In Preparation* .

Tilley, Matt A, Erika M Harnett and Robert M Winglee. 2016. "Extrasolar giant magnetospheric response to steady-state stellar wind pressure at 10, 5, 1, and 0.2 AU." *The Astrophysical Journal* 827(1):77.

Tokar, RL, RJ Wilson, RE Johnson, MG Henderson, MF Thomsen, MM Cowee, EC Sittler, DT Young, FJ Crary, HJ McAndrews et al. 2008. "Cassini detection of water-group pick-up ions in the Enceladus torus." *Geophysical Research Letters* 35(14).

Toon, Owen B, CP McKay, TP Ackerman and K Santhanam. 1989. "Rapid calculation of radiative heating rates and photodissociation rates in inhomogeneous multiple scattering atmospheres." *Journal of Geophysical Research: Atmospheres* 94(D13):16287–16301.

Varela, J, V Reville, AS Brun, F Pantellini and P Zarka. 2016. "Radio emission in Mercury magnetosphere." *Astronomy & Astrophysics* 595:A69.

Vasyliunas, VM. 1983. "Plasma distribution and flow." *Physics of the Jovian magnetosphere* pp. 395–453.

Vasyliunas, Vytenis M., Joseph R. Kan, George L. Siscoe and S.-I. Akasofu. 1982. "Scaling relations governing magnetospheric energy transfer." *Planetary and Space Science* 30(4):359 – 365.
URL: *http://www.sciencedirect.com/science/article/pii/0032063382900411*

Verronen, PT, Esa Turunen, Th Ulich and E Kyrölä. 2002. Modelling the effects of the October 1989 solar proton event on mesospheric odd nitrogen using a detailed ion and neutral chemistry model. In *Annales Geophysicae*. Vol. 20 Copernicus GmbH pp. 1967–1976.

Vida, K, Zs Kővári, A Pál, K Oláh and L Kriskovics. 2017. "Frequent Flaring in the TRAPPIST-1 SystemUnsuited for Life?" *The Astrophysical Journal* 841(124):6pp.

Vidotto, AA, M Jardine and Ch Helling. 2010. "Early UV ingress in WASP-12b: measuring planetary magnetic fields." *The Astrophysical Journal Letters* 722(2):L168.

Waite, JH, DT Young, TE Cravens, AJ Coates, FJ Crary, B Magee and J Westlake. 2007. "The process of tholin formation in Titan's upper atmosphere." *Science* 316(5826):870–875.

Wakeford, HR, David K Sing, D Deming, NP Gibson, JJ Fortney, AS Burrows, G Ballester, N Nikolov, Suzanne Aigrain, G Henry et al. 2013. "HST hot Jupiter transmission spectral survey: detection of water in HAT-P-1b from WFC3 near-IR spatial scan observations." *Monthly Notices of the Royal Astronomical Society* 435(4):3481–3493.

Walkowicz, Lucianne M, Christopher M Johns-Krull and Suzanne L Hawley. 2008. "Characterizing the near-UV environment of M dwarfs." *The Astrophysical Journal* 677(1):593.

Wang, C., J. P. Han, H. Li, Z. Peng and J. D. Richardson. 2014. "Solar wind-magnetosphere energy coupling function fitting: Results from a global MHD simulation." *Journal of Geophysical Research: Space Physics* 119(8):6199–6212.
URL: *http://dx.doi.org/10.1002/2014JA019834*

Williams, Darren M. 2013. "Capture of terrestrial-sized moons by gas giant planets." *Astrobiology* 13(4):315–323.

Wilson, RJ, F Bagenal, PA Delamere, M Desroche, BL Fleshman and V Dols. 2013. "Evidence from radial velocity measurements of a global electric field in Saturn's inner magnetosphere." *Journal of Geophysical Research: Space Physics* 118(5):2122–2132.

Wilson, RJ, F Bagenal, T Cassidy, BL Fleshman and F Crary. 2015. "The relative proportions of water group ions in Saturn's inner magnetosphere: A preliminary study." *Journal of Geophysical Research: Space Physics* 120(8):6624–6632.

Wilson, RJ, RL Tokar, MG Henderson, TW Hill, MF Thomsen and DH Pontius. 2008. "Cassini plasma spectrometer thermal ion measurements in Saturn's inner magnetosphere." *Journal of Geophysical Research: Space Physics* 113(A12).

Winglee, RM, E Harnett and A Kidder. 2009. "Relative timing of substorm processes as derived from multifluid/multiscale simulations: Internally driven substorms." *Journal of Geophysical Research: Space Physics* 114(A9).

Winglee, Robert and Erika Harnett. 2016*a*. "The influence of temperature anisotropies in controlling the development of magnetospheric substorms." *arXiv preprint arXiv:1605.01399* .

Winglee, Robert M and Erika M Harnett. 2016*b*. "Magnetosphere Magnetic Field Wobble Effects on the Dynamics of the Jovian Magnetosphere." *arXiv preprint arXiv:1607.02167* .

Wolszczan, Aleksander and Dail A Frail. 1992. "A Planetary System Around the Millisecond Pulsar PSR1257 (Plus) 12." *Nature* 355(6356):145.

Wood, BE, H-R Müller, GP Zank, VV Izmodenov and JL Linsky. 2004. "The heliospheric hydrogen wall and astrospheres." *Advances in Space Research* 34(1):66–73.

Wood, Brian E. 2004. "Astrospheres and solar-like stellar winds." *Living Reviews in Solar Physics* 1(1):2.

Wood, Brian E, H-R Müller, Gary P Zank, Jeffrey L Linsky and Seth Redfield. 2005. "New mass-loss measurements from astrospheric Lyα absorption." *The Astrophysical Journal Letters* 628(2):L143.

Wood, Brian E and Jeffrey L Linsky. 1997. "A new measurement of the electron density in the local interstellar medium." *The Astrophysical Journal Letters* 474(1):L39.

Wood, Brian E, Jeffrey L Linsky, Hans-Reinhard Müller and Gary P Zank. 2001. "Observational estimates for the mass-loss rates of α Centauri and Proxima Centauri using Hubble Space Telescope Lyα spectra." *The Astrophysical Journal Letters* 547(1):L49.

Yashiro, S, S Akiyama, N Gopalswamy and RA Howard. 2006. "Different power-law indices in the frequency distributions of flares with and without coronal mass ejections." *The Astrophysical Journal Letters* 650(2):L143.

Yelle, Roger, Helmut Lammer and Wing-Huen Ip. 2008. "Aeronomy of extra-solar giant planets." *Space Science Reviews* 139(1-4):437–451.

Youngblood, Allison, Kevin France, RO Loyd, Alexander Brown, James P Mason, P Christian Schneider, Matt A Tilley, Zachory K Berta-Thompson, Andrea Buccino, Cynthia S Froning et al. 2017. "The MUSCLES Treasury Survey IV: Scaling Relations for Ultraviolet, Ca II K, and Energetic Particle Fluxes from M Dwarfs." *arXiv preprint arXiv:1705.04361* .

Yung, Yuk Ling and William B DeMore. 1999. *Photochemistry of planetary atmospheres*. Oxford University Press on Demand.

Zarka, P. 2006. Hot Jupiters and Magnetized Stars: Giant Analogs of the Satellite-Jupiter System. In *Planetary Radio Emissions VI*, ed. H. O. Rucker, W. Kurth and G. Mann. p. 543.

Zarka, Philippe. 1998. "Auroral radio emissions at the outer planets: Observations and theories." *Journal of Geophysical Research: Planets* 103(E9):20159–20194.

Zarka, Philippe. 2007. "Plasma interactions of exoplanets with their parent star and associated radio emissions." *Planetary and Space Science* 55(5):598–617.

Zarka, Philippe, Joseph Lazio and Gregg Hallinan. 2015. "Magnetospheric Radio Emissions from Exoplanets with the SKA." *PoS* p. 120.

Zarka, Philippe, Rudolf A Treumann, Boris P Ryabov and Vladimir B Ryabov. 2001.

Magnetically-driven planetary radio emissions and application to extrasolar planets. In *Physics of Space: Growth Points and Problems*. Springer pp. 293–300.

Zuluaga, J. I. and S. Bustamante. 2016. "Geomagnetic properties of Proxima Centauri b analogues." *ArXiv e-prints, arXiv:1609.00707* .

Zurbuchen, Thomas H, Jim M Raines, George Gloeckler, Stamatios M Krimigis, James A Slavin, Patrick L Koehn, Rosemary M Killen, Ann L Sprague, Ralph L McNutt and Sean C Solomon. 2008. "MESSENGER observations of the composition of Mercury's ionized exosphere and plasma environment." *Science* 321(5885):90–92.